Experimental Study on Turbulent Characteristics of Surface Attaching Jets

by

Mohammad Shajid Rahman

A Thesis submitted to the Faculty of Graduate Studies of
The University of Manitoba
in partial fulfillment of the requirements for the degree of

DOCTOR OF PHILOSOPHY

Department of Mechanical Engineering
University of Manitoba
Winnipeg

ABSTRACT

The characteristics of turbulent jets interacting with a free surface were investigated experimentally. The experiments were performed to quantify the effects of offset height and nozzle geometry on the turbulent characteristics at low Reynolds number (Re = 5500). The offset height ratio of a square jet was varied from 1 to 4. For the nozzle geometry effect, four nozzle configurations including circular, square, rectangular with minor axis oriented parallel to the surface-normal direction, and rectangular with its major axis oriented parallel to the surface-normal direction were tested with a fixed offset height ratio of 2. A particle image velocimetry system was used to perform the velocity measurements. Various quantities were investigated, including instantaneous velocities and turbulent statistics up to the fourth order moment. The jet-surface interaction was examined using mean surface velocity, velocity defect, vorticity thickness and surface turbulence intensities. The turbulent structures in the interaction region were investigated using two-point correlations, joint probability density functions and proper orthogonal decomposition (POD).

Turbulent statistics along the free surface revealed that the surface was in the state of stretching and contracting due to the alternating velocity gradient. The straining effect became more severe for shallower jet. For a given offset height ratio, the greatest mean strain at the free surface was produced by the jet issuing in the minor plane of the rectangular nozzle. This nozzle configuration also led to enhancements in the peak values of the surface velocity (about 37%) and turbulence intensities (up to 24%) compared to the circular, square and the jet discharged in the major plane of the rectangular nozzle.

The two-point correlations and POD results indicated that the spatial coherence of the velocity fluctuations reduced in the upper shear layer than the lower shear layer. Shorter offset height ratio experienced a slower fractional energy convergence due to a reduction in the structure size under confinement. The re-orientation of the rectangular nozzle to major axis increased the spatial coherence in the interaction region, which led to an about 21% higher fractional energy contribution of the most dominant POD mode (the first mode) compared to the other configurations.

ACKNOWLEDGMENTS

I would like to acknowledge the invaluable guidance and support of my supervisor, Professor Mark F. Tachie. My gratitude also goes to the other members of my Ph.D. committee, Professor Shawn Clark and Professor Robert Derksen for their patience and useful suggestions. I am thankful to the external examiner, Professor Peter Oshkai for his critical review and suggestion to improve the quality of the thesis.

The financial support of Natural Sciences and Engineering Research Council (NSERC) of Canada, and the University of Manitoba is gratefully acknowledged.

I salute all of my colleagues including Dr. Baafour Nyantekyi-Kwakye and Dr. Godwin F. K. Tay for their co-operation and friendship. I would like to thank the technicians in the Mechanical Engineering department especially, Mr. Paul Krueger for their diverse technical assistance.

Finally, but not the least, my thanks go to all of my friends right here in Canada for their patient friendship in the course of this program.

DEDICATION

It was about six years back, when I was writing the dedication note for my master's thesis to my mother who always comes first in my mind in every living condition, I decided to dedicate the next one to my deprived father. But later the thoughts changed. I noticed that I used to avoid the importance of three precious persons in my life who possess such a gifted strength that nothing is capable of blemish their innocence. This thesis is dedicated to my elder sister; her son, Ashik; and her daughter, Rupa.

I believe, not all of the following 290 pages written in English, only this small dedication letter is enough to make a smile on the face of my poor father.

TABLE OF CONTENTS

LIST OF TABLES

LIST OF FIGURES

LIST OF EQUATIONS

NOMENCLATURE

English Symbols

a	growth rate for the profile of $<u^2>^{0.5}/\Delta U$ or $<v^2>^{0.5}/\Delta U$ vs x'
A	an arbitrary quantity in two-point correlation
A_n	cross-sectional area of the nozzle
b	increasing rate of y^{**}
B	an arbitrary quantity in two-point correlation
B_i	systematic uncertainty limits
B_R	total systematic error
B_1	fitting parameter for $\Delta U/U_j$ distribution
B_2	fitting parameter for $\Delta U/U_m$ distribution
C	auto-covariance matrix
C_μ	k-ε RANS modelling coefficient
d	nozzle width
d_l	light sheet thickness
d_p	particle diameter
d_t	particle image diameter
D_a	aperture diameter
E	prescribed LSE condition
E_R	total uncertainty
E_T	total turbulent kinetic energy in all modes
f	focal length of camera
$f^\#$	f number of camera
F_u	flatness of streamwise velocity fluctuation
F_v	flatness of surface-normal velocity fluctuation
F_α	flatness of velocity fluctuations
Fr	Froude number
g	acceleration due to gravity

h	offset height of the center of the nozzle from the free surface
H	Distance between the center of the nozzle and the bottom wall
I	intensity of the laser sheet
I_o	peak intensity of the laser sheet
I_p	particle image intensity
k	turbulent kinetic energy
K	confidence coefficient in error estimation
K_d	maximum velocity decay rate
$K_{d,f}$	maximum velocity decay rate of free jet
K_s	spread rate
L_a	attachment length
L_p	potential core length
Lx_{uu}	streamwise extent of R_{uu}
Lx_{vv}	streamwise extent of R_{vv}
$Lx_{\lambda\lambda}$	streamwise extent of $R_{\lambda\lambda}$
Ly_{uu}	surface-normal extent of R_{uu}
Ly_{vv}	surface-normal extent of R_{vv}
$Ly_{\lambda\lambda}$	surface-normal extent of $R_{\lambda\lambda}$
m	number of POD modes used for reconstruction
m'	increasing rate of mass flux
M_v	number of the velocity vectors in each snapshot
M_f	magnification factor
n_{uv}	total number of the velocity pairs (u, v) per bin
n'	increasing rate for the profile of $<u^2>^{0.5}/\Delta U$ or $<v^2>^{0.5}/\Delta U$ vs x^*
N_b	total number of the velocity pairs (u, v) in the sample
N_s	number of snapshots
p	index corresponding to number of velocity vector in each snapshot
P	pressure
P_i	random uncertainty limits
P_k	production of TKE
P_k^*	production of TKE normalized by U_m^3/h

P_n	production of the normal component of TKE
P_n^*	production of the normal component of TKE normalized by U_m^3/h
P_R	total random error
P_s	production of the shear component of TKE
P_s^*	production of the shear component of TKE normalized by U_m^3/h
P_{u^2}	production of streamwise Reynolds normal stress
P_{v^2}	production of surface-normal Reynolds normal stress
P_{-uv}	production of Reynolds shear stress
q	index corresponding to number of snapshot
R	a measured variable
R_{uu}	two-point auto-correlation of streamwise velocity fluctuation
R_{vv}	two-point auto-correlation of surface-normal velocity fluctuation
R_{uv}	two-point cross-correlation between streamwise and surface-normal velocity fluctuation
$R_{\lambda u}$	two-point cross-correlation between swirling strength and streamwise velocity fluctuation
$R_{\lambda v}$	two-point cross-correlation between swirling strength and surface-normal velocity fluctuation
$R_{\lambda\lambda}$	two-point auto-correlation of swirling strength
Re	Reynolds number
S	scale factor
S_R	standard deviation of a sample size of a measured quantity
S_u	skewness of streamwise velocity fluctuation
S_v	skewness of surface-normal velocity fluctuation
S_α	skewness of velocity fluctuations
St	Stokes number
u	streamwise fluctuating velocity
$<u^2>$	streamwise Reynolds normal stress
$<u^3>$	triple velocity correlation
$<uv>$	Reynolds shear stress in x-y plane

$<uv^2>$	triple velocity correlation
$<u^2v>$	triple velocity correlation
$<uw>$	Reynolds shear stress in x-z plane
U	streamwise mean velocity
U_i	streamwise instantaneous velocity
U_j	jet exit velocity
U_m	local maximum streamwise mean velocity
U_s	streamwise mean velocity at the free surface
v	surface-normal fluctuating velocity
v_s	settling velocity of seeding particle
$<v^2>$	surface-normal Reynolds normal stress
$<v^3>$	triple velocity correlation
$<vw>$	Reynolds shear stress in y-z plane
V	surface-normal mean velocity
V_i	surface-normal instantaneous velocity
w	spanwise fluctuating velocity
w_1	length of the nozzle exit in spanwise direction
$<w^2>$	spanwise Reynolds normal stress
W	spanwise mean velocity
x	streamwise flow direction
x_g	geometric virtual origin
x_o	kinematic virtual origin
x_{ref}	reference streamwise distance
x_1	fitting parameter for $\phi/(U_m d)$ curve
x_2	fitting parameter for the profile of $<u^2>^{0.5}/\Delta U$ or $<v^2>^{0.5}/\Delta U$ vs x^*
x_3	fitting parameter for the profile of $<u^2>^{0.5}/\Delta U$ or $<v^2>^{0.5}/\Delta U$ vs x'
x_4	fitting parameter for y^{**}
$x_{\lambda\lambda}$	total streamwise extent of $R_{\lambda\lambda}$
x^*	$(x - L_a)/h$
x'	$(x - L_a)/d$
x''	$(x - L_p)/d$

X	matrix of fluctuating velocity components
y	surface-normal flow direction
y_{ref}	reference surface-normal distance
$y_{0.5}$	half-velocity width
$y_{\lambda\lambda}$	total surface-normal extent of $R_{\lambda\lambda}$
y^s	surface-normal distance measured from the free surface
$y^s{}_{0.5}$	half-velocity width measured from the free surface
y'	surface-normal distance measured relative to the location of U_m
y^*	$\phi/(U_m d)$
y^{**}	normalized extents of $R_{\lambda\lambda}$
z	spanwise flow direction
$z_{0.5}$	spanwise jet half width

Greek Symbols

α	velocity fluctuations (u or v)
α_T	entrainment coefficient
$\Lambda_{ci,z}$	signed swirling strength
ε	average least-squares truncation error
μ_f	dynamic viscosity of fluid
ν	kinematic viscosity
ν_t	Eddy viscosity
ϕ_m	mass flux
ρ_f	fluid density
ρ_p	particle density
$\rho_{-<uv>}$	correlation coefficient of $-<uv>$
$\rho_{-<uw>}$	correlation coefficient of $-<uw>$
τ_p	response time of seeding particle
λ_l	wavelength of the laser light
λ_{ci}	imaginary eigenvalue, swirling strength
$\lambda_{ci,z}$	swirling strength associated with the spanwise vortex core
λ_{cr}	real eigenvalue

ω_z	spanwise mean vorticity
ω'_z	spanwise vorticity fluctuation
θ_i	sensitivity coefficients
Δ	width of the bin in JPDF
Δs	particle displacement
Δt	laser pulse separation time
ΔU	mean velocity defect
Δx	spatial separation in the streamwise direction

Acronyms

AP	attachment point
AR	aspect ratio
CCD	charge-coupled device
CFD	computational fluid dynamics
DNS	direct numerical simulation
EGH	exponential-Gaussian hybrid
FFT	fast Fourier transform
FOV	field of view
HWA	hotwire anemometry
IA	interrogation area
JPDF	joint probability density function
LDV	laser Doppler velocimetry
LES	large eddy simulation
MM	micromanometer
PIV	particle image velocimetry
POD	proper orthogonal decomposition
RANS	Reynolds averaged Navier-Stokes
SAR	super abrasion resistant
TKE	turbulent kinetic energy
T/NTI	turbulent/non-turbulent interface
WJPDF	weighted joint probability density function

CHAPTER 1

INTRODUCTION AND OBJECTIVES

1.1 Introduction

Turbulent jets interacting with a free surface are encountered in a wide range of engineering and environmental applications. Examples include household or industrial wastewater discharge into shallow water bodies, excess water release from hydro-electric power dams, purification of water through water aerators, and pump jets of ships. In these examples, the jet configuration is known as a surface attaching jet because the jet upon discharge deflects towards and attaches to the free surface. In many practical applications such as industrial waste disposal and water aerators, turbulence near the free surface has a significant impact on the entrainment and mixing characteristics of the jet. Also, the presence of the free surface introduces a kinematic boundary condition that complicates the flow dynamics in the vicinity of the surface. Thus, understanding of the fundamental physical mechanisms controlling the jet-surface interaction is important for the optimal design of surface-jet producing machinery.

Turbulent free jet is often referend to as the simplest jet configuration where there is no boundary effect. Considerable research attention has been given to the study of turbulent free jets, including turbulent jets issuing from circular nozzles (e.g., Ricou and Spalding, 1961; Wygnanski and Fiedler, 1969; Quinn and Militzer, 1989; Hussein et al., 1994; Mi et al., 2001; Kwon and Seo, 2005; Quinn, 2006) and those issuing from non-circular nozzles (e.g., Grinstein et al., 1995; Lozanova and Stankov, 1998; Mi and Nathan, 2010; Ghasemi et al., 2015; Aleyasin et al., 2017a, 2017b; Aleyasin et al., 2018). The conclusions from these studies suggest that non-circular nozzles are a better configuration for augmenting the jet spreading rate and enhancing turbulent mixing compared to a circular nozzle. It is generally accepted that turbulence is not completely random but may be envisioned as comprising certain organized structures called coherent structures. The archival literature on turbulent jets suggests that the turbulence in both the near and far field of the jet is strongly influenced by the dynamics of large-scale coherent structures (Crow and Champaign, 1971; Brown and Roshko, 1974; Hussain and Zaman, 1981; Gordeyev and Thomas, 2000, 2002; Bi et al., 2003; Gamard et al., 2004; Shinneeb et al., 2008a, 2008b). These coherent structures are believed to be not only responsible for the mass, momentum and heat transfer within the jet, but also control the mixing and entrainment characteristics of the jet.

Despite the large body of literature on the mixing and turbulent characteristics of free jets, far less is documented with regards to surface attaching jets. A schematic of a surface attaching jet in the vertical jet symmetry plane is shown in Fig. 1.1. The jet is formed when a nozzle of width (d) and exit velocity, U_j, is placed at an offset height (h) relative to the free surface. The height, h, is measured from the center of the nozzle to the free surface. The origin of the Cartesian coordinate system adopted herein is located at the center of the nozzle in the jet exit plane; x and y represent the streamwise and surface-normal directions, respectively. U, V, u, and v represent the streamwise mean velocity,

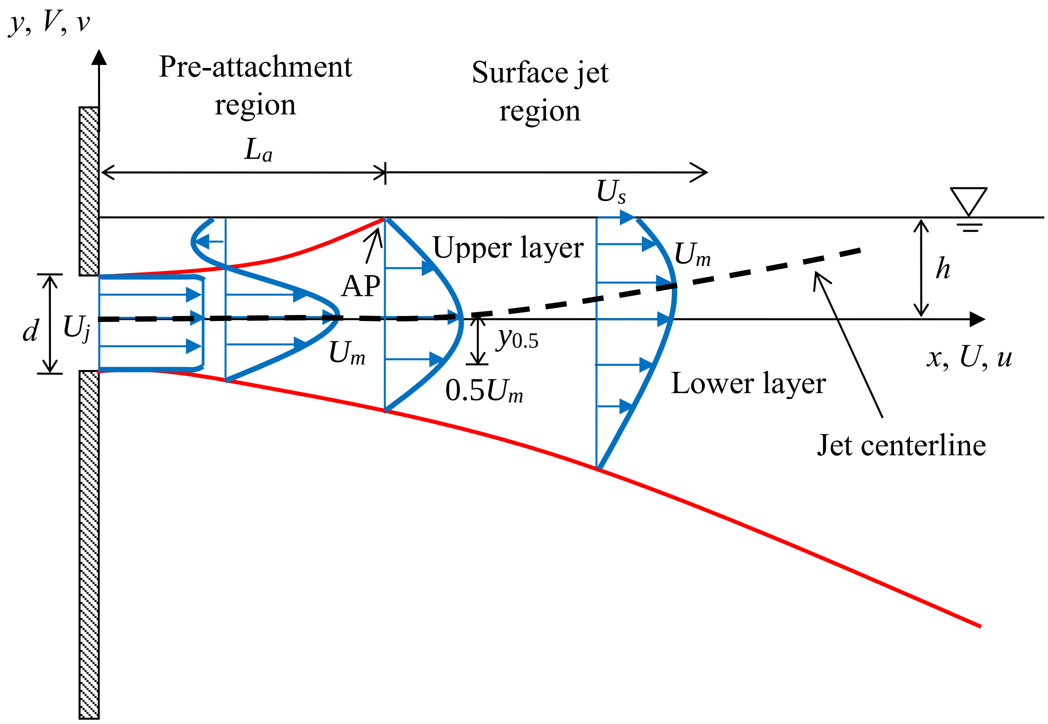

Figure 1.1. Schematic diagram of surface attaching jet.

surface-normal mean velocity, streamwise fluctuating velocity and surface-normal fluctuating velocity, respectively. The spanwise direction, and mean and fluctuating velocities are denoted by z, W and w, respectively. The jet is discharged in to the fluid medium with an exit velocity of U_j. Upon discharge, a low-pressure region is created between the jet and the free surface which in turn causes the jet to attach to the free surface at a point referred to as the attachment point (AP). The streamwise distance from the nozzle exit to the attachment point is termed as the attachment length, L_a. The flow field can be divided into the pre-attachment and surface jet regions. The pre-attachment region starts from the nozzle exit and ends at the attachment point. The surface jet region is located downstream from the attachment point, and within this region, the streamwise mean velocity at the free surface (U_s) is non-zero. The jet is a two-shear-layer flow separated by the loci of local maximum streamwise mean velocity, U_m. The dashed line passing through the loci of U_m is termed as the jet centerline. It is noted that the jet centerline of surface attaching jet moves towards the free surface with the development of the jet downstream (Madnia and Bernal, 1994). The upper and lower portion of the jet centerline within the jet flow region are subsequently referred to as the upper and lower shear layers, respectively; $y_{0.5}$ represents the jet half-velocity width, the surface-normal distance from the location of U_m to $0.5U_m$ in the lower shear layer.

The evolution of the surface attaching jet depends on a number of dimensionless parameters, including the exit Reynolds number, $Re = U_j d/v$, where v is the kinematic viscosity; Froude number, $Fr = U_j/(gh)^{0.5}$, where g is the acceleration of gravity. The flow is also influenced by the nozzle exit geometry (i.e., whether round or non-circular), nozzle exit profile (whether contoured or sharp-edged), and nozzle orientation.

Various measurement methodologies were employed in the past to characterize the influence of the above governing parameters on the mean and turbulence characteristics of the flow. These include pointwise measurement techniques such as hotwire anemometry (HWA) and laser Doppler velocimetry (LDV); and whole-field measurement techniques such as particle image velocimetry (PIV). Oftentimes computational fluid dynamics (CFD) approaches are used such as direct numerical simulation (DNS), Reynolds averaged Navier-Stokes (RANS) calculations, and large eddy simulation (LES). DNS is used to solve turbulent jets at relatively low Reynolds numbers. In RANS calculations, the closure terms in the averaged equations are replaced by a turbulence model, while LES helps in reducing the complexity of the governing equations by application of low-pass filtering.

1.2 Mixing and Jet Spread Quantification

The entrainment and mixing performance of turbulent jets are generally investigated by the decay of local maximum streamwise mean velocity, U_m with the jet development downstream. The streamwsie evolution of the local maximum streamwise mean velocity, U_m, in the far field of the jet is given by the straight line

$$\frac{U_j}{U_m} = K_d\left(\frac{x}{d} - \frac{x_o}{d}\right), \tag{1.1}$$

where, K_d is the slope of the line and x_o is the intercept on the x/d axis. Equation 1.7 suggests that U_m varies with streamwise distance x as x^{-1}. The constant K_d represents the far-field local maximum streamwise mean velocity decay rate of the jet, while x_o represents the kinematic virtual origin. The value of $K_d \approx 0.172$ has been reported for a self-similar turbulent round free jet (Hussein et al., 1994; Pope, 2000).

Madnia and Bernal (1994) suggested that in the limit of low Froude number the free surface behaves as a symmetry plane with the submerged jet merging with its twin or image jet above the free surface. By scaling the normalized velocity profiles and streamwise distance with the offset height ratio, *h/d*, it was shown that the maximum mean streamwise velocity in the far field of the surface attaching jet follows the straight line

$$\frac{U_j d}{U_m h} = \frac{K_{d,f}}{\sqrt{2}}\left(\frac{x}{h} - \frac{x_o}{h}\right), \tag{1.2}$$

where, $K_{d,f}$ is the decay rate of the corresponding free jet, and the scaling factor of $\sqrt{2}$ is introduced to account for the momentum of the image jet above the free surface.

The shear layer spreading of the jet is often quantified using the half-velocity width, $y_{0.5}$. The spread rate is estimated by a least-squares fit of the following straight line on the profile of the half-velocity width with respect to streamwise distance:

$$\frac{y_{0.5}}{d} = K_s \left(\frac{x}{d} - \frac{x_g}{d}\right) \tag{1.3}$$

where, K_s and x_g denote the spread rate and geometric virtual origin, respectively. The value of $K_s \approx 0.100$ has been reported for a self-similar turbulent round free jet (Panchapakesan and Lumley, 1993; Hussein et al., 1994; Pope, 2000).

1.3 Research Motivation and Objectives

Although most previous investigators employed pointwise measurement techniques to measure the mixing and turbulence characteristics of surface attaching jets (e.g., Anthony and Willmarth, 1992; Madnia and Bernal, 1994; Walker et al., 1995; Sankar et al., 2008, 2009), fewer studies employed the particle image velocimetry method (e.g., Tian et al., 2012; Wen et al., 2014a, 2014b; Tay et al., 2017). Pointwise measurement techniques such as HWA and LDV are generally more challenging to use for measuring the surface statistics and examining the large-scale organized structures in the flow. On the other hand, as a whole-field measurement technique, PIV does not only measure the turbulent statistics close the free surface but also provides instantaneous two-dimensional velocity fields for visualizing the instantaneous vortical structures. Also, the presence of simultaneous whole-field velocity data facilitates the measurement of multi-point statistics such as two-point correlations and proper orthogonal decomposition (POD). Due to the scarcity of refined particle image velocimetry experiments in the literature, there is an increasing demand for multi-point turbulent statistics for comparison with numerical simulations. One major challenge of the numerical simulation of surface attaching jets is related to the setting of the kinematic boundary condition. Because of the non-zero surface velocities, the no-slip boundary condition scheme no longer holds in the surface jet region. The sensitivity of the surface velocities to upstream conditions would imply that empirical correlations are required to aid in the setting of the kinematic boundary condition. These correlations can only be reliably developed from well-qualified experiments.

The specific objectives of the present investigation are to employ the particle image velocimetry technique to measure the effects of offset height ratio and nozzle geometry on the mixing characteristics and turbulent statistics (up to the fourth order moment) of a low Reynolds number surface attaching jet. By measuring the mean velocity and turbulence intensities along the free surface, the results will provide benchmark data for calibrating corresponding turbulence models. Various coherent structure extraction methodologies such as Galilean decomposition, linear stochastic estimation, two-point statistical correlations and POD are also employed to deepen insight into the impact of the offset height ratio and nozzle geometry on the turbulent structures of surface attaching jets.

1.4 Organization of the Report

The remainder of this report is organized as follows: In Chapter 2, a detailed literature survey is presented on the observations reported in previous turbulent free and surface attaching jet studies. The chapter also presents the various coherent structure identification techniques applied in the present investigation to analyze the turbulent structure. Chapter 3 describes the experimental setup and test conditions investigated. Details are provided of the PIV measurement system and its implementation. In Chapter 4 and 5, the results of the investigation on the offset height effect and nozzle geometry effect are presented and discussed, respectively. Finally, in Chapter 6, the experimental results are summarized, and the major conclusions are highlighted along with recommendations for future works.

CHAPTER 2

LITERATURE REVIEW

2.1 Overview

In this chapter, the results presented in previous turbulent free and surface attaching jets are discussed. In the literature, turbulent jets are often classified into two broad categories depending on the nozzle aspect ratio, AR = w_1/d, where w_1 = nozzle exit length in spanwise direction. Jets issuing from nozzles of large aspect ratio are called two-dimensional (or plane) jets. At large aspect ratios, the jet flow is characterized by mean jet propagation in the streamwise direction, jet spread in the cross-stream direction and zero entrainment in the spanwise direction. A two-dimensional jet with sidewalls is known as a rectangular jet. At lower aspect ratios, end wall effects arise that can propagate into the flow, leading to non-zero entrainment in the spanwise direction. This is called a three-dimensional jet. A schematic of a turbulent free jet is shown in Fig. 2.1.

Three-dimensional jets such as the axisymmetric (round) and square jets have been used widely in the past as benchmark cases for comparison with numerical models. In the presence of a plane boundary such as a free surface or a wall, the evolution of the jet becomes relatively complex because the jet is constrained by the boundary. A thorough understanding of the flow physics of turbulent free jets and those confined by a plane

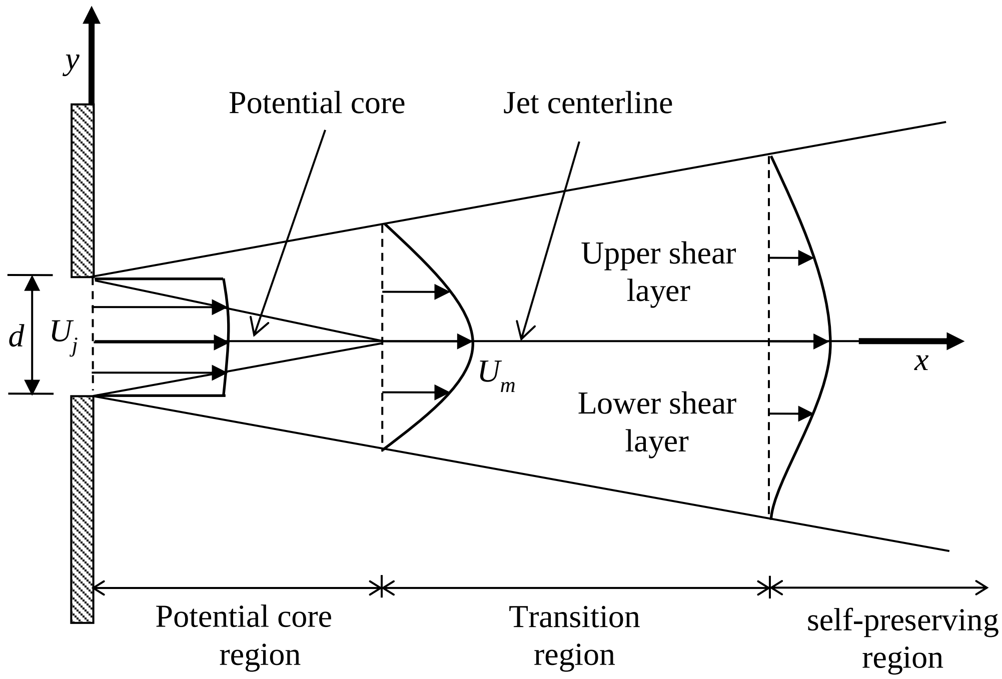

Figure 2.1. Schematic diagram of turbulent free jet.

boundary is necessary for improving the accuracy of models for predicting mixing and entrainment in practical flows.

2.2 Coherent Structures in Turbulent Jets

There is sufficient experimental evidence (e.g., Crow and Champaign, 1971; Brown and Roshko, 1974; Hussain and Zaman, 1981) that turbulence is dominated by orderly structures called coherent structures. Coherent structures have been defined in various ways such as the following: They are a connected turbulent fluid mass with instantaneously phase-correlated vorticity over its spatial extent (Hussain, 1986), or a three-dimensional region of the flow field over which at least one fundamental flow

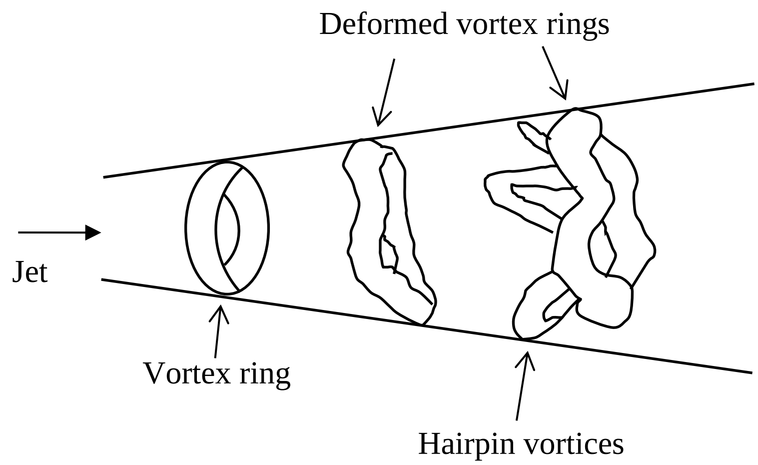

Figure 2.2. Schematic diagram of the coherent structures in a turbulent jet.

variable (e.g., velocity, density or pressure) exhibits significant correlation with itself or with another variable with length and time scales larger than the smallest scales of the flow (Robinson, 1991). The dynamics of coherent structures account for much of the mass, momentum and heat transfer in turbulent jets and the generation of aerodynamic noise. Figure 2.2 shows a schematic representation of the coherent structures in a free jet. Previous flow visualizations (Crow and Champagne, 1971; Yule, 1978; Hussain and Clarke, 1981) suggest that the turbulent structure of a jet consists of a periodic sequence (or street) of interacting and coalescing vortex rings. It has been proposed that these vortex rings are formed by the Kelvin-Helmholtz instability of the initial laminar shear layer that produces a quasi-periodic roll up of the edge of the shear layer downstream of the jet exit. The region of the flow connecting successive vortex rings is called a braid. The ring vortices and braids have been observed to dominate the turbulence structure in the near-exit region ($0 \le x/d \le 4$) of axisymmetric free jets (Crow and Champagne, 1971; Petersen and Samet, 1988). Further downstream, secondary instability of the shear layer often leads to certain interesting behaviour of the vortex rings such as vortex pairing, tearing and stretching into helical (spiral) structures.

The dynamics of large-scale coherent structures in turbulent free jets has been the subject of inquiry in many investigations (e.g., Dimotakis et al., 1983; Hussain, 1986; Lai et al., 1991; Liepmann and Gharib, 1992). Dimotakis et al. (1983) investigated the coherent structures in a round jet at low and high Reynolds numbers. Their study showed the presence of large-scale vortical structures in the form of axisymmetric and helical vortices both in the near and far field regions.

Liepmann and Gharib (1992) examined the Reynolds number effects on the streamwise vortices and entrainment in a round free jet. It was found that the number of identifiable vortical structures grows up to $Re \approx 10000$ after which it decreases rapidly. Their study showed that the initial instability grows in the braid region and are subsequently suppressed by the primary. As the flow evolves downstream, the vortex rings become unstable relative to one another and tilt towards the streamwise direction.

Some studies reported in the past considered the relationship between the vortex rings and turbulent mixing. For instance, the enhanced mixing and entrainment reported for non-circular jets compared to round jets is considered to be the result of fundamental differences in the initial vortex structure. Grinstein et al. (1995) observed that in non-circular jets, the presence of sharp corners causes a self-induced deformation of the vortex corners due to the streamwise stretching of azimuthal vorticity. As the jet propagates downstream, the self-induced deformation leads to faster-moving vertices of the vortex rings than the rest of the jet. This causes axis-switching in the spanwise plane of the jet.

Axis switching is believed to be responsible for the enhanced mixing and entrainment in non-circular jets.

2.3 Some Techniques for Educing Coherent Structures

Several methodologies have been developed in the literature for extracting coherent structures from turbulent flows. Most of these are comprehensively reviewed in a number of previous articles, including Hussain (1983) and Adrian et al. (2000a, 2000b). In this investigation, methods such swirling strength criterion, linear stochastic estimation (LSE), two-point correlations and proper orthogonal decomposition (POD) are used to characterize and reveal the coherent structures in the jet.

2.3.1 Swirling strength

Swirling strength is another name for the imaginary part of the complex eigenvalues of the velocity gradient tensor. It is used as a criterion for identifying vortex cores in a flow field. In three dimensions, the local velocity gradient tensor will have one real eigenvalue λ_{cr}, and a pair of complex conjugate eigenvalues ($\lambda_{cr} \pm i\lambda_{ci}$) when the discriminant of its characteristic equation is positive (Zhou et al., 1999). In the vertical jet symmetry plane, a two-dimensional approximation of the swirling strength can be obtained using the in-plane velocity gradients (Hutchins et al., 2005): which in the *x*-*y* plane is formulated as

$$\begin{vmatrix} \dfrac{\partial U}{\partial x} - \lambda & \dfrac{\partial U}{\partial y} \\ \dfrac{\partial V}{\partial x} & \dfrac{\partial V}{\partial y} - \lambda \end{vmatrix} = 0 \qquad (2.1)$$

This is a quadratic equation with solution given by

$$\lambda = \frac{1}{2}\left(\frac{\partial U}{\partial x} + \frac{\partial V}{\partial y}\right) \pm \frac{1}{2}\sqrt{\underbrace{\left(\frac{\partial U}{\partial x} + \frac{\partial V}{\partial y}\right)^2}_{b^2} - \underbrace{4\left(\frac{\partial U}{\partial x}\frac{\partial V}{\partial y} - \frac{\partial V}{\partial x}\frac{\partial U}{\partial y}\right)}_{4ac}} \tag{2.2}$$

Since the swirling strength, λ_{ci}, is defined at a location where the solution is complex, the magnitude of swirling strength associated with the spanwise vortex core at that location becomes

$$\lambda_{ci,z} = \frac{1}{2}\sqrt{\left|b^2 - 4ac\right|} \quad \text{where } 4ac > b^2. \tag{2.3}$$

It should be noted that in this form, the swirl has no sign information. Specifically, the swirling strength, $\lambda_{ci,z}$ is multiplied by the sign of the local in-plane instantaneous fluctuating vorticity. This corresponds to the mathematical operation

$$\Lambda_{ci,z} = \lambda_{ci,z}\left(\frac{\omega_z'}{|\,\omega_z'\,|}\right) \tag{2.4}$$

where $\Lambda_{ci,z}$ is the signed swirling strength and ω_z' is the fluctuating vorticity.

2.3.2 Linear stochastic estimation

Stochastic estimation is applied in turbulence to obtain a least-square approximation of the conditional average of the velocity fields. In general, the conditional average of a function U denoted $\langle U \mid E \rangle$ where E is a set of event data is calculated as (Adrian et al., 1989):

$$\langle U \mid E\rangle = \int \frac{f(U,E)}{f(E)} U dU , \tag{2.5}$$

where f (U, E) is the joint probability density function of U and E, and f (E) is the probability density function of E. While Equation 2.5 is the best estimate of the conditional average, its direct computation is impractical due to the large number of events that must be included for the results to converge. The stochastic estimate of the conditional average $\langle U \mid E\rangle$ where U_i is the ith component of velocity is obtained by expanding the conditional average in a Taylor series about $E = 0$; and truncating the series at some level (Adrian et al. 1989). Thus, assuming $E = (E_1, E_2, E_3, ..., E_N)$, where the E_i's are fluctuations with respect to the mean, $\langle U \mid E\rangle$ is expanded as follows (Adrian et al. 1989):

$$\langle U_i \mid E\rangle = L_{ij}E_j + M_{ijk}E_jE_k + N_{ijkl}E_jE_kE_l + ... \tag{2.6}$$

The unknown coefficients L, M, N, ... are determined by requiring that the mean-square error between the approximation and the conditional average be minimized,

$$\langle [\langle U_i \mid E\rangle - L_{ij}E_j - M_{ijk}E_jE_k - N_{ijkl}E_jE_kE_l - ...]^2\rangle = \text{minimum.} \tag{2.7}$$

In the case of linear stochastic estimation, only the first term in Equation 2.6 is retained. The minimization leads to the orthogonality principle which states that the error must be statistically uncorrelated with each of the data. That is,

$$\langle [\langle U_i \mid E\rangle - L_{ij}E_j]E_k\rangle = 0 , \quad i = 1, 2, 3 \quad j, k = 1, 2, 3, ..., N. \tag{2.8}$$

which upon expansion yields

$$\left\langle E_j E_k \right\rangle L_{ij} = \left\langle U_i E_k \right\rangle, \qquad j, k = 1, 2, 3, ..., N. \tag{2.9}$$

Expanding Equation 2.9 for indices *j* and *k* leads to a linear system of equations, which can be solved for the estimation coefficients, L_{ij}.

$$\begin{aligned}
\left\langle U_i\, E_1 \right\rangle &= L_{i1} \left\langle E_1 E_1 \right\rangle + L_{i2} \left\langle E_1 E_2 \right\rangle + ... + L_{iN} \left\langle E_1 E_N \right\rangle \\
\left\langle U_i\, E_2 \right\rangle &= L_{i1} \left\langle E_2 E_1 \right\rangle + L_{i2} \left\langle E_1 E_2 \right\rangle + ... + L_{iN} \left\langle E_2 E_N \right\rangle \\
&\cdots\cdots\cdots\cdots\cdots\cdots\cdots\cdots\cdots\cdots \\
&\cdots\cdots\cdots\cdots\cdots\cdots\cdots\cdots\cdots\cdots \\
\left\langle U_i\, E_N \right\rangle &= L_{i1} \left\langle E_N E_1 \right\rangle + L_{i2} \left\langle E_N E_2 \right\rangle + ... + L_{iN} \left\langle E_N E_N \right\rangle
\end{aligned} \tag{2.10}$$

For a scalar event *E* at the reference location (x_{ref}, y_{ref}), Equation 2.10 reduces to

$$\left\langle U_i(x_{ref} + \Delta x, y) \cdot E(x_{ref}, y_{ref}) \right\rangle = L_i \left\langle E(x_{ref}, y_{ref}) \cdot E(x_{ref}, y_{ref}) \right\rangle \tag{2.11}$$

from which the corresponding LSE coefficient is obtained as

$$L_i = \frac{\left\langle U_i(x_{ref} + \Delta x, y) \cdot E(x_{ref}, y_{ref}) \right\rangle}{\left\langle E(x_{ref}, y_{ref})^2 \right\rangle} \tag{2.12}$$

Then, using Equations 2.11 and 2.12, the LSE of the conditional average of the *i*th component of velocity (*u* or *v*) is given by

$$\left\langle U_i(x_{ref} + \Delta x, y) \,|\, E(x_{ref}, y_{ref}) \right\rangle = \frac{\left\langle U_i(x_{ref} + \Delta x, y) \cdot E(x_{ref}, y_{ref}) \right\rangle}{\left\langle E(x_{ref}, y_{ref})^2 \right\rangle} E(x_{ref}, y_{ref}) \tag{2.13}$$

Equation 2.13 allows the reconstruction of the average velocity field associated with a given value of E such as u, v, vorticity ω_z or swirling strength $\Lambda_{ci,z}$ (Christensen and Adrian, 2001).

2.3.3 Two-point correlation

The two-point correlation functions (R_{AB}) for two arbitrary quantities are defined as follows (Volino et al., 2007):

$$R_{AB}\left(x_{ref}+\Delta x,\, y_{ref}+\Delta y\right)=\frac{\langle A\left(x_{ref},\, y_{ref}\right)\, B\left(x_{ref}+\Delta x,\, y_{ref}+\Delta y\right)\rangle}{\sigma_A\left(x_{ref},\, y_{ref}\right)\, \sigma_B\left(x_{ref}+\Delta x,\, y_{ref}+\Delta y\right)} \tag{2.14}$$

where, $A(x, y)$ and $B(x, y)$ are the two variables whose two-point correlation is required; (x_{ref}, y_{ref}) is the reference location; Δx and Δy are the spatial separations between A and B in the streamwise and surface-normal directions, respectively; and σ_A and σ_B are the root-mean-square values of A and B at (x_{ref}, y_{ref}) and $(x_{ref} + \Delta x, y_{ref} + \Delta y)$, respectively.

Two-point correlation is often used to investigate the space or time over which the turbulence fields are correlated across the flow. Also, it is used to estimate the integral length scales. Integral length scale is significant in turbulent structures as it is a measure of the maximum correlation distance from the reference location indicating large-scale structures. Large-scale structures are responsible for most of the transport of momentum and energy.

2.3.4 Joint probability density function

The joint probability density function (JPDF), $P(u, v)$ is often used to examine the correlation between the instantaneous velocity fluctuations. It is useful to investigate the turbulent coherent events that contribute to the Reynolds shear stress production. The Reynolds shear stress covariance is defined as (Ong and Wallace, 1998):

$$\langle uv \rangle = \iint_{-\infty}^{+\infty} uv\, P(u,v)\, du dv \tag{2.15}$$

Following Wallace and Brodkey (1977), the joint probability density function was calculated by dividing the range between the minimum and maximum values of the velocity fluctuations into bins (or cells) of equal width; and sorting the data into the bins. For each bin, $P(u, v)$ is estimated as follows:

$$P(u, v) = \frac{n_{uv}}{N_b\, \Delta^2} \tag{2.16}$$

where, n_{uv} is the total number of the velocity pairs (u, v) that fall within the bin, N_b is the total number of the pairs in the sample and Δ denotes the width of the bins. The JPDFs reported in the present study were estimated by sorting the instantaneous velocity fluctuations into 100×100 equal-width bins. Furthermore, to examine the relative contributions of the velocity fluctuations to the Reynolds shear stress, the values of the weighted joint probability density function (WJPDF), $uv\, P(u, v)$ were calculated. To interpret the results, the quadrant analysis proposed by Lu and Willmarth (1973) was adopted to divide the dominant turbulent events into the following four quadrants based on the orientation of the shear layers: Q1, Q2, Q3 and Q4. For instance, in the upper shear layer, Q1 (+*u*, -*v*) denotes fast entrainment of ambient fluid into the jet, Q2 (-*u*, -*v*) denotes slow entrainment of ambient fluid into the jet, Q3 (-*u*, +*v*) denotes slow ejections from the jet into the ambience and Q4 (+*u*, +*v*) denotes fast ejections from the jet into the ambience. It should be noted that in the lower shear layer, this ordering will need to be reversed for the above nomenclature to still apply.

2.3.5 Proper orthogonal decomposition

Proper orthogonal decomposition (POD) is an efficient technique to study the dynamic role of the structures containing various energies. It extracts energetically dominant modes in a flow; and is capable of capture the most energetic structures with only a few modes (Holmes et al., 1996; Adrian et al., 2000a). POD requires multi-point measurement technique. The PIV data, as a whole-field measurement, with high spatial resolution is ideal for applying POD as a useful technique to study the coherent structures. The snapshot approach of the POD analysis introduced by Sirovich (1987) is applied in the present study. A brief description of the snapshot POD method following the procedure outlined by Meyer et al. (2007) is provided in Appendix A.

The POD method was first introduced by Lumley (1967) to extract structures in a turbulent flow (Holmes et al., 1996). Subsequently, it has been applied by various authors to quantify the contribution of the higher energetic structures in the turbulence field of different types of flows including free jets (e.g., Gordeyev and Thomas, 2000, 2002; Bi et al., 2003; Gamard et al., 2004; Zhou and Hitt, 2004; Sakai et al., 2006a, 2006b; Shinneeb, 2006; Iqbal and Thomas, 2007; Meyer et al., 2007; Shinneeb et al., 2008a, 2008b; Tandalam et al., 2010). The energy-containing vortices in the near (Shinneeb et al., 2008a) and far field region (Shinneeb et al., 2008b) of turbulent round free jet were identified using POD. In the near field region (Shinneeb et al., 2008a), POD exposed toroidal vortices with alternating rotating motions. Furthermore, the reconstructed velocity field using 10 POD modes extracted about 48% of turbulent kinetic energy in the near field region which is comparable to the value reported by Fiedler (1988) (~50%) contained by the large-scale structures in that region. The size of the vortical structures increased with the jet development downstream by pairing process while the mean circulation of the vortices is preserved in the axial direction (Shinneeb et al., 2008b).

2.4 Previous Investigations on Turbulent Free Jets

Over the past decades, studies have been conducted to investigate the turbulent characteristics of free jets extensively. These include plane jets (e.g., Gutmark and Wygnanski, 1976; Hanjalić and Launder, 1980; Antonia et al., 1986; Namer and Ötügen, 1988; Terashima et al., 2014) and three-dimensional jets (e.g., Ricou, and Spalding, 1961; Wygnanski and Fiedler, 1969; Obot et al., 1984; Quinn and Militzer, 1989; Hussein et al., 1994; Lozanova and Stankov, 1998; Mi et al., 2001; Kwon and Seo, 2005; Bogey and Bailly, 2006; Quinn, 2006; Aleyasin et al., 2017a, 2017b, 2018). For instance, Wygnanski and Fiedler, (1969); and Hussein et al. (1994) measured three velocity components of a round free jet and reported turbulent quantities that includes Reynolds stresses, triple velocity products, energy budget terms, skewness and flatness factors, two-point correlation functions and turbulent length scales. Table 2.1 presents a summary of the previous free jet investigations for a wide range of initial conditions. The initial conditions

Table 2.1. Summary of previous free jets.

Author	**Technique**	**Nozzle**	***Re***	**Major quantities**
Ricou and Spalding (1961)	MM	Circular (Orifice)	> 25000	Entrainment rate
Wygnanski and Fiedler (1969)	HWA	Circular (Contour)	100000	U, $\langle u^2\rangle^{0.5}$, $\langle v^2\rangle^{0.5}$, $\langle w^2\rangle^{0.5}$, $-\langle uw\rangle$, third and fourth order moments, energy budget, two-point correlations
Gutmark and Wygnanski (1976)*	HWA	AR = 38.5 (Orifice)	30000	U, $y_{0.5}$, $\langle u^2\rangle^{0.5}$, $\langle v^2\rangle^{0.5}$, $\langle w^2\rangle^{0.5}$, $-\langle uv\rangle$, third and fourth order moments, two-point correlations
Namer and Ötügen (1988)*	HWA, LDV	AR = 56 (Contour)	1000 - 7000	U, U_m, $y_{0.5}$, $\langle u^2\rangle^{0.5}$, two-point correlations
Quinn and Militzer (1989)	HWA	Circular (Orifice, contour)	208000	U, $y_{0.5}$, $\langle u^2\rangle^{0.5}$, $\langle v^2\rangle^{0.5}$
Lozanova and Stankov (1998)	HWA	AR = 3 – 10 (Orifice, contour)	100000-216000	U, jet momentum and entrainment, $\langle u^2\rangle^{0.5}$, $-\langle uv\rangle$
Mi et al. (2001)	HWA	Circular (Orifice, contour, pipe)	16000	U, $\langle u^2\rangle^{0.5}$
Kwon and Seo (2005)	PIV	Circular (Contour)	177 - 5142	U, V, U_m, $y_{0.5}$, $\langle u^2\rangle^{0.5}$, $-\langle uv\rangle$
Quinn (2006)	HWA	Circular (Orifice, contour)	184000	U, U_m, $y_{0.5}$, $\langle u^2\rangle^{0.5}$, $\langle v^2\rangle^{0.5}$, $-\langle uv\rangle$, two-point correlations
Deo et al. (2007)*	HWA	AR = 15 – 72 (Contour)	18000	U, U_m, $y_{0.5}$, $\langle u^2\rangle^{0.5}$, skewness, flatness
Paillat and Kaminski (2014)*	PIV	AR = 185 – 925 (Orifice)	59 - 424	U, $y_{0.5}$, $-\langle uv\rangle$, $\langle u^2\rangle$, $\langle v^2\rangle$
Ghasemi et al. (2015)	PIV	Square (Contour)	10000 - 41000	U, $\langle u^2\rangle^{0.5}$, $\langle v^2\rangle^{0.5}$, $-\langle uv\rangle$, T/NTI
Aleyasin et al. (2017a)	PIV	Various (Contour + Orifice)	10000	U, ω_z, U_m, $y_{0.5}$, $\langle u^2\rangle^{0.5}$, $\langle v^2\rangle^{0.5}$, $\langle w^2\rangle^{0.5}$, $-\langle uv\rangle$, $-\langle uw\rangle$, third order moments, two-point correlations
Aleyasin et al. (2017b)	PIV	Circular, square, ellipse: AR = 2, 3 (Orifice)	2500 - 17000	U, U_m, $y_{0.5}$, ω_z, $\langle u^2\rangle^{0.5}$, swirling strength, $-\langle uv\rangle$, ν_t, JPDF, WJPDF

Authors with (*) studied plane jets and others were 3D jets; MM = micromanometer; LDV = laser Doppler velocimetry; HWA = hotwire anemometry; PIV = particle image velocimetry; AR = aspect ratio; Various = circular, square, cross, eight-corner star, six-lobe daisy, triangle, ellipse, rectangle with AR = 2; T/NTI = turbulent/non-turbulent interface; JPDF = joint probability density function; WJPDF = weighted JPDF.

(e.g., exit Reynolds number and nozzle geometry) have significant influence on the mixing and entrainment characteristics as well as the evolution of turbulent jets.

2.4.1 Effects of jet exit Reynolds number

Effects of the jet exit Reynolds number have been investigated extensively in the past for both the entrainment characteristics and turbulent quantities. For instance, Ricou and Spalding (1961) and Obot et al. (1984) performed measurements of the entrainment coefficient of a round jet over a range of Reynolds numbers. They found that entrainment coefficient is independent of the exit Reynolds number for $Re > 10000$. At lower Reynolds numbers, they observed a decrease in jet entrainment with increasing Reynolds number.

Namer and Ötügen (1988) performed extensive velocity measurements both in the near and far fields of a turbulent plane jet at moderate Reynolds numbers. By keeping other initial conditions constant, a reduction in entrainment and jet spreading rate were observed with increasing Reynolds number. It was concluded that the influence of Reynolds number is to promote a more rapid decay of the centerline mean streamwise velocity and enhance the turbulence intensities in the near field region.

Kwon and Seo (2005) examined the Reynolds number effects on the mean and turbulent characteristics of a turbulent round jet. They observed enhancements in the normalized Reynolds shear stress with increasing Reynolds number.

Fellouah et al. (2009) investigated the flow field of a round jet at Reynolds numbers spanning the range associated with mixing transition ($6000 \leq Re \leq 30000$). It was found that in the near field region the mean streamwise velocity profiles were independent of Reynolds number. On the other hand, profiles of the streamwise turbulence intensity showed an increase with Reynolds number in the shear layer but a decrease with *Re* in the core jet.

Tandalam et al. (2010) applied POD to identify vortices in the near field region of free jets at various Reynolds numbers ranging from *Re* = 10000 to 55000. Results showed that vortices started appearing closer to the nozzle exit with the increase of Reynolds number. The mean circulation close to the nozzle exit was found the largest at the lowest Reynolds number (*Re* = 10000), while the variation of that mean circulation was insignificant at higher Reynolds number.

Ghasemi et al. (2015) examined Reynolds number effects on the mean and turbulence characteristics in the near field of a square jet. They found that the shear layer grows at a much faster rate at lower Reynolds number (*Re* = 10000) than at higher Reynolds numbers (*Re* > 10000). They reported that the mean velocity, turbulent intensities and centerline anisotropy ratio are more sensitive to Reynolds number effects at low Reynolds number than at high Reynolds numbers.

Recently, Aleyasin et al. (2017b) studied Reynolds number effect within the range of $2500 \leq Re \leq 17000$ using circular, square and elliptic nozzle. They found that the nozzle geometry effects were more pronounced at higher Reynolds number. The streamwise locations of axis-switching and asymptotic values of streamwise turbulence intensity were found nearly independent of Reynolds number. Subsequently, the effects of Reynolds number within the range of $6000 \leq Re \leq 20000$ on the turbulent characteristics of triangular and circular jets were reported by Aleyasin et al. (2018). Results on the circular jets showed a reduction in the mixing performance with the increase in Reynolds number, while the triangular jets experienced negligible effect of Reynolds number on the length of the potential core, the decay and spread rates, the axis-switching locations and the value of local Reynolds number. POD analysis was performed and the results showed turbulent structures with similar energy content in the minor and major plane of the triangular jet.

2.4.2 Effects of nozzle geometry

Another area of interest that has received attention in the free jet study is the influence of the nozzle geometry on the flow characteristics. It has been known that differently shaped nozzles possess different entrainment and mixing characteristics because the spatial evolution of the jet is strongly dependent on exit geometry. The effects of nozzle upstream shaping on the downstream development of turbulent free jets have been examined by Mi et al. (2001), Quinn (2006). Mi et al. (2001), whose study investigated the mixing characteristics of jets issuing from smooth contraction, orifice plate and long pipe nozzles found that the highest mixing occurs in the orifice plate jet followed by the smooth contraction and long pipe jets. Similar results were obtained by Quinn (2006) for smooth contraction and orifice plate nozzles. Quinn (2006) also reported several turbulent quantities including the Reynolds stresses and two-point correlations that were more significantly enhanced in the sharp-edged orifice jet compared to those observed in the smooth contraction jet. The preceding results are also complemented by instantaneous flow visualization results by Mi et al. (2007) that indicate that the flow structure in the near field of the orifice jet is more three-dimensional than that of the smooth contraction jet.

A common phenomenon occurred in non-circular jets is “axis-switching”, where the jet can develop downstream through similar shape as the exit geometry but with a rotation of the axis of the jet geometry (Sfeir, 1979; Krothapalli et al., 1981; Tsuchiya, et al., 1986; Ho and Gutmark, 1987; Quinn and Militzer, 1988; Gutmark et al., 1989; Hussain and Husain, 1989). The axis-switching can be considered as an artefact of a deformation of the vortex rings introduced by non-uniform curvature of the jet exit perimeter and interaction between azimuthal and streamwise vorticities (Gutmark and Grinstein, 1999). Experimental and computational results depict effect of initial conditions, such as, exit type and shape of the nozzle, turbulence level on the occurrence of axis-switching (Koshigoe et al., 1989; Hussain and Husain, 1989; Grinstein et al., 1995). It is considered as a key mechanism for enhanced entrainment and mixing for non-circular jets (Grinstein, 2001).

Quinn (2007) investigated the influence of nozzle geometry on the mixing and turbulence characteristics of free jets in the near and intermediate regions by comparing the time- and phase-averaged velocity statistics measured for differently shaped nozzles: a sharp-edged elliptic nozzle, a sharp-edged round nozzle and a contoured round nozzle. The results indicate that the mixing and entrainment in a sharp-edged elliptic jet are much higher than in jets issuing from sharp-edged and contoured round nozzles. It was found that the elliptic nozzle produces a more rapid centerline mean streamwise velocity decay, larger drop in mean static pressure within the near field, and significantly higher centerline turbulence intensities than sharp-edged and contoured round nozzles.

Mi et al. (2010) also reported measurements of the centerline evolution of the turbulent statistics for a larger set of differently shaped nozzles; and extended the results to the far field region. They concluded that the faster centerline mean streamwise velocity decay and higher centerline turbulence intensities in the near field can be attributed to the loss of jet axisymmetry introduced by sharp changes in curvature at the corners of the nozzle. This is most pronounced for an isosceles-triangular jet than rectangular, cruciform, star and circular nozzles. Their results indicate that the effects of nozzle geometry are relatively stronger in the near field region than the far field region of the jet. Their findings are consistent with the results by Mi and Nathan (2010) where the effect of nozzle geometry was found insignificant on the variation of turbulent length scales (integral length scale, Taylor micro-scale and Kolmogorov length scale) and higher order moments (skewness and flatness factors) at far downstream.

Measurements of the centerline and one-dimensional radial profiles of jets issuing from round, hexagonal and cruciform nozzles were reported by Manivannan and Sridhar (2013). Their results indicate that the cruciform nozzle produces a more superior mixing performance and larger turbulent intensities than the hexagonal and circular nozzles.

Recently, Aleyasin et al. (2017a) studied the effects of nozzle geometry on the turbulent characteristics of free jets using the following eight different shapes of nozzle: round, square, cross, eight-corner star, six-lobe daisy, equilateral triangle as well as ellipse and rectangle each with aspect ratio of 2. They found that the jets issuing from the elliptic and rectangular nozzles exhibits the best mixing performance while the least effective mixing was observed in the star jet. The distributions of the Reynolds stresses and turbulent diffusion were sensitive to nozzle geometry, and integral length scales were found nearly independent of nozzle geometry.

2.5 Previous Investigations on Turbulent Confined Jets

Confined jets such as those offset from a solid wall (wall attaching jets) have been extensively investigated in the past. (e.g., Bourque and Newmann, 1960; Sawyer, 1960; Davis and Winarto, 1980; Nozaki et al., 1981; Lund, 1986; Pelfrey and Liburdy, 1986; Nasr and Lai, 1998; Gao and Ewing, 2007; Agelin-Chaab and Tachie, 2011a, 2011b, 2011c; Nyantekyi-Kwakye et al., 2015a, 2015b). Sawyer (1960) for instance, presented an analytical solution of a two-dimensional wall attaching jet that compared well with experimental data. Nozaki et al. (1981) examined the influence of the nozzle exit plane turbulence intensity on the flow characteristics in a three-dimensional wall attaching jet, while Bourque and Newmann (1960), Lund (1986), and Gao and Ewing (2007) considered the influence of offset height on a two-dimensional wall attaching jet.

There are research efforts on the characteristics of the jets confined by a free surface (surface attaching jet). A summary of previous work on the surface attaching jets is given in Table 2.2. The earliest investigation of a turbulent surface attaching jets was reported by Evans (1955). He demonstrated that upon interaction with the free surface the jet forms a current beneath the surface. It was shown that when the surface waves and

Table 2.2. Summary of previous surface attaching jets.

Author	**Technique**	**Nozzle**	***Re***	***Fr***	***h/d***	**Major quantities reported**
Anthony and Willmarth (1992)	LDV	Circular (Contour)	12700	5.66	2	U, V, W, $\langle u^2 \rangle^{0.5}$, $\langle v^2 \rangle^{0.5}$, $\langle w^2 \rangle^{0.5}$, $-\langle uv \rangle$, $-\langle uw \rangle$, $-\langle vw \rangle$
Madnia and Bernal (1994)	HWA	Circular (Contour)	12700	4.30 – 8.00	1 – 3.5	U, U_m, y_m, $y_{0.5}$, $z_{0.5}$, $y^s_{0.5}$, $\langle u^2 \rangle^{0.5}$, U_s
Walker et al. (1995)	LDV	Circular (Contour)	12700 - 102000	1.00 – 8.00	2	U, V, $\langle u^2 \rangle^{0.5}$, $\langle v^2 \rangle^{0.5}$, $\langle w^2 \rangle^{0.5}$, $-\langle uv \rangle$, $-\langle uw \rangle$, stress ratios, $\rho_{-\langle uv \rangle}$, $\rho_{-\langle uw \rangle}$
Tsunoda et al. (2006)*	PIV	AR = 40 (Contour)	2500	0.60 - 1.20	7.5 - 30	L_a, U_m, y_m, $y_{0.5}$, $\langle u^2 \rangle^{0.5}$, $\langle v^2 \rangle^{0.5}$
Sankar et al. (2008)	LDV	Square (Contour)	40000	0.75 - 1.60	1 – 4.5	L_a, U, $\langle u^2 \rangle$, $\langle v^2 \rangle$, $-\langle uv \rangle$, third order moments
Rainford and Khan (2009)	Prandtl tube	Circular (Orifice)	38000-51000	4.20 – 8.00	2 - 4	U, U_m, y_m, $y_{-0.5}$
Sankar et al. (2009)	LDV	Square (Contour)	40000	0.55	2	L_a, U, $\langle u^2 \rangle$, $-\langle uv \rangle$
Tian et al. (2012)	PIV	Circular (Contour)	28000	4.00	5	U, V, W, $\langle u^2 \rangle^{0.5}$, $\langle v^2 \rangle^{0.5}$, $\langle w^2 \rangle^{0.5}$, $-\langle uv \rangle$, $-\langle uw \rangle$
Wen et al. (2014a)	PIV	Circular (Pipe)	1920 - 3480	1.71 – 3.10	2	POD
Wen et al. (2014b)	PIV	Circular (Pipe)	3480	1.79 – 3.10	2 - 6	POD
Tay et al. (2017)	PIV	Square, Rectangular: AR = 2 – 4 (Orifice)	7900	1.29	2.7	U, V, U_m, $y_{0.5}$, ω_z, $\langle u^2 \rangle^{0.5}$, $\langle v^2 \rangle^{0.5}$, $-\langle uv \rangle$, stress ratios, $\rho_{-\langle uv \rangle}$, U_s, ΔU, Galilean decomposition, swirling strength, JPDF, WJPDF, two-point correlations

Authors with (*) studied plane jets and others were 3D jets; LDV = laser Doppler velocimetry, HWA = hotwire anemometry, PIV = particle image velocimetry, AR = aspect ratio, POD = proper orthogonal decomposition.

surface current move in the same direction the wave amplitude decreases resulting in an increase in the wavelength.

Rajaratnam and Humphries (1984) reported mean streamwise velocity measurements for three types of surface jets: a plane surface jet, and surface jets issuing from circular and rectangular nozzles mounted flush with the free surface. They found that the spreading rates of the surface jets are considerably lower than those in their free counterparts. For the jets at high Froude numbers, a characteristic decrease was observed in the mean velocity in the vicinity of the free surface. Swean et al. (1989) performed mean streamwise velocity and turbulence intensity measurements in a plane surface jet in a channel of limited depth. They observed a decrease in the jet spreading rate and an increase the mean streamwise velocity decay rate due to the jet confinement.

Mean velocity and momentum flux measurements were reported by Ead and Rajaratnam (2001) for a plane surface jet at varying offset heights relative to the channel bed. The presence of confinement (reservoir wall and channel bed) was found to result in flow reversal and a decrease in the momentum flux by amounts that increase with increasing offset height ratio. The effects of confinement by both the free surface and a solid wall have been investigated for a plane jet (Tsunoda et al. 2006) and a circular jet (Rainford and Khan 2009). Tsunoda et al. (2006) was able to demonstrate that whether the jet deflects towards the wall or free surface depends on the offset height ratio. When the nozzle is at the same offset height from the wall and free surface, the direction of the jet deflection was unpredictable.

Anthony and Willmarth (1992) measured the mean velocity and turbulence intensity profiles of a submerged round jet placed at an offset height ratio of 2. They reported a decrease in the surface-normal turbulence intensity accompanied by an increase in the streamwise and spanwise turbulence intensities. The reduction in surface-normal turbulence intensity was attributed to the redistribution of the turbulent kinetic energy from the surface-normal velocity fluctuations to the streamwise and spanwise velocity fluctuations. Their spanwise measurements indicated that beneath a clean free surface, there exists a shallow outward spreading layer of fluid (called the surface current) moving predominantly downstream, with spanwise extent much greater than the jet flow beneath it.

Madnia and Bernal (1994) conducted an experimental investigation of the interaction between a round jet and the free surface. Shadowgraph visualizations revealed vortex-ring-like structures near the jet exit that interact with the free surface to produce surface waves. It was found that these surface waves propagate with the vortex rings in the streamwise direction at angles that increase with increasing Froude number. Also, they suggested that in the limit of low Froude number, the free surface behaves as a symmetry plane with the submerged jet merging with its twin or image jet above the free surface. Based on that image-jet model, the length and velocity scale of h and $U_j d/h$, respectively that account for various offset heights were proposed to normalize streamwise variation of local maximum streamwise mean velocity, centerline turbulence intensity and mean surface velocity.

Walker et al. (1995) extended the work of Anthony and Willmarth (1992) to characterize the influence of the Reynolds number and Froude number on the interaction between the jet and free surface. It was found that the damping effect of the free surface on the surface-normal fluctuation is independent of Reynolds number but decreases with increasing Froude number and downstream distance. It was demonstrated that the turbulent kinetic energy redistribution mechanism and the outward spreading of the surface current are the direct results of the interaction of the streamwise component of the instantaneous vorticity vector with the free surface.

The first study of the impact of nozzle aspect ratio on surface attaching jets was reported recently by Tay et al. (2017). Significant enhancements were observed in the jet spreading and maximum mean streamwise velocity decay rates at large aspect ratios whereas the turbulence intensities and Reynolds shear stress were independent of aspect ratio. Measurements of the surface mean velocity and turbulence intensities revealed that the free surface is in a state of strain that dampens the vortical structures and reduces the surface-normal turbulence intensities relative to the streamwise turbulence intensities at the free surface.

POD was applied to investigate the turbulent structures in the surface attaching jets (e.g., Shinneeb et al., 2011; Wen et al., 2014a, 2014b). Shinneeb et al. (2011) performed POD in the jet confined by both the free surface and a solid wall. They performed POD within the streamwise range of $10 < x/d < 80$ and results showed that the size of the large-scale structures was restricted by the boundary in the vertical plane, while there was no restriction in the horizontal plane to increase. The effects of Reynolds number on the turbulent structures were investigated by Wen et al. (2014a) using POD. They examined two Reynolds numbers, Re = 1920 and 3480 with a fixed offset height ratio of h/d = 2. The scale of vortical structures was found smaller in high Reynolds number jet. Furthermore, the downward motion of large-scale structures observed in the interaction region of the low Reynolds number jet was absent in high Reynolds number jet. The effects of offset height were studied by varying the offset height ratio from h/d = 2 to 6 at a Reynolds number of Re = 3480 (Wen et al., 2014b). The intense interaction of shallower jet caused surface vibration which resulted in an up-down motion of the structures and there were spatial differences in the dominant structures in the vertical and horizontal plane as mentioned earlier in the study by Shinneeb et al. (2011). The effects of the free surface reduced with the increase of the offset height showing almost symmetric pattern of the dominant structures both in the vertical and horizontal plane.

2.6 Summary of the Literature

Several investigations have been conducted in the past to understand the impact of initial conditions on mixing and turbulence properties of turbulent free jets. A variety of flow measurement techniques such as hotwire anemometry (HWA), laser Doppler velocimetry (LDV) and particle image velocimetry (PIV) were employed to measure mainly the one-dimensional profiles of the time-averaged mean flow and turbulent statistics. These investigations revealed that the mixing characteristics and turbulent quantities are invariant with Reynolds number at large Reynolds numbers, while low Reynolds number jets experience relatively higher jet spread rate and centerline streamwise mean velocity decay rate. Also, a fewer number of vortex rings were observed at higher Reynolds numbers than at lower Reynolds numbers.

The literature also reported differences in the downstream development of a turbulent jet due to differences in nozzle exit shaping and geometry. It was revealed that mixing and turbulent characteristics are significantly higher for jets issuing from sharp-edged nozzles than those issuing from contoured nozzles and long pipes. Nozzles with sharp corners such as square, rectangular, triangular and cruciform nozzles were found to enhance the mixing performance, turbulence intensities and Reynolds stresses in comparison to a round nozzle.

Although deep or free jets have been thoroughly investigated, the characteristics of surface attaching jets have received far less attention. For the relatively few surface attaching jets reported, important quantities such as surface velocity and turbulence intensity distributions, two-point correlations, proper orthogonal decomposition were not considered in detail. Distributions of two-point correlations and POD, which are easy to measure with PIV are useful tools for gaining insight into the influence of confinement on the coherent structures. On the other hand, measurement of surface velocity and turbulence intensity distributions would assist in developing empirical correlations that can aid numerical modeling.

CHAPTER 3

EXPERIMENTAL SETUP AND MEASUREMENT PROCEDURE

This chapter presents details of the experimental setup used for the velocity measurements. These include a description of the test facility, a summary of the test conditions investigated, a description of the planar particle image velocimetry (PIV) system and the measurement uncertainty.

3.1 Description of the Test Facility

The experiments were conducted in an open recirculating water channel as shown in Fig. 3.1. The test section of the channel is 2500 mm long and has a cross section of dimensions 200 mm × 200 mm. The side and bottom walls of the channel were made from smooth super abrasion resistant (SAR) clear acrylic plate that facilitates optical access. The flow in the channel was driven by a centrifugal pump through a series of flow conditioning units that include a settling chamber fitted with perforated plate, a hexagonal honey-comb and a 6.5:1 converging section. The resulting fine-scale flow then passed through the nozzle mounted at the inlet section of the channel. In order to facilitate easy installation of the nozzles, a nozzle assembly consisting of a dam and nozzle plates was used. The nozzle plates were made of acrylic of thickness 3 mm. The thickness of the nozzle is small enough to provide a sharp-edged orifice type nozzle. Each nozzle plate

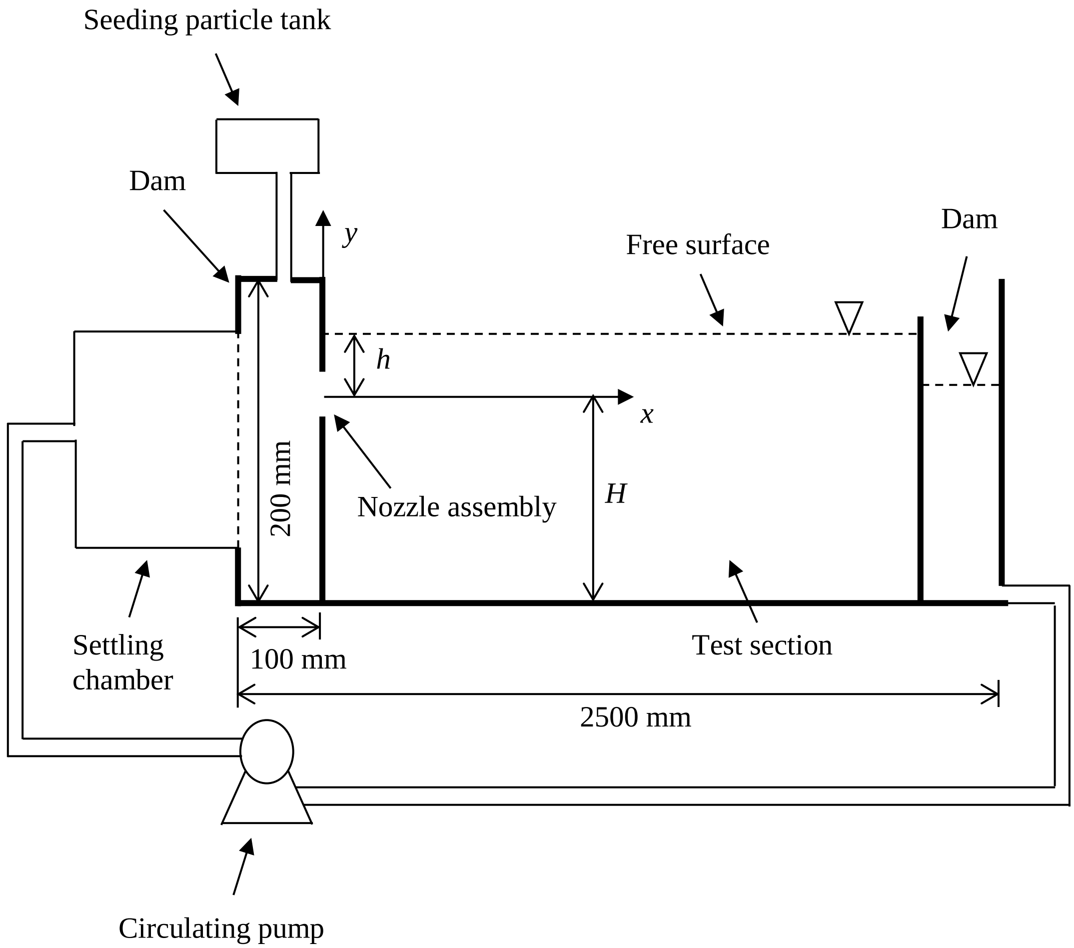

Figure 3.1. Schematic diagram of the water channel.

was mounted 100 mm from the inlet section of the channel. The center of the nozzle was located at a distance *h* from the free surface or *H* from the bottom wall to produce surface attaching jet. It is noted that *H* was sufficiently large that there was no effect of the bottom wall of the test section on the jet flow field in the current test conditions, except having a signature of the presence of a recirculation region near the wall at downstream region which is discussed in Chapter 4. Another dam was used at the end portion of the test section to maintain a constant tail water depth.

3.2 Test Conditions

Experiments were conducted in three phases by varying three major initial conditions: Reynolds number, offset height and nozzle geometry. A summary of the test conditions is provided in Table 3.1. In order to examine the Reynolds number dependency, at first, six Reynolds numbers ranging from Re = 2300 to 11900 based on exit velocity and nozzle width, were tested using a square nozzle with the width, d = 10 mm at a fixed offset height ratio, h/d = 2. The corresponding Froude numbers were Fr = 0.5 to 2.7 based on exit velocity and the offset height. As shown in Appendix B, the effect of Fr was negligible on the spatial evolving of the jet. Furthermore, it was found that the exit profiles of streamwise mean velocity and streamwise turbulence intensity were nearly independent of Reynolds number. Results from the potential core length, attachment length, maximum velocity decay rate, spread rate and entrainment coefficient showed similar near field mixing and entrainment characteristics of the jets at $Re \geq 3700$. The profiles of streamwise mean velocity and turbulence intensities along the free surface, and the surface-normal profiles of streamwise mean velocity and Reynolds stresses showed similar Reynolds number independency at $Re \geq 3700$ in the interaction region.

Based on the results from the investigation of Reynolds number effect, Re = 5500 was selected to study the effects of offset height ratio and nozzle geometry on surface attaching jet characteristics. For offset height effects, experiments were conducted in square jet by varying the offset height ratios from h/d = 1 to 4. It should be noted that for the offset heights and ranges of Reynolds numbers and Froude numbers examined, the free surface remained nearly undisturbed. This is critically important to avoid distortion

Table 3.1. Summary of the test conditions.

Tests	**Nozzle geometry**	***h/d***	***Re***	***Fr***
Effect of Reynolds number	Square	2	2300	0.5 - 2.7
			3700	
			5500	
			7900	
			10300	
			11900	
Effect of Offset height	Square	1	5500	0.8 - 1.7
		2		
		3		
		4		
Effect of nozzle geometry	Circular	2	5500	1.2
	Square			
	Rect_minor			
	Rect_major			

of the laser sheet illuminating which could severely compromise the quality of the PIV data.

For nozzle geometry effects, the following shapes of the nozzle with the equal cross-sectional area of A_n = 100 mm^2 were tested at a fixed offset height ratio of h/d = 2: circular, square and rectangular with aspect ratio of 3. Since the rectangular nozzle is not

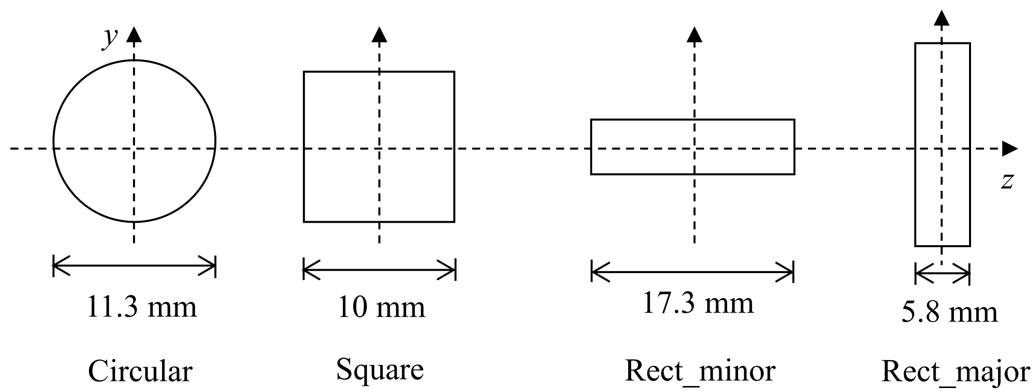

Figure 3.2. Schematic diagram of the four nozzle configurations.

symmetric, it was oriented in minor (Rect_minor) and major (Rect_major) axis along *y* direction. Figure 3.2 shows schematic representation of the four nozzle-exit configurations used in this investigation.

3.3 Planar Particle Image Velocimetry

Particle image velocimetry (PIV) is an optical technique for measuring the velocity of small particles moving with a carrier fluid from the images of the particles captured by a digital camera. In the case of small neutrally buoyant particles ($St << 1$, $\rho_p/\rho_f \approx 1$; where St, ρ_p and ρ_f are Stokes number, particle density and fluid density, respectively), the particles are considered to follow the fluid motion closely so that the particle velocities can be used to approximate the fluid velocities. In planar PIV, the method is applied to a two-dimensional flow region. Generally, pulsed sheets of laser fired at precise time intervals are used to illuminate the flow field and the images of the light scattered by the particles are recorded on the sensor array of a charge-coupled device

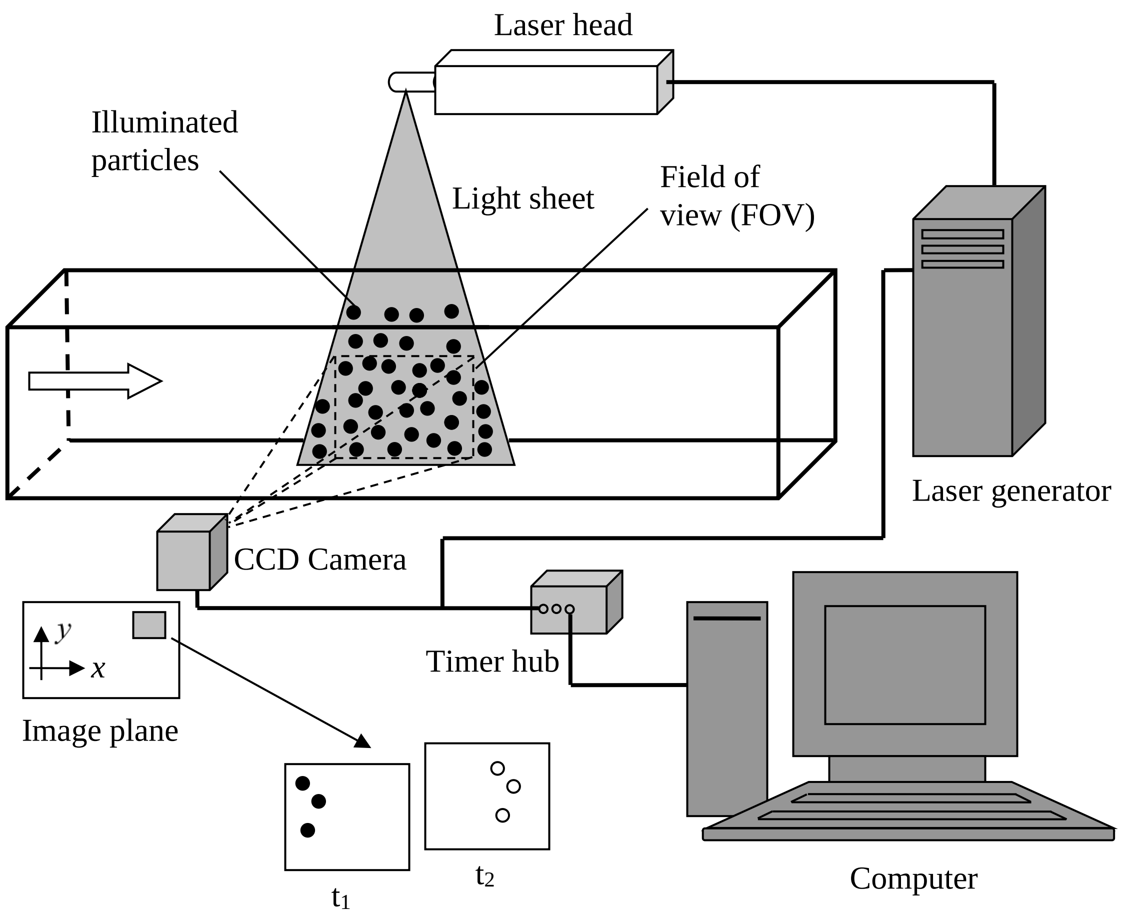

Figure 3.3. A typical setup of a planar PIV system.

(CCD) camera. Image processing methods are then applied to estimate the displacement of the particles within the images.

Figure 3.3 shows the schematic of a typical setup of a planar PIV. The setup consists of a flow carrying small particles, a laser that illuminates the particles in a target window called the field of view (FOV), a charge-coupled device (CCD) camera that captures the images of the illuminated particles, a timer hub that synchronizes the camera with the laser and a computer that controls the entire image acquisition system. During illumination, the laser emits two pulses at times t_1 and t_2 (the time interval Δt depending on the mean flow velocity and the magnification at imaging), and the light scattered by the particles is recorded either on a single frame or on two separate frames of the camera. A computer program is used to divide the image plane into a grid of smaller areas called interrogation areas. For each interrogation area (IA), an auto-correlation or cross-correlation algorithm (depending on number of frames recorded) is applied to statistically determine the local displacement vector ΔX of particles between the first and second illuminations. The velocity vector, V_1, within the interrogation area is then calculated as $V_1 = \Delta X/\Delta t$. A velocity vector map of the field of view is obtained by repeating the correlation for each interrogation area over the entire image. The velocities in the FOV are then calculated by taking into account the magnification between sizes of the FOV and the image plane.

3.3.1 Illumination and recording

Lasers are widely used to illuminate particles in PIV. Their monochromatic light and high-energy intensity makes it possible to form thin sheets of light. A laser consists of three main components, namely, the laser material consisting of atomic or molecular gas, semiconductor or solid material; the pump source that excites the laser material by electromagnetic energy or chemical energy, and the mirror arrangement allowing an oscillation within the laser material. Lasers with double-oscillator systems allow the adjustment of the time interval between the two illuminations irrespective of the pulse intensity. To provide light sheets of high intensity, laser beams with good and stable properties as well as high energy pulses are required. One such laser is the Nd: YAG (neodymium-doped yttrium aluminium garnet) laser in which the laser beam is generated by Nd^{3+} ions. The laser material can be incorporated into various mediums, and has a high amplification and good thermal properties. Excitation is produced by optical pumping in broad energy bands and non-radiating transitions in to a high energy level. Frequency doubled Nd: YAG lasers emit infra-red radiation whose frequency is doubled to produce green light of wavelength 532 nm. In order to obtain short bursts of light energy, the laser is triggered by means of a quality switch (Q-switch) in which the laser beam is linearly polarized. The intensity of the light sheet produced is considered to follow a Gaussian distribution of the form

$$I = I_o \exp\left(-8z_1^2 / d_l^{\,2}\right) \tag{3.1}$$

where I_o is the peak intensity of the sheet and d_l is the light sheet thickness, defined at the $I_o e^{-2}$ intensity level (where $z_1 = d_l/2$).

The most widely used recording device for PIV is the charge-coupled device (CCD) camera, the primary function of which is to provide images at two precisely specified times. The major component of a CCD camera is the CCD sensor which consists of an array of photosensitive cells called pixels. CCD cameras employed in PIV use high-performance progressive scan interline CCD chips. The chip consists of an array of photosensitive cells and an equal number of storage cells. When the first laser pulse is triggered and the particles are illuminated, the first image is acquired and immediately transferred from the photosensitive cells to the storage cells. When the second laser pulse is triggered, the photosensitive cells again are used to store the second image. Both images are then transferred sequentially from the camera to the computer for storage. CCD sensors are available as large arrays of pixels, the number of pixels depending on the spatial resolution required. Some common examples are 1024 × 1024 pixel (1M pixels) and 2048 × 2048 pixel (4M pixels).

Two general image recording modes are used in PIV: single-frame/multi-exposure recording and multi-frame/single-exposure recording. In single-frame/multi-exposure mode, two or more exposures are made on the same frame, resulting in multiple images of the same particle within the frame. The method is successful only when a relatively small number of particles are involved since too many particles in the flow leads to overlapping images. Another disadvantage relates to the effect that particle motion can not be determined uniquely as there is no way to decide which image comes from the first illumination or the second illumination. This directional ambiguity is easily overcome by multi-frame/single-exposure techniques that record particle images on two or more frames within a single exposure. The particle image intensity is approximated by a two-dimensional Gaussian distribution of the form

$$I_p(x,y) = I \exp\left[-8\left(\left(x - x_{p1}\right)^2 + \left(y - y_{p1}\right)^2\right)/d_t^{\,2}\right] \tag{3.2}$$

where, I is the laser sheet intensity distribution given by Equation 3.1, (x_{p1}, y_{p1}) is the location of the peak intensity and d_t is the particle image diameter given by (Adrian, 1991):

$$d_t = \left(M_f^{\,2} d_p^{\,2} + d_s^{\,2}\right)^{1/2} \tag{3.3}$$

where M_f is the magnification and d_s is the width of the Airy function of a diffraction limited lens. For a camera of *f*-number, $f^{\#} = f / D_a$, where f is the focal length and D_a the aperture diameter, the Airy function width is given by (Adrian 1991):

$$d_s = 2.44\,(1 + M_f)\, f^{\#}\, \lambda \tag{3.4}$$

where, λ is the wavelength of the light. Knowing the particle intensity distribution, the corresponding particle pixel value is the integral over the area of the pixel:

$$I_{px}(x, y) = I \iint \exp\left(-8 \frac{(x - x_{p1})^2 + (y - y_{p1})^2}{d_t^{\,2}} \right) dxdy \tag{3.5}$$

3.3.2 Statistical evaluation of recorded images

The images recorded in a PIV are processed numerically using a correlation algorithm to determine the displacements of the particle images. To calculate the particle displacement for a given interrogation area (IA), the pixel intensity values are statistically correlated with one another over the same IA (auto-correlation), or with the pixel intensity values of a corresponding IA in another image (cross-correlation). Thus, for an image divided into interrogation areas of size $K \times L$ (where the sizes are in pixels), the general formulation for the correlation for a spatial domain is given by

$$R(x, y) = \sum_{i=-K}^{i=K} \sum_{j=-L}^{j=L} I_1(i, j) I_2(i + x, j + y) \tag{3.6}$$

where the intensity values I_2 belong to either the same IA, or the corresponding IA of a second image, depending on the approach used.

In practice, the evaluation of the spatial correlations is found to be computationally intensive due to large pixel array sizes of most CCD cameras. Thus, to reduce the cost of calculations, the more efficient two-dimensional fast Fourier transform (FFT) algorithm is utilized. This makes use of the mathematical correlation theorem which is applied to compute cross-correlations of two variables as the inverse Fourier transform (IFFT) of the complex conjugate multiplication of the Fourier transform of the variables. The correlation results in a two-dimensional correlation map with three peaks for auto-correlation and two peaks for cross-correlation. The three peaks in an auto-correlation map correspond to a large central peak (or self-correlation peak) and two displacement peaks, one on each side of the central peak. The distance from the central peak to either of the displacement peaks gives the average displacement of the particle in the interrogation area. The two peaks in a cross-correlation map, on the other hand, correspond to a large (signal) peak and one smaller (noise) peak. The distance of the larger peak from the origin gives the displacement of the particle. A detailed discussion of the mathematical background of the two correlation methods in PIV and their limitations can be found in Westerweel (1997) and Raffel et al. (1998).

An advanced form of the cross-correlation algorithm known as adaptive-correlation is commonly used in evaluating PIV images. As an iterative method it relies on the knowledge of an initial guessed velocity distribution which is used to introduce an offset from the first interrogation area to the second interrogation area. The result of each single displacement calculation is then used as an input to evaluate the interrogation parameters for the subsequent iteration. The process is terminated after a prescribed number of iterations. The use of adaptive correlation helps to provide two major benefits, including increased signal-to-noise ratio, and the possibility of using multigrid calculations in which coarse grids are used to estimate the offset velocity distribution.

3.4 Measurement Procedure

A planar PIV system was used to conduct detailed velocity measurements in the vertical symmetry plane of the jets. An image of the PIV set up is shown in Fig. 3.4 and the major experimental parameters of the PIV system are summarized in Table 3.2. The flow was seeded with 10 μm silver-coated hollow glass spheres. The specific gravity of the seeding particles was 1.4. The settling velocity (v_s) and response time (τ_p) of the particles are estimated from the following equations:

$$v_s = \frac{\left(\rho_p - \rho_f\right)\, g\, d_p^2}{18\,\mu_f} \tag{3.7}$$

$$\tau_p = \frac{\rho_p\, d_p^2}{18\,\mu_f} \tag{3.8}$$

where, μ_f is dynamic viscosity of fluid. The values of the estimated settling velocity and response time were 2.18×10^{-5} m/s and 7.78×10^{-5} s, respectively, which ensured that the particles followed the flow faithfully. An Nd:YAG double-pulsed laser with maximum energy of 120mJ per pulse at 532 nm wavelength was used to illuminate the seeding particles. The thickness of the laser sheet was maintained at about 1 mm which reduced the number of de-focused particles within the measurement planes. The reflected beam from the seeding particles was captured by a 12-bit $f^{\#}$10 charge-coupled device (CCD) camera with a resolution of 2048 pixel × 2048 pixel and a pixel pitch of 7.4 μm. The field

Figure 3.4. Image of the PIV setup.

of view of the camera was set to values specified in Table 3.2, and measurements were acquired in up to three overlapping planes which span, $0 \leq x/d < 25$. Based on a preliminary statistical convergence test result included in Appendix C, an ensemble size of 5000 images was found to be sufficient for the flow statistics to converge. The data were post-processed using the adaptive correlation option of DynamicStudio. The

Table 3.2. Summary of the experimental parameters of PIV.

Parameter	**Value**		
	***Re* effect**	**Geometry effect**	***h/d* effect**
Field of view (FOV)	84×84 mm^2	84×84 mm^2	135×135 mm^2
Pulse separation (Δt)	2.63×10^{-3} s	2.63×10^{-3} s	1.01×10^{-3} s
Scale factor (S)	5.55	5.55	7.25
Camera pixel pitch	7.4 μm		
Maximum laser power	120 mJ/pulse		
f number	10		
Light sheet thickness	1.0 mm		
Diameter of tracer particles	10 μm		
Image sampling frequency	4 Hz		
Nyquist frequency	2 Hz		

interrogation area size of the correlation was set to 32 pixels × 32 pixels with 50% overlap in both x and y directions. The adaptive correlation algorithm used a multi-pass FFT with a one-dimensional Gaussian peak-fitting function to determine the average particle displacement within the interrogation area. Steps were taken during the image acquisition to ensure that the maximum particle displacement was less than ¼ of the IA size. As shown in Appendix D, initial data processing was performed using a variety of IA sizes to assess the effects of spatial resolution on the mean velocity and higher order turbulence statistics. The results show that an IA size of 32 pixels × 32 pixels with 50% overlap is appropriate. With an IA size of 32 pixels × 32 pixels, the maximum particle displacement in the streamwise direction was 8 pixels with a dynamic range of 80. From the processed images, the mean velocities and higher order turbulence statistics were calculated and used to characterize the jet-free surface interaction.

3.5 Uncertainty Estimates

Measurement uncertainty analysis was made following the AIAA (American institute of aeronautics and astronautics) standard derived and explained by Coleman and Steele (1995). In general, a complete uncertainty analysis involves identifying and quantifying both the bias and precision errors in each part of the measurement chain. Detailed analyses of bias and precision errors inherent in PIV are available in Prasad et al. (1992) and Forliti et al. (2000). Forliti et al. (2000) have shown that a Gaussian peak-fitting algorithm has the lowest bias and precision errors. In the present study, the uncertainties in the mean velocity, turbulence intensities, Reynolds stresses, third order moments and fourth order moments at the 95% confidence level were estimated to be ±3%, ±7%, ±10%, ±12% and ±15%, respectively. Details of the uncertainty estimates are presented in Appendix E.

CHAPTER 4

RESULTS AND DISCUSSION ON OFFSET HEIGHT EFFECT

As mentioned in the previous chapter (Chapter 3), the experiments were conducted in three phases, namely Reynolds number effect, offset height effect and nozzle geometry effect. The effects of Reynolds number on the mixing and turbulent characteristics of surface attaching jets are presented in Appendix A. In this chapter, results related to the effects of offset height ratio (h/d = 1, 2, 3 and 4) on the turbulent characteristics and coherent structures in surface attaching jets are discussed. First, the effects of offset height on the instantaneous and mean velocity fields are examined. Next, the mean velocity and higher order turbulent statistics of up to the 4th order moments are discussed. Finally, the turbulent structures are analyzed using two-point correlations of velocity fluctuations and swirling strength, joint probability density functions and proper orthogonal decomposition (POD) technique.

4.1 Flow Visualization

4.1.1 Instantaneous velocity field

In order to reveal some qualitative features of the surface attaching jets, instantaneous velocity fields at various offset heights are examined. Galilean decomposition and linear stochastic estimation (LSE) technique are applied on the velocity fields to explore spanwise vortices and associated flow fields. Results for the two extreme conditions (h/d = 1 and 4) are discussed below:

4.1.1.1 Galilean decomposition

Figure 4.1 shows selected instantaneous velocity vector fields for the two extreme offset height ratios, h/d = 1 and 4. The region of visualization ($0 \leq x/d \leq 12$) covers both the near field and part of the interaction region of the jets. A Galilean decomposition is performed on each field by subtracting a constant convective velocity of $0.15U_j$ from the instantaneous streamwise velocity to reveal the small-scale vortices propagating at that velocity (Agrawal and Prasad, 2002). Zero velocity contour lines, indicated by solid lines, are superimposed on the plots to indicate the centres of the spanwise vortex cores at the edge of the shear layer produced by the Kelvin-Helmholtz instability mechanism (Grinstein et al., 1995). These contour lines should be interpreted as roughly coinciding with the turbulent/non-turbulent interface (T/NTI) in the instantaneous velocity fields. Also superimposed on the plots are the contours (red and blue patches) of normalized swirling strength ($\lambda_{ci,z}\, d/U_j$) associated with spanwise vortex cores. The decomposition reveals counter-clockwise rotating (retrograde) spanwise vortex cores at the edge of the upper shear layer and clockwise rotating (prograde) spanwise vortex cores at the edge of the lower shear layer. The swirling strength patches touching or lining up along the zero velocity contour lines are also coincident with the spanwise vortex cores. Braid-like structures can also be observed within $0 < x/d < 7$, which

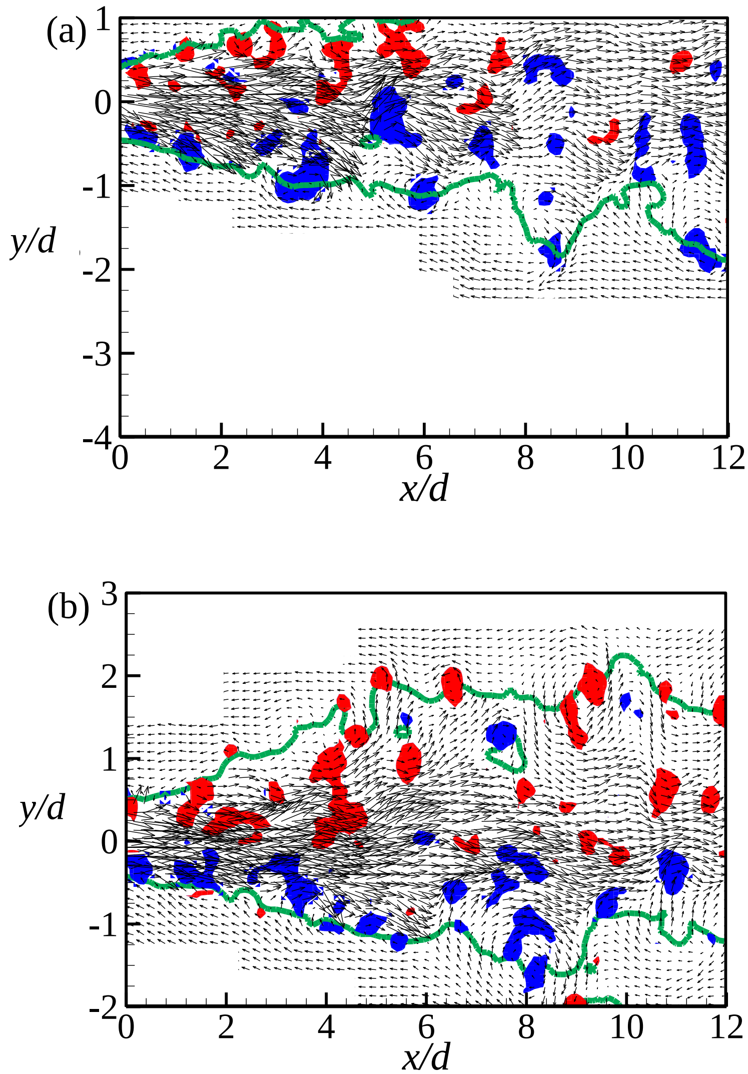

Figure 4.1. Instantaneous velocity field for (a) h/d = 1 and (b) h/d = 4.

in the vertical symmetry plane, correspond to the vortex rings propagating in the downstream direction. In Fig. 4.1a, the absence of swirling strength near the free surface in the interaction region is consistent with the notion that the jet-free surface interaction limits the T/NTI as well as the generated vortices for jets issuing very close to the free surface.

4.1.1.2 Linear stochastic estimation

The Galilean decomposition discussed earlier revealed spanwise vortex cores at the edge of the shear layer. To determine the average flow structure associated with these vortex cores, conditional averages of the flow fields were calculated using the linear stochastic estimation (LSE) technique. As mentioned in Chapter 2, the LSE of the conditional average of the *i*th component of velocity is given by Equation 2.13 as

$$\langle U_i(x_{ref} + \Delta x, y) | E(x_{ref}, y_{ref}) \rangle = \frac{\langle U_i(x_{ref} + \Delta x, y) \cdot E(x_{ref}, y_{ref}) \rangle}{\langle E(x_{ref}, y_{ref})^2 \rangle} E(x_{ref}, y_{ref})$$

where E is the prescribed condition at the reference location, (x_{ref}, y_{ref}), and Δx is the spatial separation in the streamwise direction. In calculating the LSE, attention was focused on the near field of the jets ($0 < x/d < 5$) due to its association with the onset of the vortex generating instability mechanism. Figure 4.2 presents vector plots of the LSE of the flow fields for $h/d = 1$ and 4 conditioned on the presence of vortex cores at the edge of the shear layer ($x_{ref}/d \approx 1$ and $y_{ref}/d \approx \pm 0.75$). Figures 4.2a and 4.2b present the vector plots of the LSE for $h/d = 1$ and 4, respectively, for a retrograde vortex prescribed at $x_{ref}/d \approx 1$ and $y_{ref}/d \approx 0.75$. The solid circles depicted in the plots indicate the centres of the spanwise vortex cores captured by the conditional averaging process. It should be noted that the velocity vectors were normalized by their corresponding magnitudes in order to reveal weaker motions away from the event location (Christensen and Adrian, 2001). The LSE is successful in revealing secondary vortex cores in addition to the event vortex. The vortices, which may be considered as a train of ring modes, reside along the edge of

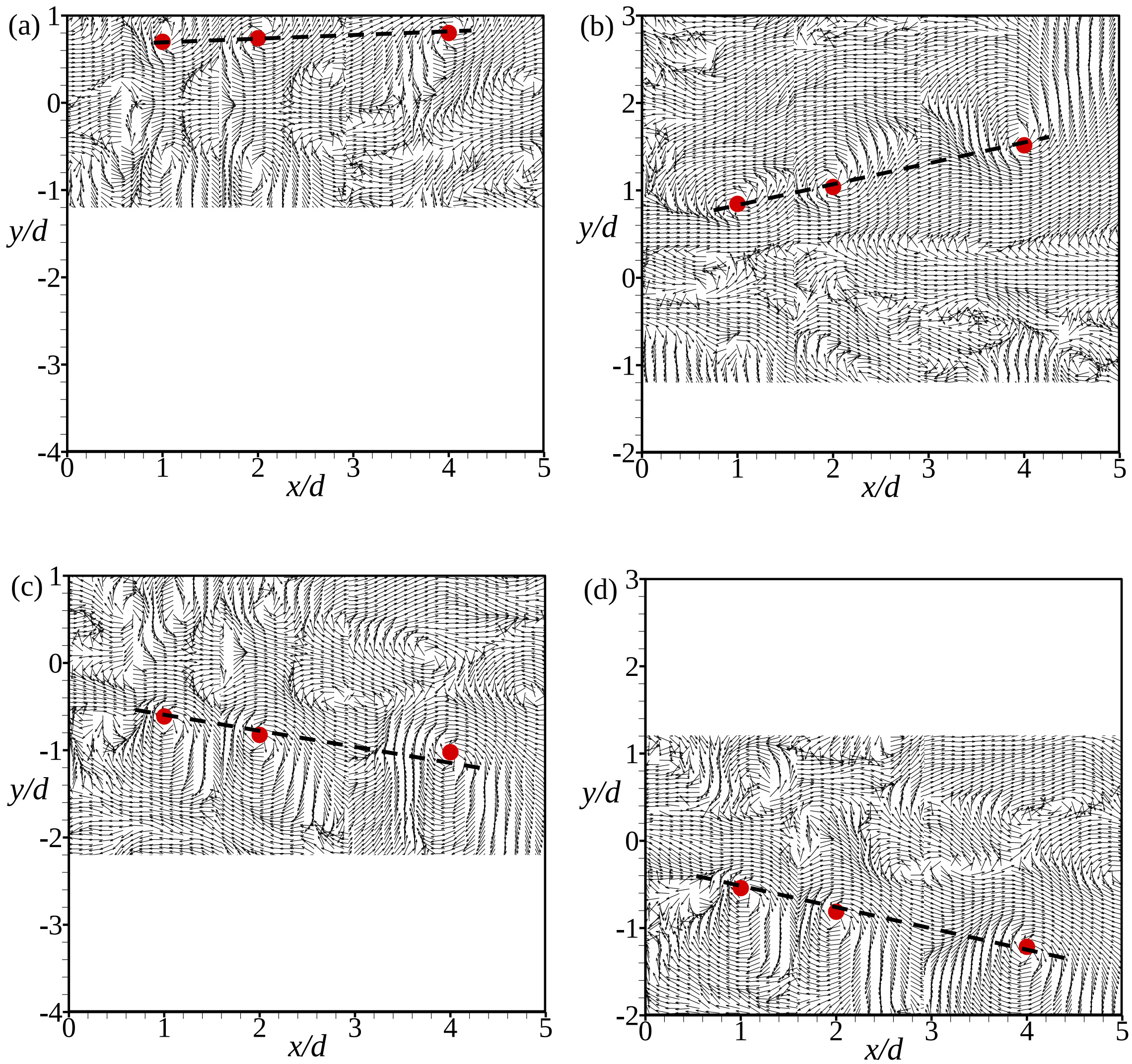

Figure 4.2. LSE at x/d = 1 in the edge of the shear layer for (a) h/d = 1 in the upper edge, (b) h/d = 4 in the upper edge, (c) h/d = 1 in the lower edge and (d) h/d = 4 in the lower edge.

the shear layer. This is consistent with the results observed in the Galilean decomposition results. Also worth commenting on is the shallow streamwise inclination of the connecting line of the ring modes. The inclination angles obtained by a least squares line fit through the vortex centres are approximately 2º and 14º for h/d = 1 and 4, respectively. Figures

4.2c and 4.2d depict the corresponding LSE results for a prograde vortex prescribed at the reference location $x_{ref}/d \approx 1$ and $y_{ref}/d \approx -0.75$ in the lower shear layer. While the inclination angles are symmetrical for $h/d = 4$, the magnitude of the inclination angle for $h/d = 1$ is about four times as large as that observed in the upper shear layer.

4.1.2 Contours of mean velocity and turbulent quantities

4.1.2.1 Streamwise mean velocity

The iso-contours of the normalized streamwise mean velocity, U/U_j, for $h/d = 1$ and 4, are shown in Fig. 4.3. The plots indicate that the effect of confinement is to reduce the outward growth of the jet in the upper shear layer relative to the lower shear layer. This effect diminishes with increasing offset height ratio. The reduced growth of the jet at smaller depths suppresses mixing in the near-exit region, leading to larger extents of the potential core. The interaction between the jet and the free surface is also evident in the contours (see Fig. 4.3a for instance). The attachment point (AP) is located using the following three approaches: the zero-velocity contour level which attaches to the free surface, the contour level of $U/U_j \approx 0.0125$ (minimum streamwise mean velocity level obtained from the dynamic range of the PIV system) which attaches to the free surface, and from the profiles of streamwise mean velocity along the free surface, where positive U starts increasing. The attachment lengths (L_a) determined using these approaches vary within $\pm 0.3d$ which is within measurement uncertainty. The attachment lengths determined from the contour level of $U/U_j \approx 0.0125$ are summarized in Table 4.1 for all four offset height ratios. For $h/d = 1$, the jet immediately attaches to the free surface soon after discharge ($L_a/d = 1.0$), but as the offset height ratio increases, a monotonic increase

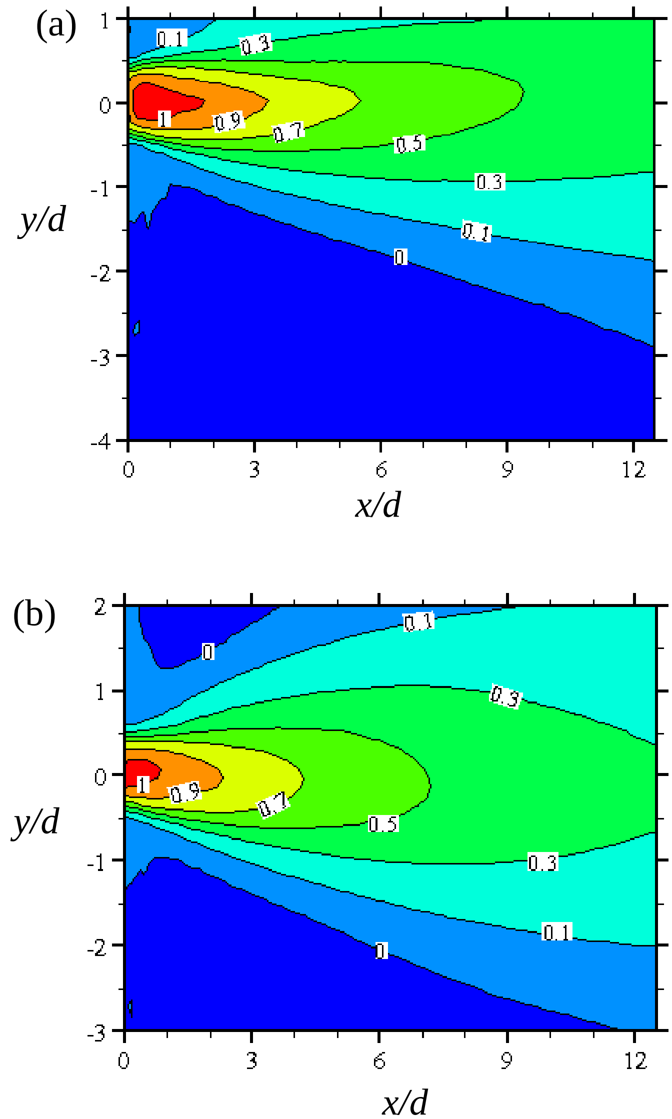

Figure 4.3. Contour plots of streamwise mean velocity for (a) h/d = 1 and (b) h/d = 4.

of L_a/d is observed. When normalized by the offset height, the L_a is of the same magnitude as the offset height for h/d = 1. At offset heights larger than 1, L_a is about three times as large as the offset height.

Table 4.1. Summary of the values of the attachment length.

h/d	***L_a/d***	***L_a/h***
1	1.0	1.0
2	6.4	3.2
3	9.3	3.1
4	12.3	3.0

4.1.2.2 Spanwise mean vorticity

Iso-contours of the normalized spanwise mean vorticity, $\omega_z d/U_j$ (where ω_z is spanwise mean vorticity) for the two cases are shown in Fig. 4.4. The mean spanwise vorticity reaches peak values in the near-exit region. At *h/d* = 1, the stronger confinement by the free surface stretches the upper shear layer contours almost parallel to the surface. With increasing offset height ratio, this effect is relaxed so that the contours recover their streamwise inclination to the axis. The contours show a damping effect on the mean spanwise vorticity in the upper shear layer due to the confinement in comparison to the lower shear layer. At larger offset height ratios, the mean spanwise vorticity is generally lower than corresponding values at smaller offset height ratios. For *h/d* = 1, the presence of finite vorticity near the free surface would be expected to have a significant impact on the energy redistribution mechanism at the free surface.

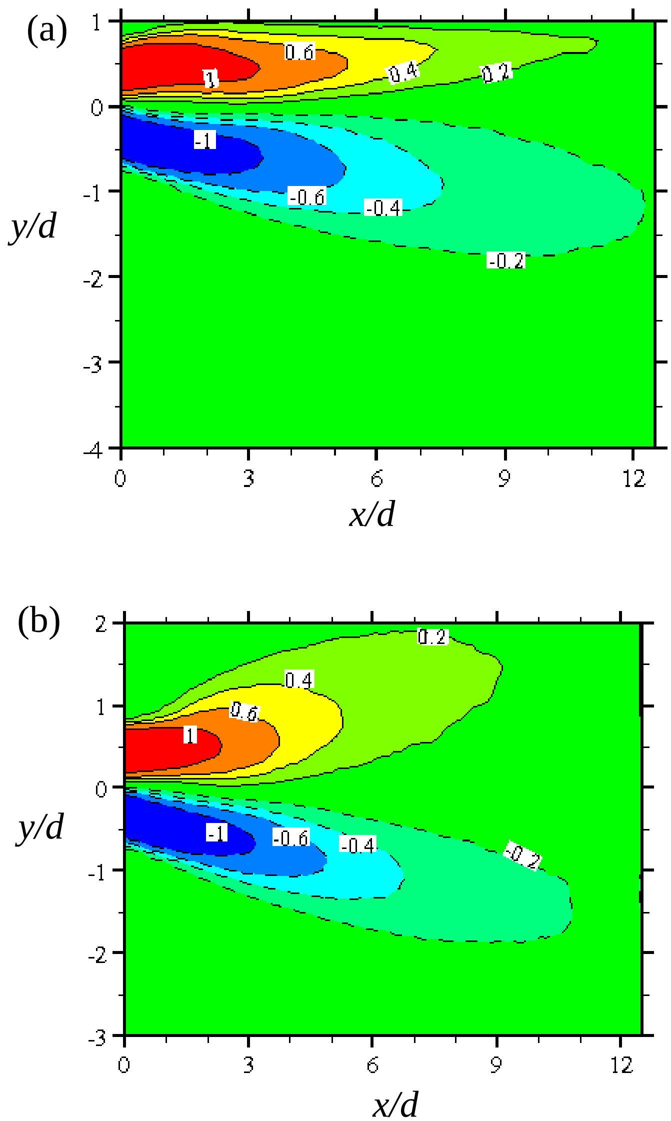

Figure 4.4. Contour plots of spanwise mean vorticity for (a) *h/d* = 1 and (b) *h/d* = 4.

4.1.2.3 Reynolds shear stress

Figures 4.5 shows the comparison of the iso-contours of the normalized Reynolds shear stress, $-\langle uv \rangle / U_j^2$ between *h/d* = 1 and 4. The plots show a negative distribution in the upper shear layer and a positive distribution in the lower shear layer,

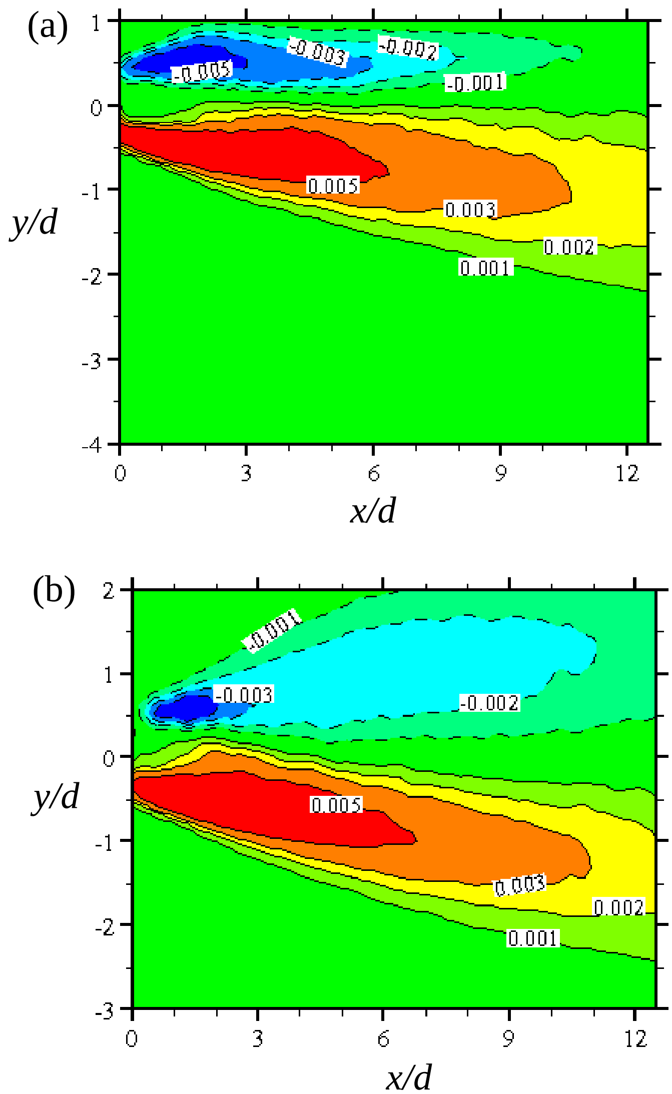

Figure 4.5. Contour plots of Reynolds shear stress for (a) h/d = 1 and (b) h/d = 4.

mimicking the direction of the mean streamwise velocity gradient in the shear layers. The plots indicate that the effect of the free surface is to reduce the spread of the Reynolds shear stress distribution in the upper shear layer compared to the lower shear layer.

4.2 Streamwise Evolution of Local Maximum Mean Velocity, Half-Velocity Width and Centerline Turbulence Intensities

The streamwise development of the jet is often characterized by the decay of the local maximum streamwise mean velocity, half-velocity width and turbulence intensities along the jet centerline. The mixing and entrainment capability of the jets are reflected in these mean and turbulent quantities. The effects of the offset height on these quantities are discussed below:

4.2.1 Local maximum mean velocity decay

The streamwise evolution of the local maximum mean velocity is shown in Fig. 4.6 for the four offset height ratios. Figure 4.6a shows the profiles of the maximum mean streamwise velocity normalized by the jet exit velocity, U_j, and the streamwise distance normalized by the nozzle width, *d*. The solid lines in the plots correspond to Equation 1.1, a least-squares fit of the straight line

$$\frac{U_j}{U_m} = K_d\left(\frac{x}{d} - \frac{x_o}{d}\right)$$

to the measured data in the range $5 \leq x/d \leq 23$, where the slope K_d of the line represents the far-field mean streamwise velocity decay rate and the constant x_o represents kinematic virtual origin of the jet. The profiles indicate that the mean streamwise velocity decay scales with the classical variables U_j and d only for $h/d \geq 3$. With reduced offset height ratio, the jet entrainment rate diminishes, resulting in increasingly lower mean velocity decay rates compared to the deeper jets. The fitted values of the decay parameters, K_d and

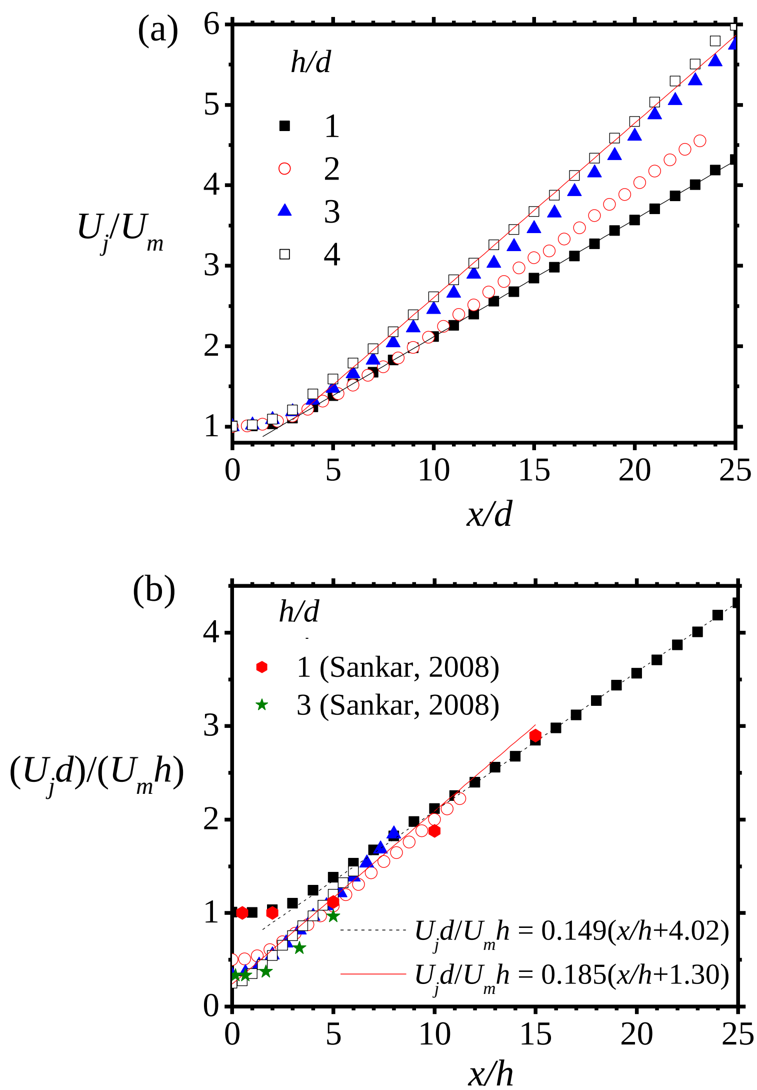

Figure 4.6. Streamwise evolution of the local maximum streamwise mean velocity decay: (a) Velocity decay in classical scaling, (b) velocity decay in similarity variables.

x_o/d are summarized in Table 4.2. The present values of K_d for $h/d \geq 3$ are almost similar to the value (0.203) reported by Mi and Nathan (2010) for the free jet issuing from a sharp-edged square nozzle at *Re* = 15000; and are approximately upto 8% larger than free round jet reported by Aleyasin et al. (2017b) at *Re* = 17000 for orifice nozzle. Faster decay rate at $h/d \geq 3$ compared to round jet could be attributed to better mixing capability of non-

Table 4.2. Summary of the jet maximum velocity decay parameters for various offset heights.

h/d	K_d	x_o/d	**Range**
1	0.149	-4.0	$5 \leq x/d \leq 23$
2	0.176	-2.4	$5 \leq x/d \leq 23$
3	0.213	-1.5	$5 \leq x/d \leq 23$
4	0.217	-2.0	$5 \leq x/d \leq 23$

circular nozzle than round jet (Quinn, 2007). Table 4.2 also reveals that slower decay rate leads a higher magnitude of kinematic virtual origin as observed for $h/d = 1$. With the increase of offset height ratio, $h/d \geq 2$, the magnitude of kinematic virtual origin reduces and lies within the value of $x_o/d = 2.0 \pm 0.5$. It should be noted that there is discrepancy between the value of x_o/d in the present study and previous free jet studies (e.g, Quinn and Militzer, 1988; Quinn, 2005; Mi and Nathan, 2010; Hashiehbaf and Romano, 2013; Aleyasin et al., 2017b), as the kinematic virtual origin is sensitive to initial conditions such as the type and shape of the nozzle, Reynolds number, exit turbulence level (Aleyasin et al., 2017b).

Figure 4.6b shows the maximum mean streamwise velocity decay profiles with U_m and x normalized using the similarity variables proposed by Madnia and Bernal (1994), $U_j d/h$ and h, respectively. Also included in the plots for reference are data from Sankar et al. (2008) measured at $h/d = 1$ and 3. The similarity scaling performs a better job of collapsing the data for $h/d \geq 2$. At $h/d = 1$, the profiles undergo a change in slope at the location $x/h \approx 11$. This downstream location, representing the point of crossover from the jets at offset height ratio $h/d \geq 2$ to the jets at $h/d = 1$ corresponds to the location where the shear layer interacts with the free surface the most. The slope-change at $h/d = 1$ indicates a stronger interaction between the shear layer and the free surface for these jets compared to the deeper jets. Based on the image jet model of Madnia and Bernal (1994) the straight line in Equation 1.2 as

$$\frac{U_j d}{U_m h} = \frac{K_{d,f}}{\sqrt{2}}\left(\frac{x}{h} - \frac{x_o}{h}\right)$$

is fitted to the profiles in Fig. 4.6b, where $K_{d,f}$ is the decay rate of the corresponding free jet, assumed herein to be approximately equal to 0.217, with a scaling factor of √2 introduced to account for the momentum of the image jet above the free surface. The least squares fit of the above equation to the data yields slopes of approximately 0.185 for $h/d \geq 2$ and 0.149 for $h/d = 1$. As noticed in previous investigations (Madnia and Bernal, 1994; Wallker et al., 1995), for the shallow jet ($h/d = 1$), the slope 0.149 is in reasonable agreement with the value of 0.217/√2 (≈ 0.153).

4.2.2 Half-velocity width

The spreading rate of the jet is quantified using the profiles of the half-velocity width. Figure 4.7a shows the streamwise evolution of the jet half-velocity width, $y_{0.5}$, measured from the jet centerline to the location below the jet axis where the streamwise mean velocity is half of the local maximum streamwise mean velocity. The profiles indicate that the half-velocity width in the lower shear layer is nearly independent of the

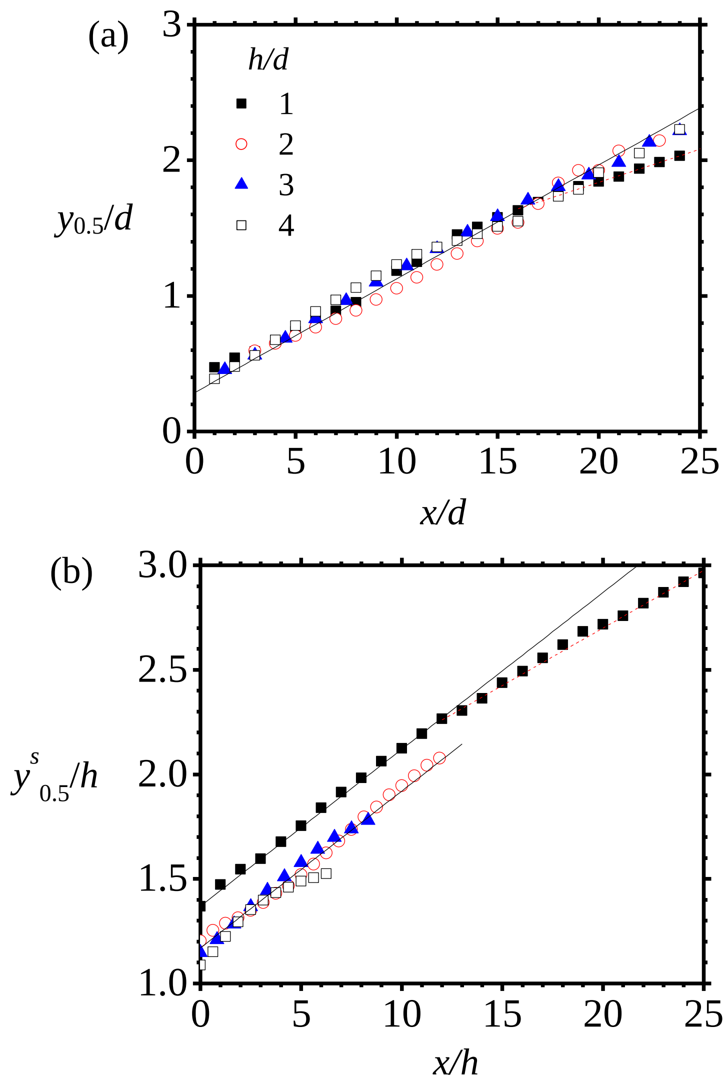

Figure 4.7. Streamwise evolution of the half velocity width: (a) Half velocity width measured from the location of U_m and (b) half velocity width measured from the free surface. Straight lines denote the least-squares linear fits to the half-width distributions.

offset height ratio for $h/d \geq 2$. In order to quantify the spread rate, the following least squares linear fit (Equation 1.3) is used to the data:

$$\frac{y_{0.5}}{d} = K_s \left(\frac{x}{d} - \frac{x_g}{d}\right)$$

where, K_s and x_g denote the spread rate and geometric virtual origin, respectively. The values of K_s and x_g are estimated as approximately 0.085 and -3.4, respectively within 5 ≤ x/d < 25 for h/d ≥ 2. This value of K_s is comparable to the range of the values (0.081 – 0.088) reported previously for free jets (Obot et al., 1984; Quinn and Militzer, 1988; Aleyasin et al., 2017b). For h/d = 1, the profile follows the others closely only within x/d ≤ 18. Beyond x/d ≈ 18, the jet is too close to the free surface to propagate and entrain ambient fluid. This leads to a reduced spread rate of about 0.049 due to the relatively strong confinement by the free surface in this case. The results presented in the literature (Madnia and Bernal, 1994; Ead and Rajaratnam, 2001) also show a similar change in slope at small offset height ratios in the interaction region.

Figure 4.7b shows the profiles of the jet half- velocity width, $y^s_{0.5}$, measured from the free surface to the half-velocity location below the jet centerline, as a function of x/h. Within the streamwise range x/h < 13, use of the similarity scaling, h, results in approximately linear distributions, with $y^s_{-0.5}/h$ values that are approximately 17% larger for h/d = 1 than h/d ≥ 2. Within this range, least squares line fits to the distributions give spreading rates of approximately 0.075. For h/d = 1, this value reduces to approximately 0.055 for x/h > 11. Madnia and Bernal (1994) reported a slope of 0.078 for x/h < 24 using this scaling, followed by a slight decline for x/h ≥ 24.

4.2.3 Turbulence intensities along the jet centerline

The variations of the streamwise and surface-normal turbulence intensities along the jet centerline are shown in Fig. 4.8. The corresponding centerline turbulence

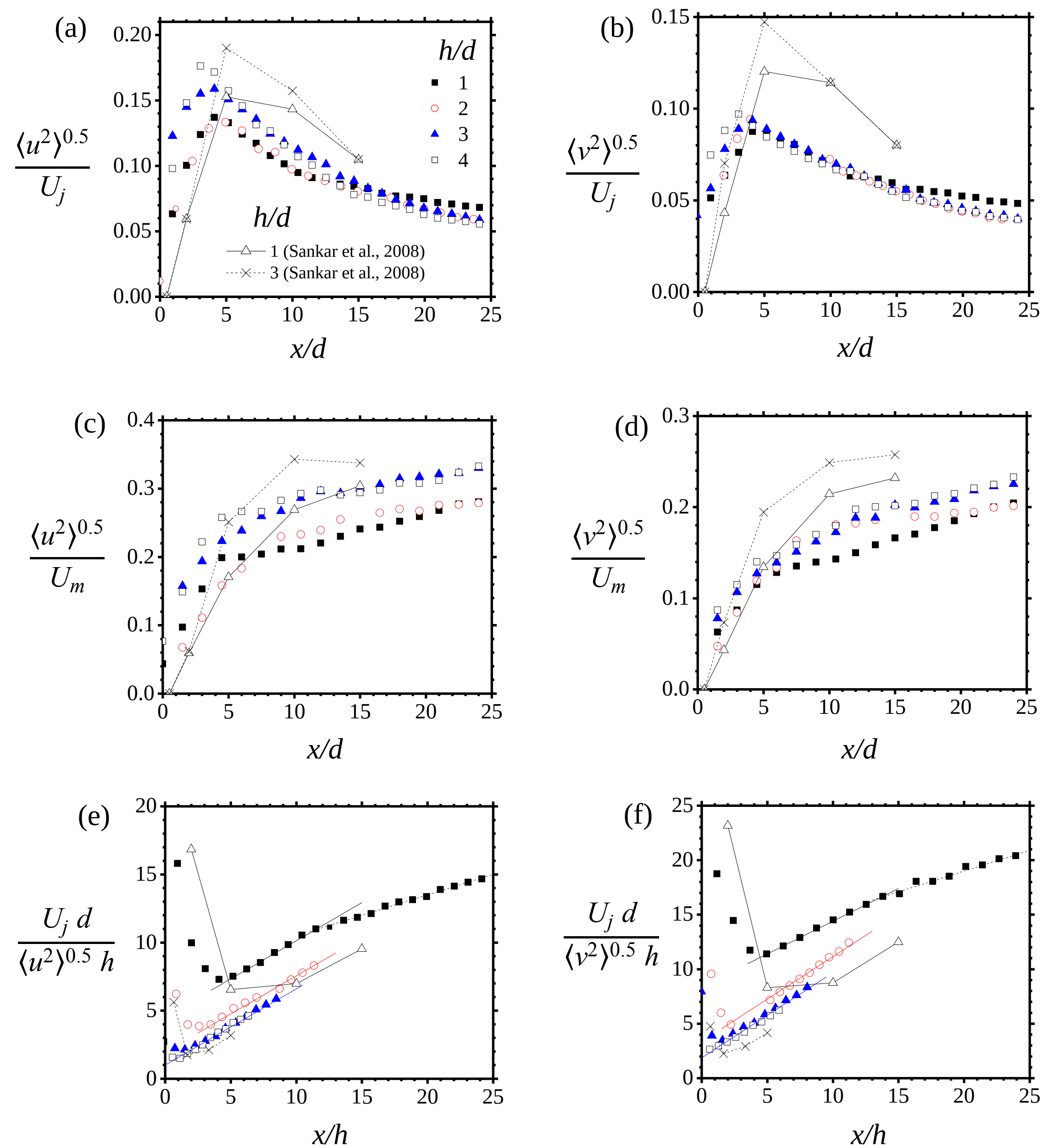

Figure 4.8. Streamwise evolution of the turbulence intensities along the jet centerline: (a) Streamwise turbulence intensity normalized by U_j, (b) surface-normal turbulence intensity normalized by U_j, (c) streamwise turbulence intensity normalized by U_m, (d) surface-normal turbulence intensity normalized by U_m, (e) streamwise turbulence intensity normalized by similarity variables and (f) surface-normal turbulence intensity normalized by similarity variables.

intensities from the smoothly contracting submerged square nozzle of Sankar et al. (2008) are also included for comparison. The streamwise and surface-normal turbulence intensities normalized by the jet exit velocity are depicted in Figs. 4.8a and 4.8b, respectively. A steep increase is observed in both turbulence intensities in the initial region (x/d < 5). This increase is considered to be an artefact of the large-scale coherent structures arising from the Kelvin-Helmholtz instability of the shear layer in the initial region (Ball et al., 2012) and the concomitant high turbulence production associated with large mean velocity gradients in this region. In the plots, the peak turbulence intensities occur at locations coinciding with the downstream end of the potential core regions. For the streamwise turbulence intensity, although no significant change occurs in the peak value from h/d = 1 to h/d = 2, moderate enhancements of 24% and 40% are observed for h/d = 3 and 4, respectively. The increase in the peak value of the surface-normal turbulence intensity is smaller (about 9% to 12%). For a given offset height ratio, the Sankar et al. (2008) results peak at substantially higher values albeit at a more gradual rate than the present data. The more gradual rise and higher peak values of the reference results can be attributed to the differing upstream conditions in that case: that is, smoothly contracting nozzle and higher Reynolds number (40000). After the initial region, the intensities then decrease to final values which are nearly independent of offset height ratio. From Figs. 4.8a and 4.8b, it is evident that during the jet development the magnitude of $<v^2>^{0.5}$ is always less than that of $<u^2>^{0.5}$, which provides an indication of anisotropy of the Reynolds stress components in the jets.

When normalized by the local maximum streamwise mean velocity (Figs. 4.8c and 4.8d), increasingly higher values are observed in the far field region, due to the decreasing local mean streamwise velocities. In the far field of the jet, no discernible differences are observed between *h/d* = 1 and 2, and between *h/d* = 3 and 4, but as indicated by the results of Sankar et al. (2008), the far-field turbulence intensities of the deeper jets (*h/d* = 3 and 4) are about 18% – 20% larger than those of the shallower jets (*h/d* = 1 and 2). At *x/d* = 23, the streamwise and surface-normal turbulence intensities for $h/d \geq 3$ are approximately 33% and 23%, respectively. The corresponding far-field streamwise and transverse turbulence intensity values reported for square free jets are, respectively, 22% and 20% (Quinn and Militzer, 1988; Ball et al., 2012;). The disparity between the present two values can be attributed to the strong anisotropy of Reynolds stresses in the free surface jets.

Figures 4.8e and 4.8f show turbulence intensities normalized by the similarity variables, $U_j d/h$ and *h* proposed by Madnia and Bernal (1994) which reduces scattered data. Due to the initial rise and fall of the centerline and values (see Figs. 4.8a and 4.8b), minima occur in the profiles. Also, because of the tendency of the similarity scaling to reduce scatter in the data, the locations of the minimum values are more clearly defined. These locations, corresponding to the potential core lengths, are evidently at increasingly larger streamwise distances with decreasing offset height ratio, as suggested by the streamwise mean velocity contours (Fig. 4.3). The profiles in Figs. 4.8e and 4.8f show a change in slope around the location of the minimum value, collapse at larger offset height ratios (*h/d* = 3 and 4), and enhancements with further reduction in offset height ratio.

Downstream of the minimum value, the slope of the streamwise turbulence intensity profiles, estimated from a least squares linear fit to the data, is approximately 0.560. This is about 25% lower than the value of 0.739 measured by Madnia and Bernal (1994) for their submerged round jet. For the shallow jet (h/d = 1), a further change in slope to a value of approximately 0.300 can be observed at $x/h \approx 11$. In case of the surface-normal turbulence intensity, the slopes are slightly larger: 0.780 for $h/d \geq 2$, and 0.600 for h/d = 1, which reduce to 0.380 beyond $x/h \approx 11$. At h/d = 1, the observed changes in slope of the turbulence intensity profiles at $x/h \approx 11$ is consistent with the changes in slope of the corresponding streamwise mean velocity decay profile in Fig. 4.6b and the half-velocity width distribution in Fig. 4.7b.

4.3 Streamwise Evolution of Surface Velocity, Vorticity Thickness and Surface Turbulence Intensities

The flow characteristics of the surface attaching jets largely depend on the kinematic condition of the free surface. Also, the mean and turbulent statistics at the free surface would provide information on the boundary condition in modeling purpose. In the present study, the free surface is characterized by streamwise mean surface velocity, mean velocity defect, vorticity thickness and turbulence intensities along the free surface. It is noted that due to the challenge of measuring the turbulent quantities exactly at the free surface, the surface quantities reported in the present study are obtained at about two interrogation area sizes (≈ 2 mm) below the air-water interface of the PIV images in order to avoid erroneous data. Discussions on the mean and turbulent quantities along the free surface are provided below:

4.3.1 Streamwise mean surface velocity and velocity defect

Profiles of the surface streamwise mean velocity (U_s/U_j) for various offset heights are presented in Fig. 4.9a. Negligible surface velocity before the attachment point is evident in the figure. The surface velocities increase rapidly beyond the attachment point to a local maximum value and decrease gradually downstream, in agreement with the results of Madnia and Bernal (1994). In the absence of surface deformation, the rapid increase ($\partial U_s/\partial x > 0$) is associated with the stretching of the free surface while the gradual decrease ($\partial U_s/\partial x < 0$) indicates contracting of the free surface in the streamwise direction. This implies that the jet-free surface interaction causes straining of the free surface which is more severe as offset height ratio decreases. Figure 4.9b shows the profiles of the streamwise mean surface velocity normalized by the similarity scaling of Madnia and Bernal (1994). The streamwise distance is first shifted by the attachment length so that the origin is now at the attachment point. The shifted distance is then normalized by the jet offset height. The similarity scaling collapses the profiles over a limited extent of the interaction region, $(x-L_a)/h < 5$.

The mean velocity defect (ΔU) is useful in determining the vorticity thickness discussed in the following section. The values of ΔU is estimated as

$$\Delta U = U_m - U_s \tag{4.1}$$

The profiles for $\Delta U/U_j$ are examined in Fig. 4.9c. The $\Delta U/U_j$ decreases monotonically with streamwise distance, indicating that U_m approaches the value of U_s in the far field of the surface jet. For instance, $\Delta U/U_j$ for h/d = 1 is about 4% at x/d = 15 and 16% - 26% at

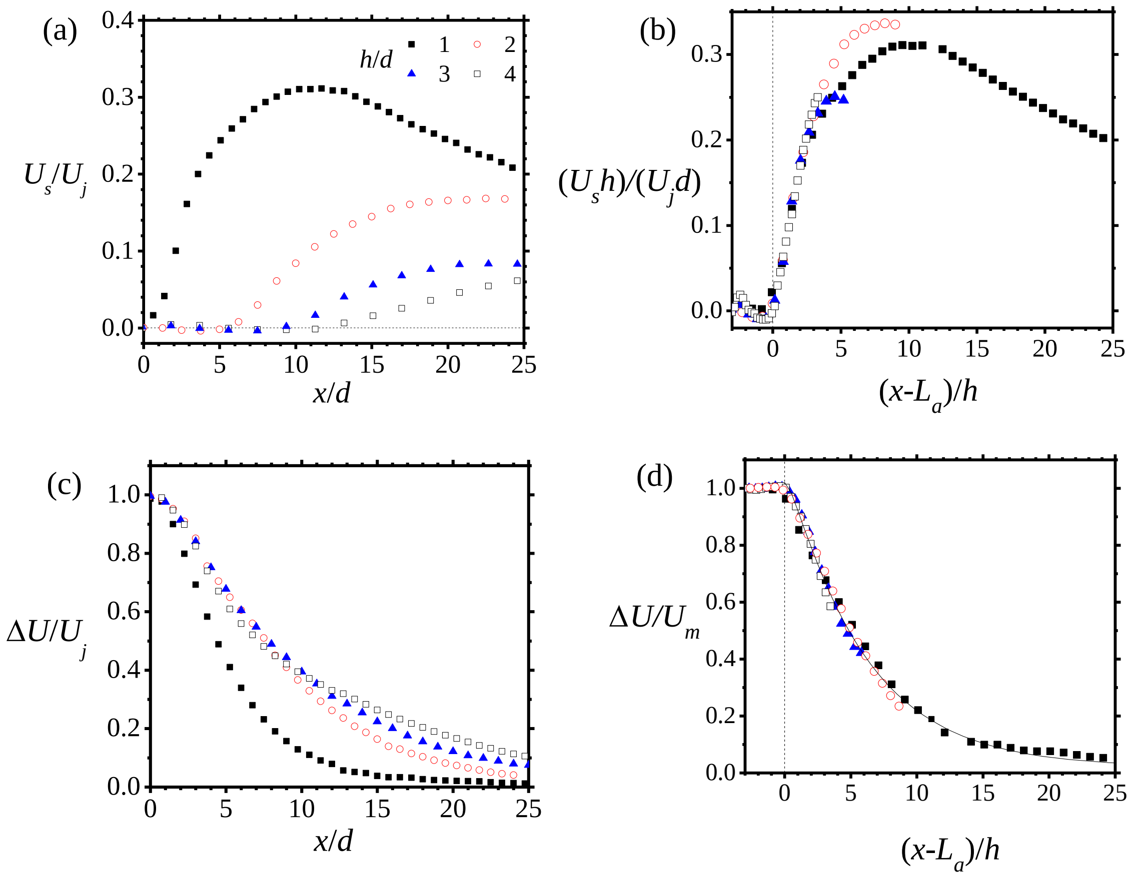

Figure 4.9. Streamwise evolution of streamwise mean surface velocity and velocity defect: (a) Surface velocity normalized by U_j, (b) surface velocity normalized by similarity variables; (c) velocity defect normalized by U_j and (d) velocity defect normalized by similarity variables. The solid line in (d) is the least-squares fit of the exponential-Gaussian hybrid distribution.

x/d = 15 for h/d = 2 to 4. Figure 4.9d shows profiles of the mean surface velocity defect, normalized by the local maximum mean streamwise velocity, U_m, with respect to the streamwise distance relative to the attachment point. The profiles show a good collapse for the chosen length and velocity scales and follow the exponential-Gaussian hybrid (EGH) distribution (Lan and Jorgenson, 2001),

$$\frac{\Delta U}{U_m} = 0.02 + \exp\left(\frac{-x^{*2}}{3.92 + 5.8\,x^*}\right) \tag{4.2}$$

where, $x^* = (x\text{-}L_a)/h$.

4.3.2 Vorticity thickness

The interaction of the jet with the free surface bears some resemblance to turbulent mixing layers. Therefore, the vorticity thickness, δ_ω is evaluated for each offset height ratio as follows:

$$\delta_\omega = \frac{\Delta U}{(\partial U/\partial y)_{\max}} \tag{4.3}$$

where, $(\partial U/\partial y)_{\max}$ is the maximum mean shear in the upper shear layer of the jet. The variation of the vorticity thickness with x/d is shown in Fig. 4.10. Unlike h/d = 1, the vorticity thickness for h/d = 2, 3 and 4 increases linearly in the region ($0 < x/d < 13$) and remains nearly constant downstream. The linear increase of vorticity thickness depicts the growth of the vortices generated from the instability near the jet's exit plane while the constant values are consistent with the observation that free surface limits growth of these vortical structures (Fig. 4.1). It is interesting to note that the linear growth rates of vorticity thickness for h/d = 2, 3 and 4 (0.115, 0.160 and 0.180, respectively) are comparable to values (0.120 to 0.220) reported for separated and reattached flows (Ukeiley and Murray, 2005; Bian et al., 2011; Essel and Tachie, 2015; Essel et al., 2015) and plane mixing layers (Brown and Roshko, 1974).

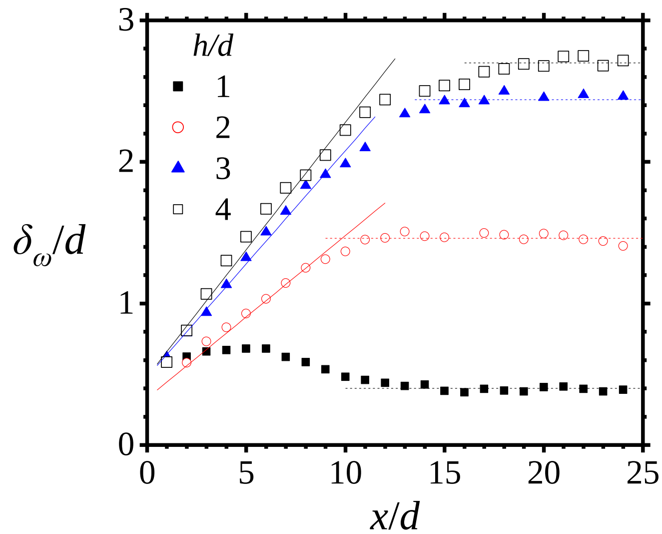

Figure 4.10. Streamwise evolution of vorticity thickness. Solid lines are least-squares linear fit.

4.3.3 Turbulence intensities along the free surface

The streamwise and surface-normal turbulence intensity profiles along the free surface are shown in Fig. 4.11. Figure 4.11a shows the streamwise surface turbulence intensity normalized by the jet exit velocity. The profiles indicate that effect of decreasing the offset height ratio is to augment the streamwise surface turbulence intensity levels. Except for *h/d* = 1, all profiles develop single peaks near the attachment point. For the *h/d* = 1 jet, two peaks are observed, one near the attachment point and a much broader one near the middle of the interaction region. This second peak is related to the stronger interaction between the *h/d* = 1 jet and the free surface, as foreshadowed by the changes in slope of the mean velocity and turbulence intensity profiles at *x/h* ≈ 11. The corresponding profiles of the surface-normal turbulence intensity show a similar enhancement with decreasing offset height ratio (Fig. 4.11b), except for a rapid decay

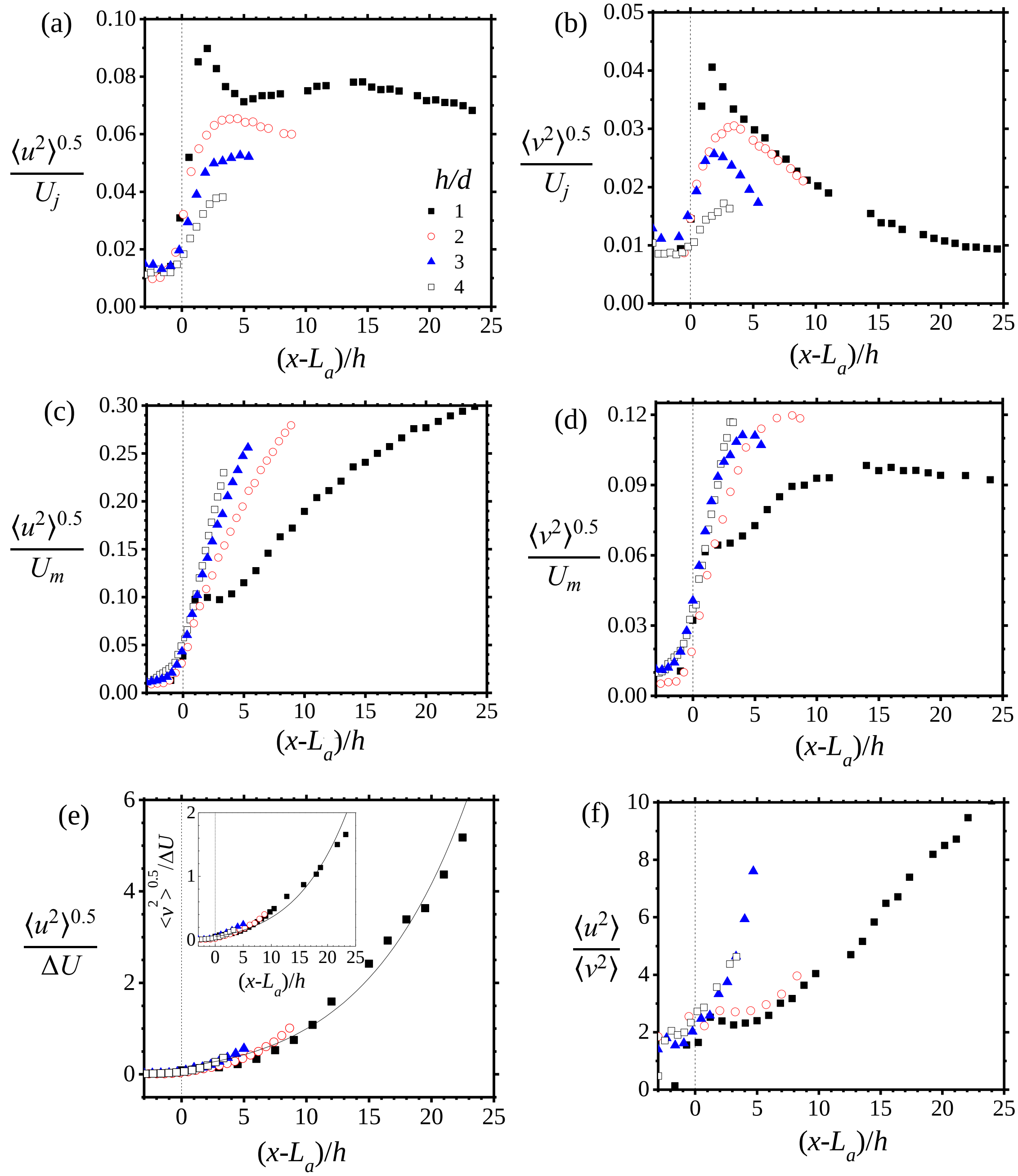

Figure 4.11. Streamwise evolution of the turbulence intensities along the free surface: (a) Streamwise turbulence intensity normalized by U_j, (b) surface-normal turbulence intensity normalized by U_j, (c) streamwise turbulence intensity normalized by U_m, (d) surface-normal turbulence intensity normalized by U_m, (e) streamwise turbulence intensity normalized by velocity defect and (f) stress ratio at the free surface. The solid curve in (e) is least-squares fit of an exponential distribution.

with downstream distance as the jet propagates through the interaction region. This damping effect of the free surface on the surface-normal component is an indication of the turbulent kinetic energy (TKE) redistribution at the free surface from the surface-normal component to the streamwise and spanwise components (Anthony and Willmarth, 1992; Wallker et al., 1995). As indicated by the plots, this TKE redistribution mechanism would be enhanced with decreasing offset height ratio. The turbulence intensities normalized by the maximum mean streamwise velocity, U_m, are plotted in Figs. 4.11c and 4.11d to check for plausible scaling with U_m. It is apparent that the maximum mean streamwise velocity is not the appropriate velocity scale for the surface turbulence intensities. Figure 4.11e shows the profiles of the streamwise surface turbulence intensity normalized by the velocity defect (inset of the figure presents the corresponding plot for the surface-normal turbulence intensity). The profiles collapse reasonably well onto a single curve represented by the following exponential distribution:

$$\frac{\langle u^2\rangle^{0.5}}{\Delta U} \text{ or } \frac{\langle v^2\rangle^{0.5}}{\Delta U} = 0.005 \exp\left(x^* - x_2\right)^{n'} \tag{4.4}$$

where, n' and x_2 denote the increasing rate of the normalized turbulence intensities and a fitting parameter, respectively; and $x^* = (x-L_a)/h$. The estimated values of n' and x_2 are summarized in Table 4.3 irrespective of offset height. Lower value of n' for $<v^2>^{0.5}/\Delta U$ (approximately 6%) compared to $<u^2>^{0.5}/\Delta U$ could be attributed to damping of the surface-normal turbulence intensity close to the free surface as mentioned earlier. Furthermore, the substantially lower values of the surface-normal component (Figs. 4.11b and 4.11d) compared to the streamwise component (Figs. 4.11a and 4.11c) indicate strong

Table 4.3. Summary of the fitting parameters of exponential curve for the profiles of surface turbulence intensities normalized by velocity defect irrespective of offset height.

Profiles	n'	x_2
$<u^2>^{0.5}/\Delta U$	0.566	-9
$<v^2>^{0.5}/\Delta U$	0.535	-5

anisotropy in the Reynolds stress field at the free surface. Figure 4.11f shows profiles of the stress ratio at the free surface, $<u^2>/<v^2>$. For the deeper jets ($h/d \geq 3$), the stress ratio increases monotonically in the interaction region. In the case of the shallow jets, an initial decrease occurs during the initial interaction, followed by a monotonic increase downstream of the initial interaction. The initial decrease of the stress ratio for the shallow jets can be attributed to the more dramatic increase in the surface-normal velocity fluctuations than the streamwise velocity fluctuations during the initial interaction.

4.4 Surface-Normal Distribution of Mean Velocity and Higher Order Moments

Effects of the offset height on the surface-normal distribution of mean velocity and higher order turbulent moments (up to the 4th order) are discussed in this section. At first, the surface-normal profiles normalized using h and U_m as the length and the velocity scales, respectively are discussed. It should be noted that using the length scale, h, puts the free surface at $y/h \approx 1$ irrespective of offset height and allows the data close to the free surface to be examined more precisely.

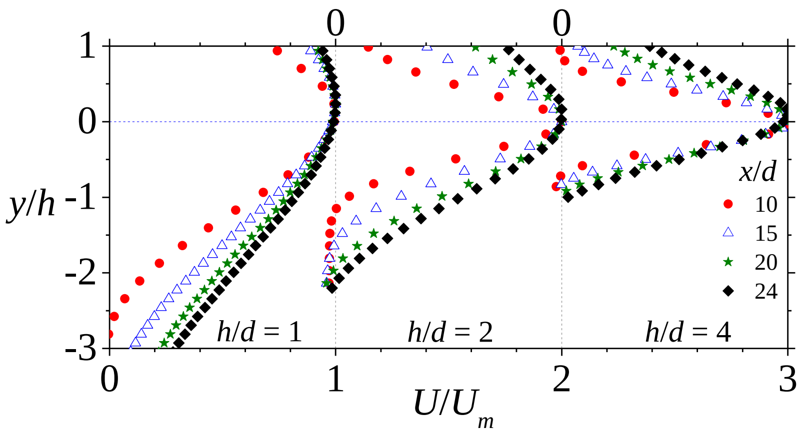

Figure 4.12. Surface-normal profiles of streamwise mean velocity with the length scale of *h* for *h/d* = 1, 2 and 4 at selected *x/d* locations.

The discussion is followed by examining the surface-normal profiles with typical similarity variables, $y_{0.5}$ and U_m as the length and velocity scale, respectively to explore self-similarity of the surface attaching jets. The profiles with similarity variables are compared to the self-similar free jet data by Hussein et al. (1994).

4.4.1 Surface-normal profiles normalized using *h* and U_m

4.4.1.1 Streamwise mean velocity

One-dimensional profiles of the streamwise mean velocity (*U*) at selected locations (*x/d* = 10, 15, 20 and 24) in the interaction region for *h/d* = 1, 2 and 4 are shown in Fig. 4.12. The dashed horizontal line at *y/h* = 0 indicates the nozzle centerline. The profile of U/U_m exhibits typical Gaussian-like distribution, almost symmetricity about the nozzle centerline before the jet-free surface interaction as shown for the *h/d* = 4 jet at *x/d* = 10, for instance. Further downstream in the interaction region, the Gaussian-like profiles of U/U_m are truncated at the free surface, in a manner that is more dramatic as offset height ratio decreases. For $x/d \geq 20$, the profiles are in reasonable agreement, especially in the lower shear layer.

4.4.1.2 Spanwise mean and fluctuating vorticity

Figure 4.13a shows the profiles of spanwise mean vorticity ($\omega_z = \partial V/\partial x - \partial U/\partial y$). Similar to free jets, the spanwise mean vorticity is anti-symmetric about the centerline but the damping effects of the free surface reduces the vorticity magnitude in the upper shear layer as the jet evolves downstream. The reduced mean vorticity in the upper shear layer is an artifact of the diminishing mean shear ($\partial U/\partial y$) near the free surface. The mean vorticity decreases with decreasing offset height ratio.

Figure 4.13b shows that the spanwise fluctuating vorticity (ω'_z) is concentrated at the nozzle's centerline for $h/d = 4$, but as offset height reduces to $h/d = 1$, the vorticity is more uniformly distributed across the jet. The reduction in spanwise fluctuating vorticity with decreasing offset height ratio is consistent with the reduction in the number of spanwise vortices identified with the swirling strength and Galilean decomposition techniques (see Fig. 4.1). Unlike the wall attaching jets, the spanwise fluctuating vorticity is non-zero at the free surface for the test cases, even though the magnitude is a strong function of h/d and x/d.

4.4.1.3 Reynolds stresses

Profiles of the Reynolds stresses ($\langle u^2 \rangle$, $\langle v^2 \rangle$ and $-\langle uv \rangle$) are presented in Fig. 4.14. The effects of decreasing offset height ratio are observed to reduce the distributions of the Reynolds stresses in the upper shear layer compared to the lower shear layer. For

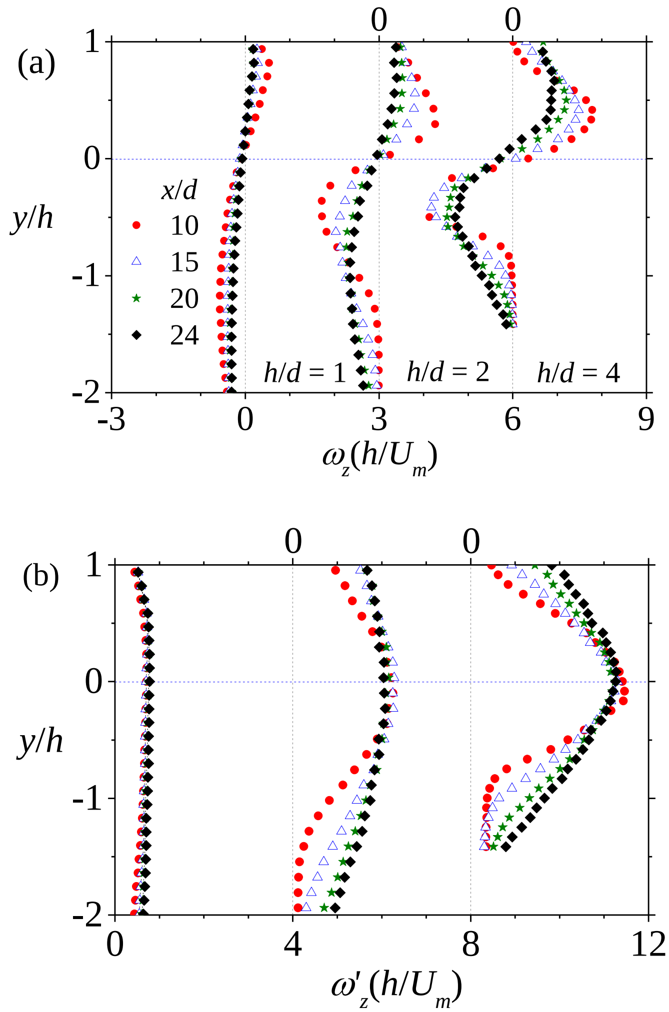

Figure 4.13. Surface-normal profiles of mean vorticity and vorticity fluctuation with the length scale of *h* for *h/d* = 1, 2 and 4 at selected *x/d* locations: (a) spanwise mean vorticity and (b) root-mean-square of spanwise vorticity fluctuation.

h/*d* = 1, the profiles of the surface-normal Reynolds normal stress (Fig. 4.14b) are reduced to negligible values at the free surface, but the streamwise Reynolds normal stress (Fig. 4.14a) profiles are enhanced near the free surface due to the energy redistribution phenomenon, that leads increase of anisotropy of turbulence near the free surface. The corresponding profiles for *h*/*d* = 2 and 4 also show similar behavior but in a more moderate form than that of *h*/*d* = 1.

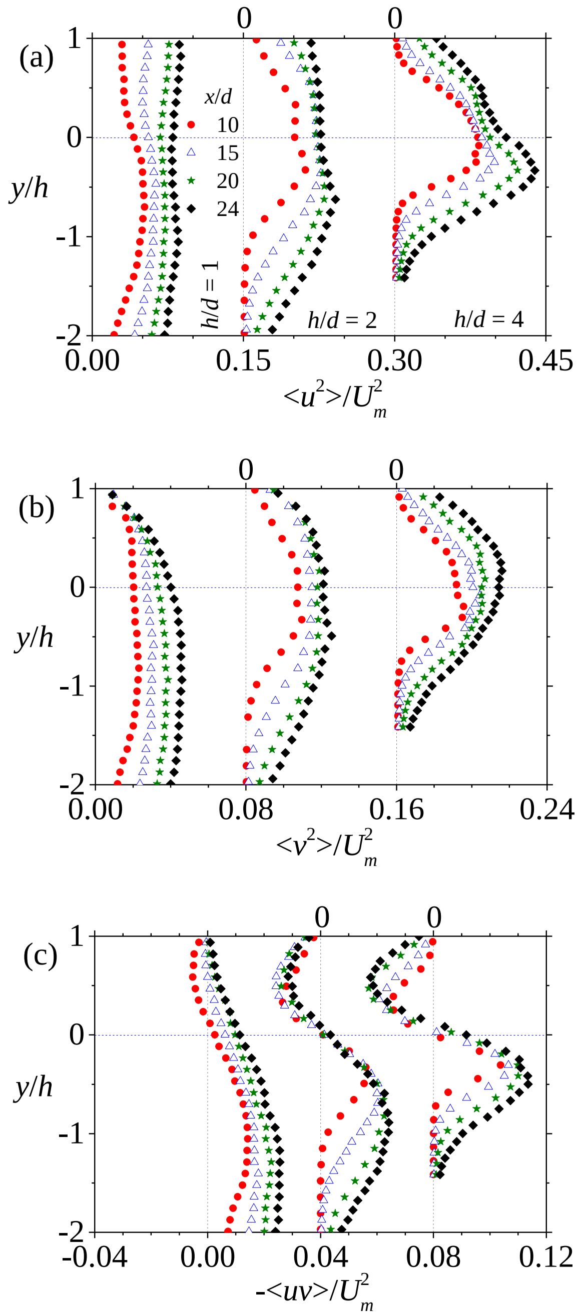

Figure 4.14. Surface-normal profiles of Reynolds stresses with the length scale of *h* for *h/d* = 1, 2 and 4 at selected *x/d* locations: (a) Streamwise Reynolds normal stress, (b) surface-normal Reynolds normal stress and (c) Reynolds shear stress.

For each offset height ratio, the peak values of the Reynolds shear stress are significantly reduced in the upper shear layer compared to the lower shear layer which is more intense for shorter offset height (Fig. 4.14c). The reduction of the Reynolds shear stress in the upper shear layer of the shallow jet could be attributed to the damping of the mean shear by the increased confinement. The surface-normal location where $-\langle uv \rangle = 0$ coincides with the nozzle centerline for $h/d = 2$ and 4, but shifts towards the free surface with increasing streamwise distance for $h/d = 1$. Since the location of U_m is close to the centerline for all offset height ratios (see Fig. 4.12), the profiles for $h/d = 1$ demonstrate that $-\langle uv \rangle$ and $\partial U/\partial y$ do not vanish at the same surface-normal location. This interesting observation indicates the occurrence of counter-gradient diffusion phenomenon, which leads to negative eddy viscosity, ($-\langle uv \rangle = \nu_t\ (\partial U/\partial y + \partial V/\partial x)$, where ν_t is the eddy viscosity). Similar displacement of the location of $-\langle uv \rangle = 0$ from the location of U_m towards the wall have also been reported in previous wall attaching jets (Agelin-Chaab and Tachie, 2011c; Nyantekyi-Kwakye et al., 2015a, 2015b).

4.4.1.4 Stress ratio and structure parameter

Figure 4.15 shows the stress ratio ($\langle u^2 \rangle / \langle v^2 \rangle$) and the Townsends structure parameter ($-\langle uv \rangle/(2k)$, where k is the turbulent kinetic energy) used to investigate the effects of offset height ratio on the large-scale anisotropy. Since the spanwise Reynolds normal stress, $\langle w^2 \rangle$ was not measured in this study, the turbulent kinetic energy was estimated as

$$k = 0.5\ (\langle u^2 \rangle + 2\ \langle v^2 \rangle) \qquad (4.5)$$

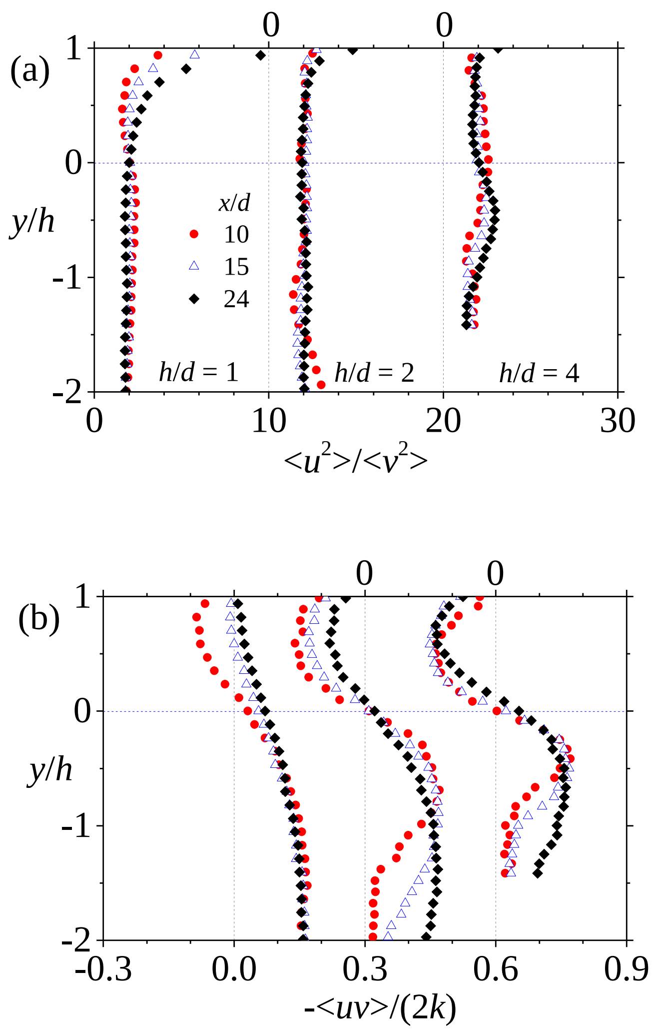

Figure 4.15. Surface-normal profiles of (a) stress ratio and (b) structure parameter with the length scale of *h* for *h/d* = 1, 2 and 4 at selected *x/d* locations.

where, $\langle w^2 \rangle$ is assumed to be similar to $\langle v^2 \rangle$, based on results of previous surface jet experiments (Anthony and Willmarth, 1992, Walker et al., 1995). In most parts of the jet, $\langle u^2 \rangle/\langle v^2 \rangle$ is approximately 2 for all offset height ratios which agrees well with the results of previous free jets (Hussein et al., 1994). The anisotropy ($\langle u^2 \rangle/\langle v^2 \rangle \neq 1$) is significantly increased as the free surface is approached, and as offset height ratio decreases.

The structure parameter is associated with the coefficient, $C_\mu = (-\langle uv\rangle/k)^2$ used in turbulence modelling. The C_μ is usually set as 0.09 which is equivalent to $-\langle uv\rangle/(2k) = 0.15$. Figure 4.15b demonstrates that the peak values of the structure parameter are comparable to 0.15, except for the reduced values in the upper shear layer for $h/d = 1$. The occurrence of counter-gradient diffusion phenomenon, enhanced anisotropy and reduced structure parameter in the upper shear layer of $h/d = 1$, which according to Craft et al. (2000) is an indication that turbulence models such as eddy viscosity models that do not explicitly solve the Reynolds stresses may fail to accurately predict the flow characteristics near free surface as offset height ratio decreases.

4.4.1.5 Production of turbulence

The effects of jet confinement on the production terms in the Reynolds stress transport equations are examined in Fig. 4.16. In these plots and hereafter, the intermediate data: $h/d = 2$ and $x/d = 15$ are excluded to preclude redundancy. The production terms in the streamwise (P_{u^2}), surface-normal (P_{v^2}) and Reynolds shear stress (P_{-uv}) transport equations for the present two-component PIV system are estimated as

$$P_{u^2} = -2\,(\langle u^2\rangle\, \partial U/\partial x + \langle uv\rangle\, \partial U/\partial y), \tag{4.6}$$

$$P_{v^2} = -2\,(\langle v^2\rangle\, \partial V/\partial y + \langle uv\rangle\, \partial V/\partial x), \tag{4.7}$$

$$P_{-uv} = \langle u^2\rangle\, \partial V/\partial x + \langle v^2\rangle\, \partial U/\partial y, \tag{4.8}$$

respectively. The values of the production terms were normalized by U_m^3/h. From Fig. 4.16a, it can be inferred that a diminishing offset height ratio results in attenuation of the

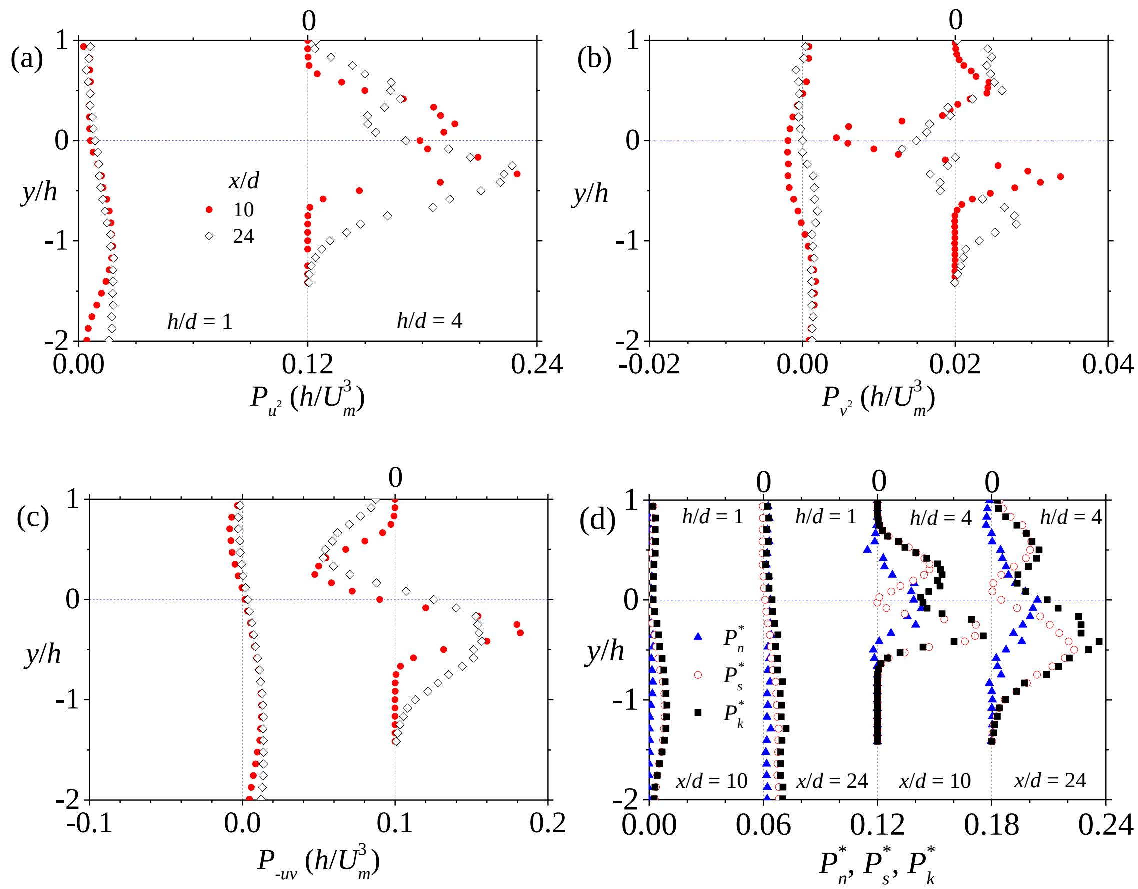

Figure 4.16. Surface-normal profiles of production of Reynolds stresses and turbulent kinetic energy for h/d = 1 and 4 at selected x/d locations: (a) Production of streamwise Reynolds normal stress, (b) production of surface-normal Reynolds normal stress, (c) production of Reynolds shear stress and (d) production of turbulent kinetic energy.

peak values of the distribution of P_{u^2}, and that the effect is more dramatic in the upper shear layer compared to the lower shear layer. For h/d = 1, the values are nearly independent of streamwise distance (x/d) within the interaction region. The differences in the distribution below $y/h \approx -1.5$ can be attributed to a shift in the location of the peak value with increasing streamwise distance. For the deeper jet (h/d = 4), the peak value is reduced by about 70% with increasing streamwise distance in the upper shear layer, but nearly independent of x/d in the lower shear layer. The comparatively larger values of the production term over a wider surface-normal range are indicative of enhanced turbulence production of the large-scale structures growing in the streamwise direction. The positive values of the production term indicate that P_{u^2} acts as a source of energy in both the upper and lower shear layers. These results are consistent with data reported by Panchapakesan and Lumley (1993) and Bogey and Bailly (2009) for a round free jet. The profiles of the normalized values of P_{v^2} are shown in Fig. 4.16b. The profiles of P_{v^2} indicate a similar suppression in peak production levels with reduced offset height ratio, albeit the values are about an order of magnitude smaller than those of P_{u^2}. At the larger offset height ratio, the profiles develop a secondary (negative) peak within the core jet, whose value diminishes as x/d increases. Such negative peaks, indicating an energy loss in the core jet, have also been reported in previous investigations (e.g., Panchapakesan and Lumley, 1993; Bogey and Bailly, 2009). Figure 4.16c shows the profiles of the normalized Reynolds shear stress production term, P_{-uv}. The Reynolds shear stress production levels are comparable to those of the streamwise Reynolds normal stress and indicate a similar rapid decay in the upper shear layer compared to the values in the lower shear layer. The attenuation of the Reynolds stress production due to the presence of confinement has also been reported in previous wall attaching jet investigations (Agelinchaab and Tachie, 2011b). It should also be noted that these damping effects of reduced offset height on the production terms is partly responsible for the reduction in peak values of the Reynolds stresses observed in Fig. 4.14c.

Figure 4.16d shows a comparison of the relative contributions of the normal and shear components of the total production term of turbulent kinetic energy, P_k at the two streamwise locations for h/d = 1 and h/d = 4. The normal and shear components of the total production term are estimated as

$$P_n = - (\langle u^2 \rangle \, \partial U/\partial x + \langle v^2 \rangle \, \partial V/\partial y), \tag{4.9}$$

$$P_s = - (\langle uv \rangle \, \partial U/\partial y + \langle uv \rangle \, \partial V/\partial x), \tag{4.10}$$

where $P_k = P_n + P_s$. In the plots, the asterisk denotes normalization by U_m^3/h. For the shallower jet, the upper shear layer samples negligibly small contributions from the normal and shear components. In the lower shear layer, however, the profiles indicate that the shear component is the more dominant contributor to the total turbulence production term. At offset height, h/d = 4, the dominant contributor to P_k is the shear component at the edge of the upper and lower shear layers, while the normal component is the dominant contributor at the center of the jet.

4.4.1.6 Triple velocity products

The triple velocity correlations are important because their gradients determine the turbulent diffusion of the Reynolds stresses in the jet. The profiles of the triple correlations normalized by U_m^3 are shown in Fig. 4.17, where again, there is a general attenuation of the peak values with decreasing offset height ratio. Figure 4.17a shows profiles of the surface-normal turbulent transport of the streamwise Reynolds normal stress ($\langle u^2v \rangle$). For h/d = 1, $\langle u^2v \rangle$ is nearly zero close to free surface at x/d = 10. An exception occurs in the far field of the interaction region (x/d = 24), where the correlation

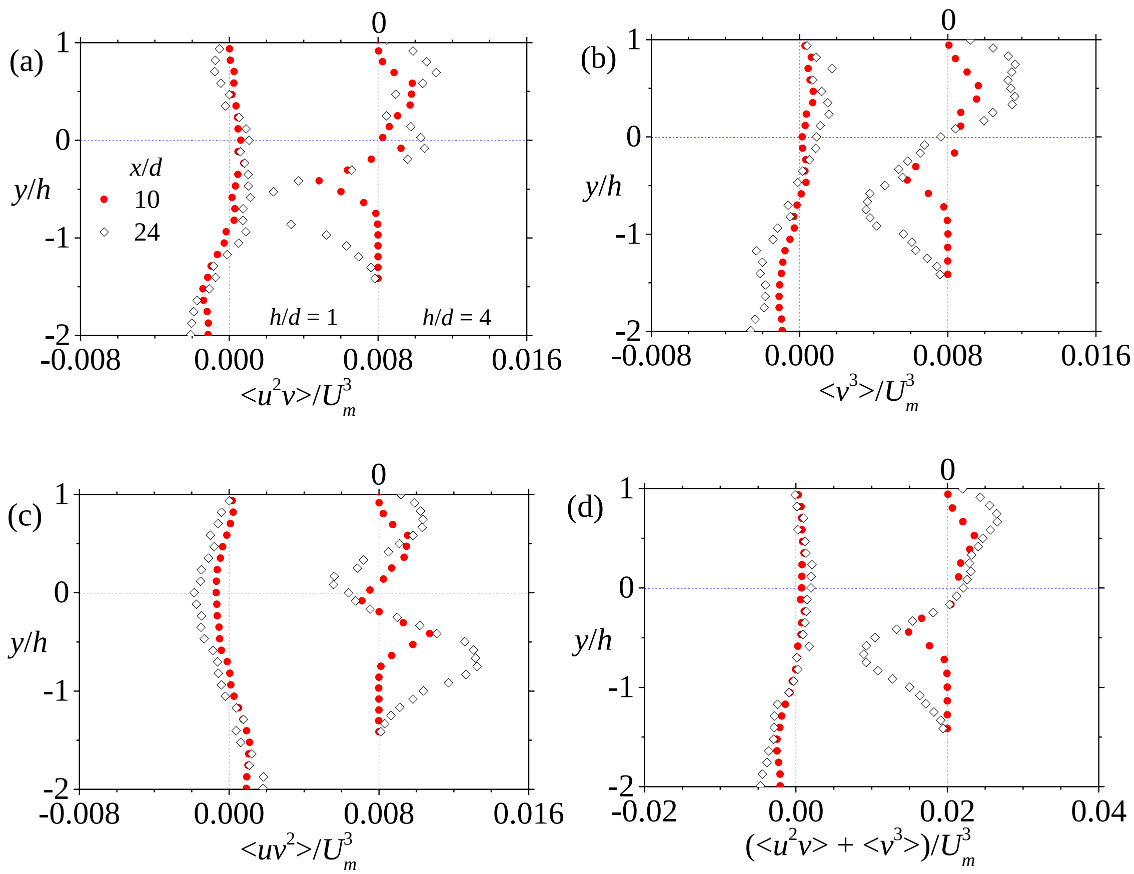

Figure 4.17. Surface-normal profiles of triple velocity products for h/d = 1 and 4 at selected x/d locations: (a) $\langle u^2v\rangle/U_m{}^3$, (b) $\langle v^3\rangle/U_m{}^3$, (c) $\langle uv^2\rangle/U_m{}^3$ and (d) $(\langle u^2v\rangle + \langle v^3\rangle)/U_m{}^3$.

develops a slight negative peak (at $y/h \approx 0.6$), indicating turbulent diffusion of streamwise Reynolds normal stress away from the free surface. The correlation turns to positive values in the core jet; the positive values persist over the inner half of the lower shear layer until at $y/h \approx -1.0$, where a sign change occurs from positive to negative values. The negative values in the lower shear layer would imply a downward turbulent diffusion (ejection of fluid from jet) into the ambient fluid. It should be noted that in the lower shear layer the profiles exhibit no dependency on streamwise distance in the interaction region.

At the larger offset height ratio, $h/d = 4$, positive excursions occur in the profiles of $\langle u^2v \rangle$ at the edge of the upper shear layer. This indicates turbulent diffusion of $\langle u^2 \rangle$ towards the free surface in these cases as opposed to the strongest confinement case ($h/d = 1$) in the upper shear layer. At a given streamwise location in the lower shear layer, the positive values of the correlation occur over a relatively smaller range of y/h. This is accompanied by larger negative excursions away from the jet centerline. The negative excursions are most dramatic for the furthest downstream location where streamwise momentum is expected to diffuse rapidly into the ambient fluid. Figure 4.17b shows profiles of the surface-normal transport of the surface-normal Reynolds normal stress ($\langle v^3 \rangle$). The profiles have positive peaks in the upper shear layer and negative peaks in the lower shear, whose magnitudes are enhanced with increasing h/d for a given streamwise location. A small saddle is observed at $x/d = 24$ for the offset height ratio, $h/d = 1$, which becomes more pronounced for the deeper jet. The saddles can be considered as the footprints of the surface-normal growth of the large-scale structures.

Figure 4.17c shows profiles of the surface-normal turbulent transport of the Reynolds shear stress ($\langle uv^2 \rangle$). For the shallowest jet, $\langle uv^2 \rangle$ is approximately zero near the free surface, negative over the rest of the upper shear layer and attains peak values at the jet centerline. Thus, $\partial \langle uv^2 \rangle / \partial y$ is positive in the upper shear layer and negative in the lower shear layer, indicating a gain in Reynolds shear stress transport by diffusion in the lower shear layer fed by Reynolds shear stress transport by diffusion in the upper shear layer. This downward diffusion of Reynolds shear stress across the jet coupled with the enhanced Reynolds shear stress production term P_{-uv} explains the larger Reynolds shear stress values observed in the lower shear layer compared to the upper shear layer. For the deeper jet, a shape change is observed in the upper shear layer, due to the positive peaks in this region. This would imply that there are structural differences in the turbulent transport of Reynolds shear stress in the upper shear for h/d = 4 compared to h/d = 1. In the core jet, nevertheless, the negative values still persist as has been observed in previous investigations of round free jets (Panchapakesan and Lumley, 1993; Hussein et al., 1994) and surface attaching jets (Sankar et al., 2008).

The profiles of the surface-normal transport of the turbulent kinetic energy, $<u^2v> + <v^3>$, are shown in Fig. 4.17d. For $h/d = 1$, $<u^2v> + <v^3>$ is negligibly small in the upper shear layer, so that the contribution to turbulent diffusion, $-\partial(<u^2v> + <v^3>)/\partial y \approx 0$. In the lower shear layer, $\partial(<u^2v> + <v^3>)/\partial y$ is positive, indicating an energy loss by diffusion at a rate that increases with streamwise distance. In the upper shear layer of the deeper jet, $\partial(<u^2v> + <v^3>)/\partial y$ is positive within $0 \leq y/h \leq 0.5$, indicating a loss by turbulent diffusion, feeding the gain by diffusion within $0.5 < y/h \leq 1$. This process is replicated in the lower shear layer, where a positive $\partial(<u^2v> + <v^3>)/\partial y$ within $-1 < y/h \leq 0$ indicates a loss in turbulent kinetic energy by diffusion, which supplies the gain in energy by diffusion for $y/h < -0.5$. The above results imply that the turbulent transport of the turbulent kinetic energy and Reynolds shear stress is strongly dependent on the presence of the free surface; thus, any turbulence model which does not explicitly account for offset height ratio effects will not be able to properly predict the transport characteristics of the jet.

4.4.1.7 Skewness and flatness factors

Figure 4.18 shows a comparison of the skewness and flatness factors of the velocity fluctuations, u and v for h/d = 1 and 4 in the interaction region. The skewness factor (S_α) estimated as

$$S_\alpha = \frac{\langle \alpha^3 \rangle}{\langle \alpha^2 \rangle^{3/2}} \tag{4.11}$$

where, α denotes u or v, is a measure of temporal asymmetry in the probability density function of the velocity fluctuations. Additionally, it provides qualitative information concerning the Reynolds shear stress producing events in the jet. The skewness factor S_u (Fig. 4.18a) is nearly Gaussian ($S_u \approx 0$) across most of the shallow jet (h/d = 1). In the outer parts of the lower shear layer, the skewness profiles indicate a modest deviation from the Gaussian value. The positive values of S_u would imply that the instantaneous streamwise velocity, U_i, is more frequently higher than its mean value in this region. At larger offset height ratios, the deviations become more substantial, both near the free surface and in the lower shear layer. Furthermore, there is a consistent decrease in skewness factor as the jet propagates downstream, which can be attributed to the tendency of the jet to decay to homogeneous shear conditions as it entrains and mixes with ambient fluid in the streamwise direction. The skewness profiles of the surface-normal velocity fluctuations (S_v) are shown in Fig. 4.18b. In all cases, S_v is positive near the free surface, Gaussian at the centerline and negative in the outer parts of the lower shear layer. Negative values of S_v in the lower shear layer would imply that the extreme negative v more frequently occurs than the positive, while the negative v corresponds downward expansion

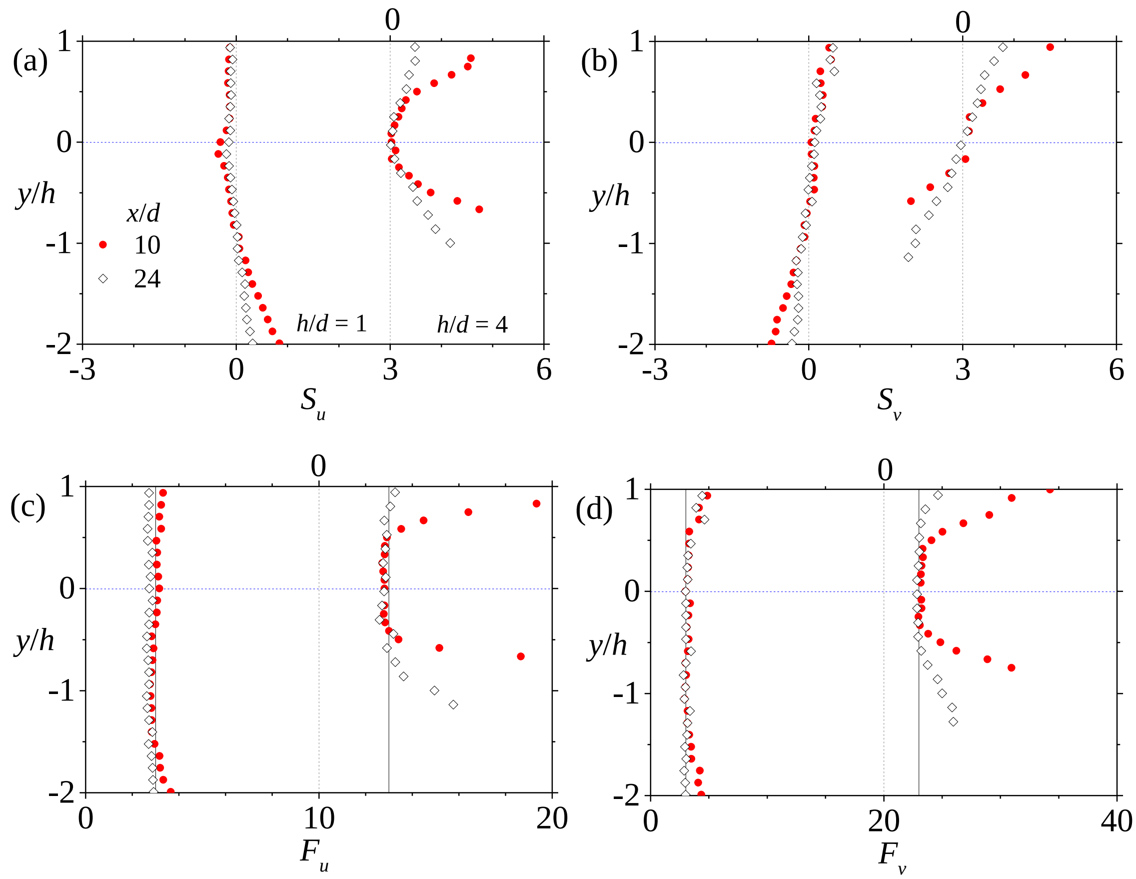

Figure 4.18. Surface-normal profiles of skewness and flatness of velocity fluctuations for h/d = 1 and 4 at selected x/d locations: (a) Skewness of streamwise velocity fluctuation, (b) skewness of surface-normal velocity fluctuation, (c) flatness of streamwise velocity fluctuation and (d) flatness of surface-normal velocity fluctuation. Solid lines in (c) and (d) indicate the Gaussian value of the flatness.

of the shear layer. Altogether, the data presented in Figs. 4.18a and 4.18b provide an indication that these frequent negative instantaneous v-fluctuations are closely associated with positive instantaneous u-fluctuations in the lower shear layer.

The flatness factor (F_α), which is often considered as a measurement of the degree of intermittence of the velocity fluctuations, is estimated as

$$F_\alpha = \frac{\langle \alpha^4 \rangle}{\langle \alpha^2 \rangle^2} \tag{4.12}$$

Figs. 4.18c and 4.18d show the flatness factors, F_u and F_v of the velocity fluctuations. The values of F_u and F_v are approximately equal to the Gaussian value of 3 for h/d = 1. At larger offset height ratios, the flatness factors assume increasingly large positive values near the free surface and in the outer parts of the lower shear layer. The larger positive values observed for h/d = 4 suggest that large velocity fluctuations are more intermittent in this jet compared to the shallow jet. For both jets, the values of F_v near the free surface and in the lower shear layer are about twice as large as those observed for F_u, an indication of greater intermittency in the surface-normal instantaneous velocity fluctuations compared to the streamwise instantaneous velocity fluctuations. The present skewness and flatness factor results for the deepest jet (h/d = 4) are in agreement with measurements reported by Wygnanski and Fiedler (1969).

4.4.2 Surface-normal profiles with similarity scaling

The distributions of the mean and turbulent quantity with the conventional similarity variables, $y_{0.5}$ and U_m are presented in this section. Streamwise mean velocity, Reynolds normal stresses and stress ratio, and Reynolds shear stress and related quantities are examined. Results from the two extreme conditions, h/d = 1 and 4 at the streamwise locations, x/d = 10, 15 and 20 in the interaction region are presented. Results from a self-similar free jet reported by Hussein et al. (1994) is used for comparison.

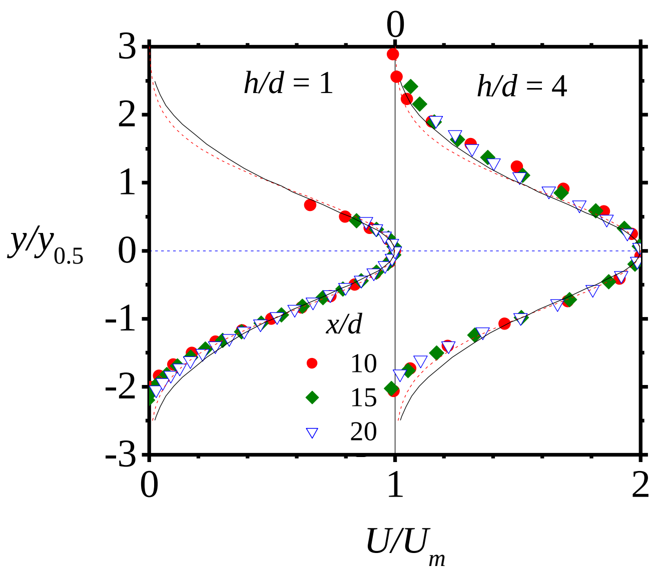

Figure 4.19. Similarity scaling of the profiles of streamwise mean velocity. Solid lines denote similarity profiles from the round jet data of Hussein et al. (1994); dashed lines denote the Gaussian streamwise mean velocity distribution.

4.4.2.1 Streamwise mean velocity

Figure 4.19 shows the profiles of the streamwise mean velocity at the selected streamwise locations for h/d = 1 and 4. In the figure, the dashed curves correspond to the following Gaussian distribution from the study by Rajaratnam and Humphries (1984):

$$U/U_m = \exp\left(-\ln 2\, (y/y_{0.5})^2\right) \tag{4.13}$$

and the solid curves correspond to the similarity profile from a round free jet reported by Hussein et al. (1994); the horizontal dashed line represents the jet centerline. The mean velocity profiles exhibit self-similarity in the interaction region. For both offset height ratios, the profiles compare well with the Gaussian distribution and the results from

Hussein et al. (1994), except near the edge of the lower shear layer where the present values are about 5% – 10% lower. These discrepancies could be attributed to the presence of recirculation near the lower wall of the test section.

4.4.2.2 Reynolds normal stresses and stress ratio

Profiles of streamwise and surface-normal Reynolds normal stresses are shown in Figs. 4.20a and 4.20b, respectively. The peak values of the normalized Reynolds normal stresses increase with streamwise distance in agreement with the literature on turbulent free jets (Wygnanski and Fiedler, 1969). The literature shows that the second order moments do not attain self-similarity until some 50 to 70 diameters downstream of the nozzle. For a given streamwise location, the effect of decreasing offset height ratio is to decrease the peak values of the Reynolds normal stresses. Figure 4.20c shows the similarity profiles of the stress ratio. As discussed in Fig. 4.15a, the present values of the stress ratio are approximately 2 over most of the flow region, except in the immediate vicinity of the free surface. Near the free surface, the stress ratio increases with streamwise distance, which is more intense for shorter offset height, due to the damping effect of the surface on the surface-normal component in the interaction region.

4.4.2.3 Reynolds shear stress and related quantities

Figure 4.21 shows the similarity profiles of the normalized Reynolds shear stress and related quantities in the interaction region. The Reynolds shear stress profiles at the selected streamwise locations are shown in Fig. 4.21a. For $h/d = 4$, the profiles exhibit the same anti-symmetric shape as the free jet distribution. Although the peak values are

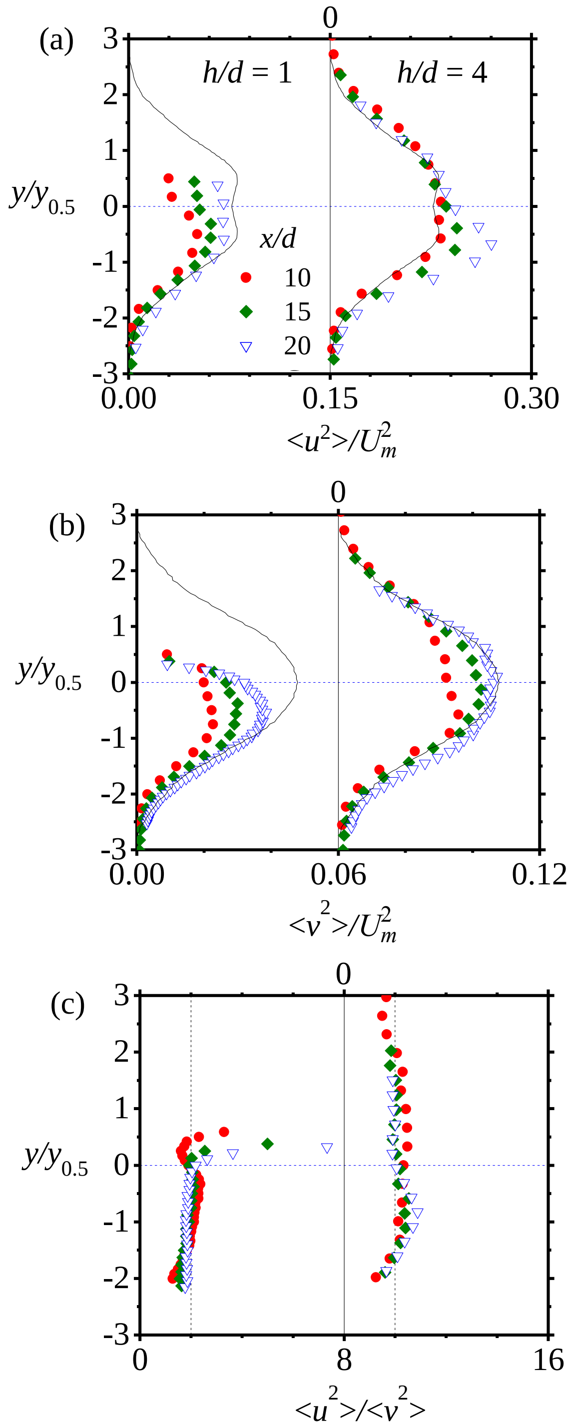

Figure 4.20. Similarity scaling of the profiles of Reynolds normal stresses and stress ratio: (a) streamwise Reynolds normal stress, (b) surface-normal Reynolds normal stress and (c) stress ratio. Solid lines denote similarity profiles from the round jet data of Hussein et al. (1994).

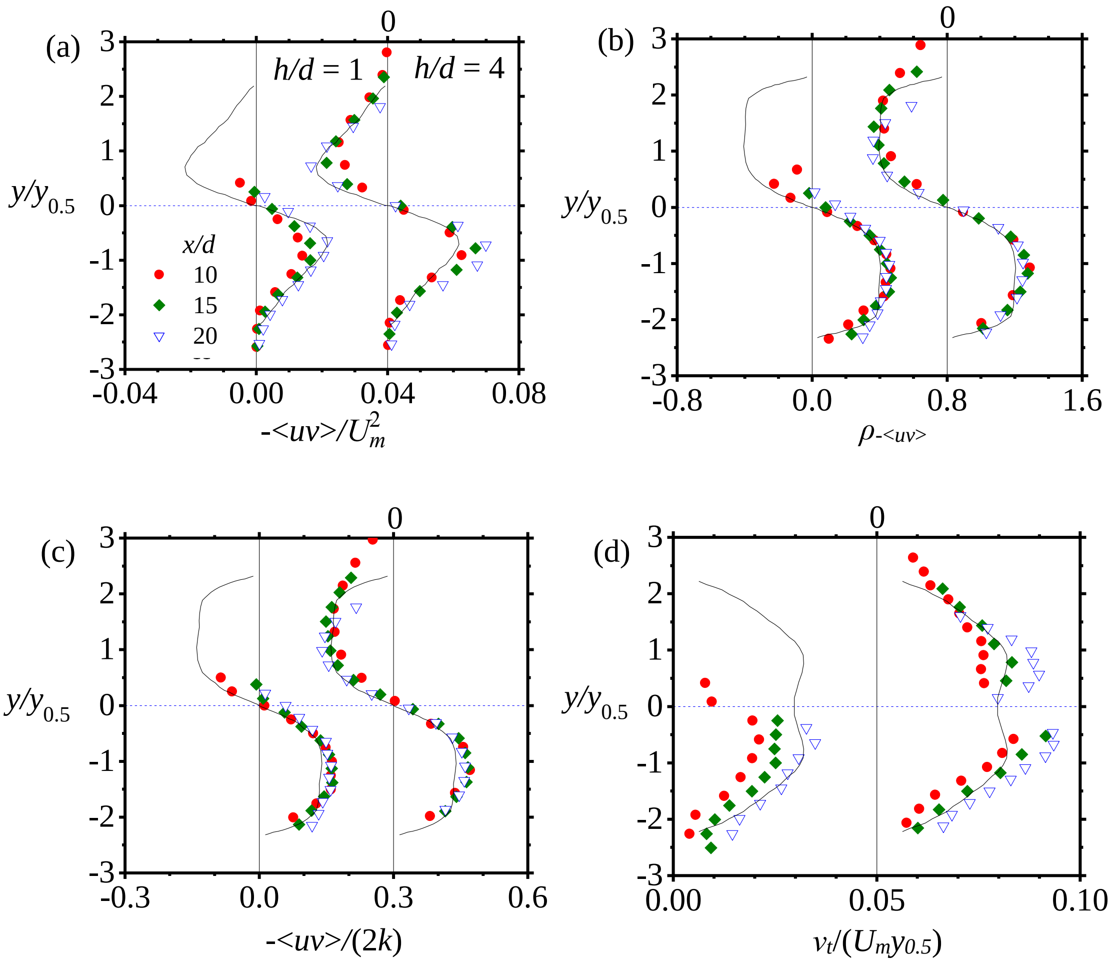

Figure 4.21. Similarity scaling of the profiles of Reynolds shear stress and related quantities: (a) Reynolds shear stress, (b) Reynolds shear stress correlation coefficient, (c) structure parameter and (d) eddy viscosity. Solid lines denote similarity profiles from the round jet data of Hussein et al. (1994).

increasing with streamwise distance, the effect is less dramatic than was observed for the normal stresses.

Profiles of the Reynolds shear stress correlation coefficient ($\rho_{-\langle uv \rangle}$) are shown in Fig. 4.21b. At both offset height ratios, the profiles show good agreement with the free jet values in the lower shear layer, with peak values of approximately 0.41 ± 0.05. In the upper shear layer, a similar peak value occurs for h/d = 4, but the profiles deviate significantly from that of the free jet near the free surface. At the lower offset height ratio, the damping effect on the Reynolds shear stress produces a commensurate diminishing effect on the correlation coefficient. Similar to $\rho_{-\langle uv \rangle}$, the profiles of the structure parameter as shown in Fig. 4.21c show good agreement with the self-similar profile of the free jet specially in the lower shear layer. Figure 4.21d shows profiles of the eddy viscosity, $\nu_t/(U_m y_{0.5})$. The plots indicate that the eddy viscosity is an increasing function of downstream distance in the interaction region and decreases with decreasing offset height ratio.

4.5 Two-Point Correlation

To provide a deeper insight into the effect of the free surface on the coherent structures, two-point correlations of the velocity fluctuations and the swirling strength are examined. Two-point correlations are performed at various streamwise and surface-normal locations within the flow field of the jets. In this section, the growth of the spatial scales along the jet centerline is reported. The effects of the free surface on the turbulent structures within the upper and lower shear layer are also discussed. In addition, two-point correlation functions at reference locations close to the free surface are examined. Results obtained from the two extreme conditions, h/d = 1 and 4 are presented herein.

4.5.1 Two-point correlation between the velocity fluctuations

As mentioned in Chapter 2, the two-point correlations between the velocity fluctuations are calculated using Equation 2.14 as

$$R_{AB}\left(x_{ref}+\Delta x,\, y_{ref}+\Delta y\right)=\frac{\langle A\left(x_{ref},\, y_{ref}\right)\, B\left(x_{ref}+\Delta x,\, y_{ref}+\Delta y\right)\rangle}{\sigma_A\left(x_{ref},\, y_{ref}\right)\, \sigma_B\left(x_{ref}+\Delta x,\, y_{ref}+\Delta y\right)}$$

where, $A(x, y)$ and $B(x, y)$ are the two variables whose two-point correlation is required; (x_{ref}, y_{ref}) is the reference location; Δx and Δy are the spatial separations between A and B in the streamwise and surface-normal directions, respectively; and σ_A and σ_B are the root-mean-square values of A and B at (x_{ref}, y_{ref}) and $(x_{ref} + \Delta x, y_{ref} + \Delta y)$, respectively.

Figure 4.22 shows the iso-contours of the two-point auto-correlation function of the streamwise velocity fluctuation, R_{uu}, centred at x/d = 3, 9 and 20 for h/d = 1 and 4. The surface-normal location where the correlations are calculated corresponds to the jet centerline (y'/d = 0, where y' denotes the surface-normal distance measured relative to the location of U_m). The plots indicate a monotonic increase in the spatial extents of R_{uu} which is consistent with the growth of the jet in the streamwise direction. For h/d = 4, the correlation contours are almost parallel to the free surface. For h/d = 1, the correlations, which are smaller for the most part, are parallel to the free surface, except at x/d = 20. At the location x/d = 20, the R_{uu} correlation in this case is attached to the free surface and is inclined at angle of approximately 11.4^{o}. This streamwise inclination is similar to the value of approximately 11^{o} observed in wall jets (Agelin-Chaab and Tachie, 2011b) and zero pressure gradient turbulent boundary layers (Volino et al, 2009).

Figure 4.23 shows the iso-contours of R_{uu} for h/d = 4 at various surface-normal locations (y'/d = ±1, ±2 and ±3; where the plus sign denotes distance measured towards the free surface, while the minus sign denotes distance measured away from the free

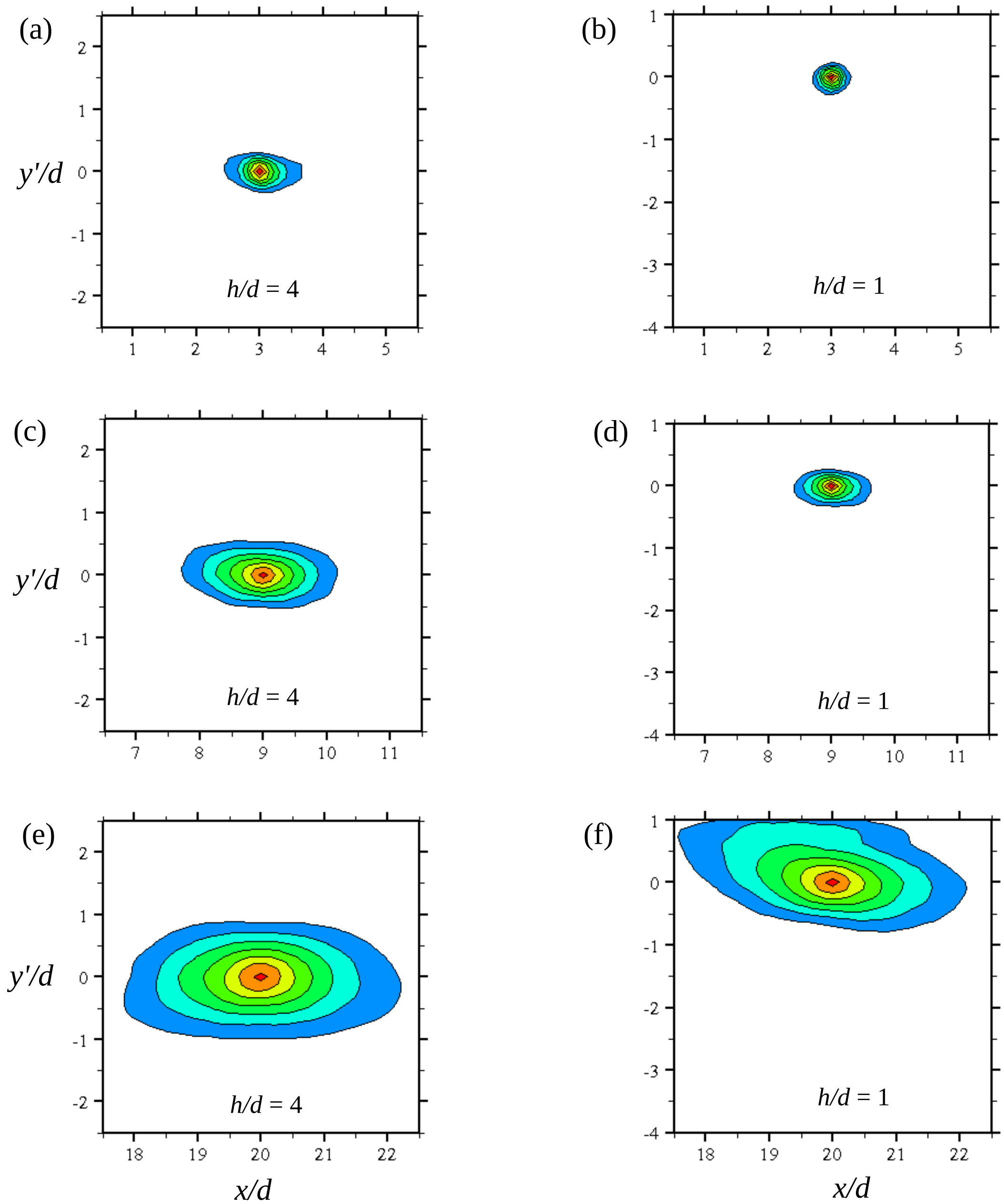

Figure 4.22. Contours of auto-correlation of streamwise velocity fluctuation, R_{uu} along the jet centerline: (a) for $h/d = 4$ at $x/d = 3$, (b) for $h/d = 1$ at $x/d = 3$, (c) for $h/d = 4$ at $x/d = 9$, (d) for $h/d = 1$ at $x/d = 9$, (e) for $h/d = 4$ at $x/d = 20$ and (f) for $h/d = 1$ at $x/d = 20$. Contour levels vary from 0.3 to 0.9 at intervals of 0.1.

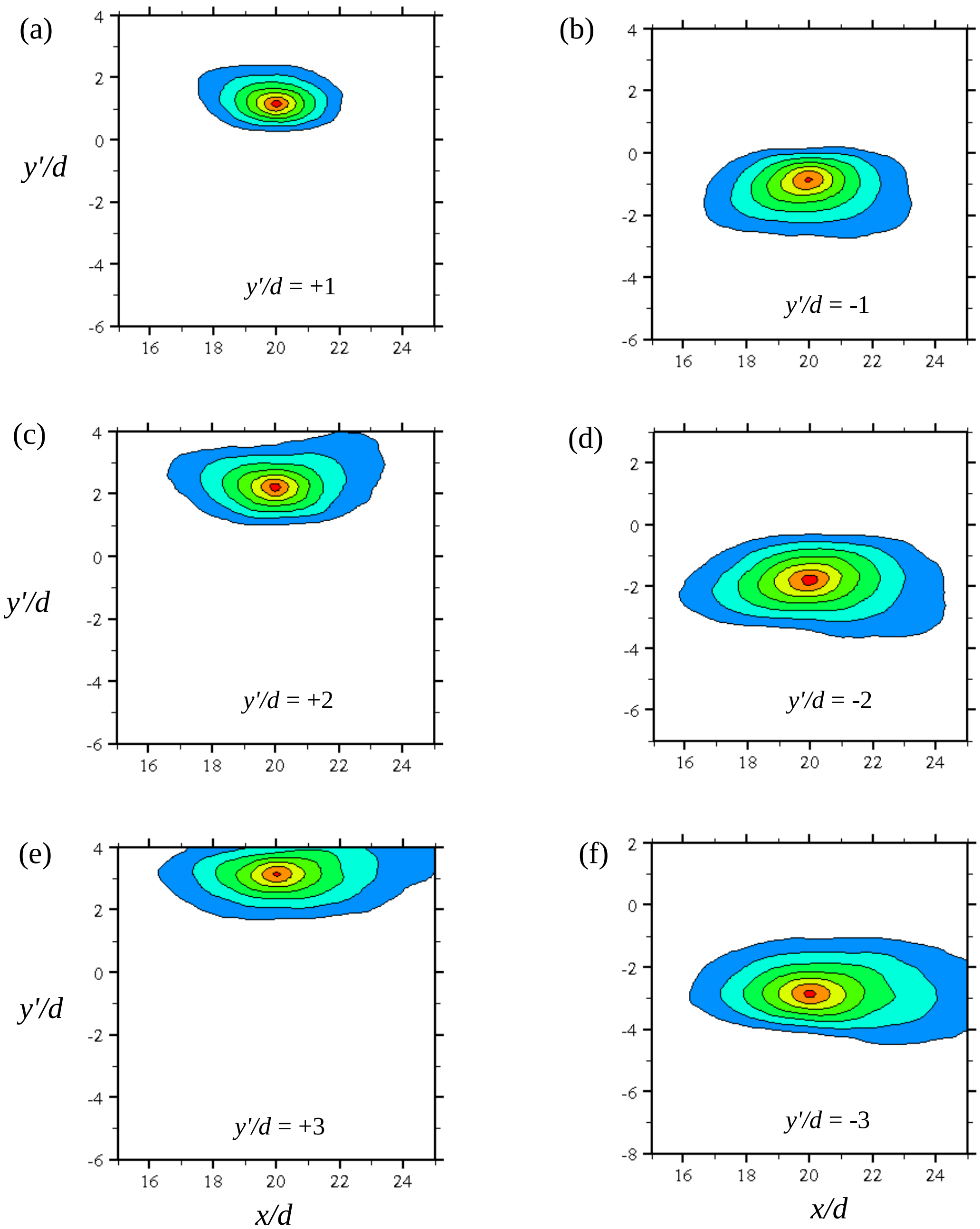

Figure 4.23. Contours of auto-correlation of streamwise velocity fluctuation, R_{uu} within upper and lower shear layers for the h/d = 4 jet at x/d = 20: (a) at y'/d = +1, (b) at y'/d = –1, (c) at y'/d = +2, (d) at y'/d = –2, (e) at y'/d = +3 and (f) at y'/d = –3. Contour levels vary from 0.3 to 0.9 at intervals of 0.1.

surface) within the upper and lower shear layer at a streamwise location, at x/d = 20 in the interaction region. In both halves of the shear layer the correlations are enhanced in the direction away from maximum velocity line. Nevertheless, in the upper shear layer, the surface confinement suppresses the correlation levels in comparison to those in the lower shear layer.

Figure 4.24 shows a comparison of the iso-contours of R_{uu} close to the free surface (y^s/d = 0.5 and 1; where y^s denotes the surface-normal distance measured from the free surface) in the interaction regions of the shallowest and deepest jets. Figs. 4.24a and 4.24c show the iso-contours of R_{uu} centered at (x/d = 10, y^s/d = 0.5) and (x/d = 20, y^s/d = 0.5), respectively, for h/d = 1. The contours are consistent with the idea that the velocity fluctuations are more strongly correlated for reference locations farther from the exit plane. Figure 4.24e shows the iso-contours of R_{uu} at x/d = 20 and y^s/d = 0.5 for h/d = 4. For h/d = 4, comparison is made only at the far downstream location because the location x/d = 10 is outside the interaction region. Compared to the corresponding distribution for h/d = 1 at x/d = 20, the contours are more elongated for h/d = 4, suggesting a considerable enhancement of the two-point correlations with increasing offset height ratio. At x/d = 20, the R_{uu} correlations are attached to the free surface and exhibit a shallow streamwise inclination of approximately 12º ± 1.5º. Figs. 4.24b, 4.24d and 4.24f show the iso-contours of R_{uu} at y^s/d = 1. At this surface-normal location, a similar growth with streamwise distance and more dramatic enhancement at the largest offset height ratio can be observed. Also, the correlations at x/d = 20 are still attached to the free surface and have the same

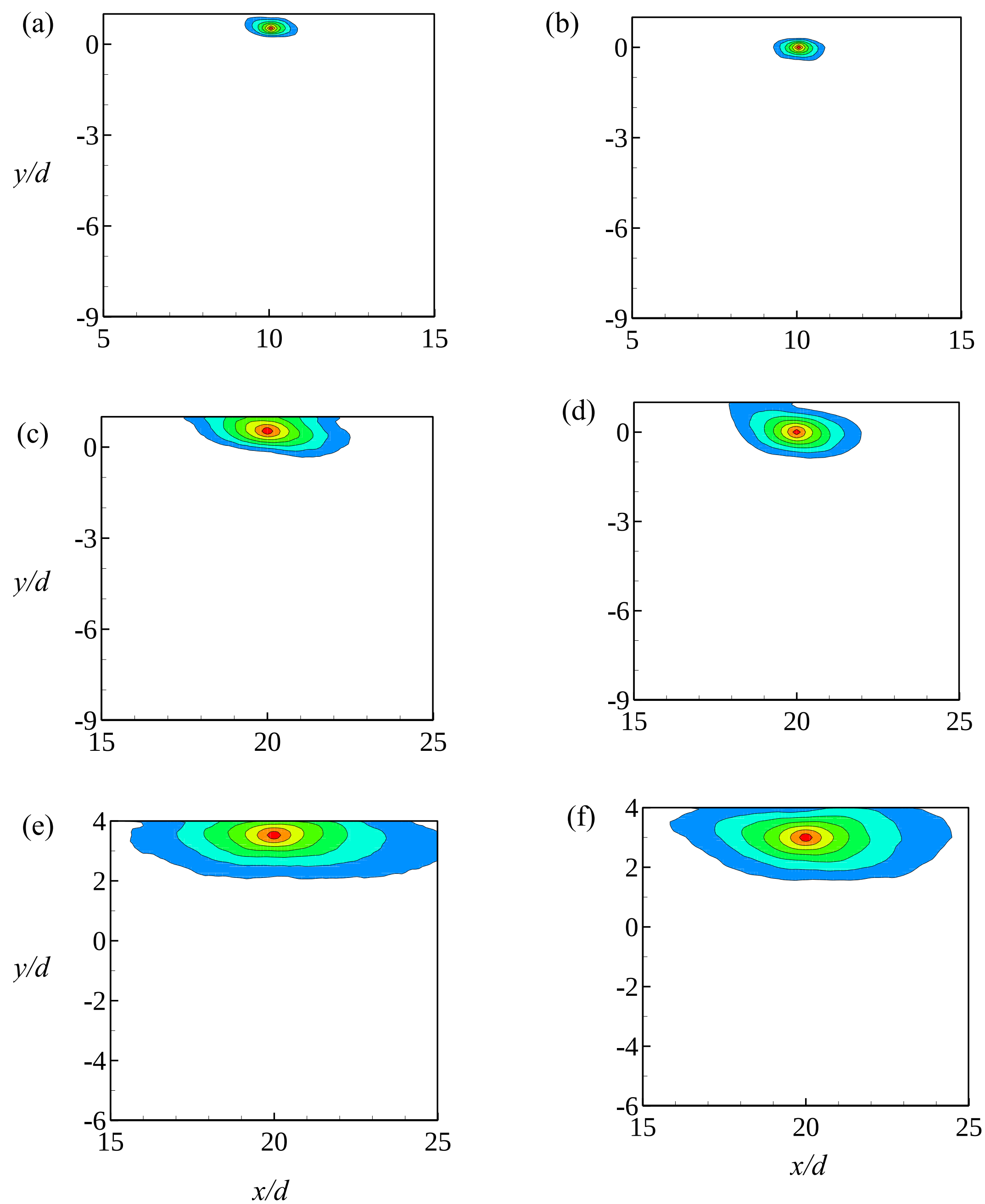

Figure 4.24. Contours of auto-correlation of streamwise velocity fluctuation, R_{uu} close to the free surface in the interaction region: (a) for h/d = 1 at x/d = 10, y^s/d = 0.5; (b) for h/d = 1 at x/d = 10, y^s/d = 1; (c) for h/d = 1 at x/d = 20, y^s/d = 0.5; (d) for h/d = 1 at x/d = 20, y^s/d = 1; (e) for h/d = 4 at x/d = 20, y^s/d = 0.5; and (f) for h/d = 4 at x/d = 20, y^s/d = 1. Contour levels vary from 0.3 to 0.9 at intervals of 0.1.

angle of inclination to the streamwise direction. The difference, however, is that the longitudinal extents of correlations are reduced in comparison to those at $y^s/d = 0.5$.

The iso-contours of the two-point auto-correlation function of the surface-normal velocity fluctuation, R_{vv}, at $y'/d = 0$ for $h/d = 1$ and 4 are shown in Fig. 4.25. These plots indicate a similar growth in the streamwise direction. However, there is a consistent reduction in the levels of R_{vv} for $h/d = 1$ compared to $h/d = 4$ irrespective of the downstream location, suggesting a stronger impact of the free surface for $h/d = 1$.

Figure 4.26 shows the iso-contours of the R_{vv} correlation at $x/d = 20$ above and below the jet center line for $h/d = 4$. In the upper shear layer (Figs. 4.26a, 4.26c and 4.26e), the free surface suppresses the surface-normal two-point correlation function, as opposed to the enhancement observed in the streamwise counterpart in this region. This is consistent with the damping effect of the free surface on the surface-normal velocity fluctuations. In the lower shear layer (Figs. 4.26b, 4.26d and 4.26f), the R_{vv} correlation is enhanced with distance away from the jet centerline as was observed for R_{uu} in this region.

The iso-contours of R_{vv} close to the free surface for $h/d = 1$ and 4 are shown in Fig. 4.27. For each row of plots, the trend is similar to those observed for R_{uu} in Fig. 4.24. The substantially smaller spatial extents of the R_{vv} contours close to the free surface is consistence with the damping effect of the free surface on the surface-normal fluctuations as mentioned earlier.

The two-point cross-correlations between the streamwise and surface-normal velocity fluctuations (R_{uv}) for $h/d = 1$ and 4 close to the free surface in the interaction

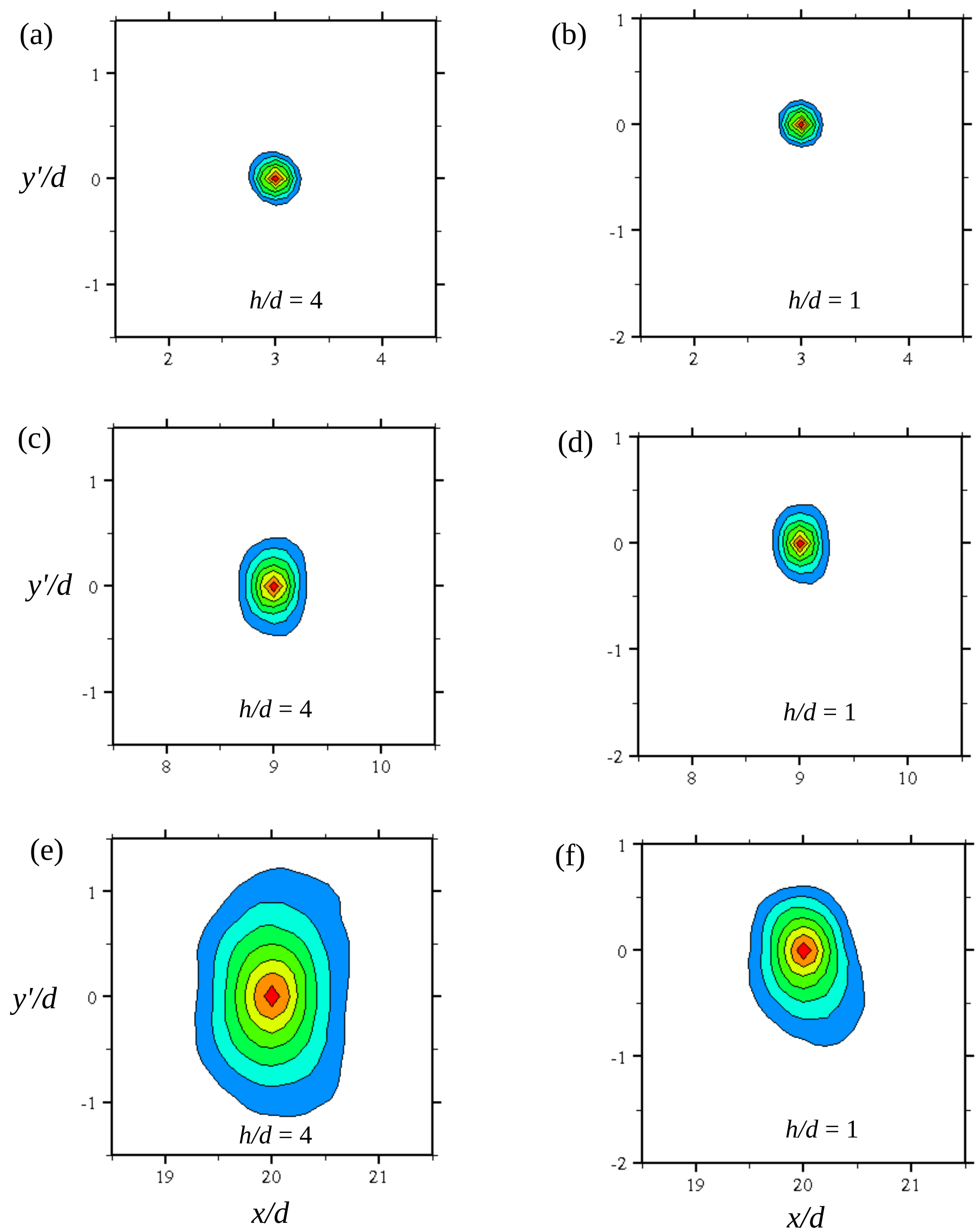

Figure 4.25. Contours of auto-correlation of surface-normal velocity fluctuation, R_{vv} along the jet centerline: (a) for h/d = 4 at x/d = 3, (b) for h/d = 1 at x/d = 3, (c) for h/d = 4 at x/d = 9, (d) for h/d = 1 at x/d = 9, (e) for h/d = 4 at x/d = 20 and (f) for h/d = 1 at x/d = 20. Contour levels vary from 0.3 to 0.9 at intervals of 0.1.

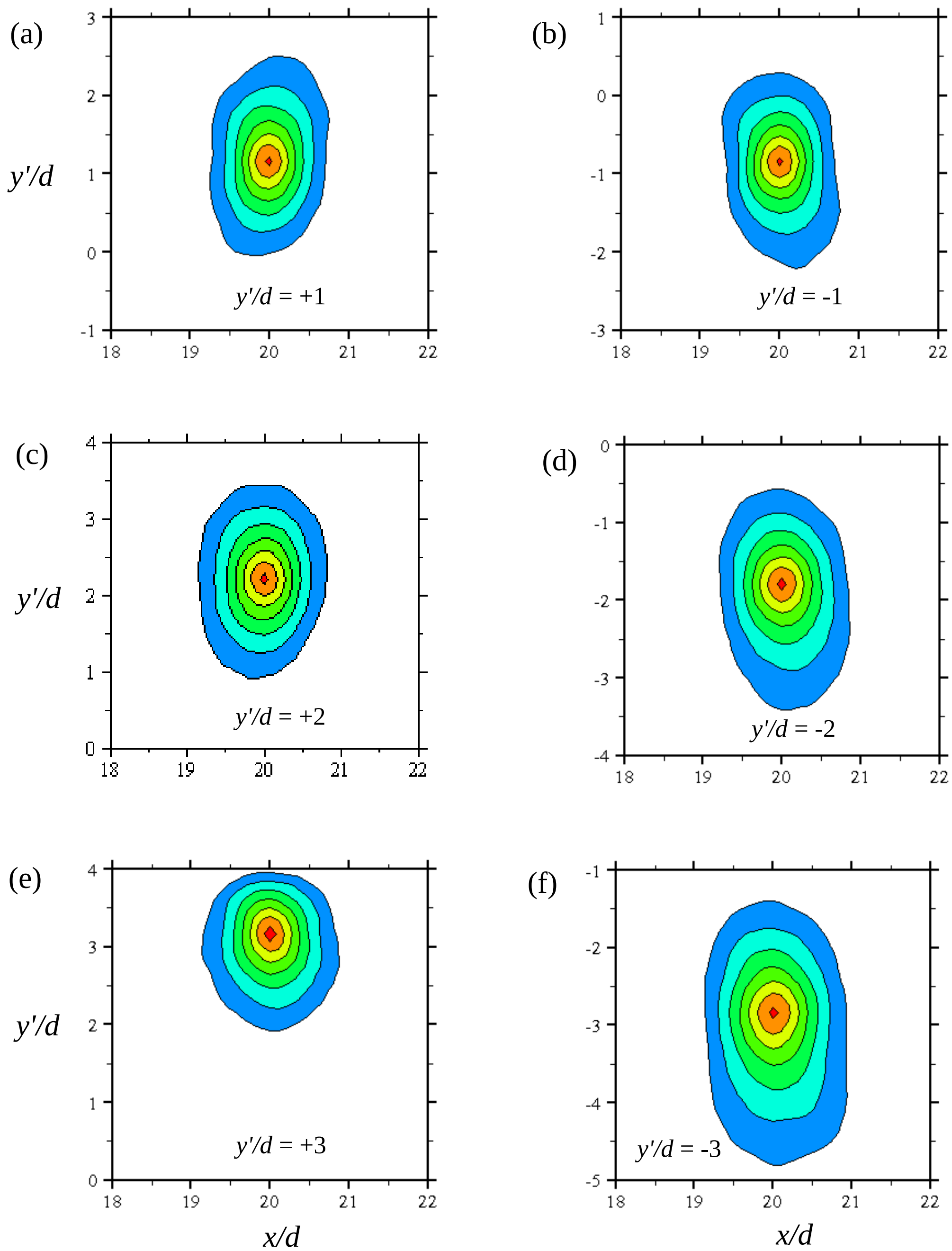

Figure 4.26. Contours of auto-correlation of surface-normal velocity fluctuation, R_{vv} within upper and lower shear layers for the h/d = 4 jet at x/d = 20: (a) at y'/d = +1, (b) at y'/d = –1, (c) at y'/d = +2, (d) at y'/d = –2, (e) at y'/d = +3 and (f) at y'/d = –3. Contour levels vary from 0.3 to 0.9 at intervals of 0.1.

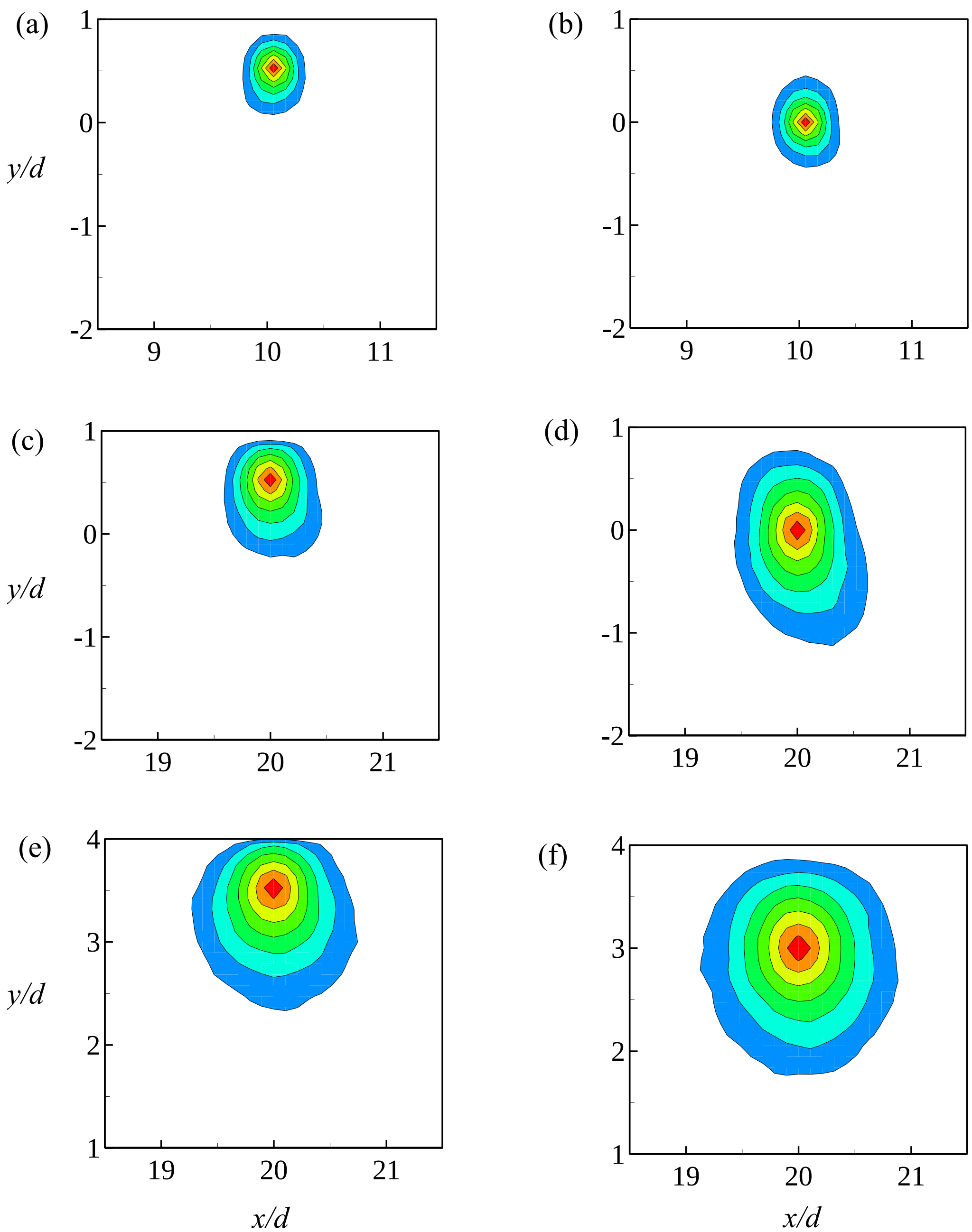

Figure 4.27. Contours of auto-correlation of surface-normal velocity fluctuation, R_{vv} close to the free surface in the interaction region: (a) for h/d = 1 at x/d = 10, y^s/d = 0.5; (b) for h/d = 1 at x/d = 10, y^s/d = 1; (c) for h/d = 1 at x/d = 20, y^s/d = 0.5; (d) for h/d = 1 at x/d = 20, y^s/d = 1; (e) for h/d = 4 at x/d = 20, y^s/d = 0.5; and (f) for h/d = 4 at x/d = 20, y^s/d = 1. Contour levels vary from 0.3 to 0.9 at intervals of 0.1.

region are examined in Fig. 4.28. For a free jet, R_{uv} calculated at a reference location on the centerline has positive and negative contours on either side of the jet centerline, specifically a negative-positive pair above the jet axis and a positive-negative pair below the jet axis due to the anti-symmetry of the Reynolds shear stress about the jet axis. For the shallow jet at reference locations close to the free surface (Figs. 4.28a and 4.28c), the negative-positive pair is non-existent because of the proximity to the free surface. The positive-negative pair captured by the correlation corresponds to the turbulent mixing zone in the lower shear layer. This supports the idea that the effect of the free surface is to limit the turbulent mixing in the upper shear layer compared to the lower shear layer. This result is also consistent with the reduction in the surface-normal extent of the auto-correlation of the surface-normal velocity fluctuation (R_{vv}) in the upper shear layer compared to the lower shear layer as mentioned earlier. As the jet develops downstream (Fig. 4.28c), the distribution of R_{uv} spreads over the flow region due to the increasing spatial size of the coherent structures with streamwise distance as observed in R_{uu} and R_{vv} contours. However, at the larger offset height ratio, h/d = 4 (Fig. 4.28e), the correlation is predominantly positive indicating a preponderance of like-signed u and v fluctuations contributing to the correlation. A typical distribution of the two-point cross-correlation at a reference location on the jet centerline (x/d = 10, y^s/d = 1) is shown in Fig. 4.28b for h/d = 1. The like-signed contours are inclined to the streamwise direction like the helical modes of the circumferential structures. The positive contours are inclined at an angle of approximately 2.3º to the downstream direction, while the negative contours are inclined at an angle of approximately 3.0º to the upstream direction. Further downstream (Fig. 4.28d) the correlations increase in scale, although the upstream inclination angle of the

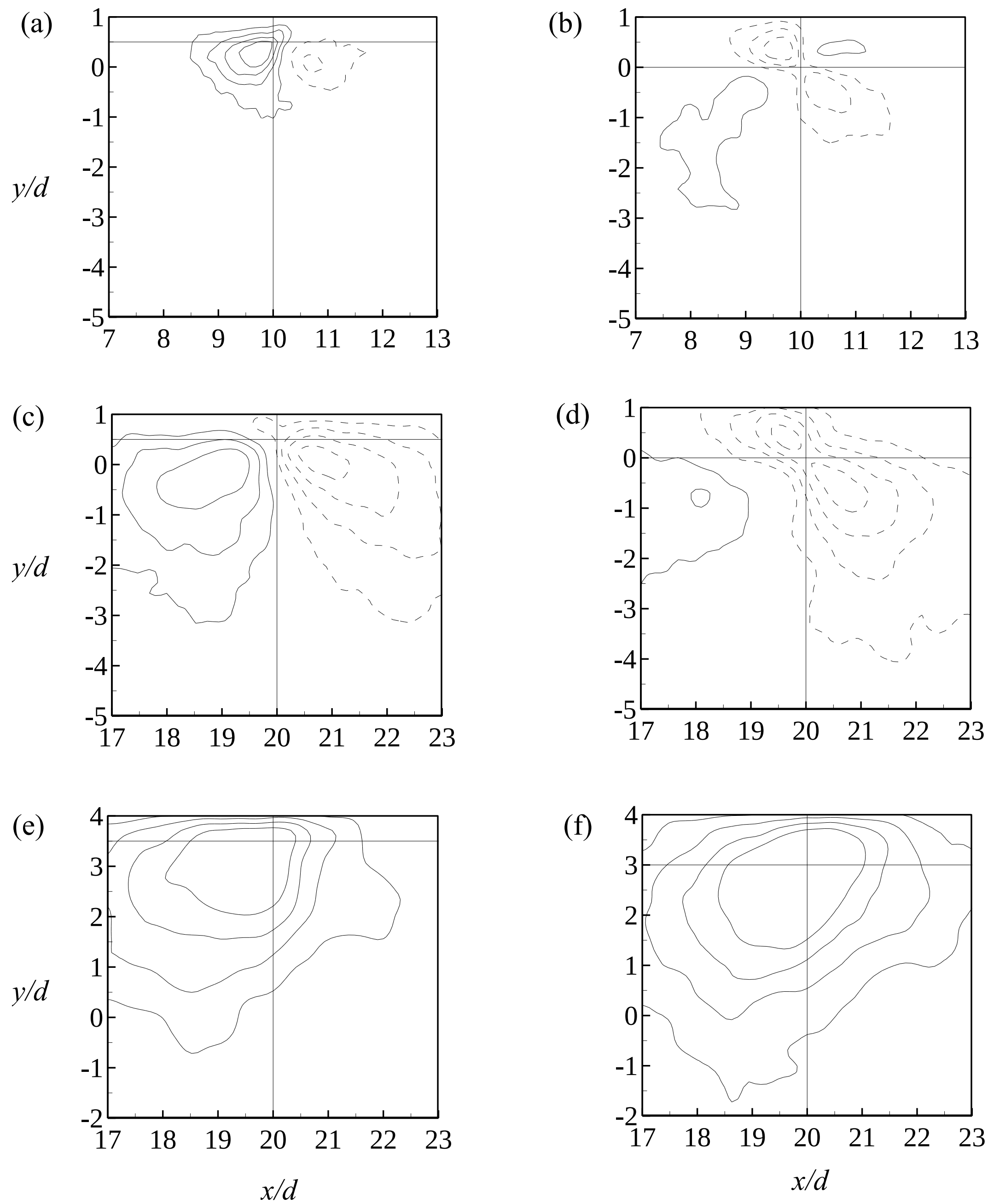

Figure 4.28. Contours of cross-correlation of velocity fluctuations, R_{uv} close to the free surface in the interaction region: (a) for h/d = 1 at x/d = 10, y^s/d = 0.5; (b) for h/d = 1 at x/d = 10, y^s/d = 1; (c) for h/d = 1 at x/d = 20, y^s/d = 0.5; (d) for h/d = 1 at x/d = 20, y^s/d = 1; (e) for h/d = 4 at x/d = 20, y^s/d = 0.5; and (f) for h/d = 4 at x/d = 20, y^s/d = 1. Contour levels vary from -0.2 to -0.05 and 0.05 to 0.2 at intervals of 0.05. Dashed contours indicate the negative correlation.

negative contours remains relatively unchanged. However, compared to the result in Fig. 4.28c, the negative R_{uv} contours are more elongated in both the upper and lower shear layers, while the positive correlations are reduced. This suggests the increasing importance of oppositely-signed u and v fluctuations in the determination of the R_{uv} correlation. For h/d = 4, a similar large-scale positive R_{uv} correlation is observed as in Fig. 4.28f but is of considerably larger size than that closer to the free surface.

The influence of the jet confinement on the average size of the turbulent scales is examined in Fig. 4.29. The average size of the turbulent scales is quantified in terms of the streamwise and surface-normal extents of the two-point correlation contours. Figure 4.29a shows functional dependence of the streamwise extent, Lx_{uu} of R_{uu} on x/d. The streamwise extent of R_{uu} is defined herein as the distance between the self-correlation peak and the most downstream location on the R_{uu} = 0.3 contour level. The variation of Lx_{uu}/d with x/d is almost linear mimicking the streamwise growth of the jet. The profiles somewhat segregate into two distinct groups of slopes, 0.057 (h/d = 1 and 2) and 0.080 (h/d = 3 and 4). Figure 4.29b shows the streamwise evolution of the streamwise extent Lx_{vv} of R_{vv}. For R_{vv} the streamwise extent is defined as the streamwise distance between the self-correlation peak and downstream locations on the R_{vv} = 0.3 contour level. These also show an approximately linear growth with x/d but the slopes are reduced to about 0.016 and 0.023 for the two groups. The surface-normal extent of R_{uu} measured from the self-correlation peak to the farthest location on R_{uu} = 0.3 contour level in the upper shear layer are plotted in Fig. 4.29c. The profiles indicate an initial decline in the Ly_{uu}/d after which it increases monotonically. For $x/d \geq 5$, the profiles approximately follow straight

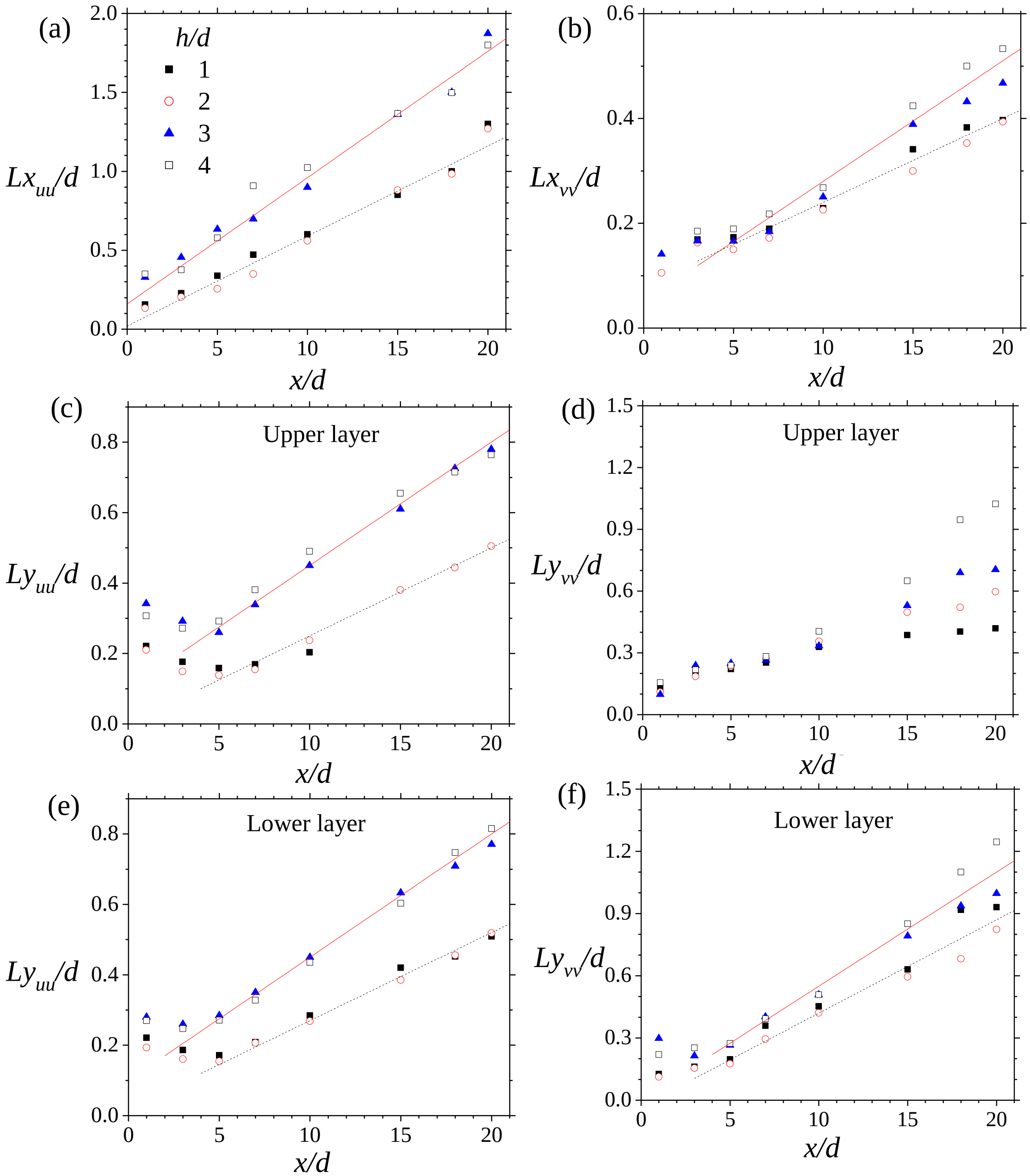

Figure 4.29. Variation of the integral scales of the auto-correlation functions with streamwise distance for various offset heights along the jet centerline: (a) Streamwise integral scale of R_{uu}, (b) streamwise integral scale of R_{vv}, (c) surface-normal integral scale of R_{uu} in the upper shear layer, (d) surface-normal integral scale of R_{vv} in the upper shear layer, (e) surface-normal integral scale of R_{uu} in the lower shear layer and (f) surface-normal integral scale of R_{vv} in the lower shear layer. Solid lines are least squares linear fit.

lines of slope 0.025 and 0.035. The corresponding profiles for R_{vv} (Ly_{vv}/d) are shown in Fig. 4.29d. Here, the correlations grow almost linearly and at the same rate for $x/d < 10$. In the interaction region, the damping influence of the free surface leads to reductions in slope by amounts that increase with decreasing offset height ratio. The surface-normal extent of R_{uu} measured from the self-correlation peak to the farthest location on $R_{uu} = 0.3$ contour level in the lower shear layer are depicted in Fig. 4.29e. These are similar to those measured in the upper shear layer, indicating a nearly uniform outward growth of streamwise correlations. The variation of the surface-normal extent of R_{vv} in the lower shear layer is shown in Fig. 4.29f. The values of Ly_{vv}/d follow an approximately linear profile of slope 0.055 for $h/d = 3$ and 4, which decreases to approximately 0.045 for $h/d = 1$ and 2 for $x/d \leq 15$. Beyond $x/d \approx 15$, the profiles exhibit a significant departure from a straight line, which is in agreement with the strong impact of the jet confinement on the surface-normal velocity fluctuations.

4.5.2 Two-point correlation between the swirling strength and velocity fluctuations

It is evident that the free surface has significant effect on the spanwise vortices (e.g., suppression of the vortices due to the confinement as discussed in Section 4.1.1) especially in the upper shear layer in the interaction region. In order to investigate the average spatial extent and strength of the vorticity fields close to the free surface, two-point auto-correlations of the swirling strength, $R_{\lambda\lambda}$ are estimated. The values of the swirling strength, $\lambda_{ci,z}$ are calculated using the two-dimensional approximation (Hutchins et al., 2005). Figure 4.30 shows the iso-contours of the two-point auto-correlations of the swirling strength, $R_{\lambda\lambda}$ at the various reference locations close to the free surface for $h/d =$

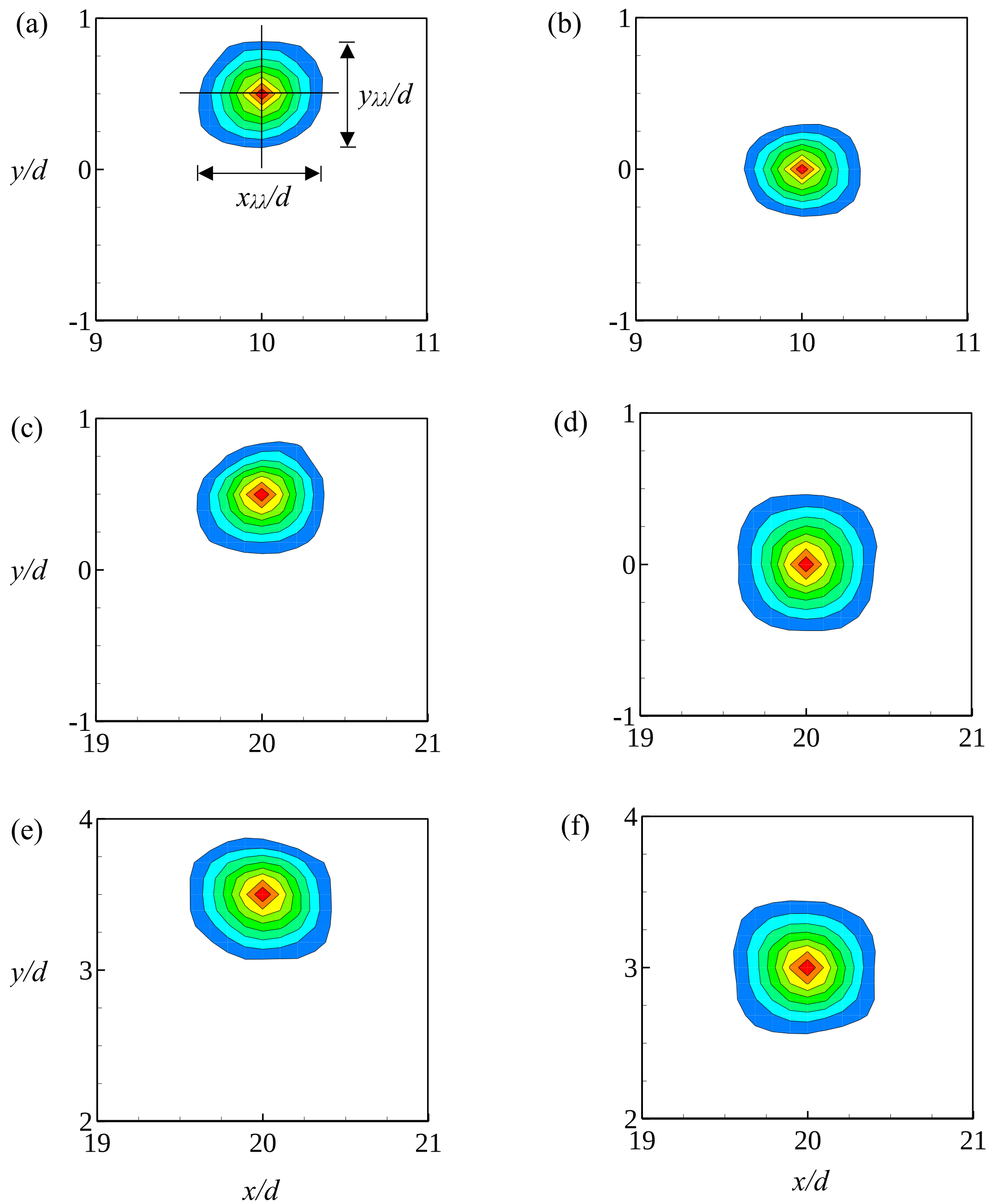

Figure 4.30. Contours of auto-correlation of swirling strength, $R_{\lambda\lambda}$ close to the free surface in the interaction region: (a) for h/d = 1 at x/d = 10, y^s/d = 0.5; (b) for h/d = 1 at x/d = 10, y^s/d = 1; (c) for h/d = 1 at x/d = 20, y^s/d = 0.5; (d) for h/d = 1 at x/d = 20, y^s/d = 1; (e) for h/d = 4 at x/d = 20, y^s/d = 0.5; and (f) for h/d = 4 at x/d = 20, y^s/d = 1. Contour levels vary from 0.2 to 0.9 at intervals of 0.1.

1 and 4. The total streamwise and surface-normal extents of $R_{\lambda\lambda}$ ($x_{\lambda\lambda}$ and $y_{\lambda\lambda}$, respectively) are estimated as the distance between the intersection points of the contour of minimum correlation level shown herein ($R_{\lambda\lambda}$ = 0.2) and the horizontal and vertical straight lines passing through the reference location, respectively as shown in Fig. 4.30a. The results show that there is an increase of approximately 3% in $x_{\lambda\lambda}$ and $y_{\lambda\lambda}$ with increasing x/d close to the free surface (y^s/d = 0.5). This limited contour growth could be attributed to the damping action of the free surface on the turbulent structures in the upper shear layer. At y^s/d = 1, the values of $x_{\lambda\lambda}$ and $y_{\lambda\lambda}$ in the far field of h/d = 1 (Fig. 4.30d) are approximately 17% and 49% higher than values at x/d = 10, respectively. At the larger offset height ratio (Fig. 4.30f), no further enhancements in $x_{\lambda\lambda}$ and $y_{\lambda\lambda}$ are observed. The streamwise growth of $R_{\lambda\lambda}$ is consistent with the growth of the two-point velocity-fluctuation auto-correlation results discussed earlier.

To investigate the relationship between the spanwise vortices identified in the instantaneous visualizations and the velocity fluctuations, the two-point cross-correlation between the swirling strength and velocity fluctuations can be used. These correlations are dynamically significant in the sense that they provide an indication of the average spatial extent and strength of the velocity fields associated with the vortices in the jet, where these vortices are identified to be pre-dominantly retrograde vortex cores in the upper shear layer and prograde vortex cores in the lower shear layer. Figure 4.31 shows the iso-contours of the two-point cross-correlation between the swirling strength and streamwise velocity fluctuation, $R_{\lambda u}$ at the various surface-normal locations within the upper and lower shear layer for the h/d = 1 and 4 jets in the interaction region at x/d = 20.

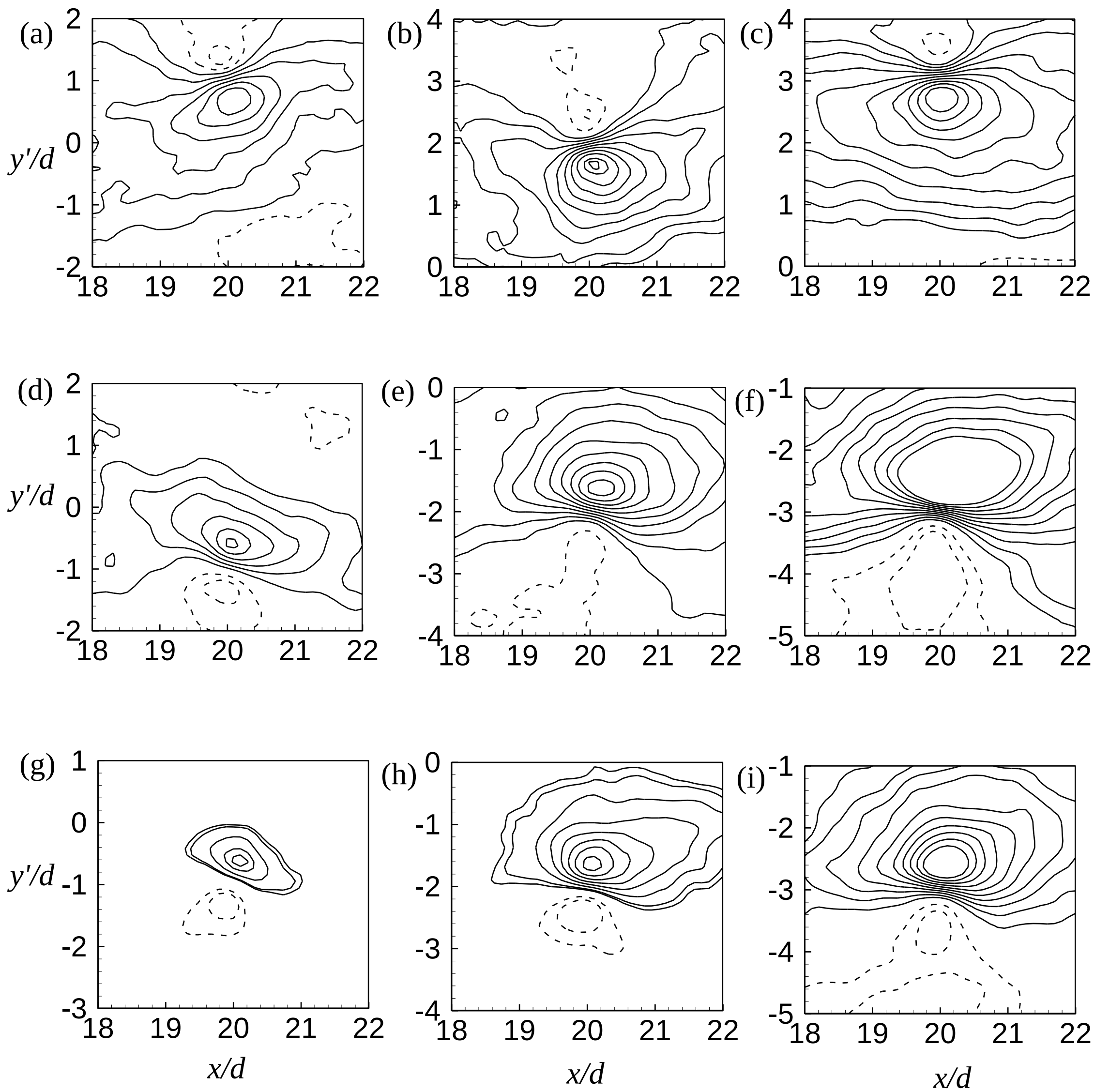

Figure 4.31. Contours of cross-correlation of swirling strength and streamwise velocity fluctuation, $R_{\lambda u}$ within upper and lower shear layers for the *h/d* = 4 and 1 jet at *x/d* = 20: (a) for *h/d* = 4 at *y′/d* = +1, (b) for *h/d* = 4 at *y′/d* = +2, (c) for *h/d* = 4 at *y′/d* = +3, (d) for *h/d* = 4 at *y′/d* = –1, (e) for *h/d* = 4 at *y′/d* = –2, (f) for *h/d* = 4 at *y′/d* = –3, (g) for *h/d* = 1 at *y′/d* = -1, (h) for *h/d* = 1 at *y′/d* = -2 and (i) for *h/d* = 1 at *y′/d* = -3. Contour levels vary from -0.04 to -0.02 and 0.02 to 0.2 at intervals of 0.02. Dashed contours indicate the negative correlation.

The iso-contours of $R_{\lambda u}$ for the reference locations in the upper shear layer for h/d = 4 are presented in Figs. 4.31a – 4.31c. For each of these cases, a retrograde vortex core is detected at the reference location, as identified by negative $R_{\lambda u}$ above the reference location and positive $R_{\lambda u}$ beneath it. At y'/d = 1, a secondary negative $R_{\lambda u}$ appears in the lower shear layer, which implies that the correlation at this reference location captures the spanwise vortex cores in both halves of the shear layer. At this location, the contours show an inclination angle of approximately 75º with respect to the upstream direction. As the reference location approaches to the free surface, the positive correlations are intensified, while the negative correlations are suppressed, with the inclination angle increasing from 75º to approximately 86º at y'/d = 3. The contours of $R_{\lambda u}$ for reference locations in the lower shear layer for h/d = 4 are presented in Figs. 4.31d – 4.31f. In the lower shear layer, $R_{\lambda u}$ is positive above the reference location and negative below the reference location, indicating the presence of a prograde vortex core at the reference location. The correlations are enhanced with increasing distance from y'/d = 0, but the streamwise inclination angle remains relatively constant at approximately 78º. Figures 4.31g – 4.13i show the iso-contours of $R_{\lambda u}$ for h/d = 1 in the lower shear layer. Due to the increased confinement, the correlation levels are smaller when compared to those of h/d = 4. Nevertheless, the streamwise inclination angle for $R_{\lambda u}$ is approximately 77º which is in good agreement with that observed for the h/d = 4 jet.

Figure 4.32 shows the iso-contours of $R_{\lambda u}$ at the various reference locations close to the free surface for h/d = 1 and 4. The iso-contours of $R_{\lambda u}$ at y^s/d = 0.5 are presented in Figs 4.32a, 4.32c and 4.32e. In each of these plots, $R_{\lambda u}$ is negative above the reference

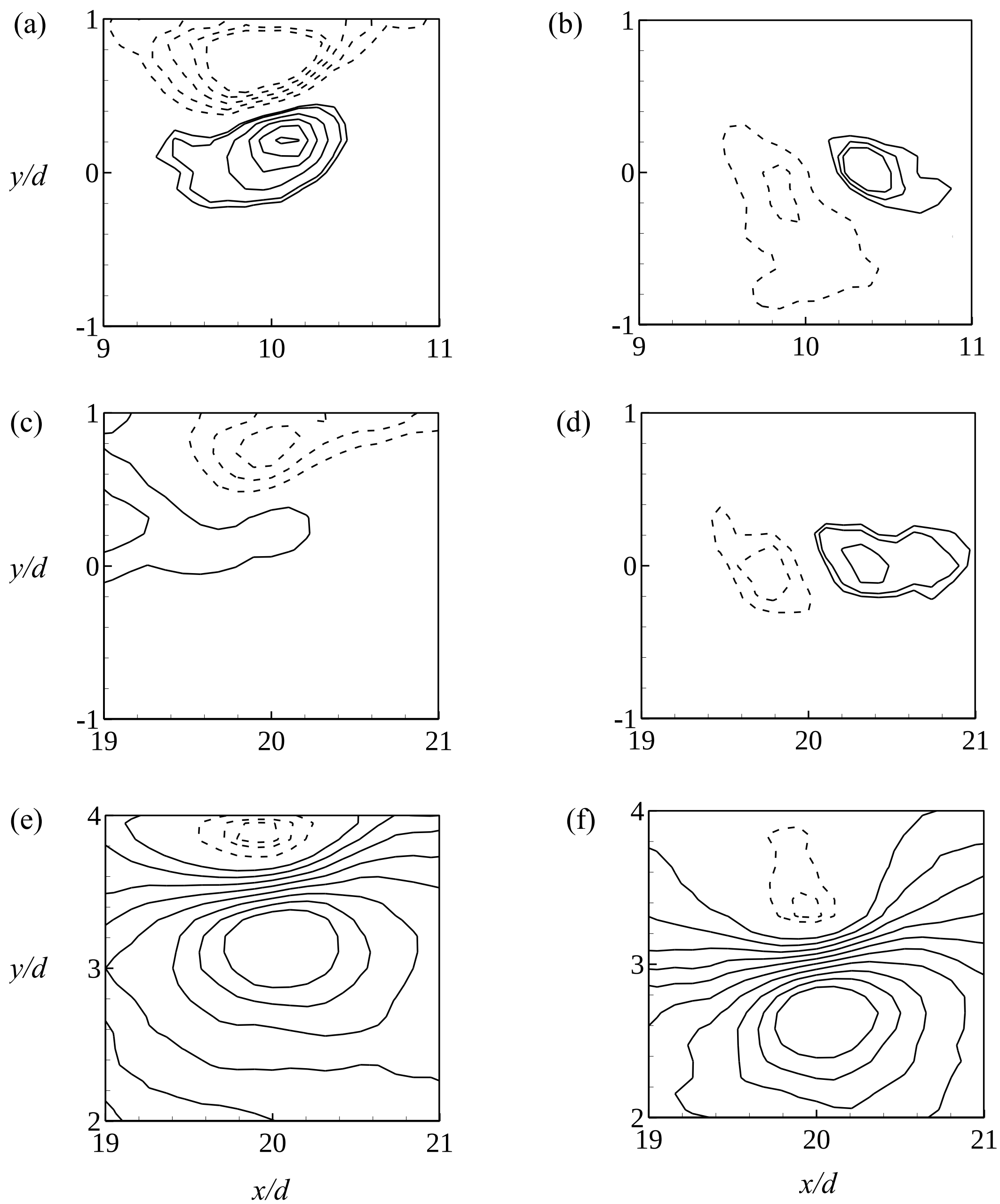

Figure 4.32. Contours of cross-correlation of swirling strength and streamwise velocity fluctuation, $R_{\lambda u}$ close to the free surface in the interaction region: (a) for h/d = 1 at x/d = 10, y^s/d = 0.5; (b) for h/d = 1 at x/d = 10, y^s/d = 1; (c) for h/d = 1 at x/d = 20, y^s/d = 0.5; (d) for h/d = 1 at x/d = 20, y^s/d = 1; (e) for h/d = 4 at x/d = 20, y^s/d = 0.5; and (f) for h/d = 4 at x/d = 20, y^s/d = 1. Contour levels vary from -0.1 to -0.02 and 0.02 to 0.16 at intervals of 0.02. Dashed contours indicate the negative correlation.

location, and positive below the reference location, which suggests that a retrograde vortex core is detected at the reference location. For the offset height h/d = 1, the correlation grows relatively weaker for streamwise locations far into the interaction region. This is despite the stronger coherence of the streamwise velocity fluctuations. On the contrary, for the larger offset height, h/d = 4, a considerably stronger coherence is observed at x/d = 20. This behavior could be explained by the intermittent nature of the swirling strength, which has a larger population density in the interaction region for h/d = 4 than h/d = 1 (see Fig. 4.1). Nevertheless, in all three plots, the self-correlation peaks of the positive and negative contours are inclined at an average angle of approximately 75º to the upstream direction. This inclination could be interpreted as a deformation or tilting of the circumferential vortex rings due to the presence of the free surface. At y^s/d = 1 (Figs. 4.32b, 4.32d and 4.32f), the correlation captures a prograde vortex at the reference locations for h/d = 1. This is evidenced by the negative $R_{\lambda u}$ values to the left of the reference locations and positive $R_{\lambda u}$ values to the right of the reference locations. The self-correlation peaks of the negative and positive contours are inclined at an average angle of approximately 7º to the downstream direction. In the case of h/d = 4 at x/d = 20, the correlation still captures a retrograde vortex at this reference location because the point (x/d = 20, y^s/d = 1) is still in the upper shear layer.

Iso-contours of the two-point cross-correlation between the swirling strength and surface-normal velocity fluctuation, $R_{\lambda v}$ in the upper and lower shear layer for h/d = 1 and 4 are shown in Fig. 4.33. Figures 4.33a – 4.33c show the iso-contours of $R_{\lambda v}$ in the upper shear layer for h/d = 4. The correlation, $R_{\lambda v}$ is negative upstream of the reference location,

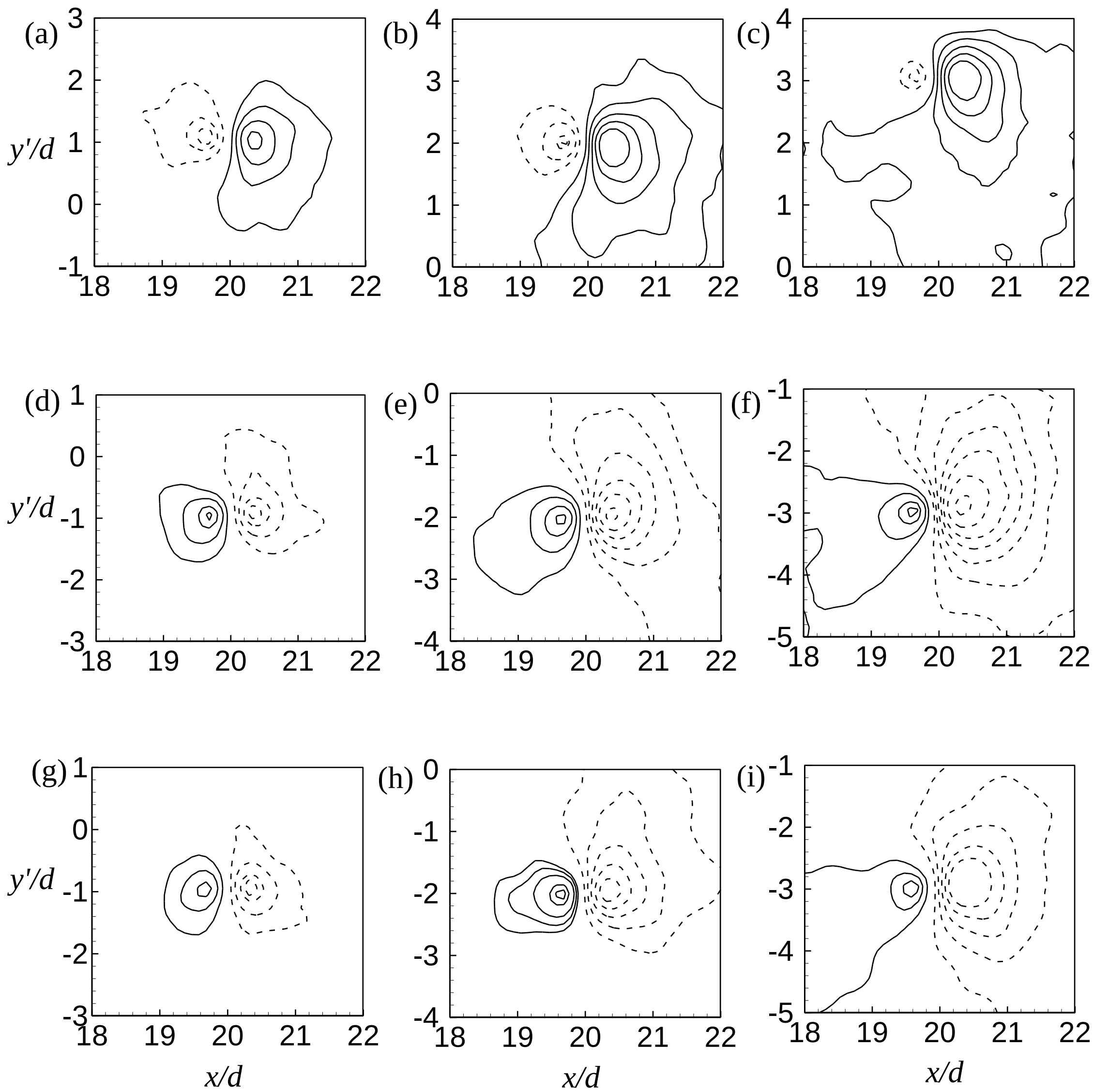

Figure 4.33. Contours of cross-correlation of swirling strength and surface-normal velocity fluctuation, $R_{\lambda v}$ within upper and lower shear layers for the *h/d* = 4 and 1 jet at *x/d* = 20: (a) for *h/d* = 4 at *y′/d* = +1, (b) for *h/d* = 4 at *y′/*d = +2, (c) for *h/d* = 4 at *y′/d* = +3, (d) for *h/d* = 4 at *y′/d* = –1, (e) for *h/d* = 4 at *y′/d* = –2, (f) for *h/d* = 4 at *y′/d* = –3, (g) for *h/d* = 1 at *y′/d* = –1, (h) for *h/d* = 1 at *y′/d* = –2 and (i) for *h/d* = 1 at *y′/d* = –3. Contour levels vary from -0.04 to -0.02 and 0.02 to 0.2 at intervals of 0.02. Dashed contours indicate the negative correlation.

and positive downstream of the reference location, indicating the flow around a retrograde vortex. Moving closer to the free surface leads to damping of the negative correlations, and enhancement of the positive correlations. The streamwise inclination angles at y'/d = 1, 2 and 3 are 7.6º, 7º and 3.2º, respectively, indicating a modest reduction in the streamwise inclination angle of the $R_{\lambda v}$ correlation. In the lower shear layer (Figs. 4.33d – 4.33f), $R_{\lambda v}$ is positive upstream and negative downstream of the reference location, as expected for the prograde vortex at this location. At larger distances from y'/d = 0, enhancements are observed while the angle of inclination remains relatively constant at approximately 7º with respect to the downstream direction. Figures 4.33g – 4.33i show the correlation functions, $R_{\lambda v}$ for h/d = 1 in the lower shear layer. Similar to $R_{\lambda u}$ as shown in Figs. 4.31g – 4.31i, the correlation levels are smaller when compared to those of h/d = 4. Also, the streamwise inclination angle for $R_{\lambda v}$ (approximately 6º) is in good agreement with the h/d = 4 jet.

Figure 4.34 shows the iso-contours of $R_{\lambda v}$ at the various reference locations close to the free surface for h/d = 1 and 4. The results presented in Figs. 4.34a, 4.34c and 4.34e are consistent with the flow pattern around a retrograde vortex. Those in Figs. 4.34b, 4.34d and 4.34f also well complement the corresponding $R_{\lambda u}$ contours as shown in Figs. 4.32b, 4.32d and 4.32f.

In order to quantify the swirling strength associated with spanwise vortices, surface-normal profiles of the swirling strength as well as its two components: prograde and retrograde are shown in Fig. 4.35 for h/d = 1 and 4 at x/d = 1, 5, 10 and 24. As expected, positive and negative signed mean swirling strength ($\Lambda_{ci,z}$ in Fig. 4.35a) in the

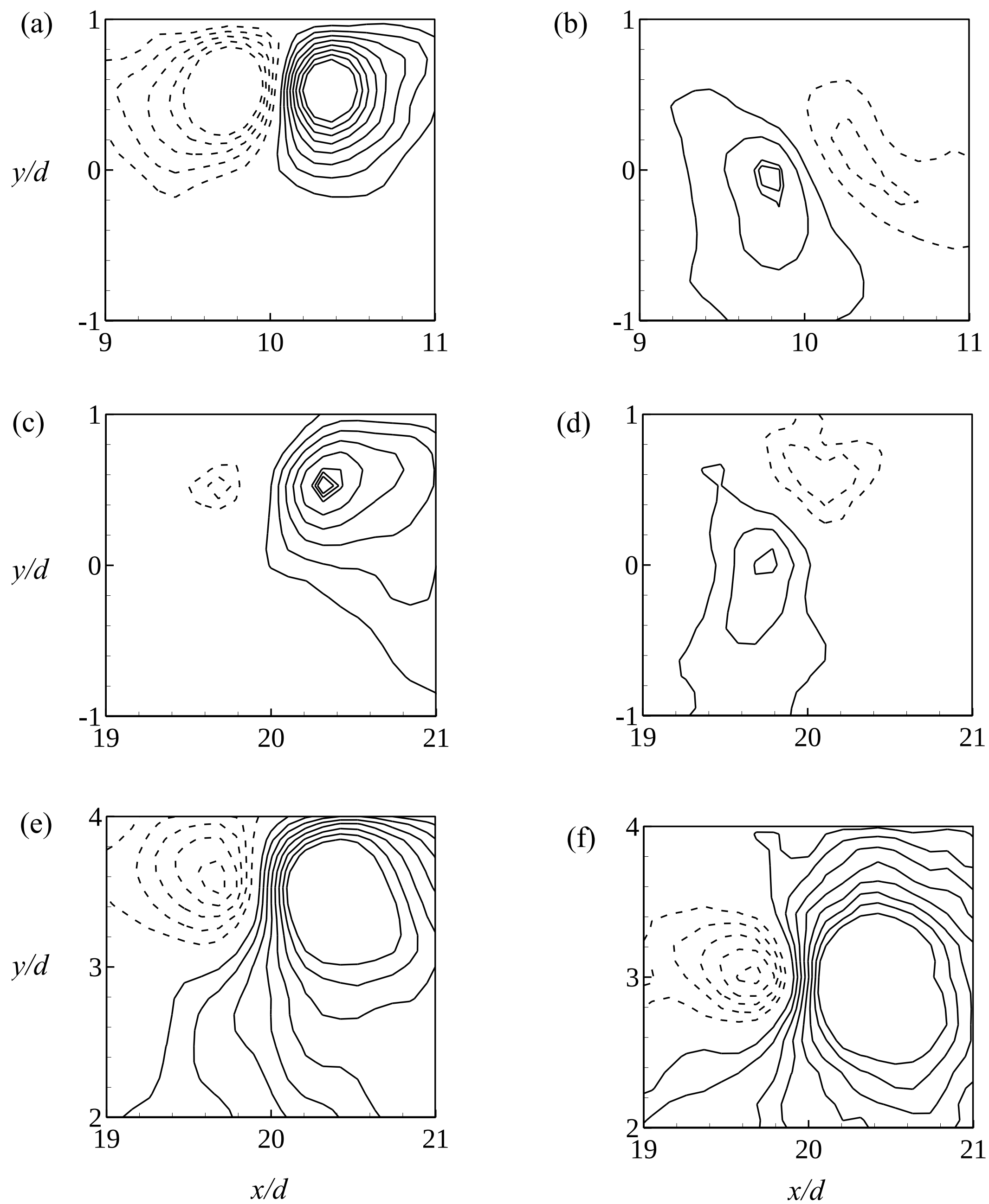

Figure 4.34. Contours of cross-correlation of swirling strength and surface-normal velocity fluctuation, $R_{\lambda v}$ close to the free surface in the interaction region: (a) for $h/d = 1$ at $x/d = 10$, $y^s/d = 0.5$; (b) for $h/d = 1$ at $x/d = 10$, $y^s/d = 1$; (c) for $h/d = 1$ at $x/d = 20$, $y^s/d = 0.5$; (d) for $h/d = 1$ at $x/d = 20$, $y^s/d = 1$; (e) for $h/d = 4$ at $x/d = 20$, $y^s/d = 0.5$; and (f) for $h/d = 4$ at $x/d = 20$, $y^s/d = 1$. Contour levels vary from -0.1 to -0.02 and 0.02 to 0.16 at intervals of 0.02. Dashed contours indicate the negative correlation.

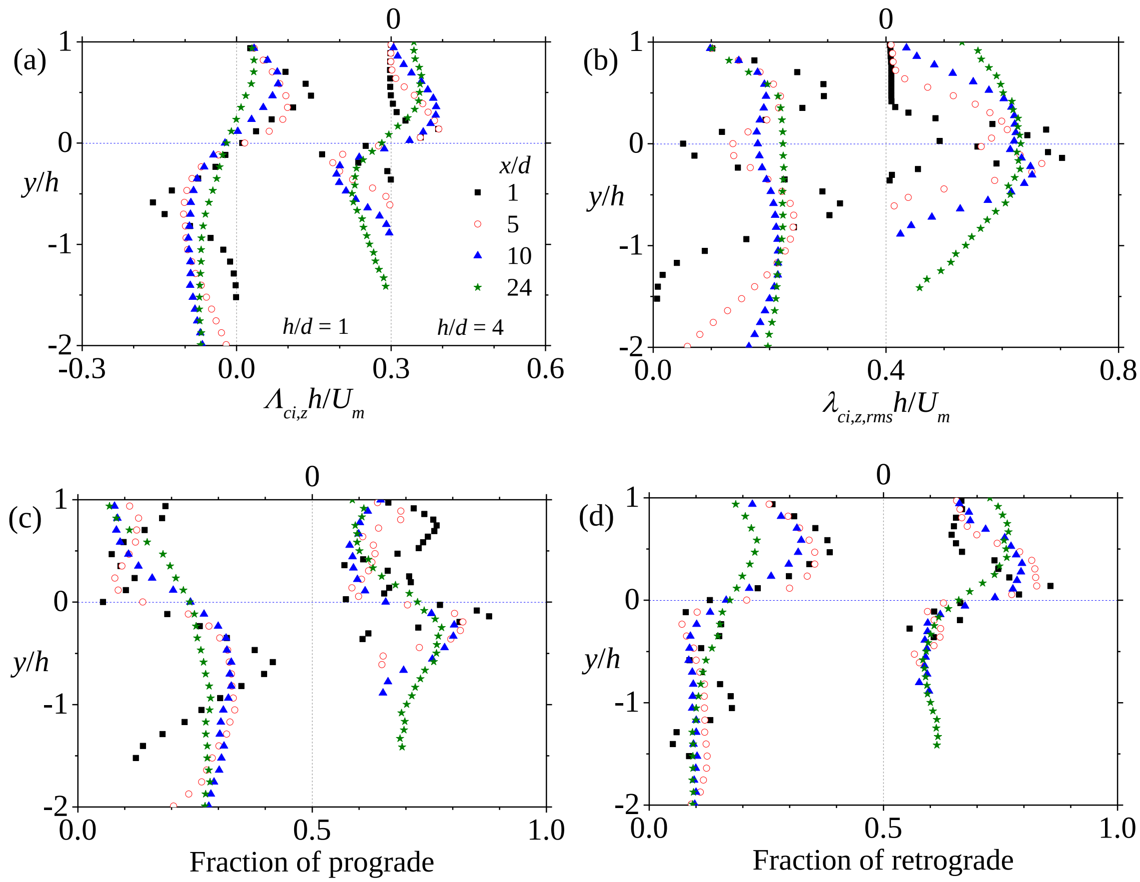

Figure 4.35. Surface-normal profiles of (a) signed swirling strength, (b) root-mean-square of swirling strength, (c) fraction of prograde and (d) fraction of retrograde for *h/d* = 1 and 4 at selected *x/d* locations.

upper and lower shear layers correspond to retrograde and prograde vortices, respectively. The peak values of the normalized mean swirling strength occur at the edge of the shear layer and have the largest magnitudes close to the jet exit. The larger values of swirling strength in the near field region are consistent with the strong circumferential vortices shed from the exit. The $\Lambda_{ci,z}$ peak values reduce with increasing *x/d*, indicating a reduction of rate of strain (weakening of the circumferential rings) as the jet develops downstream. This effect is more dramatic for *h/d* = 1 in the upper shear layer than for *h/d* = 4. The results also support the notion that the effect of the free surface is to weaken the vorticity field in the upper shear layer for the shallow jet. The root-mean-square swirling strength ($\lambda_{ci,z,rms}$ in Fig. 4.35b) shows typical transition from the double-peak to single-peak profiles with the increase of streamwise distance and the dramatic reduction of the peak values is consistent with the result of $\Lambda_{ci,z}$. The early attachment for the shallow jet (h/d = 1) causes the appearance of $\lambda_{ci,z,rms}\, h/U_m$ at the free surface earlier than the deeper jet (h/d = 4). However, at a given x/d location in the interaction region, $\lambda_{ci,z,rms}\, h/U_m$ at the free surface is lower (approximately 24% at x/d = 24, for instance) for h/d = 1 than h/d = 4, indicating a weaker vorticity field in the case of the shallow jet.

Figures 4.35c and 4.35d show the fractions of prograde and retrograde swirling strength, respectively. A higher population of the clockwise and counter-clockwise rotating spanwise vortex cores in the lower and upper shear layer, respectively as observed in Fig. 4.1, irrespective of offset height, is evident in the profiles of fraction of prograde and retrograde showing higher peak value in the lower and upper shear layer, respectively. Also, a dramatic reduction of the fraction of retrograde in the upper shear layer with the increase of x/d location for h/d = 1 supports the attenuation of the vortices due to surface confinement.

4.6 Joint Probability Density Functions

To provide a deeper insight into the correlation between the instantaneous velocity fluctuations, the values of the joint probability density function (JPDF), $P(u, v)$ are calculated. In the present study, the JPDFs are estimated by sorting the velocity fluctuations into equal-width 100 × 100 bins. Figure 4.36 shows the streamwise evolution of the JPDF of *u* and *v* for *h/d* = 1 and 4 along the jet centerline. The iso-contours are plotted at the three streamwise locations; *x/d* = 3, 9 and 20. The surface-normal location in each case corresponds to the location of the local maximum mean streamwise velocity, U_m. As shown in Fig. 4.36a, the straight lines passing through the origin, divide the plots into the following four quadrants of the *u*-*v* plane: Q1, Q2, Q3 and Q4, where Q1 (+*u*, -*v*) denotes fast entrainment of ambient fluid; Q2 (-*u*, -*v*) denotes slow entrainment of ambient fluid; and Q3 (-*u*, +*v*) and Q4 (+*u*, +*v*) denote slow and fast ejections, respectively based on the orientation of the upper shear layer. At this surface-normal location, the contours are almost elliptical and show no preferred orientation for any of the four quadrants. A streamwise growth of the probability contours is observed in both cases suggesting the increasing importance of extreme Reynolds shear stress producing events. The slight shift of the maximum probability in favor of the +*u* direction, indicates a dominance of fast *u* fluctuations in generating the Reynolds shear stress. For a given streamwise location, the effect of reducing the offset height ratio is to diminish the probability of extreme Reynolds shear stress producing events. This damping effect on the JPDFs is consistent with the reduced Reynolds shear stress at smaller offset height ratios of the jet.

Figure 4.37 shows the JPDFs at *x/d* = 20 for *h/d* = 4 at various surface-normal locations in the upper and lower shear layer. Above the jet centerline (Figs. 4.37a, 4.37c and 4.37e), the JPDF contours are inclined towards the second and fourth quadrants (Q2 and Q4), indicating slow entrainments and fast ejections to be the dominant contributors to the mean Reynolds shear stress (-<*uv*>) in the upper shear layer. There is a diminishing

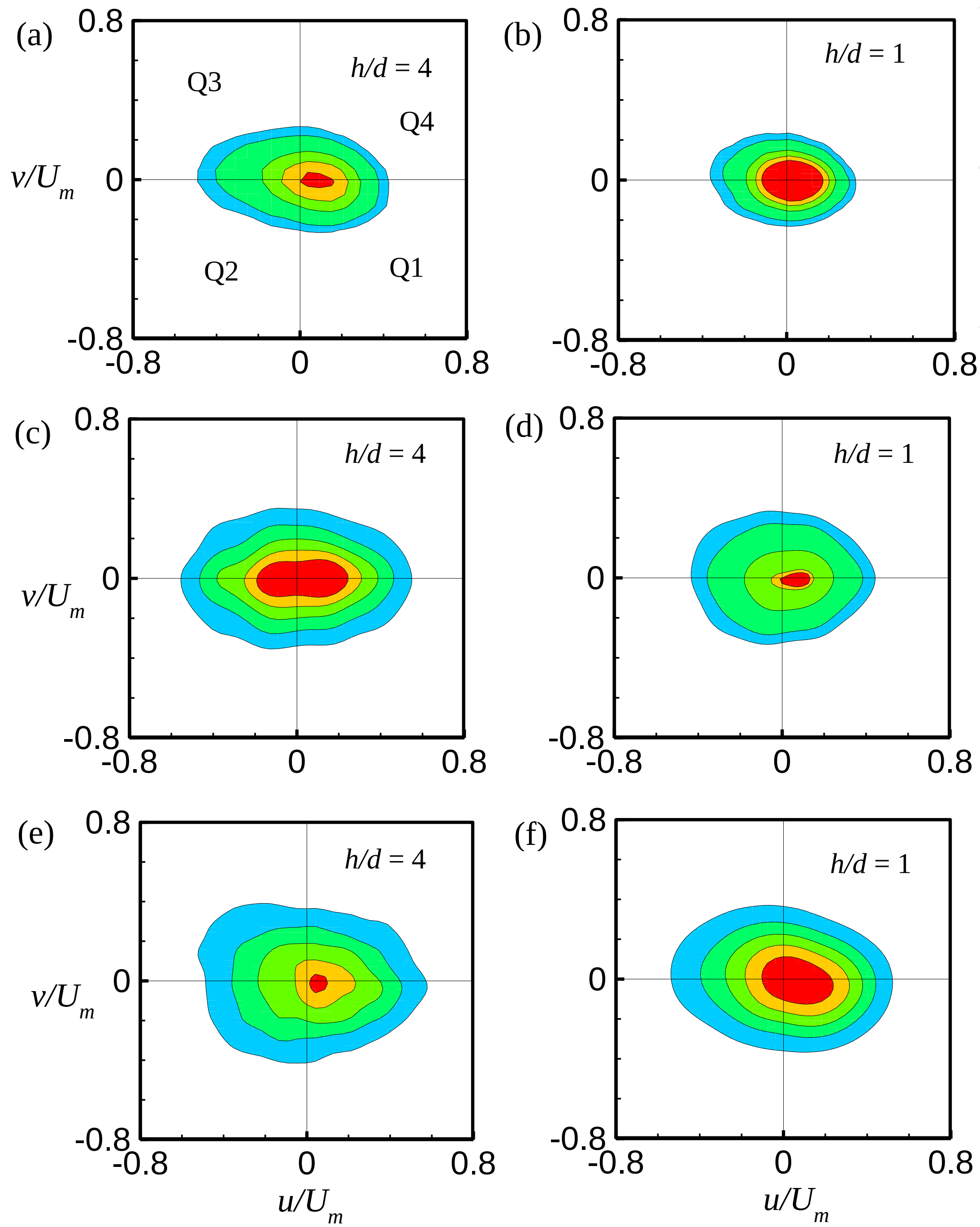

Figure 4.36. Contours of JPDF along the jet centerline: (a) at x/d = 3 for h/d = 4, (b) at x/d = 3 for h/d = 1, (c) at x/d = 9 for h/d = 4, (d) at x/d = 9 for h/d = 1, (e) at x/d = 20 for h/d = 4 and (f) at x/d = 20 for h/d = 1. Contour levels vary from 0.5 to 2.5 at intervals of 0.5.

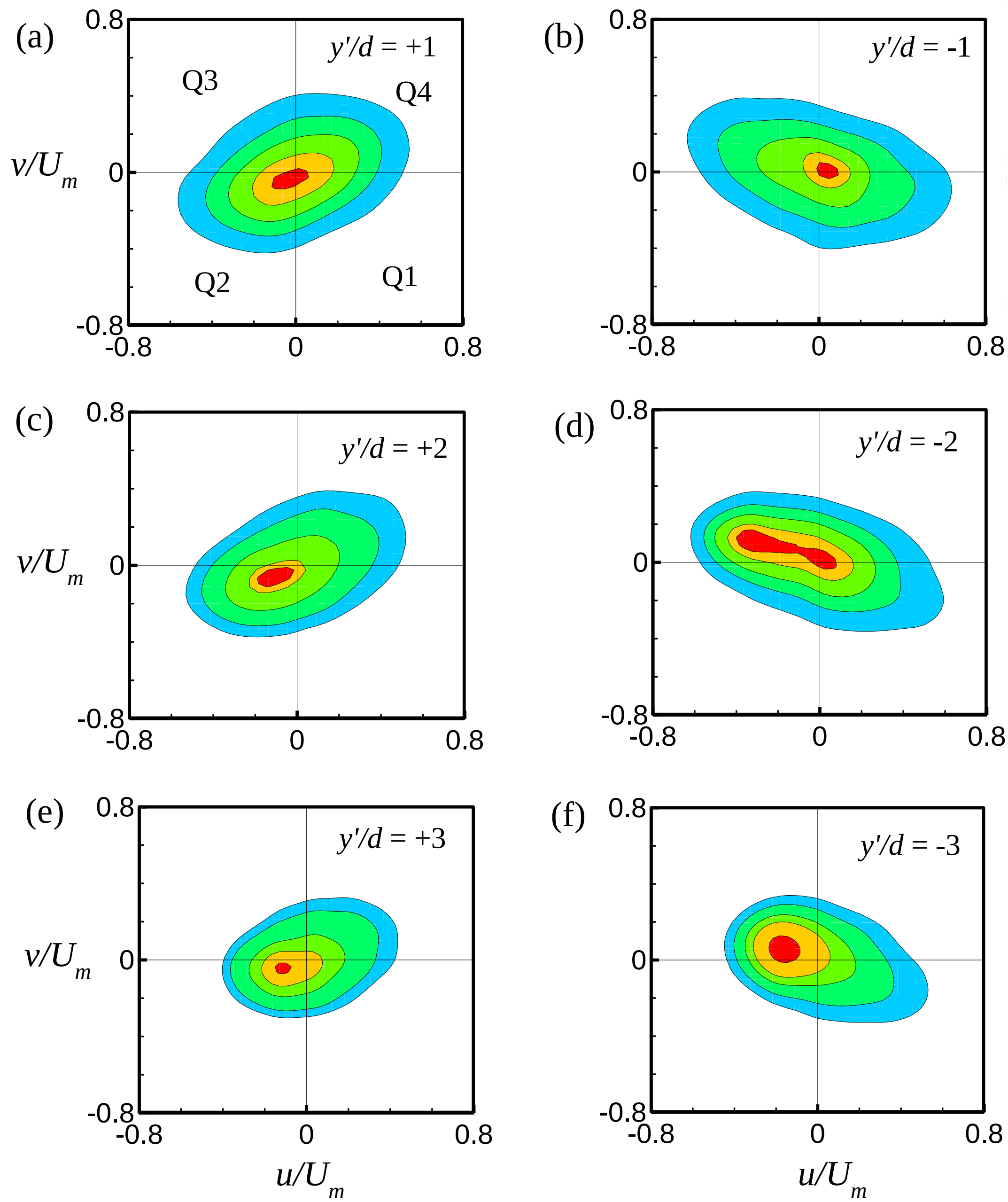

Figure 4.37. Contours of JPDF within upper and lower shear layers for the h/d = 4 jet at x/d = 20: (a) at y'/d = +1, (b) at y'/d = –1, (c) at y'/d = +2, (d) at y'/d = –2, (e) at y'/d = +3 and (f) at y'/d = –3. Contour levels vary from 0.5 to 2.5 at intervals of 0.5.

effect in the direction of the free surface due to the decay in Reynolds shear stress as the free surface is approached. Also, as the free surface is approached, the maximum joint probability shifts in favor of Q2. Since the Reynolds shear stress must be approaching zero, a shift of the maximum in favor of one quadrant should be balanced by a corresponding increase in magnitude of the fluctuations in the opposite quadrant. This effect is depicted by the increasing contraction of the contour levels in Q2 and expansion of the contour levels in Q4. Figs. 4.37b, 4.37e and 4.37f show the corresponding JPDF contours below the jet centerline (lower shear layer). Due to the reverse orientation of the lower shear layer relative to the upper shear layer, the contour inclinations in this case are mirrored as major contribution to the mean Reynolds shear stress is from the events of ($+u$, $-v$) and ($-u$, $+v$). The contours also indicate a diminishing effect in the direction away from the centerline, but they are wider in comparison with those in the upper shear layer. The larger contours in the lower shear layer are consistent with the larger Reynolds shear stress magnitudes in the lower shear layer.

Figure 4.38 shows the distributions of the JPDFs close to the free surface for $h/d = 1$ and 4 at selected streamwise locations in the interaction region. Figure 4.38a shows the JPDF distribution for offset height ratio $h/d = 1$ at $x/d = 10$ and $y^s/d = 0.5$. At this streamwise location, the iso-probability contours are centered on the origin but are inclined towards the second and fourth quadrants. This suggests that slow entrainment and fast ejections are the dominant contributors to the mean Reynolds shear stress at this location. Figure 4.38c shows the JPDF distribution for $h/d = 1$ at $x/d = 20$ and $y^s/d = 0.5$. Here, the contours are more elongated, indicating growth with downstream distance, but

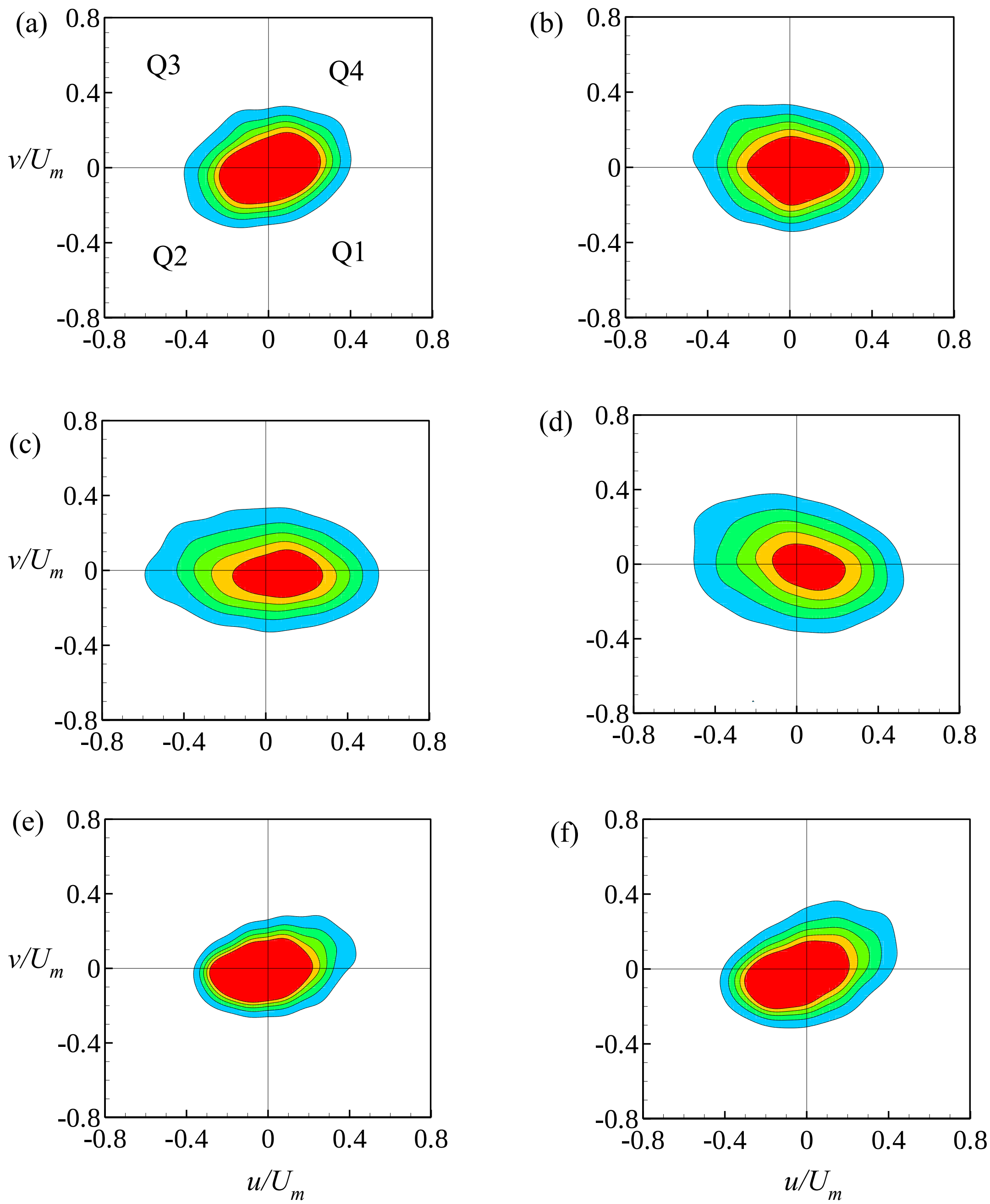

Figure 4.38. Contours of JPDF close to the free surface in the interaction region: (a) for $h/d = 1$ at $x/d = 10$, $y^s/d = 0.5$; (b) for $h/d = 1$ at $x/d = 10$, $y^s/d = 1$; (c) for $h/d = 1$ at $x/d = 20$, $y^s/d = 0.5$; (d) for $h/d = 1$ at $x/d = 20$, $y^s/d = 1$; (e) for $h/d = 4$ at $x/d = 20$, $y^s/d = 0.5$; and (f) for $h/d = 4$ at $x/d = 20$, $y^s/d = 1$. Contour levels vary from 0.5 to 2.5 at intervals of 0.5.

the location of maximum probability undergoes a slight shift towards the $+u$ direction. The slight shift of the maximum probability in favour of the $+u$ direction indicates a dominance of fast u fluctuations in generating the Reynolds shear stress at this streamwise location. Since this is at the expense of surface-normal fluctuations, it would lead to diminishing Reynolds shear stress, as observed at $y/h \approx 0.5$ for the $h/d = 1$ case in Fig. 4.14c. Figure 4.38e depicts the JPDF distribution for the offset height ratio $h/d = 4$ at $x/d = 20$ and $y^s/d = 0.5$. At $x/d = 20$, the iso-probability contours for the larger offset height ratio are more compact (which is to say, much closer to the maximum probability contour level), indicating a larger Reynolds shear stress magnitude when compared to $h/d = 1$. Also, the Q2-Q4 orientation of the distribution indicates a dominance of Q2 and Q4 events in producing the Reynolds shear stress. Figure 4.38b is the JPDF plot for $h/d = 1$ at $x/d = 10$ and $y^s/d = 1$. The contours are less elliptical, indicating lack of preference for any particular quadrant. This is consistent with the almost negligible Reynolds shear stress magnitude near the jet centerline for $h/d = 1$ (see Fig. 4.21a). Further downstream (Fig. 4.38d), the orientation of the contour in favour of the events of $(+u, -v)$ and $(-u, +v)$ suggests the location is within the lower shear layer. This result is also consistent with the non-zero Reynolds shear stress value observed at this location. On the contrary, though, the corresponding distribution for $h/d = 4$ (Fig. 4.38f) exhibits the opposite orientation (Q2-Q4) and is more compact than that for $h/d = 1$. The orientation is different because this location still resides within the upper shear layer for $h/d = 4$.

To examine the relative contributions of the velocity fluctuations to the Reynolds shear stress, the values of the weighted JPDF (covariance integrand), $uvP(u, v)$ are calculated (WJPDF). WJPDF supplements the results obtained from the JPDF providing insight into the strength of the correlation between the velocity fluctuations. Figure 4.39 shows the iso-contours of the WJPDF along the jet centerline. There is no systematic trend in the positive and negative distributions, except for the smaller lobes on the positive u side, which are compensated for by the larger lobes on negative u side of the horizontal axis. This mimics the JPDF distributions shown in Fig. 4.36. It should be noted though that for h/d = 1, the contours at x/d = 20 indicate a slight orientation in favor of (+u, -v) and (-u, +v) (not quite obvious from Fig. 4.36f, that may be explained by the deflection of the jet away from the free surface at this location).

The WJPDF computed on either side of the jet centerline at x/d = 20 are shown in Fig. 4.40 for h/d = 4. In the upper shear layer, the positive WPDFs are substantially larger than the negative WPDFs in agreement with the dominance of Q2 and Q4 events in this region. Towards the free surface, the WJPDFs are diminishing as observed in the corresponding JPDF. In the lower shear layer, the negative WJPDFs are substantially larger than the positive WJPDFs, and the same damping effect is observed away from the jet centerline.

Figure 4.41 shows the iso-contours of the WJPDF close to the free surface in the interaction region for the h/d = 1 and h/d = 4 jet. For the shallow jet at x/d = 10 and y^s/d = 0.5 (Fig. 4.41a), the positive lobes of the distribution are slightly larger than the negative lobes, thereby favouring events in Q2 and Q4 in concert with the results in Fig. 4.38a. At x/d = 20 and y^s/d = 0.5 (Fig. 4.41c), all four lobes exhibit a similar streamwise elongation as observed for the corresponding JPDF distribution. For h/d = 4 at x/d = 20 and y^s/d =

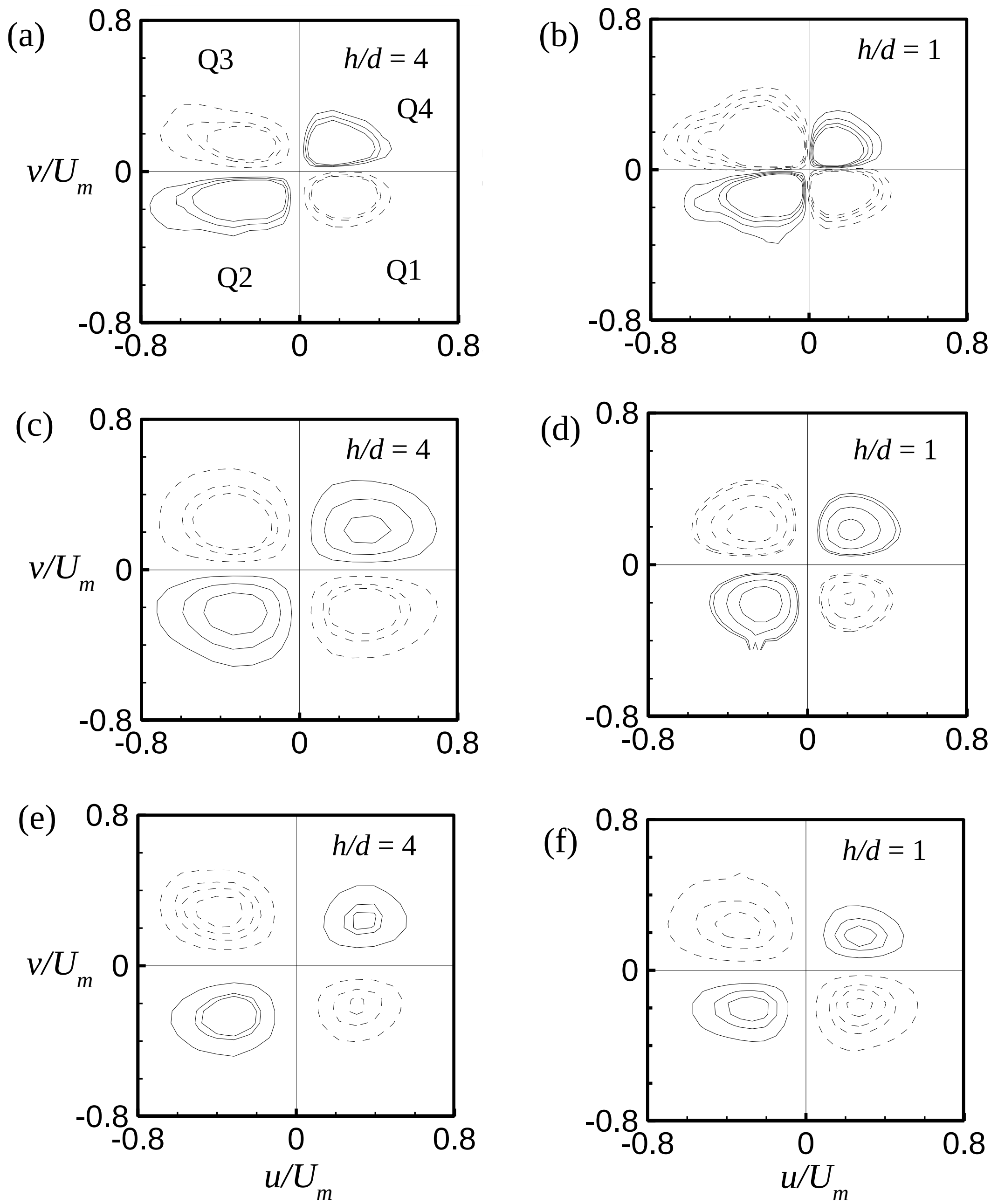

Figure 4.39. Contours of WJPDF along the jet centerline: (a) for h/d = 4 at x/d = 3, (b) for h/d = 1 at x/d = 3, (c) for h/d = 4 at x/d = 9, (d) for h/d = 1 at x/d = 9, (e) for h/d = 4 at x/d = 20 and (f) for h/d = 1 at x/d = 20. Contour levels vary from -0.0016 to -0.0004 and 0.0004 to 0.0016 at intervals of 0.0004. Dashed contours indicate the negative correlation.

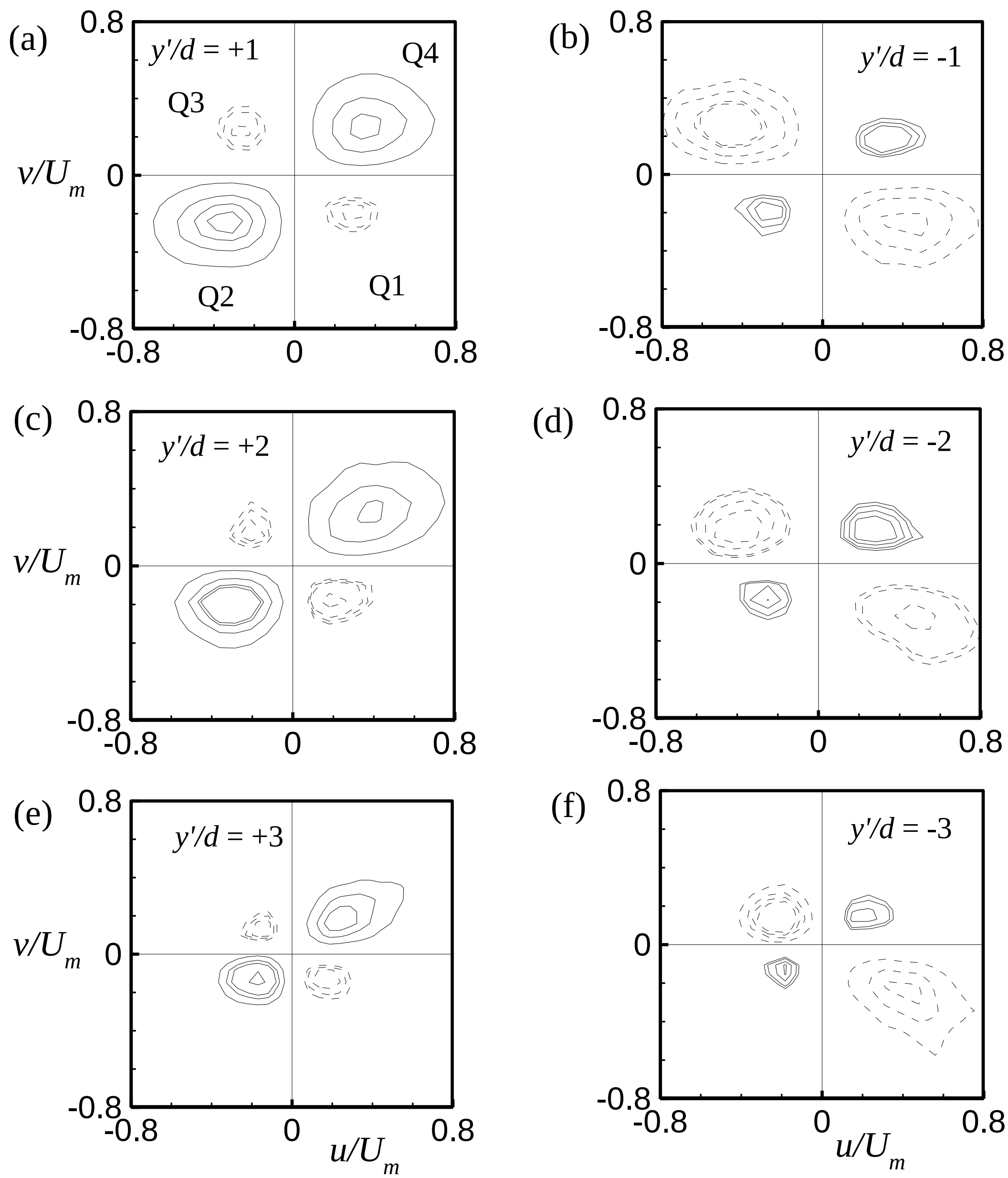

Figure 4.40. Contours of WJPDF within upper and lower shear layers for the h/d = 4 jet at x/d = 20: (a) at y'/d = +1, (b) at y'/d = –1, (c) at y'/d = +2, (d) at y'/d = –2, (e) at y'/d = +3 and (f) at y'/d = –3. Contour levels vary from -0.0016 to -0.0004 and 0.0004 to 0.0016 at intervals of 0.0004. Dashed contours indicate the negative correlation.

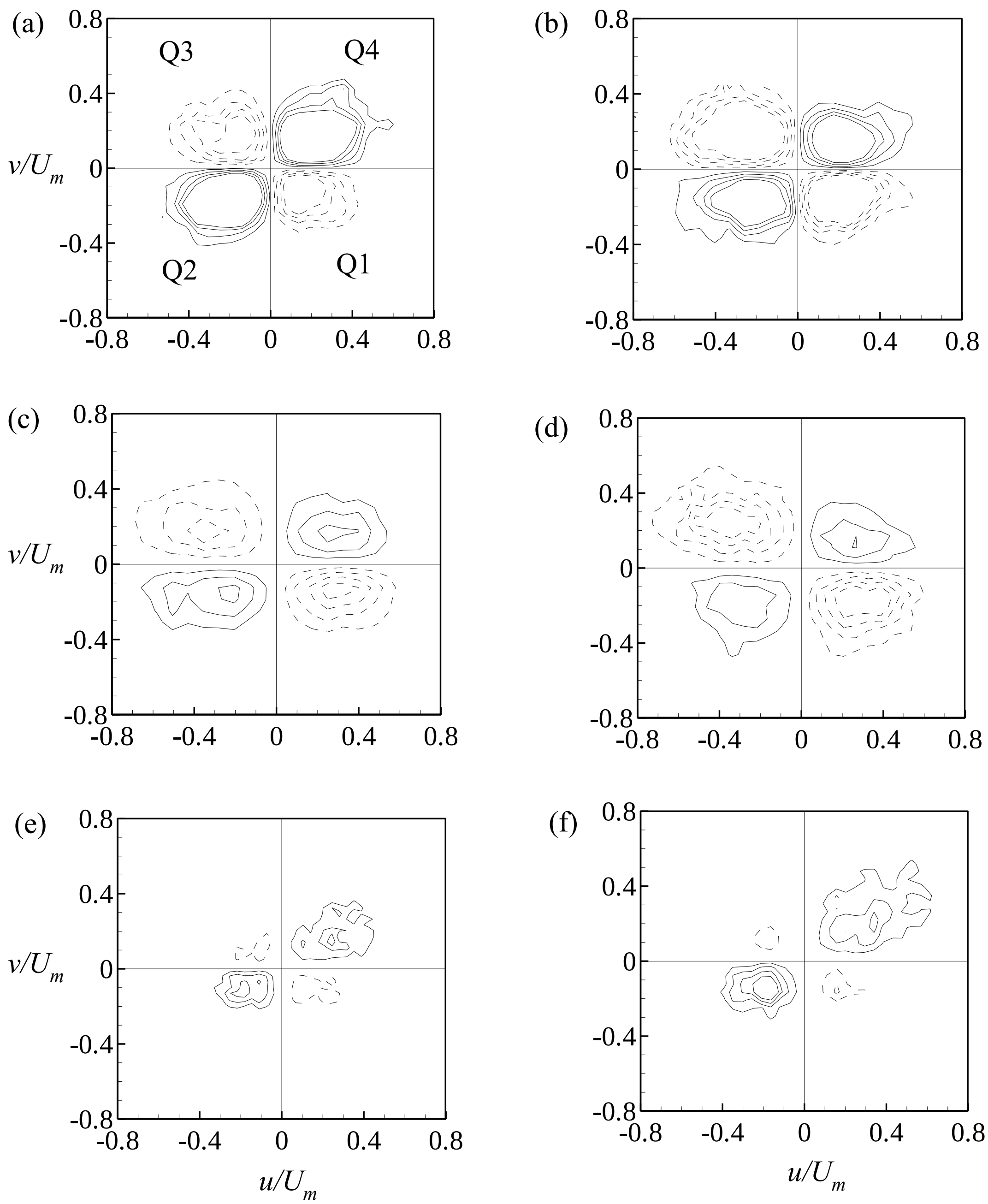

Figure 4.41. Contours of WJPDF close to the free surface in the interaction region: (a) for h/d = 1 at x/d = 10, y^s/d = 0.5; (b) for h/d = 1 at x/d = 10, y^s/d = 1; (c) for h/d = 1 at x/d = 20, y^s/d = 0.5; (d) for h/d = 1 at x/d = 20, y^s/d = 1; (e) for h/d = 4 at x/d = 20, y^s/d = 0.5; and (f) for h/d = 4 at x/d = 20, y^s/d = 1. Contour levels vary from -0.0016 to -0.0004 and 0.0004 to 0.0016 at intervals of 0.0004. Dashed contours indicate the negative correlation.

0.5, the Q2 and Q4 lobes predominate over the Q1 and Q3 lobes, which is consistent with the results in Figure 4.38e. The lack of a well-defined asymmetry in the distributions for the shallow jet could be considered as an artifact of the relatively weak values of the skewness and flatness values at this surface-normal location. In contrast, the asymmetric shape of distribution for the deeper jet at x/d = 20 are in agreement with the relatively strong values of the corresponding skewness and flatness factors. The WJPDFs at y^s/d = 1 (Figs. 4.41b, 4.41d and 4.41f) share a similar correspondence with their JPDF counterparts in Fig. 4.38 and are consistent with the skewness and flatness factor distributions.

4.7 Proper Orthogonal Decomposition

In order to investigate the role of the energetic structures in the flow field of the surface attaching jets, the proper orthogonal decomposition (POD) analysis is performed. As mentioned in Chapter 2, the snapshot approach of the POD analysis introduced by Sirovich (1987) is applied in the present study and a brief description of the method is provided in Appendix A. The analysis is performed for the two extreme conditions (h/d = 1 and 4) in the two symmetry planes (Plane 1 and Plane 2). It should be noted that the vertical and horizontal edges of the two planes are trimmed in order to exclude spurious data at the extremities of the symmetry planes from the analysis. This reduces the streamwise extents of Plane 1 and Plane 2 to $0.5 \leq x/d \leq 12$ and $13 \leq x/d \leq 24.5$, respectively, and the surface normal extent of each plane is 7.95d starting from the surface-normal location 0.05d below the free surface.

4.7.1 Convergence of turbulent kinetic energy

In order to capture the energy content for a given POD mode adequately, sufficient number of snapshots (N_s) is necessary. The number of snapshots required to obtain converged result varies with the type and complexity of the flow examined. Previous studies suggest that the snapshot procedure improves with the increase of N_s (e.g., Breuer and Sirovich, 1991). In this study, a convergence test is performed to determine if the present sample size of N_s = 5000 snapshots is sufficient for the POD analysis. In the convergence test, the turbulent kinetic energy content in the individual POD mode (fractional energy) and the cumulative energy for the mode numbers, *m* are obtained using varying number of snapshots from N_s = 100 to 5000. Results obtained for the *h/d* = 1 and 4 jets in Plane 1 and Plane 2 are presented in Fig. 4.42. Results show collapsed profiles of the fractional and cumulative energy for $N_s \geq 4000$. Thus, the 5000 snapshots used in the present study are sufficient to converge the POD results.

4.7.2 Fractional and cumulative energy distribution

The distribution of fractional energy for *h/d* = 1 and 4 in Plane 1 is presented in Fig. 4.43a. As expected, the distribution of fractional energy shows a decreasing trend with the increase of mode numbers. The deeper jet shows higher energy content in the individual lower order modes, with a fractional energy in mode 1 which is almost twice as large as that for a shallower jet. A similar increase in fractional energy at low order modes with increasing offset height ratio was reported for wall attaching jets (Nyantekyi-Kwakye et al., 2015b). Compared to the wall attaching jet of Nyantekyi-Kwakye et al. (2015b) at *H/d* = 4.5, the present fractional energy of mode 1 for *h/d* = 4 is approximately

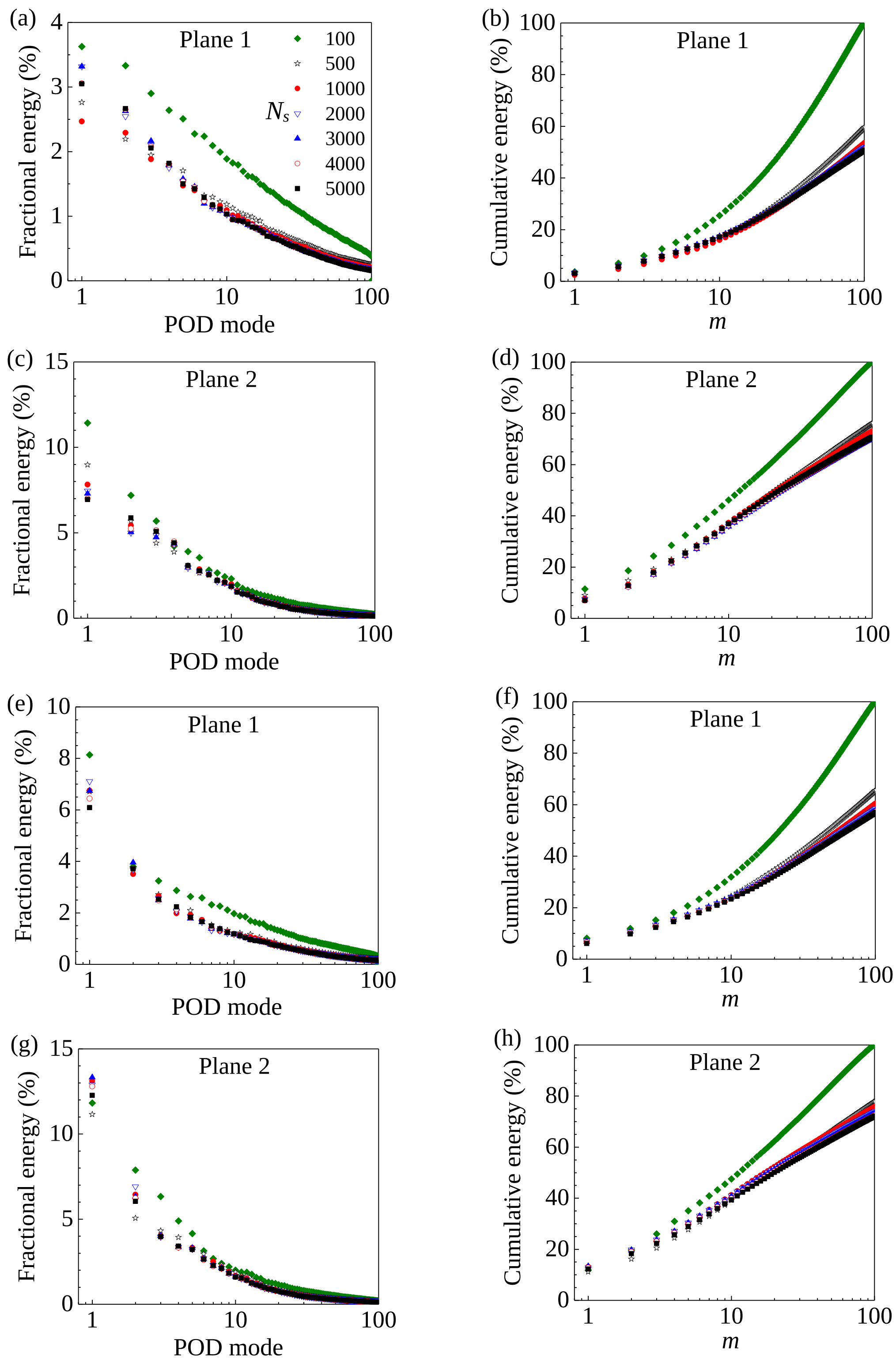

Figure 4.42. Fractional and cumulative energy distribution obtained using various number of snapshots in Plane 1 and Plane 2 for (a - d) h/d = 1 and (e - h) h/d = 4.

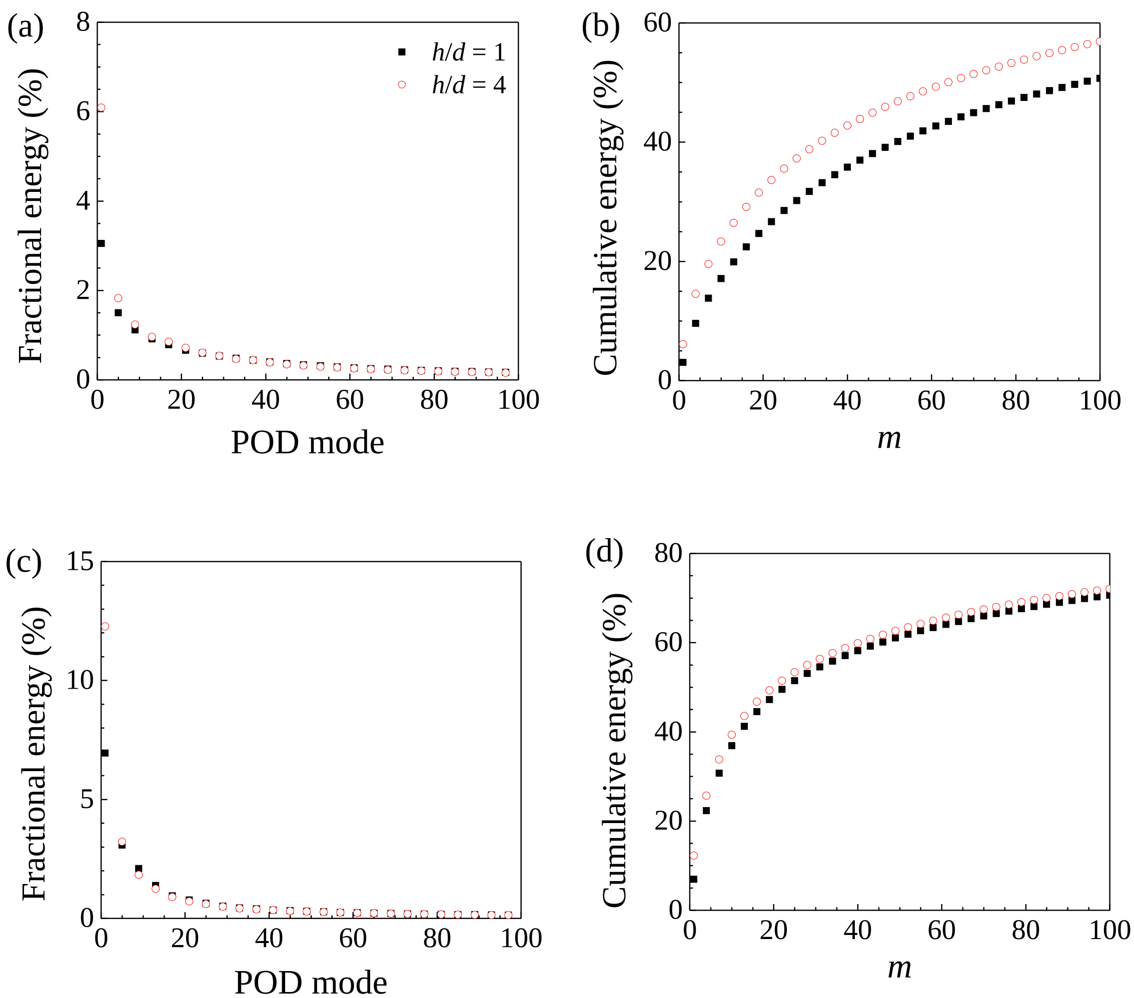

Figure 4.43. Comparison of the fractional and cumulative energy distributions between the *h/d* = 1 and 4 jets in Plane 1 and Plane 2: (a) Fractional energy in Plane 1, (b) cumulative energy in Plane 1, (c) fractional energy in Plane 2 and (d) cumulative energy in Plane 2.

29% lower in Plane 1. This is indicative of the presence of less energetic eddies in the near-field region of the surface attaching jet compared to the wall attaching jet. The profiles of fractional energy in Plane 2 (Fig. 4.43c) reveal a qualitatively similar trend to Plane 1 except for the fractional energy content of the most energetic eddies. For instance, in Plane 2, the fractional energy in mode 1 is approximately 56% and 50% higher than that in Plane 1 for h/d = 1 and 4, respectively, which is consistent with the growth of the organized coherent structures as the jet develops downstream.

Figure 4.43b shows the variation of the cumulative energy fraction with mode number, m for Plane 1. Higher energy content in the individual modes at larger offset height ratios leads to a commensurate increase in the cumulative energy fraction. For the shallow jet, a higher number of modes are required in order to capture a specific cumulative energy fraction of the total turbulent kinetic energy (TKE) in comparison to the deeper jet. For instance, for h/d = 1, as many as 96 modes are required in order to capture up to 50% of total turbulent kinetic energy, while only 64 modes are required for h/d = 4. This implies a slower rate of convergence to total energy for the shallower jet due to an increasing range of turbulent length scale (Nyantekyi-Kwakye et al., 2015b). The value of m required to achieve 50% of energy in Plane 1 for h/d = 4 is more than twice as high as the value of m = 31 required for a wall attaching jet at H/d = 4.5 by Nyantekyi-Kwakye et al. (2015b), which is consistent with the lower energy content for the surface attaching jet. In Plane 2 (Fig. 4.43d), fewer modes (m = 23 and 20 for h/d = 1 and 4, respectively) are required to capture up to 50% of the total energy for both offset height ratios due to faster convergence in Plane 2 than in Plane 1.

4.7.3 Reconstructed velocity vectors

In order to explore the role of various energetic modes on the dynamics of large scale motion in the near field region, the velocity vectors reconstructed from various modes for h/d = 1 and 4 in Plane 1 are presented in Figs. 4.44 and 4.45, respectively.

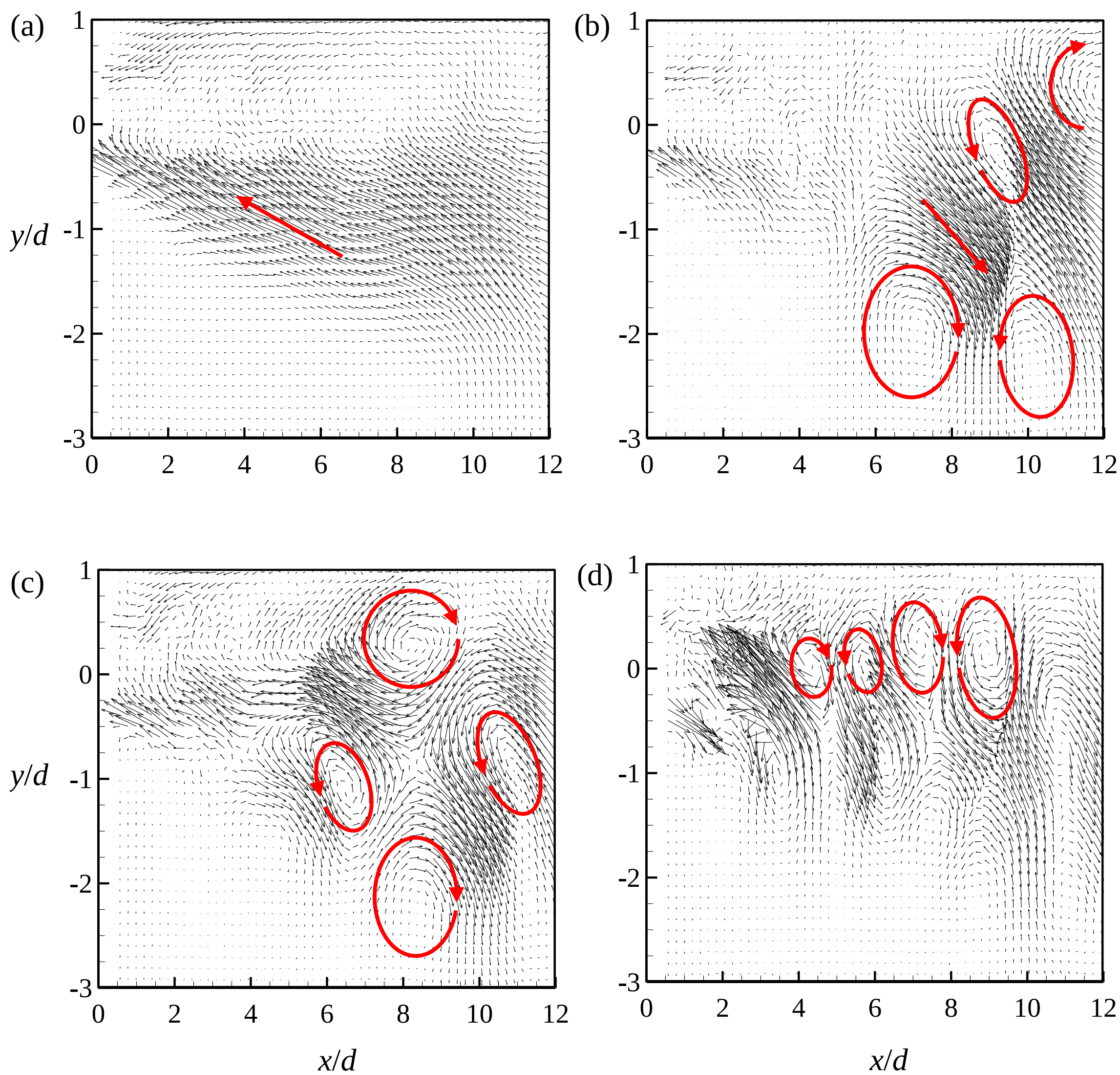

Figure 4.44. Vector plots of the POD modes for *h/d* = 1 in Plane 1: (a) mode 1, (b) mode 3, (c) mode 5 and (d) mode 10.

Results from modes 1, 3, 5 and 10 are presented in the figures. The 1st, 3rd, 5th and 10th modes contain approximately 3.0%, 2.0%, 1.5% and 1.0% of the total turbulent kinetic energy, respectively, for *h/d* = 1 (Fig. 4.44). The most energetic mode, which is considered to represent the flapping motion of the shear layer is shown in Fig. 4.44a. The plot shows a large-scale region of low-momentum fluid below the jet centerline whose size is increasing in the streamwise direction. The positioning of the large-scale structure below the jet axis can be attributed to the downward displacement of the vortex rings by the free surface. Figures 4.44b – 4.44d show several smaller-scale structures of different sizes positioned at random locations in the flow field. This indicates that while mode 1 contributes to the larger-scale structure of the jet, the higher order modes are responsible for the smaller-scale spanwise vortex cores in the jet. The randomness in size and position of the vortices is consistent with the lack of correlation between the POD modes. The higher order modes also show alternating regions of low and high-momentum fluid between counter-rotating spanwise vortex cores helping to transport turbulent kinetic energy across the jet centerline. These results are qualitatively consistent with previous POD results reported for wall attaching jets (Nyantekyi-Kwakye et al., 2015b) and surface attaching jets (Shinneeb et al., 2011; Wen et al., 2014a).

For the deeper jet, the vector plot for mode 1 (Fig. 4.45a) shows a larger low-momentum region than that for h/d = 1, and it is nearly symmetric with respect to the jet centerline. The larger low-momentum zone is consistent with the faster convergence and higher energy fraction of mode 1 for deeper jets than the shallow jet. On the other hand, the near symmetry about the jet centerline is due to the reduced confinement for h/d = 4 compared to h/d = 1. The vector plot of mode 3 for h/d = 4 (Fig. 4.45b) shows a central region of positive streamwise momentum, representing the core jet, that is bounded by counter-rotating spanwise vortices inducing the core jet. The vortical structures also induce large-scale regions of low-momentum fluid, indicative of entrainment towards the

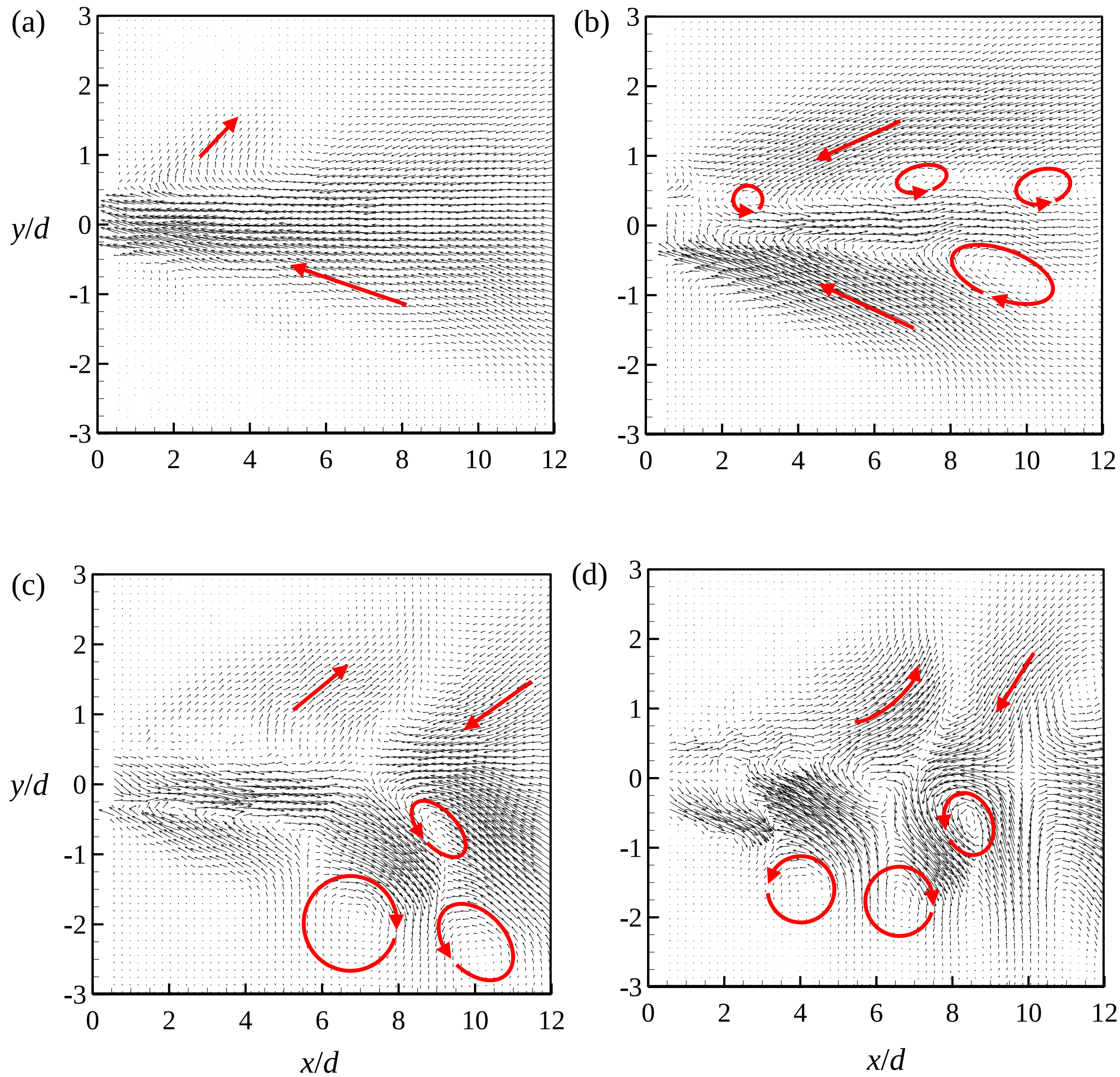

Figure 4.45. Vector plots of the POD modes for *h/d* = 4 in Plane 1: (a) mode 1, (b) mode 3, (c) mode 5 and (d) mode 10.

jet centerline. The fact that the large-scale structure of the jet is retained as far as mode 3 is not unexpected considering the higher fractional energy of mode 3 for *h/d* = 4 than *h/d* = 1. Nevertheless, at successively higher modes, the well-organized large-scale structure is gradually replaced by smaller-scale spanwise vortices, representing the effects of the velocity fluctuations superimposed on the mean motion.

Figure 4.46 shows side by side comparison of the vector plots of the reconstructed flow fields based on modes 1, 5, and 10 in Plane 2. For mode 1, the directions of the vectors for h/d = 1 (Fig. 4.46a) and h/d = 4 (Fig. 4.46b) are opposite to those in Plane 1, mimicking the streamwise periodicity of the most energetic eigenfunction. In Plane 2, the reconstructed field for h/d =1 based on mode 1 shows an extensive region of high-momentum fluid below the jet centerline. This is structurally different from that observed for h/d = 4, which consists of a low-momentum region above the centerline and a high-momentum region below the centerline. The flow fields of mode 5 for h/d = 1 (Fig. 4.46c) and h/d = 4 (Fig. 4.46d) are dissimilar and both are distinctly different from their Plane 1 counterparts. In Plane 2, though, mode 5 produces two counter-clockwise vortices interacting with the free surface for h/d = 1 compared to the disparate zones of uniform momentum in the case of h/d = 4, although the motions induced by the vortices in plane 2 are significantly larger than those in Plane 1. For mode 10 (Figs. 4.46e and 4.46f), only one dominant spanwise vortex core is produced in either case, albeit significantly larger and closer to the center of the field of view for h/d = 4 than h/d = 1.

4.7.4 Reconstructed profiles of Reynolds stresses

The contributions of the first m modes to the Reynolds stresses for h/d = 1 and 4 in the interaction region are shown in Fig. 4.47. Also included for comparison are the original PIV data and profiles reconstructed from the first m modes that captured up to

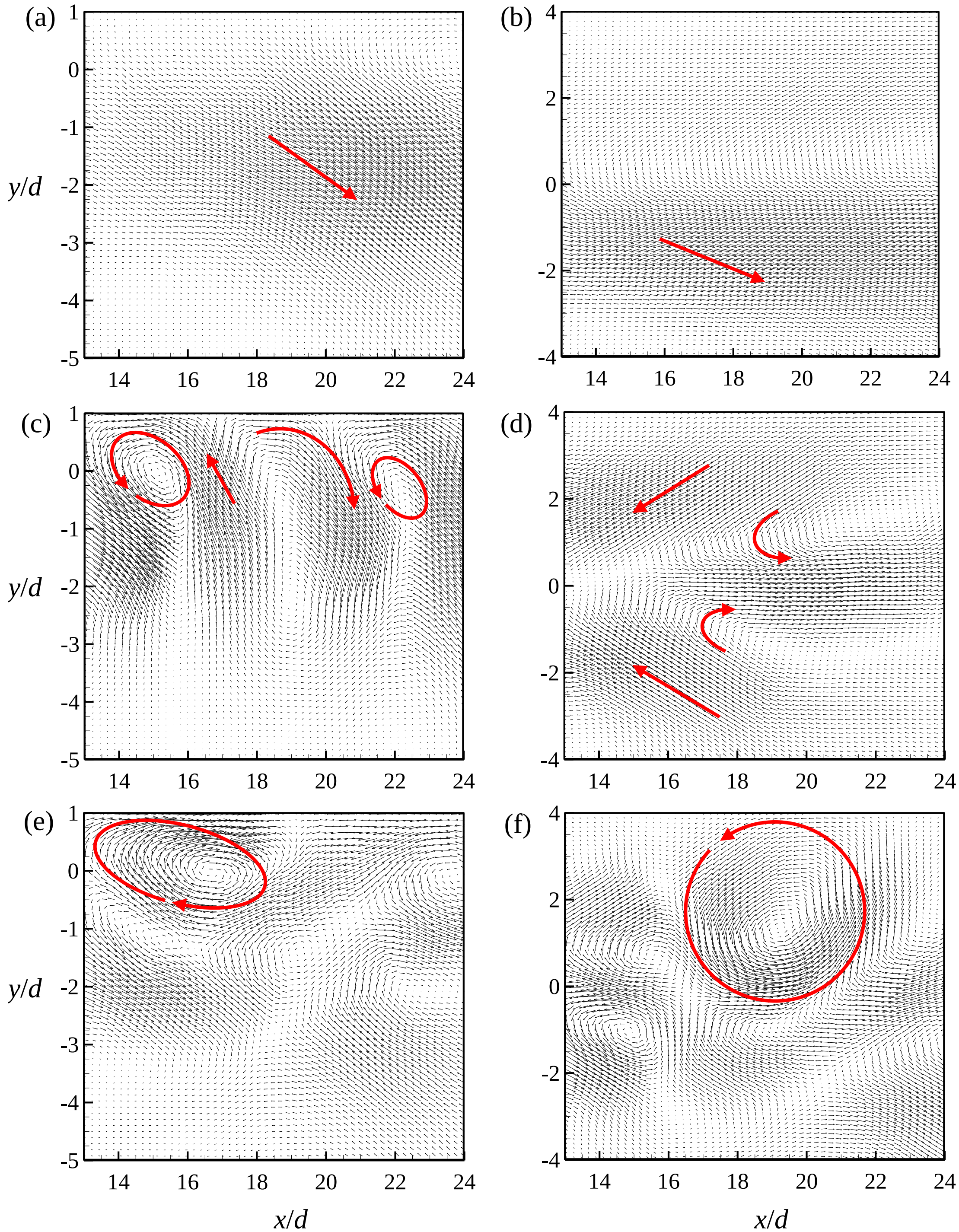

Figure 4.46. Vector plots of POD modes in Plane 2: (a) mode 1 for *h/d* = 1, (b) mode 1 for *h/d* = 4, (c) mode 5 for *h/d* = 1, (d) mode 5 for *h/d* = 4, (e) mode 10 for *h/d* = 1 and (f) mode 10 for *h/d* = 4.

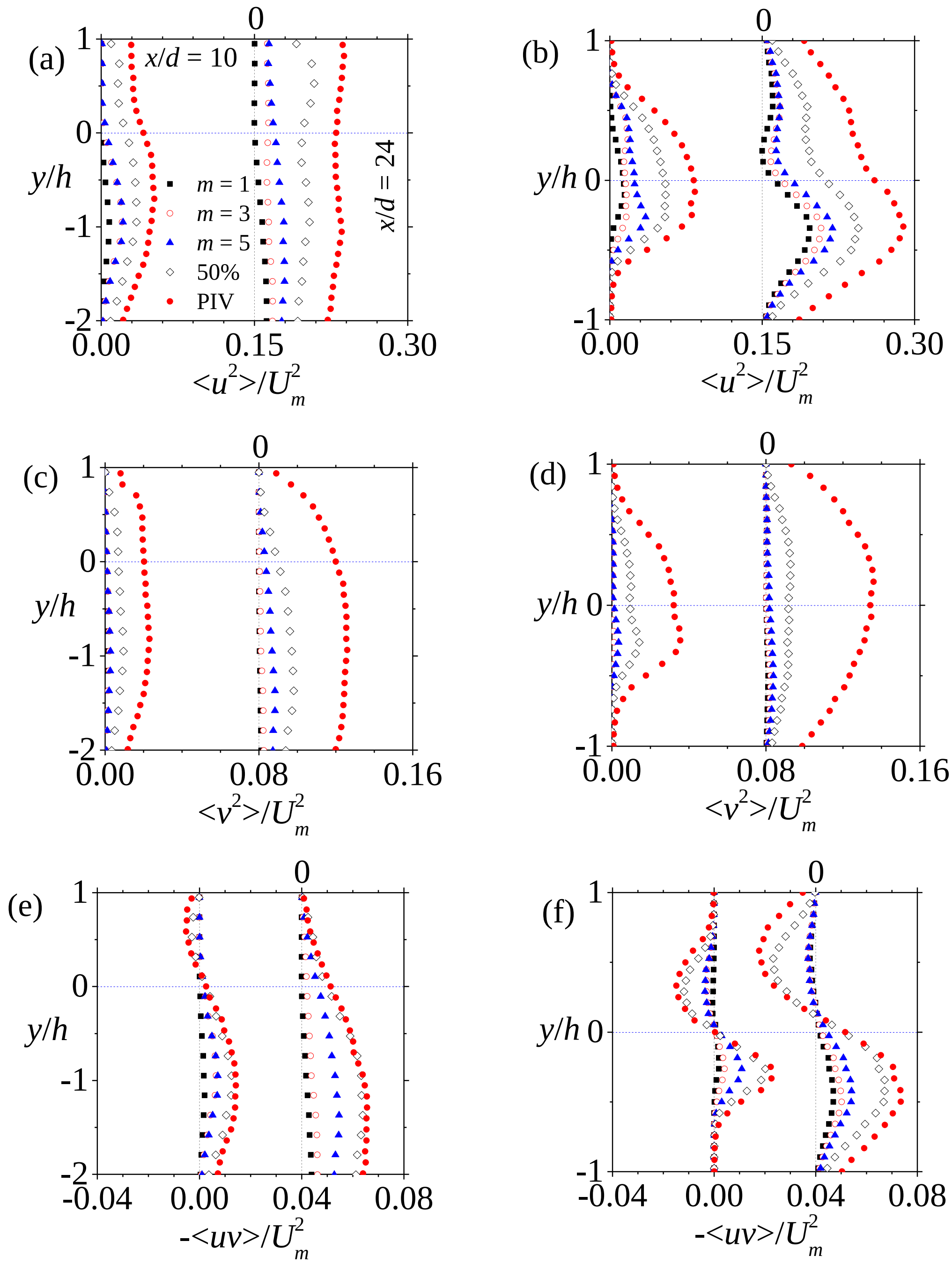

Figure 4.47. Reconstructed profiles of Reynolds stresses for h/d = 1 and 4 for various modes: (a) streamwise Reynolds normal stress for h/d = 1, (b) streamwise Reynolds normal stress for h/d = 4, (c) surface-normal Reynolds normal stress for h/d = 1, (d) surface-normal Reynolds normal stress for h/d = 4, (e) Reynolds shear stress for h/d = 1 and (f) Reynolds shear stress for h/d = 4.

50% of the total energy. As should be recalled, m = 96 and 64 modes are required in order to capture up to 50% of the total TKE for h/d = 1 and 4, respectively, in Plane 1. In Plane 2, these values reduced to approximately m = 23 and 20 modes for h/d = 1 and 4, respectively. The profiles of the streamwise, surface-normal and Reynolds shear stresses for h/d = 1 are shown in Figs. 4.47a, 4.47c and 4.47e, respectively. The results for m = 1, which represents the contribution from the most energetic POD mode are negligibly small, especially in the upper shear layer. Similar results are observed when 3 and 5 modes were used in the reconstruction. With the first 96 modes the normalized streamwise and surface-normal stresses are about 34% - 67% and 60% - 78% lower than the original data, respectively. The surface-normal stress at both streamwise locations converge more slowly to the original data in comparison to the streamwise stress. This is because the lower-order modes (larger-scales), whose effects are explored in the figure, have a greater contribution to the streamwise Reynolds stress than the surface-normal stress, while the higher-order modes (smaller-scales), excluded from the low-order reconstruction are the dominant contributors to the surface-normal stress. On the contrary, a closer agreement is observed in the case of the Reynolds shear stress at both streamwise locations, suggesting that the Reynolds shear stress producing motions are responsible for nearly 50% of the total turbulent kinetic energy in the jet.

For h/d = 4, the data trend remains the same but differences between reconstructed and original data are larger in comparison to h/d = 1. However, the peak values of $\langle u^2 \rangle / U_m^2$ (Fig. 4.47b) are significantly higher in the lower shear layer for h/d = 4 compared to h/d = 1. The deviations observed in the surface-normal stress profiles (Fig.

4.47d) between the reconstructed and original data are even more dramatic than in the streamwise counterparts because the deeper jet increases the size of the larger-scale structures in the decomposition relative to the smaller scales, thus overshadowing the contribution of the smaller scales to the surface-normal stress. This results in a relatively slower convergence of the reconstructed Reynolds shear stress profiles (Fig. 4.47f). For the Reynolds shear stress, convergence at 50% total TKE occurs to within approximately 8% at x/d = 10. Further downstream, more than 20 modes are required for the Reynolds shear stress to converge.

CHAPTER 5

RESULTS AND DISCUSSION ON NOZZLE GEOMETRY EFFECT

The effects of the nozzle geometry on the turbulent characteristics and structures of surface attaching jets are discussed in this chapter. Results obtained from four nozzle geometries of circular, square, Rect_minor and Rect_major are examined. Instantaneous and mean velocity fields and turbulent statistics of up to the fourth order moments are used to characterize the flow. Two-point correlations of velocity fluctuations and swirling strength, joint probability density functions and proper orthogonal decomposition (POD) are used to examine the turbulent structures.

5.1 Flow Visualization

5.1.1 Instantaneous velocity field

Instantaneous velocity vectors are used to examine some qualitative features of the surface attaching jets with various nozzle geometries. Galilean decomposition and linear stochastic estimation (LSE) technique are applied on the velocity fields to explore the effect of nozzle geometry on the spanwise vortices and associated flow fields. It is noted that as the flow topology of the circular and square jet is almost similar, results obtained from the square, Rect_minor and Rect_major are presented.

5.1.1.1 Galilean decomposition

Velocity vectors within the range of streamwise distance, $0 \leq x/d \leq 7$ are shown in Fig. 5.1 that includes near-field and intermediate region of the jets which is significant in mixing and entrainment (Capone, et al., 2013). Galilean decomposition is applied on the velocity fields using a convective velocity of $0.15U_j$ (Agrawal and Prasad, 2002) to expose the vortices roughly at the turbulent-nonturbulent interface (edges of the shear layers in the instantaneous velocity field) where entrainment mechanism takes place (Westerweel et al., 2005). The interface is marked by the zero velocity contour lines which passe through the center of the vortices. As expected, the decomposition reveals anti-clockwise (retrograde) and clockwise rotating (prograde) rotating vortices at the edge of the upper and lower shear layer, respectively. Contours of signed swirling strength are superimposed on the plots to highlight the velocity field associated with spanwise vortex cores. The swirling strength contours coincide with the edges of the shear layers; and are less pronounced at the upper edge compared to the lower edge indicating weaker spanwise vortex cores at the upper shear layer in the presence of a free surface. Furthermore, the surface-normal expansion of the shear layers with the jet development downstream is observed following the zero velocity contour lines. Qualitatively, Rect_minor jet experiences a wider expansion of the shear layers compared to the other nozzle geometries tested, whereas, shear layers of Rect_major jet develops almost parallel to the free surface within the said range of the streamwise distance. A wider expansion of the shear layers of in Rect_minor jet is an indication of enhanced mixing and entrainment of ambient fluid into the jet flow region. Similar observation regarding better mixing and entrainment of

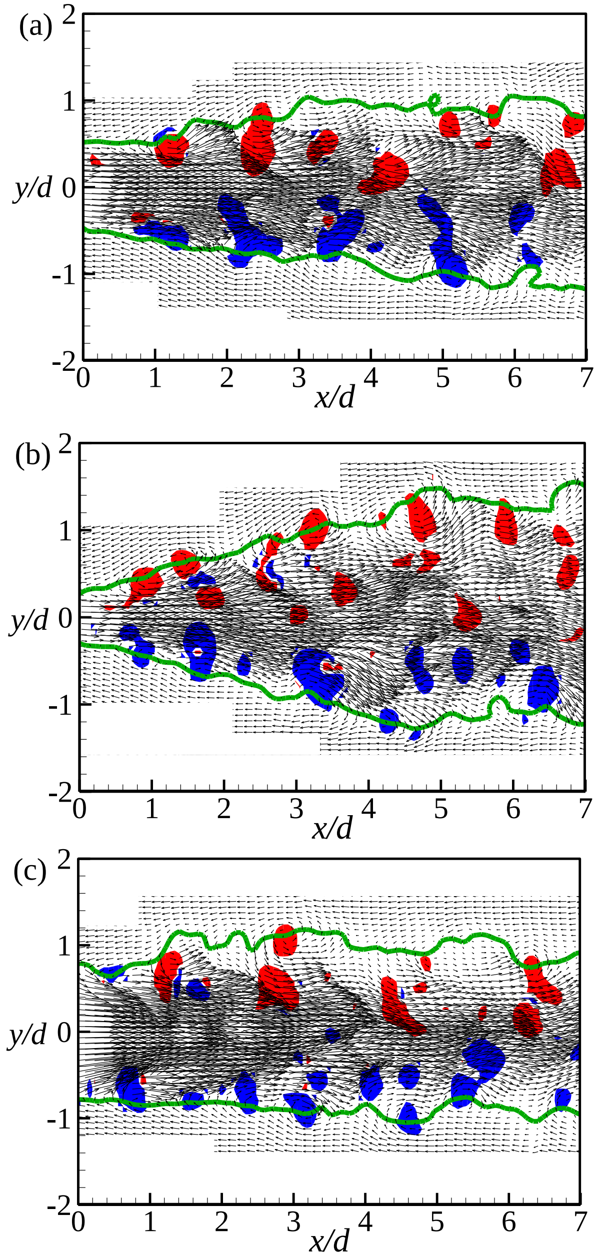

Figure 5.1. Instantaneous velocity field for (a) square, (b) Rec_minor and (c) Rec_major jet.

Rect_minor jet in the *x*-*y* plane in comparison to circular or square jets were reported in a previous free jet study (Aleyasin et al., 2017a).

5.1.1.2 Linear stochastic estimation

To determine the average flow structure associated with the vortex cores exposed from the Galilean decomposition at the edges of the shear layers, conditional averages of the flow fields are calculated using linear stochastic estimation (LSE). LSE is performed at the event location of x/d = 1 at the edges of the shear layer ($y_{ref}/d \approx \pm 0.75$) focusing on the near field region, $0 \leq x/d \leq 4$, due to its significance in vortex generating instability mechanism. Results obtained from the upper and lower shear layer of the square, Rect_minor and Rect_major jets are shown in Fig. 5.2. The velocity vectors are normalized by their corresponding magnitudes to avoid wiping out of the weaker motions away from the event location (Christensen and Adrian 2001). In the figure, the dot indicates the event locations; the solid and dashed circles indicate anti-clockwise (retrograde) and clockwise (prograde) rotating vortices, respectively. In the upper shear layer, a retrograde vortex is identified at the event location (Figs. 5.2a, 5.2c and 5.2e). This is accompanied by the detection of one or more retrograde vortices farther downstream along the edge of the shear layer. These and the primary (event) vortex are demarcated by the red circles. The LSE also exposed spanwise vortex cores (demarcated by blue circles) in the lower shear layer, which are the clockwise-rotating counterparts of those in the upper shear layer. The counter rotating vortex pairs imply typical generation of vortex ring in near field region of the jet (Tandalam et al., 2010). In the vector fields of the square and Rect_minor jets, the vortex size is growing with the outward growth of the shear layer. These results are consistent with those observed in the Galilean decomposition. Comparison of the LSE results from the various geometries suggest that

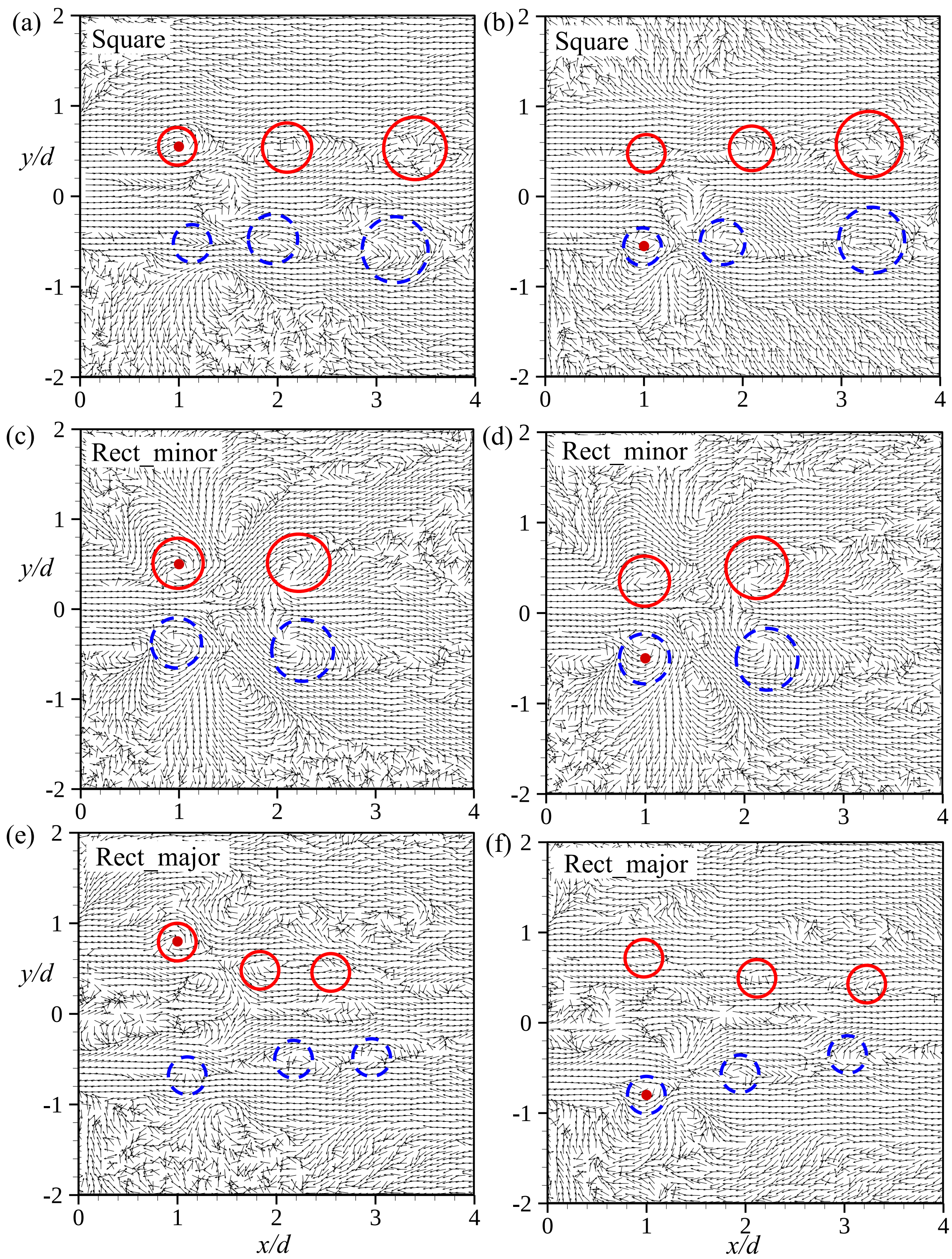

Figure 5.2. LSE at x/d = 1: (a) Square jet in the upper shear, (b) square jet in the lower shear, (c) Rect_minor jet in the upper shear, (d) Rect_minor jet in the lower shear, (e) Rect_major jet in the upper shear and (f) Rect_major jet in the lower shear layer.

relatively fewer vortices were exposed in the Rect_minor jet. This is because the vigorous near-field mixing of the Rect_minor jet reduces the spatial coherence of the vortical structures, preventing their detection by the conditional averaging. However, the production of incoherent turbulence in the near field of the Rect_minor jet will cause enhancements in corresponding turbulence intensities. The LSE plot in Fig. 5.2e shows that the effect of the major-axis orientation of the rectangular nozzle is to inhibit the streamwise growth of the structures in the near-field region. As illustrated in the plot, this can be attributed to the initial contraction of the jet. With relocation of the event to the lower shear layer (Figs. 5.2b, 5.2d and 5.2f), a prograde vortex is detected at the event location. In the square and Rect_minor jets, the same conjugate pairs of spanwise vortices are exposed by the LSE as before when the event was located in the upper shear layer. However, in the major plane of the rectangular nozzle, there is a slight streamwise shift in the location of the vortices in the upper shear layer relative to their mates in the lower shear layer. This is an artefact of the "axis-switching", a well-known phenomenon that generally occur in non-circular jets (Chen and Yu, 2014; Aleyasin et al., 2017a, 2017b), as mentioned in Section 2.4.2, in the major plane of the rectangular nozzle.

5.1.2 Contours of mean velocity and turbulent quantities

5.1.2.1 Streamwise and surface-normal mean velocity

Iso-contours of streamwise and surface-normal mean velocities for the square, Rect_minor and Rect_major jets are shown in Fig. 5.3. The free surface is located at the top of each plot (y/d = 2). From the contours of streamwise mean velocity, U/U_j (Fig. 5.3a, 5.3c and 5.3e), a rapid expansion of the shear layers of Rect_minor jet compared to the

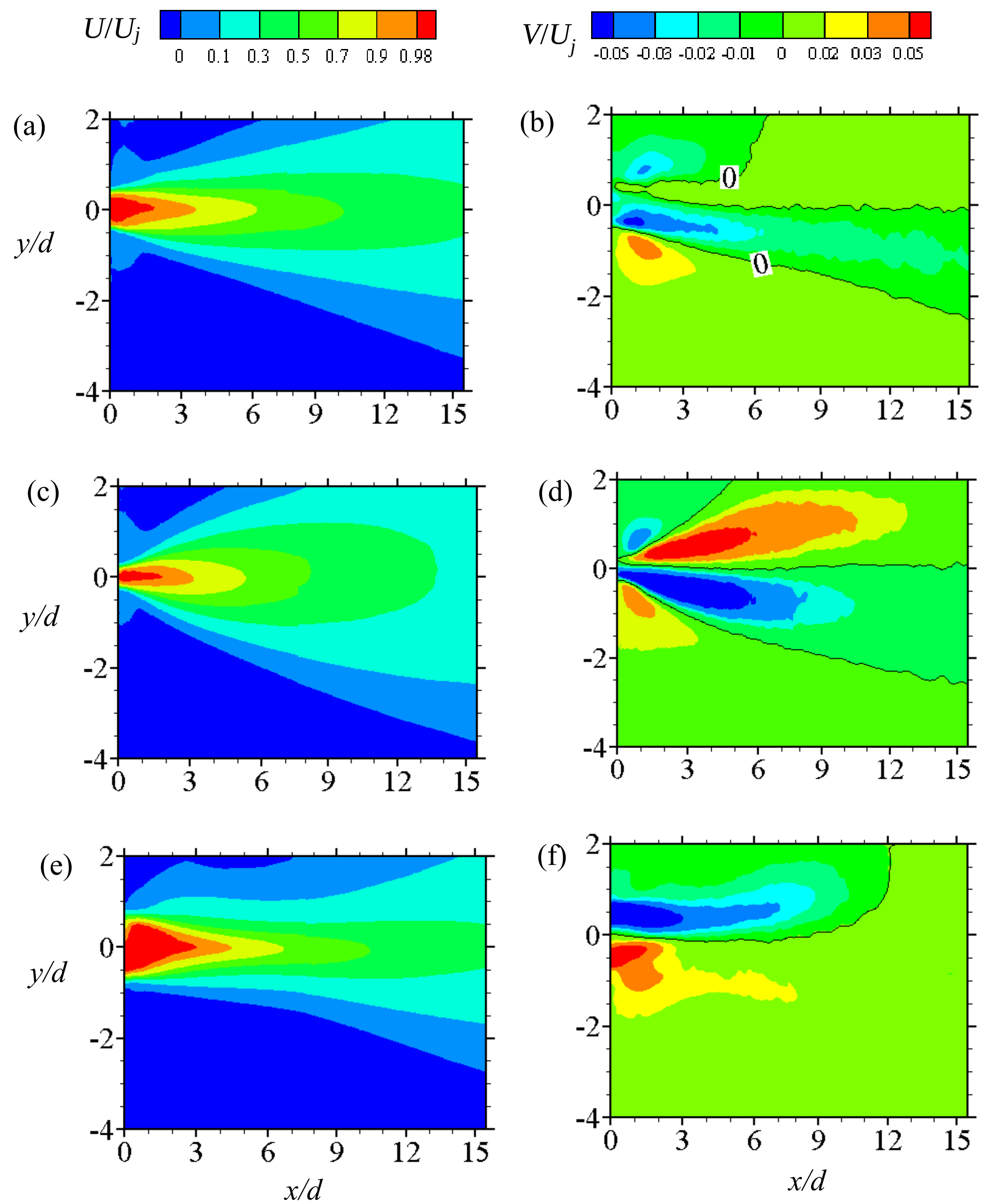

Figure 5.3. Iso-contours of streamwise and surface-normal mean velocities: (a) Streamwise mean velocity of square jet, (b) surface-normal mean velocity of square jet, (c) streamwise mean velocity of Rect_minor jet, (d) surface-normal mean velocity of Rect_minor jet, (e) streamwise mean velocity of Rect_ major jet, and (f) surface-normal mean velocity of Rect_ major jet.

Table 5.1. Summary of the potential core length and attachment length for various nozzle geometries.

Geometry	L_p/d	L_a/d
Circular	3.0	6.4
Square	2.0	6.4
Rect_minor	2.0	4.8
Rect_major	3.0	7.7

other nozzle configurations, as observed in the instantaneous velocity field (see Fig. 5.1), is evident. The potential core region of the jets within which streamwise mean velocity remains up to approximately 98% of the jet exit velocity (Aleyasin et al., 2017a), are visible in the plots. The streamwise lengths of the potential core, L_p for the four nozzle configurations are estimated and summarized in Table 5.1. Shorter potential core lengths of square and Rect_minor jet (approximately up to 33%) compared to circular one reflect enhanced near-field mixing for non-circular jets as reported previously for free jets (e.g., Aleyasin et al., 2017a; Mi and Nathan, 2010). Larger potential core length of Rect_major jet supports reduced near-field mixing compared to Rect_minor jet. In the Rect_major jet (Fig. 5.3e), a characteristic surface-normal contraction (convergence) occurs in the contours mainly in the core jet within $0 \leq x/d < 6$, which can be attributed to the axis-switching of the jet for this nozzle orientation. A similar axis-switching phenomenon was reported in the major planes of non-circular jets by Aleyasin et al. (2017a, 2017b), Chen and Yu (2014). The interaction between the upper shear layer of the jets and the free surface is visible in the plots. The mean attachment point (AP) is located using the following three approaches: (i) the streamwise location where the zero-velocity contour attaches to the free surface, (ii) the location where the contour of $U/U_j \approx 0.0125$ (minimum streamwise mean velocity level obtained from the dynamic range of the PIV system) attaches to the free surface, and (iii) the location where streamwise mean velocity starts increasing from $U/U_j \approx 0.0125$ in the U/U_j profile along the free surface. The variations in attachment lengths (L_a) determined using these approaches are not more than ± $0.3d$, which is within measurement uncertainty. The value of L_a/d determined from the contour level of $U/U_j \approx 0.0125$ are summarized in Table 5.1, and it is clear that circular and square jets show similar attachment length due to their similar growth characteristics. A shorter attachment length of Rect_minor jet (approximately 25%) is consistent with its rapid expansion of shear layers which start interacting with the free surface earlier compared to the circular jet. The larger attachment length of Rect_major jet can be attributed to reduced expansion of the shear layer which delays the onset of jet-free surface interaction. The present value of the attachment length of square jet is approximately 22% larger than the value reported by Sankar et al. (2008) for surface attaching square jet with similar offset height ratio (h/d = 2) but considerably higher Reynolds number of 40000. It should be noted that Sankar et al. (2008) determined the attachment length of the jet onto the free surface from visual observation. Since the Reynolds number effect on the attachment length in the present study (Appendix B) suggests that the attachment length is nearly independent of Reynolds number for $Re \geq 3700$, the differences in the attachment lengths in the present result and those from Sankar et al. (2008) can be partially attributed to the different methods used to estimate the attachment length.

The surface-normal expansion of the shear layers of the jets is further investigated using surface-normal mean velocity (V/U_j) contours (Fig. 5.3b, 5.3d and 5.3f). The zero-velocity contour lines, as shown in the plots, demarcate the positive and negative *V* in the flow field. For the square and Rect_minor jets, *V* is positive and negative in both halves of the shear layer. In those cases, positive and negative values of *V* in the region with upper shear layer ($y/d > 0$) correspond to outward expansion of that shear layer and inward entrainment of ambient fluid, respectively. As expected, the direction of *V* changes in the lower shear layer ($y/d < 0$). On the contrary, the *V* contours in the Rect_major jet are predominantly negative in the upper shear layer and positive in the lower shear layer. This would imply that the axis-switching of the Rect_major jet and the concomitant contraction of the jet result in entrainment of ambient fluid into jet. Also, higher positive and negative *V* in the upper and lower shear layer, respectively over larger streamwise distance for Rect_minor jet, indicate a faster outward expansion of the shear layers.

5.1.2.2 Reynolds shear stress and turbulent kinetic energy

The contours of Reynolds shear stress, $-\langle uv \rangle / U_j^2$ are presented in Fig. 5.4a, 5.4c and 5.4e for the three cases. The Reynolds shear stress is predominantly negative in the upper shear layer and positive in the lower shear layer. This is consistent with the direction of the mean streamwise velocity gradient ($\partial U/\partial y$) in the shear layers. Because they represent the mixing zones in the shear layers, the distributions mimic the outward spread of the jet. In all cases, the maximum Reynolds shear stress occurs at the edge of the shear layer, where $\partial U/\partial y$ is a maximum, and is it located in the near field region. The proximity

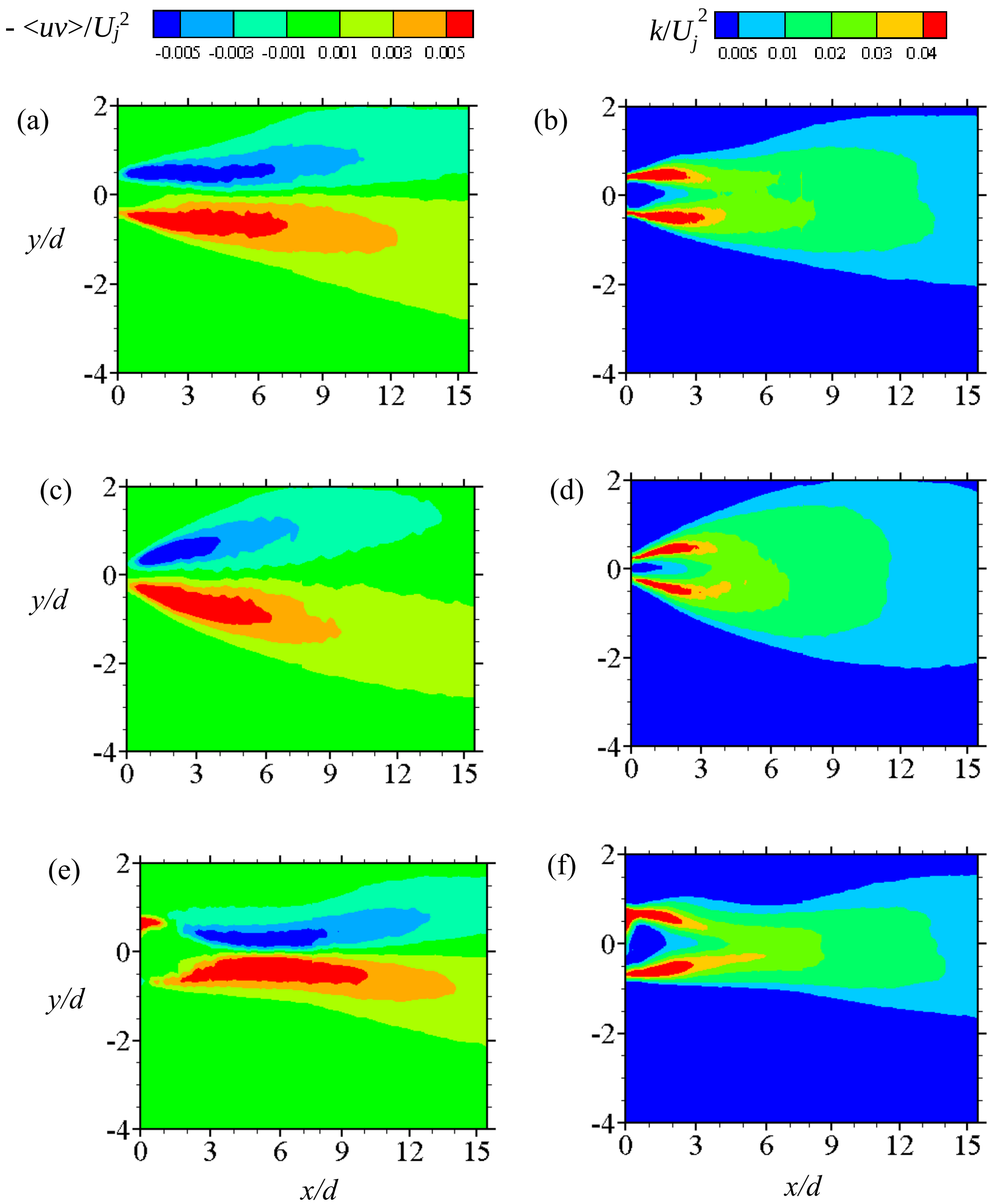

Figure 5.4. Iso-contours of Reynolds shear stress and turbulent kinetic energy: (a) Reynolds shear stress of square jet, (b) turbulent kinetic energy of square jet, (c) Reynolds shear stress of Rect_minor jet, (d) turbulent kinetic energy of Rect_minor jet, (e) Reynolds shear stress of Rect_ major jet, and (f) turbulent kinetic energy of Rect_ major jet.

of the maximum Reynolds shear stress to jet exit is consistent with the idea that the near field is the most dominant region for mixing. The effect of the free surface is to reduce the area of significant Reynolds shear stress in the upper shear layer relative to the lower shear layer. The effect of using the rectangular (Rect_minor) nozzle is to broaden the region of significant Reynolds shear or create larger mixing zones in the shear layers in comparison to the square and circular nozzles. In the near field zone, this is noticeable as a wider angle of divergence of the maximum contours from the axis. Re-orientation of the rectangular nozzle caused an inward shift of the maximum Reynolds shear stress contours towards the axis and away from the exit plane. This behaviour is attributable to the axis-switching in the major plane of the rectangular jet. It is worth pointing out that a sign change of Reynolds shear stress in the upper shear layer of Rect_major jet within $0 \leq x/d \leq 1$ can be an indication of axis-switching (Aleyasin et al., 2017b). The Reynolds shear stress contours herein provide a further indication that, among all three geometries, the Rect_minor configuration is the most resilient to the reduction in spreading and mixing performance by the free surface.

Figures 5.4b, 5.4d and 5.4f show the contours of the turbulent kinetic energy, k/U_j^2 for the three jets. As mentioned in Chapter 4, the turbulent kinetic energy is approximated as $k = 0.5(<u^2> + 2<v^2>)$, assuming $<v^2> \approx <w^2>$ as per previous three-dimensional free jet study (Hussein et al., 1994) and surface attaching jet study (Anthony and Willmarth, 1992), where w is spanwise fluctuating velocity component (not measured in the present planar PIV experiment). The turbulent kinetic energy is negligible within the potential core of the jet; and has maximum values at the edge of the shear layer. The maximum values occur close to the exit of the jet because of the high turbulence intensity associated with the Kelvin–Helmholtz structures in the near field of the jet. The maximum energy values lie within a narrow band, whose streamwise extent is slightly smaller in the upper shear layer than the lower shear layer. This is similar to the reduced mixing zone in the upper shear layer caused by the confinement in relation to the lower shear layer. In each case, a large region of significant turbulent kinetic energy is observed downstream of the potential core. The turbulent kinetic energy region is considerably larger for Rect_minor than the other cases. In the near field of the Rect_minor jet, the contours of maximum turbulent kinetic energy mimic the wider angle of inclination that was observed for the Reynolds shear stress. This is another indication of a more rapid near field mixing in the Rect_minor jet in comparison to the square and Rect_major jets. The results also indicate a more energetic flow near the free surface of the Rect_minor jet, with significant turbulent kinetic energy appearing at the free surface soon after attachment when compared to the square and Rect_major jets.

5.2 Streamwise Evolution of Local Maximum Mean Velocity, Half-Velocity Width and Centerline Turbulence Intensities

The streamwise development of the jet is characterized by the decay of the local maximum streamwise mean velocity, half-velocity width and turbulence intensities along the jet centerline. The mixing and entrainment capability of the jets are reflected in these mean and turbulent quantities. The effects of the nozzle geometry on these quantities are discussed below:

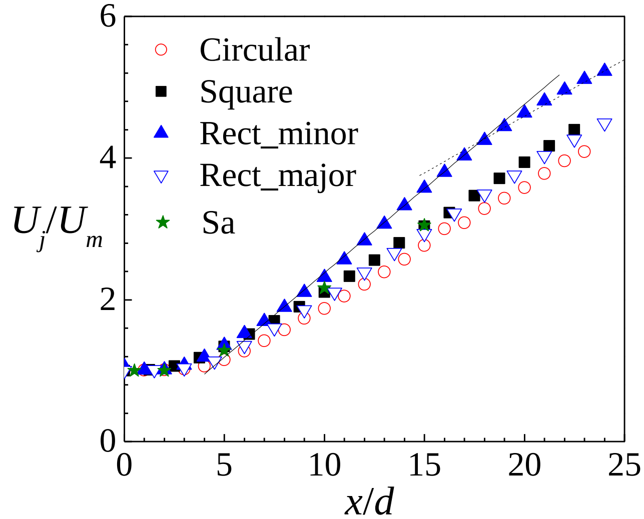

Figure 5.5. Streamwise variation of maximum velocity decay. Sa = Sankar et al. (2008). The straight lines are least-squares fit on the profiles.

5.2.1 Local maximum mean velocity decay

The variation of local maximum streamwise mean velocity (U_j/U_m) with streamwise distance is shown in Fig. 5.5. Data obtained from a surface attaching square jet study by Sankar et al. (2008) with a similar offset height ratio (h/d = 2) is included for comparison. As expected, results about the potential core length is reflected in the profiles showing negligible variation of U_m within the potential core region ($0 \leq x/d < 3$). Further downstream, U_j/U_m increases almost linearly as U_m is reduced by the entrainment and mixing of the jet. The present result of square jet shows good agreement with the result of Sankar et al. (2008). The decay rate is estimated by the following least-squares linear fit (Equation 1.1) to the U_m profiles:

$$U_j/U_m = K_d\,(x/d - x_0/d)$$

Table 5.2. Summary of the decay rate for various nozzle geometries.

Geometry	K_d	**Range (x/d)**
Circular	0.170	$5 \leq x/d \leq 24$
Square	0.176	$5 \leq x/d \leq 24$
Rect_minor	0.238, 0.160	$5 \leq x/d \leq 18$, $18 \leq x/d < 24$
Rect_major	0.176	$5 \leq x/d \leq 24$
Circular (Aleyasin et al., 2017b)	0.200	$6 \leq x/d \leq 14.5$
Circular (Madnia and Bernal, 1994)	0.162	$x/d \geq 12$
Square (Sankar et al., 2008)	0.176	$5 \leq x/d \leq 15$

where, K_d denotes the decay rate. A summary of the decay rates and the range of streamwise distance over which they were estimated is given in Table 5.2, for the four geometries. The decay rates of the square, circular and Rect_major jets are comparable, but these values are 26% - 29% lower than that of the Rect_minor jet. The decay rate of the circular jet is approximately 15% slower than the free circular jet studied by Aleyasin et al. (2017b) using a similar orifice nozzle at Re = 17000. The slower decay rate of the surface attaching circular jet could be attributed to the reduced entrainment from the upper side of the jet by the confinement. This effect was also observed in other studies (e.g., Madnia and Bernal, 1994). Compared to the circular jet, the Rect_minor jet enhanced the velocity decay rate by approximately 30% within the range $5 \leq x/d \leq 18$. This is consistent with the more rapid expansion, faster spreading and enhanced mixing capability of the

Rect_minor jet compared to other configurations. In the far field of the interaction region (x/d > 18), the Rect_minor decay rate declines by approximately 33%. This is marked by a characteristic change in slope of the decay curve and represents a reduction in entrainment as the jet momentum is used to accelerate the surface flow. Similar far-field declines were reported by Madnia and Bernal (1994). It is worth noting that for the Rect_minor jet, the region experiencing diminished rate of maximum mean streamwise velocity decay implies its stronger interaction with the free surface.

5.2.2 Half-velocity width

The profiles of the half-velocity width ($y_{0.5}/d$), which is often used to quantify the jet spread, are shown in Fig. 5.6a. Downstream of the potential core, the spreads of the square, circular and Rect_minor jets are approximately linear. For the Rect_major jet, on the other hand, there is an initial shrinkage of the jet due to the axis-switching effect. The location of the axis-switching is defined following the approach by Aleyasin et al. (2017a) as the intersecting location of the $y_{0.5}/d$ profile for Rect_minor and Rect_major. The axis-switching location is estimated as $x/d \approx 2.5$. This reduces the half width in the near field region ($0 \leq x/d \leq 6$) of the Rect_major configuration. Even though the spread of the jet is restored after the initial region, it does not fully recover to that of the Rect_minor jet. This behaviour of the half-width distribution in the major plane of the rectangular jet is common in asymmetric nozzles oriented in the major axis (e.g., Aleyasin et al., 2017a, 2017b). It is noted that the present value of the axis-switching location lies within the range of x/d = 1 to 3.5 reported in previous rectangular and elliptical orifice and contoured jets (Hussain and Husain, 1989; Aleyasin et al., 2017a). The spread rate for

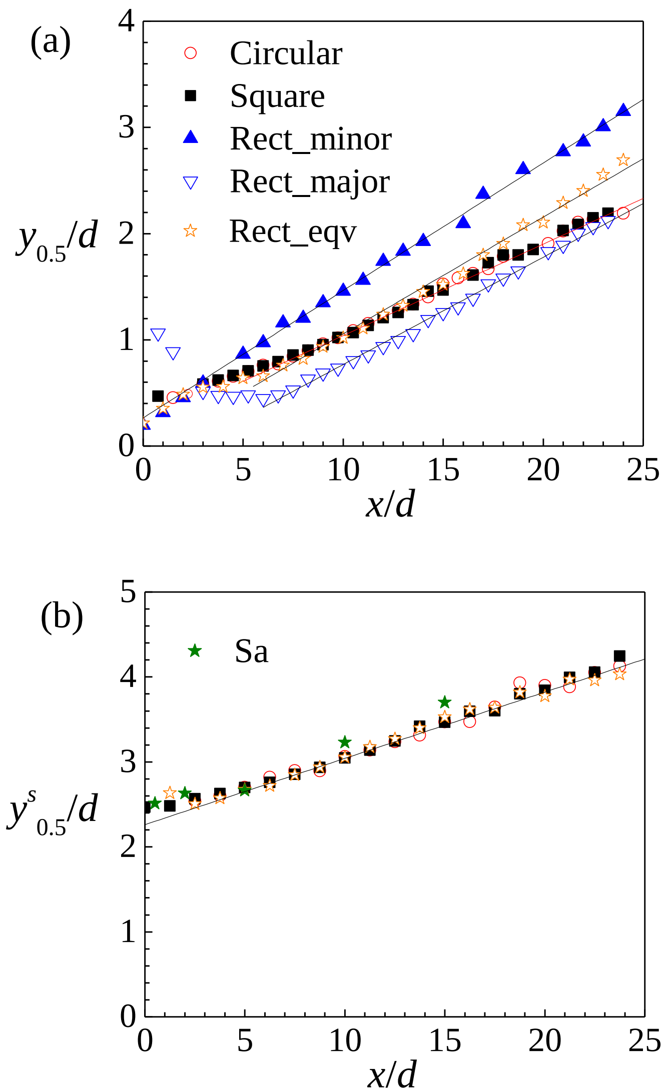

Figure 5.6. Streamwise variation of (a) half velocity width measured from the location of U_m, and (b) half velocity width measured from the free surface. Sa = Sankar et al. (2008). The straight lines are least-squares fit on the profiles.

different nozzle geometries is estimated by the following least-squares linear fit (Equation 1.3) to the $y_{0.5}$ profiles:

$y_{0.5}/d = K_s\,(x/d - x_g/d)$

Table 5.3. Summary of the spread rate for various nozzle geometries.

Geometry	$\boldsymbol{K_s}$	**Range ($\boldsymbol{x/d}$)**
Circular	0.086	$5 \leq x/d \leq 24$
Square	0.086	$5 \leq x/d \leq 24$
Rect_minor	0.120	$0 \leq x/d \leq 24$
Rect_major	0.101	$6 \leq x/d \leq 24$
Rect_eqv	0.110	$6 \leq x/d \leq 24$
Circular (Wygnanski and Fiedler, 1969)	0.088	$25 < x/d < 90$
Square (Quinn and Militzer, 1988)	0.087	$9.8 \leq x/d \leq 22.4$

where, K_s denotes the spread rate. A summary of the spread rate and the range of streamwise distance within which the spread rate is estimated is provided in Table 5.3. The spread rates of the circular and square jets are similar, which speaks to the nearly similar downstream evolution of both jets. These values are comparable to values of $K_s \approx$ 0.087 (Quinn and Militzer, 1988) and $K_s \approx 0.088$ (Wygnanski and Fiedler, 1969) reported for free square and round jets, respectively. For the Rect_minor configuration, however, the spread rate is enhanced by approximately 40% in comparison to the square and circular jets. In the major plane of the rectangular this enhancement is reduced by approximately 8% so that the net gain in spread rate is approximately 28% in comparison to the square and circular jets. An equivalent half-velocity width, $(y_{0.5})_{eqv}$, is often defined for asymmetric nozzles to provide an "average" spread rate of the jet (e.g., Mi et al., 2010; Xu et al., 2013). This corresponds to a hypothetical equivalent rectangular jet (Rect_eqv) with spread rate given by (Mi et al. 2010):

$$\left(y_{0.5}\right)_{\text{eqv}} = \sqrt{\left(y_{0.5}\right)_{\text{minor}} \times \left(y_{0.5}\right)_{\text{major}}} \tag{5.1}$$

where $(y_{0.5})_{minor}$ and $(y_{0.5})_{major}$ denote the half velocity widths in the minor and major planes of the rectangular jet, respectively. The spread rate of Rect_eqv is intermediate to those of the Rect_minor and Rect_major jets because it represents the geometric mean of both spreading rates. However, it is approximately 8% higher than the spread rate of the Rect_major jet and exceeds the spread rate of the square and circular jets by 22%. The higher spread rate of Rect_eqv, which represents the average growth of the lower shear layer, is consistent with similar rapid growth of rectangular free jets studied in the past (Aleyasin et al., 2017a) compared to square and circular jets.

As shown in Fig. 5.6b, when the half velocity width is measured relative to the free surface ($y^s_{0.5}$), the current profiles and that of Sankar et al. (2008) collapse reasonably well on to the same line. The slope of the line was estimated to be approximately 0.078, which is in good agreement with that reported for confined round jets by Madnia and Bernal (1994).

5.2.3 Turbulence intensities along the jet centerline

The streamwise ($<u^2>^{0.5}$) and surface-normal ($<v^2>^{0.5}$) turbulence intensities along the jet centerline are shown in Fig. 5.7 with different scaling parameters. For reference, experimental data from the literature, including free jets (Quinn and Militzer, 1988; Hussain and Husain, 1989; Xu and Antonia, 2002; Quinn, 2007; Mi and Nathan, 2010; Aleyasin et al. 2017a) and confined jets (Madnia and Bernal, 1994; Sankar et al., 2008) are added. In the plots, various turbulence intensity scaling options are used to test

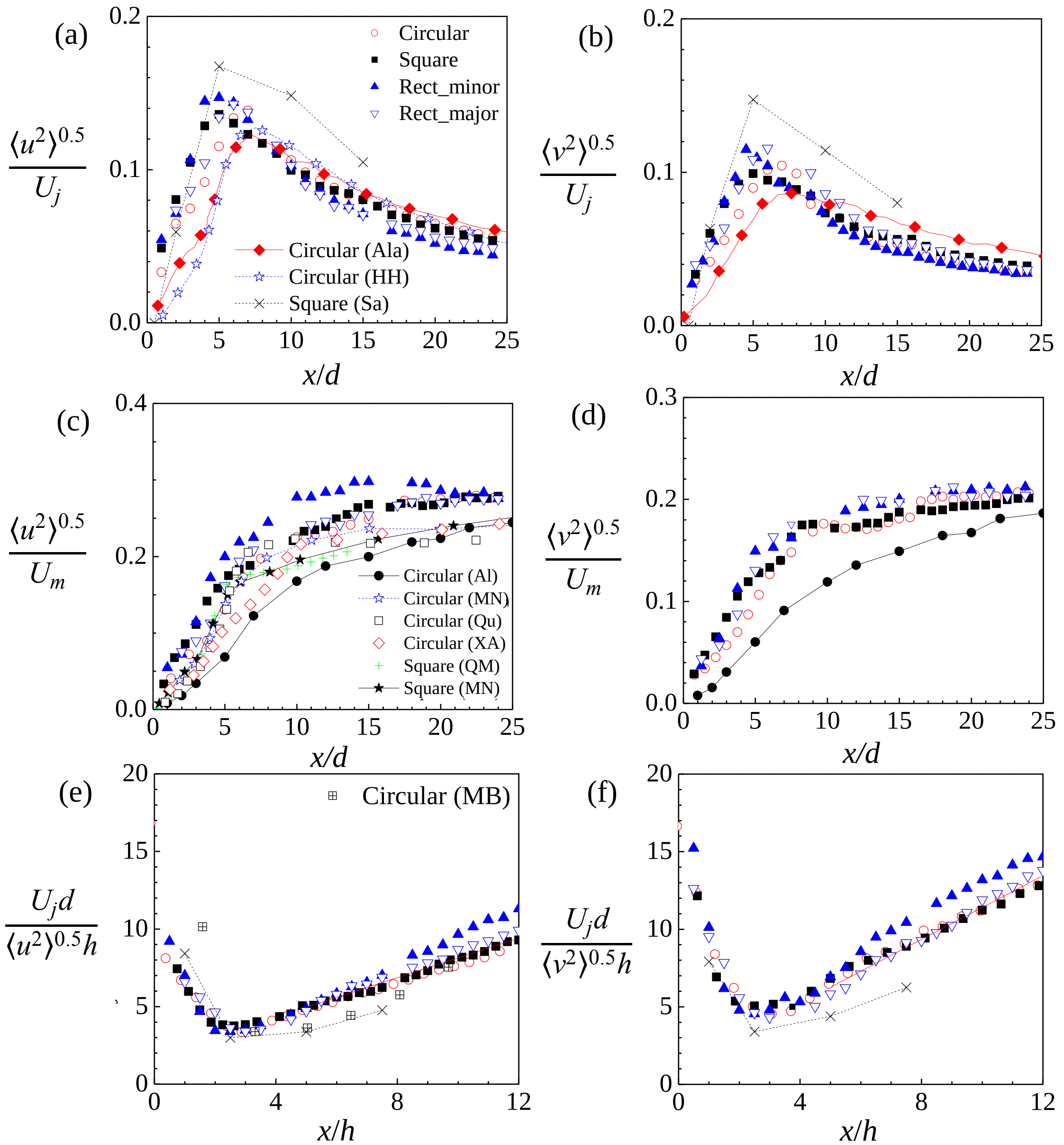

Figure 5.7. Streamwise evolution of the turbulence intensities along the jet centerline: (a) Streamwise turbulence intensity normalized by U_j, (b) surface-normal turbulence intensity normalized by U_j, (c) streamwise turbulence intensity normalized by U_m, (d) surface-normal turbulence intensity normalized by U_m, (e) streamwise turbulence intensity normalized by similarity variables and (f) surface-normal turbulence intensity normalized by similarity variables. Ala = Aleyasin et al., 2017a; HH = Hussain and Husain, 1989; Sa = Sankar et al., 2008; Al = Aleyasin et al., 2018; MN = Mi and Nathan, 2010; Qu = Quinn, 2007; XA = Xu and Antonia, 2002; QM = Quinn and Militzer, 1988; MB = Madnia and Bernal, 1994.

the collapse of the data. The profiles of streamwise and surface-normal turbulence intensities normalized by the jet exit velocity are shown in Figs. 5.7a and 5.7b, respectively. A steep increase is observed in both turbulence intensities in the near field region ($0 < x/d < 5$). This increase is caused by the large-scale coherent structures arising from the Kelvin-Helmholtz instability of the shear layer in the initial region (Ball et al., 2012). As the structures grow with streamwise distance, they generate high turbulence intensity by causing steep gradients in the mean velocity in the upper and lower shear layers (Quinn and Azad, 2013), and they help to transport the turbulence by convection and diffusion to the centerline of the jet. The distributions reach peak values near their respective ends of the potential core and decrease monotonically to relatively low intensity levels in the far field region. It has been reported (e.g., Quinn, 1992) that the peak centerline turbulence intensities are due to the large velocity fluctuations that accompany merging of the large-scale structures at the end of the potential core. The rectangular nozzle with minor-axis orientation causes the largest peak in the streamwise turbulent intensity and the fastest decay in its magnitude in the far field region (Fig. 5.7a). This is tied to the more rapid near field mixing in the minor plane of the rectangular nozzle. The far field decay of the centerline turbulent intensity in the square and circular jets is nearly similar but is more gradual in comparison to the rectangular nozzle. In the major plane of the rectangular nozzle there is no significant modification in the peak value of the centerline turbulent intensity but for a slight downstream shift in the location of the peak value. This shift is due to the axis-switching in the major plane of the rectangular jet. The results indicate that the far field decay of the streamwise turbulence intensity is independent of the nozzle orientation. Within the potential core no significant differences are observed between the profiles of the square and rectangular jets. However, this near field similarity does not extend to the circular jet. Instead, there is a persistent decline in centerline turbulence intensity with the circular nozzle in comparison to the square and rectangular nozzles. This discrepancy can be explained by the non-circular cross section of the square and rectangular nozzles. Comparing the square and circular jets, for example, there will be additional turbulence generated by the square nozzle due to the self-induced deformation of the vortex rings caused by the non-uniform azimuthal curvature of the square cross section. Similar observations were reported by previous studies comparing the near field dynamics of non-circular and circular nozzles (Grinstein et al., 1995; Hassan and Meslem, 2010). The profiles of the present square and Rect_minor jets are in reasonably good agreement with that of Sankar et al. (2008) within the potential core region. Compared to the free round jets from the literature, the present confined circular jet shows values that are about 30% - 50% higher in the near field region. Further out, the centerline streamwise turbulence intensity of the confined and free circular jets collapse. The comparatively larger peak value measured by Sankar et al. (2008) can be attributed to differences in upstream conditions between this and that study. These differences include their use of a smoothly contracting square nozzle, an exit Reynolds number of 40000 and a Froude number of 1.13. As shown in Fig. 5.7b, the near field growth of the centerline surface-normal turbulence intensity with streamwise distance follows the same trend as the streamwise counterpart. In the interaction region, the streamwise decay of centerline surface-normal turbulence intensity is independent of nozzle geometry and orientation. Within the intermediate region, $5 \leq x/d \leq 10$, the re-orientation of the rectangular nozzle caused a similar displacement of the location of the peak value as streamwise turbulence intensity, as well as up to approximately 18% increase in the turbulence intensity in comparison to the Rect_minor configuration. In the interaction region, the surface-normal turbulence intensity of the confined jets is significantly reduced in comparison to the free jet.

Figures 5.7c and 5.7d show the streamwise evolution of the centerline streamwise and surface-normal turbulence intensities, respectively, normalized by the local maximum mean streamwise velocity. In the region $0 < x/d < 5$, where the centerline turbulence intensities rise rapidly, and the local maximum velocity is relatively constant, $<u^2>^{0.5}/U_m$ and $<v^2>^{0.5}/U_m$ are increasing functions of streamwise distance. In the intermediate region ($5 < x/d < 10$), the rapid increase in the normalized turbulence intensities is diminishing because the decrease in U_m is far outweighed by the decay in the centerline turbulence intensities. The profiles of $<u^2>^{0.5}/U_m$ and $<v^2>^{0.5}/U_m$ level off in the interaction region, reaching asymptotic values of approximately 28% and 20%, respectively. The streamwise turbulence intensity profiles of the square, circular and Rect_major jets are similar. However, the large mean streamwise velocity decay in the interaction region of the Rect_minor jet (see Fig. 5.5) increases $<u^2>^{0.5}/U_m$ within $5 < x/d < 20$. This is another indication of the more vigorous mixing of the jet in the minor plane of the rectangular nozzle compared to the square, circular and Rect_major configurations. On the contrary, use of the velocity scale U_m collapses the centerline surface-normal turbulence intensities among the various confined jets fairly well. The present centerline turbulence intensity data mimic the streamwise evolution of the data from the literature but the asymptotic values of $<u^2>^{0.5}/U_m$ and $<v^2>^{0.5}/U_m$ are approximately 11% higher than those reported in the free jets shown in the plots. The larger values in the present study can be partly attributed to higher turbulence intensity due to limiting momentum transfer for the jet confined by a free surface.

Figures 5.7e and 5.7f explore similarity scaling of the centerline turbulence intensities. Here, the turbulence intensities are normalized by the velocity scale, $U_j d/h$, proposed by Madnia and Bernal (1994), while the streamwise distance is normalized by the offset height. The profiles have a negative slope in the near field region and a positive slope farther downstream. These are due to the near field increase and far field decay of the turbulence intensities, respectively. The profiles collapse fairly well in both the near and far field regions, except for a slight increase in slope in the far field region in the minor plane of the rectangular jet. The positive slopes of the curve were obtained from least-squares line fits to the profiles within $x/h > 5$. The positive slopes of streamwise and surface-normal turbulence intensities of the present confined jets are approximately 0.66 and 1.01, respectively, which increase to approximately 0.85 and 1.10, respectively, in the minor plane of the rectangular jet. In Fig. 5.7e the near field values of the normalized streamwise turbulence intensity of the present data and those of Sankar et al. (2008) are comparable but the result for Madnia and Bernal (1994) was affected by measurement uncertainty in that experiment. In the far field region, both reference measurements follow a line of approximate slope 0.74, which is about 11% higher than that measured for present square and circular jets. The difference can be attributed to the relatively higher Reynolds numbers in the reference experiments. The near field surface-normal turbulence intensity of Sankar et al. (2008) also shows good agreement with the present data (Fig. 5.7f). In the far field region, the reference data follows a line of approximate slope 0.57.

5.3 Streamwise Evolution of Surface Velocity, Vorticity Thickness and Surface Turbulence Intensities

As mentioned in Chapter 4, the flow characteristics of the surface attaching jets depend on the kinematic condition of the free surface. Thus, the effects of the nozzle geometry on the mean and turbulent quantities along the free surface (about two interrogation area sizes ≈ 2 mm below the air-water interface of the PIV images) are investigated. Discussions on streamwise mean surface velocity, mean velocity defect, vorticity thickness and surface turbulence intensities are provided below:

5.3.1 Streamwise mean surface velocity and velocity defect

Figure 5.8a shows the profiles of streamwise mean surface velocity, U_s/U_j for the four nozzle geometries with respect to the streamwise distance. The streamwise distance is measured relative to the attachment length, L_a which makes the origin at the AP as indicated by the vertical dashed line at $(x\text{-}L_a)/d = 0$ to focus the discussion on the interaction region. In all four configurations, the mean surface flow accelerates to a maximum at a streamwise location some ten nozzle widths downstream of the attachment point and decelerates downstream of this location. In all cases, the deceleration is much slower than the acceleration. Similar observations were reported by Madnia and Bernal (1994). The profiles collapse for the circular, square and Rect_major jets in the interaction region, within the limits of experimental uncertainty. However, the more vigorous

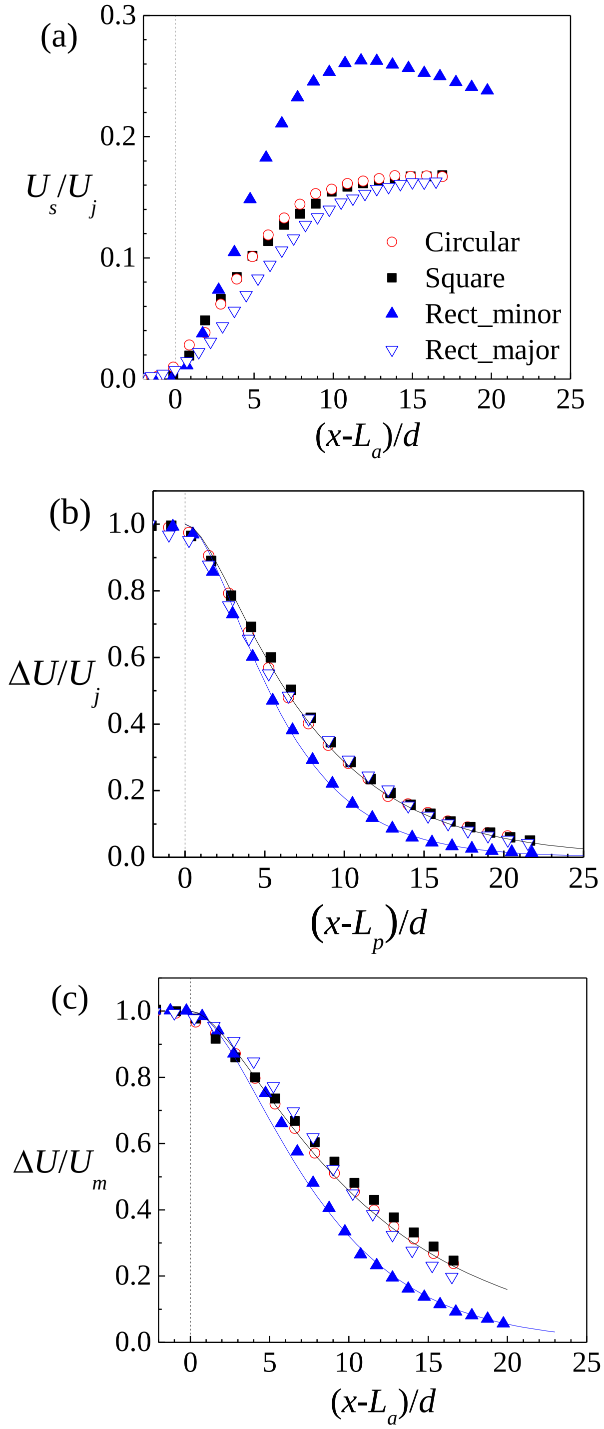

Figure 5.8. Streamwise variation of (a) streamwise mean surface velocity, (b) mean velocity defect normalized by U_j and (c) mean velocity defect normalized by U_m. The solid lines in (b) and (c) are the least-squares fit of the exponential-Gaussian hybrid distribution.

expansion of the Rect_minor jet caused a more dramatic increase in U_s compared to the other jets. Farther downstream, this effect was followed by a deceleration of the surface mean flow, albeit to a level that is still substantially higher than the other jets. In the absence of mean surface deformation, the surface mean flow profiles suggest that the free surface is severely strained, due to the alternating acceleration ($\partial U_s/\partial x > 0$) and deceleration ($\partial U_s/\partial x < 0$). This is typically the state of the free surface for confined jets issuing at low offset height ratio from the free surface (e.g., Madnia and Bernal, 1994). The results in Fig. 5.8a suggest that the free surface is more severely strained in the Rect_minor jet than in the square, circular and Rect_major jets.

Figure 5.8b shows profiles of the mean velocity defect, $\Delta U = U_m - U_s$, normalized by U_j. The origin of the x axis is shifted by the potential core length, L_p in an attempt to focus on the streamwise evolution of the velocity defect downstream of the potential core. The mean surface velocity defect decays exponentially with streamwise distance. The decay is at nearly the same rate for the square, circular and Rect_major jets but proceeds at a much faster rate in the minor plane of the rectangular nozzle. The more rapid decay in the Rect_minor jet can be attributed to how U_m and U_s contribute to the velocity defect under the rapid expansion of that jet: U_m, which is monotonically decreasing with $(x - L_p)$; and is decaying more rapidly in the minor plane of the rectangular jet than the other nozzle geometries. At the same time, the surface mean velocity (U_s) for Rect_minor is consistently larger than corresponding values measured in the other three configurations. Thus, ΔU is not only a monotonically decreasing quantity but the difference of U_m and U_s is declining more rapidly for Rect_minor than the other jets. To quantify the decay average decay rates of the surface velocity defect profiles, the following least-squares exponential-Gaussian hybrid distribution (Lan and Jorgenson, 2001) is fitted to the profiles:

$$\Delta U/U_j = \exp\left(\frac{-\,x''^2}{20 + B_1\, x''}\right) \tag{5.2}$$

where, $x'' = (x - L_p)/d$, and B_1 is a fitting parameter. The value of B_1 is estimated as 6.0 for circular, square and Rect_major jets. For the Rect_minor jet, B_1 ($\approx$ 3.8) is approximately 37%, which is consistent with the more vigorous expansion of the jet compared to the other nozzle configurations. The profiles of the mean surface velocity defect normalized by the local maximum mean streamwise velocity are plotted in Fig. 5.8c as a function of $(x - L_a)/d$. The results show that using the velocity and coordination translation scales, U_m and L_a, respectively, collapses the defect profiles for the square, circular and Rect_major jets within the experimental uncertainty limits. As before, the collapse only works for the moderately spreading jets. In the minor plane of the rectangular jet, $\Delta U/U_m$ decays more dramatically than the square, circular and Rect_major jets. The decay rates of the profiles in Fig. 5.8c are estimated by a least-squares fit of the EGH distribution:

$$\Delta U/U_m = \exp\left(\frac{-\,x'^2}{38 + B_2\, x'}\right) \tag{5.3}$$

where, $x' = (x - L_a)/d$, and B_2 is a fitting parameter. Lower value of B_2 for Rect_minor jet (5.0) compared to the estimated value of B_2 = 9.0 for circular, square and Rect_major jets is consistent with the result of B_1.

5.3.2 Vorticity thickness

The vorticity thickness (δ_ω), which is often used to investigate the growth of the shear layer (Ashcroft and Zhang, 2005), is estimated using Equation 4.3 as

$$\delta_\omega = \frac{\Delta U}{(\partial U/\partial y)_{\max}}$$

where, $(\partial U/\partial y)_{\max}$ is the maximum rate of change of U in the upper shear layer. The variation of δ_ω for the four nozzle geometries is shown in Fig. 5.9. The vorticity thickness grows almost linearly with streamwise distance in the pre-attachment region. The growth is the most rapid in the minor plane of the rectangular nozzle and the least in the major plane of the rectangular nozzle. These results are consistent with the expansion of the shear layers in the near field region. The vorticity thickness values of the circular and square nozzle are quasi-similar over the entire range of measurement. This implies that the vortices generating the turbulence in both jets are structurally similar since the vorticity fields are often considered as the main source of the growth of the vorticity thickness (McMullan et al., 2007). The linear increase of δ_ω in the pre-attachment region is consistent with the LSE results that indicate a streamwise growth of the vortices generated in near field region. The growth rate, $d\delta_\omega/dx$, of the vorticity thickness is estimated as the slope of the least-squares line fitted to the data in the pre-attachment region. The calculations yielded $d\delta_\omega/dx$ values of approximately 0.115 for the circular and square jets; 0.270 for Rect_minor jet and 0.080 for the Rect_major jet. The vorticity thickness is not a well-documented parameter for surface attaching jets. However, the present values from the circular, square and Rect_minor jets are within the range of 0.110

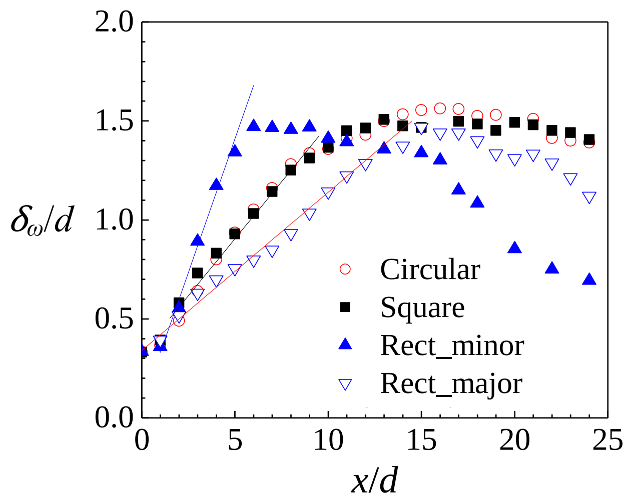

Figure 5.9. Streamwise variation of vorticity thickness. The solid lines are the least-squares linear fit.

– 0.270 reported in the literature for a wide variety of turbulent flows, including mixing layers (e.g., Brown and Roshko, 1974), separated and reattached shear layers over forward facing steps (e.g., Essel et al., 2015; Nematollahi and Tachie, 2018), backward facing steps (e.g., Essel and Tachie, 2015; Gentile et al., 2016), and two-dimensional cavities (e.g., Ukeiley and Murray, 2005; Bian et al., 2011). In the interaction region, the free surface limits the growth of the upper shear layer, causing δ_ω to remain relatively constant up to some ten nozzle widths downstream of the attachment point. This is noticeable within $5 < x/d < 15$ for the Rect_minor jet and within approximately $10 < x/d < 20$ for the square and circular jets. The plateau is absent for the Rect_major jet because the axis-switching in this jet will continue the growth of the structures over a larger streamwise distance than the other jets. The relatively constant values of δ_ω would suggest that within the early parts of the interaction region of the square, circular and Rect_minor jets the surface-normal scale of the vortices is approximately constant. This observation will be examined further in the section on two-point correlations of swirling strength. Farther downstream, a characteristic decay of the δ_ω values occur, which can be partly attributed to shrinkage of the vorticity field in the upper shear layer as the jet deflects towards the free surface.

5.3.3 Turbulence intensities along the free surface

The profiles of streamwise and surface-normal turbulence intensity ($<u^2>^{0.5}$ and $<v^2>^{0.5}$, respectively) along the free surface are shown in Fig. 5.10. Figures 5.10a and 5.10b show the profiles of the streamwise and surface-normal turbulence intensities, respectively, normalized by the jet exit velocity. The surface turbulence intensities increase rapidly in the early interaction region, reaching peak values at a streamwise location approximately six nozzle widths downstream of the attachment point. The location of the peak values corresponds to the inflection point in the surface mean streamwise velocity profile. The surface turbulence intensities from the square, circular and Rect_major jets compare fairly well. However, the larger mean strain imposed on the free surface by the rapidly expanding Rect_minor jet produces a hump in the turbulence intensity profiles. The peak values of the streamwise and surface-normal turbulence intensities in Rect_minor are approximately 19% and 24% larger than in the other geometries, respectively. In the far downstream region, the surface turbulence intensities decay to levels that are independent of nozzle geometry. In all cases, the surface-normal turbulence intensity is significantly lower than the streamwise counterpart. This is an indication of strong anisotropy of the Reynolds stress field at the free surface. The results also reveal that there is a more dramatic far field decay in the surface-normal turbulence

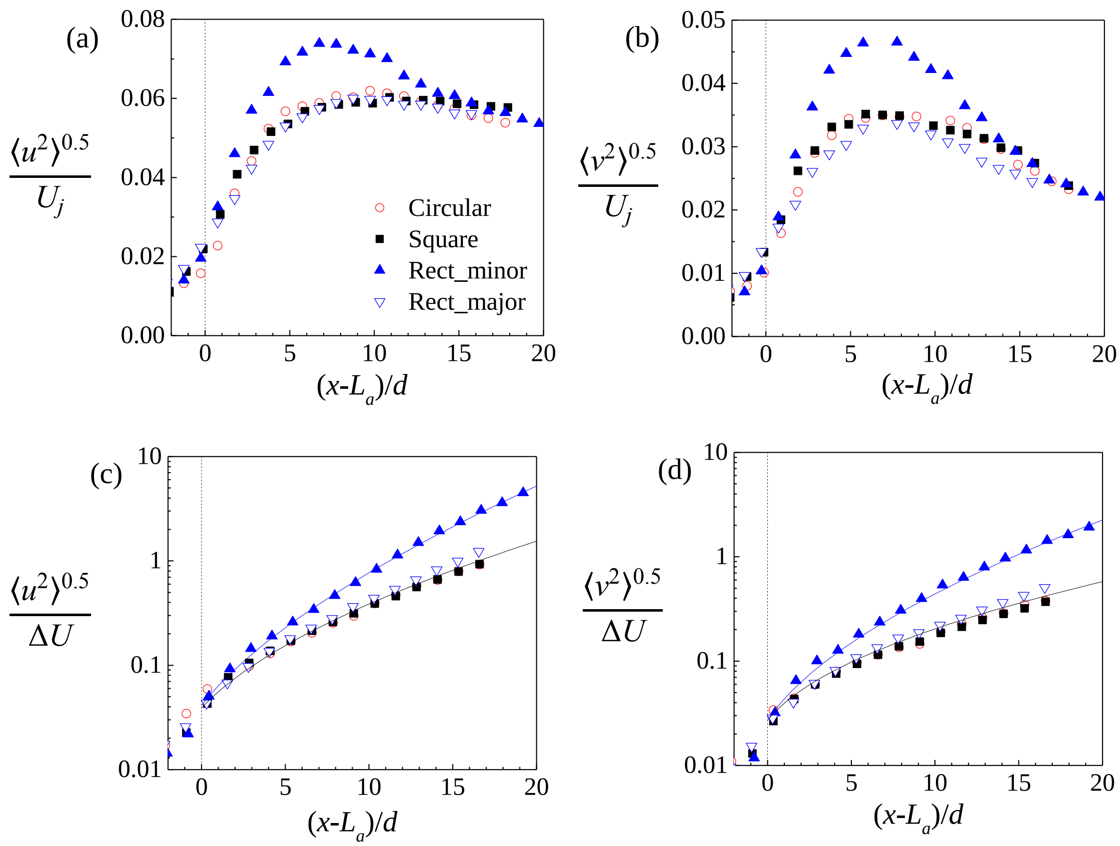

Figure 5.10. Streamwise variation of turbulence intensities along the free surface: (a) streamwise turbulence intensity normalized by U_j, (b) surface-normal turbulence intensity normalized by U_j, (c) streamwise turbulence intensity normalized by ΔU, and (d) surface-normal turbulence intensity normalized by ΔU. The solid lines in (c) and (d) are the least-squares fit of the exponential distribution.

intensity than the streamwise turbulence intensity. As noted in previous investigations (Anthony and Willmarth, 1992; Walker et al., 1995), this is consistent with the damping of the surface-normal velocity fluctuations by the free surface. The suppression of the surface-normal velocity fluctuations is also consistent with the large anisotropy reported near the free surface (Swean et al., 1989; Anthony and Willmarth, 1992; Walker et al.,

1995) due to energy redistribution from the surface-normal velocity fluctuations to the parallel velocity fluctuations.

The profiles presented in Figs. 5.10c and 5.10d are used to probe the velocity scale, ΔU as a possible similarity variable for scaling the surface turbulence intensities. The profiles are plotted on semi-logarithmic in order to more distinctly reveal the differences between the profiles, if any. The results show that the surface velocity defect successfully collapsed the data from the square, circular and major plane of the rectangular jet in the interaction region. On the contrary, the high turbulent activity generated at the free surface by the interaction of the Rect_minor shear layer with the free surface led to increasingly higher values of the corresponding normalized turbulence intensities in the interaction region. The turbulence intensities normalized by the surface mean velocity defect follow exponential distributions given by:

$$\frac{\langle u^2\rangle^{0.5}}{\Delta U} \text{ or } \frac{\langle v^2\rangle^{0.5}}{\Delta U} = 0.01\ \exp(x' - x_3)^a \tag{5.4}$$

where, a and x_3 denote the growth rate and a fitting parameter, respectively. The values of a and x_3 are summarized in Table 5.4. Higher value of a for the Rect_minor jet (about 12% and 17% for $<u^2>^{0.5}$ and $<v^2>^{0.5}$, respectively) than the other geometries is attributed to faster decay of mean velocity defect. It is noted that a reduction of a for $<v^2>^{0.5}$ than $<u^2>^{0.5}$ (approximately 12% for circular, square and Rect_major jet; and 7% for Rect_minor jet) implies damping of the surface-normal velocity fluctuation which enhances large-scale anisotropy at the free surface.

Table 5.4. Summary of the fitting parameters of exponential curve for $<u^2>^{0.5}/\Delta U$ and $<v^2>^{0.5}/\Delta U$ profiles for various nozzle geometries.

Geometry	$<u^2>^{0.5}/\Delta U$		$<v^2>^{0.5}/\Delta U$	
	a	x_3	a	x_3
Circular	0.525	-1.8	0.460	-1.0
Square	0.525		0.460	
Rect_minor	0.595		0.555	
Rect_major	0.525		0.460	

5.4 Surface-Normal Distribution of Mean Velocity and Higher Order Moments

Effects of nozzle geometry on the surface-normal distribution of the mean and the turbulent statistics up to the fourth order moment at selected streamwise locations in the jet-surface interaction region are discussed in this section. Following the approach in Chapter 4, the profiles normalized by h and U_m are discussed, which is followed by examining the self-similarity using typical similarity variables of $y_{0.5}$ and U_m as the length and velocity scale. Since, the profiles for circular and square jet are almost similar, results obtained from square, Rect_minor and Rect_major jets are presented.

5.4.1 Surface-normal profiles normalized using h and U_m

5.4.1.1 Streamwise mean velocity

Figure 5.11 shows the profiles of streamwise mean velocity, U/U_m for square, Rect_minor and Rect_major jet at the selected streamwise locations of x/d = 10, 15 and

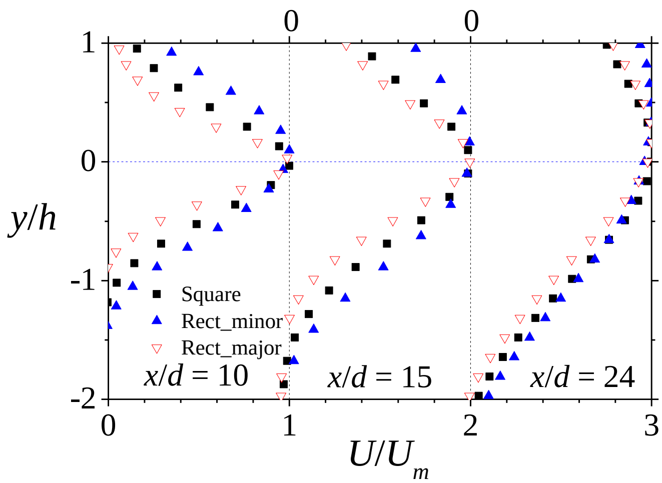

Figure 5.11. Surface-normal profiles of streamwise mean velocity normalized by *h* and U_m for square, Rect_minor and Rect_major jet at the selected *x/d* locations.

24 in the interaction region. The dashed horizontal line at *y/h* = 0 denotes the nozzle centerline; and the free surface is located at *y/h* = 1, irrespective of nozzle geometry. Result shows that the mean streamwise velocity is affected by nozzle geometry. At *x/d* = 10, the mean velocity profile of the Rect_major jet is almost Gaussian because of the delayed onset of interaction between its upper shear layer and the free surface. For the square and Rect_minor configuration, the upper shear layer is advancing much faster than the lower shear layer. This persists throughout the interaction region, resulting in increasingly large velocities at the free surface, or in an accelerating surface current. Throughout the interaction region, the upper shear layer of Rect_minor is accelerating the fastest, while that of Rect_major catches up to the square jet. In the lower shear layer, the disparities among the profiles become negligibly small in the far field region. The accelerating surface current has the effect of flattening the mean streamwise velocity profile in the upper shear layer. This causes a progressive decrease in the surface-normal gradient of the mean velocity ($\partial U/\partial y$) in the interaction region.

5.4.1.2 Reynolds stresses

The distribution of streamwise ($<u^2>/U_m^2$) and surface-normal ($<v^2>/U_m^2$) Reynolds normal stresses are shown in Fig. 5.12a and 5.12b, respectively. In the interaction region, the profiles from square and Rect_major jets are comparable, except at $x/d \approx 10$ where the centerline values of $<u^2>/U_m^2$ and $<v^2>/U_m^2$ were enhanced by 20% and 34%, respectively, by the Rect_major configuration in comparison to the square jet. The minor-axis orientation of the rectangular jet caused substantial enhancements in the Reynolds normal stresses away from the centerline for most of the interaction region. The profiles exhibit the presence of significant turbulent activity near the free surface, whose streamwise and surface-normal fluctuations are growing and decaying, respectively. The profiles also demonstrate the strong anisotropy of the normal Reynolds stresses, both at the free surface and within the jets with values of $<u^2>/U_m^2$ that approximately twice as large as $<v^2>/U_m^2$.

The profiles of the Reynolds shear stress, $-<uv>/U_m^2$ are presented in Fig. 5.12c. At $x/d \approx 10$, the peak values of the Reynolds shear stress in the square and Rect_minor jets are comparable but are approximately 26% lower than peak values for the Rect_major jet in both halves of the shear layer. The locations of the peak Reynolds shear stress in Rect_major are closer to the centerline than in the square and Rect_minor jets because of the slower growth rate of the Rect_major jet. With increasing streamwise distance, the peak Reynolds shear stress in the upper shear layer decreases as the mixing zone shrinks under the influence of confinement. The effect is most dramatic for the Rect_minor jet in comparison to the other jets. This can be explained by the increasingly flat shape of the

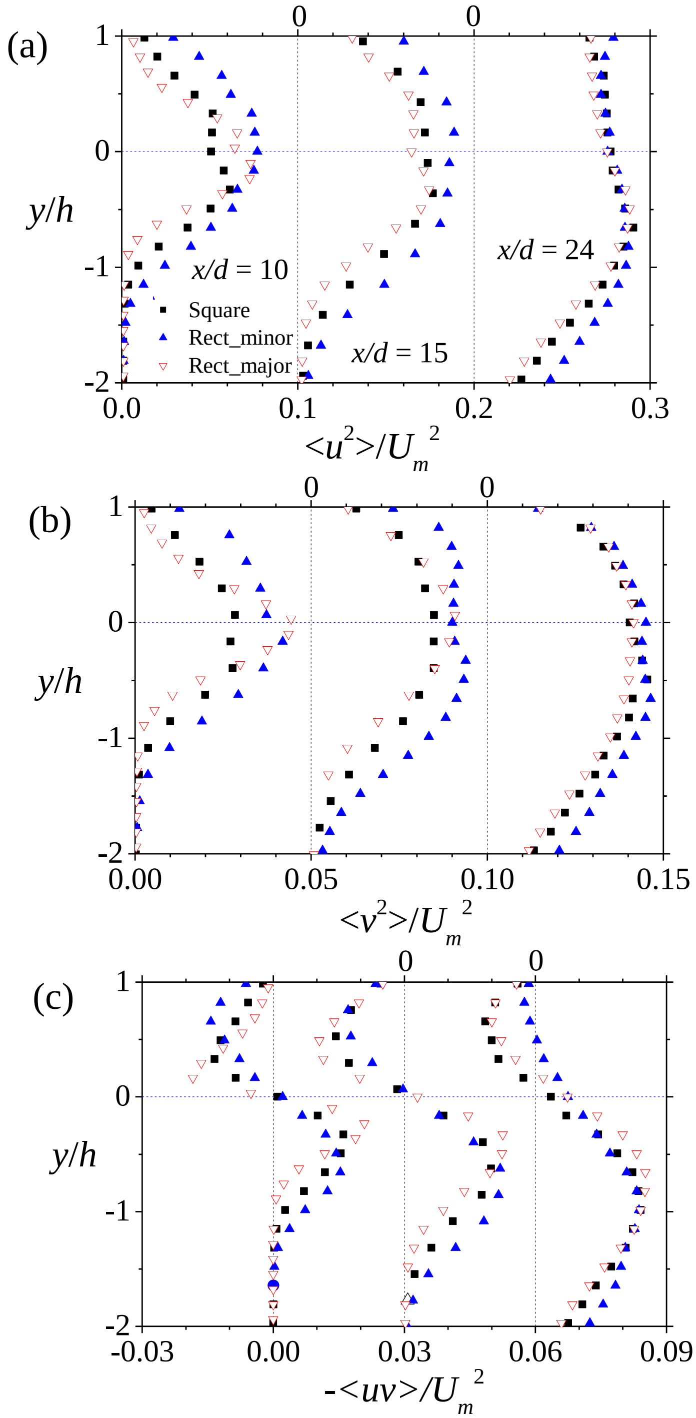

Figure 5.12. Surface-normal profiles of Reynolds stresses normalized by h and U_m for square, Rect_minor and Rect_major jet at the selected x/d locations: (a) streamwise Reynolds normal stress, (b) surface-normal Reynolds normal stress and (c) Reynolds shear stress.

mean velocity profile and the corresponding rapid decay of the mean strain rate $\partial U/\partial y$ as the jet evolves downstream. On the other hand, as the lower shear layer evolves, the corresponding peak values of the Reynolds shear stress persistently increase, but these are not affected by differences in nozzle geometry. The effect of nozzle geometry in the lower shear layer is seen in the widening area of the zone of significant Reynolds shear stress. The results indicate enhancements of the Reynolds shear stress for Rect_minor in the mixing region of the lower shear layer.

5.4.1.3 Stress ratio and structure parameter

To explore the anisotropy of the normal Reynolds stresses and the possible ramifications of the rapid decline of the Reynolds shear stress, values of the anisotropy parameter $\langle u^2\rangle/\langle v^2\rangle$ and the structure parameter $-\langle uv\rangle/(2k)$ are calculated. Figure 5.13a shows the profiles of the stress ratio, $\langle u^2\rangle/\langle v^2\rangle$. Results depict a stress ratio value of approximately 2 (50% higher than isotropic flow) irrespective of nozzle geometry as like free jets (Hussein et al., 1994) over most of the flow region except in the vicinity of the free surface. Near the free surface, enhanced damping effect of the surface-normal Reynolds normal stress on Rect_minor jet results in increase of anisotropy showing approximately 18% higher value of $\langle u^2\rangle/\langle v^2\rangle$ at x/d = 24, for instance, compared to square or Rect_major jet.

The profiles of Townsend's structure parameter, $-\langle uv\rangle/(2k)$ which is a measure of the magnitude of Reynolds shear stress relative to turbulent kinetic energy, are shown in Fig. 5.13b. The value of the structure parameter reaches to a maximum of approximately 0.15 in the lower shear layer irrespective of nozzle geometry at the selected

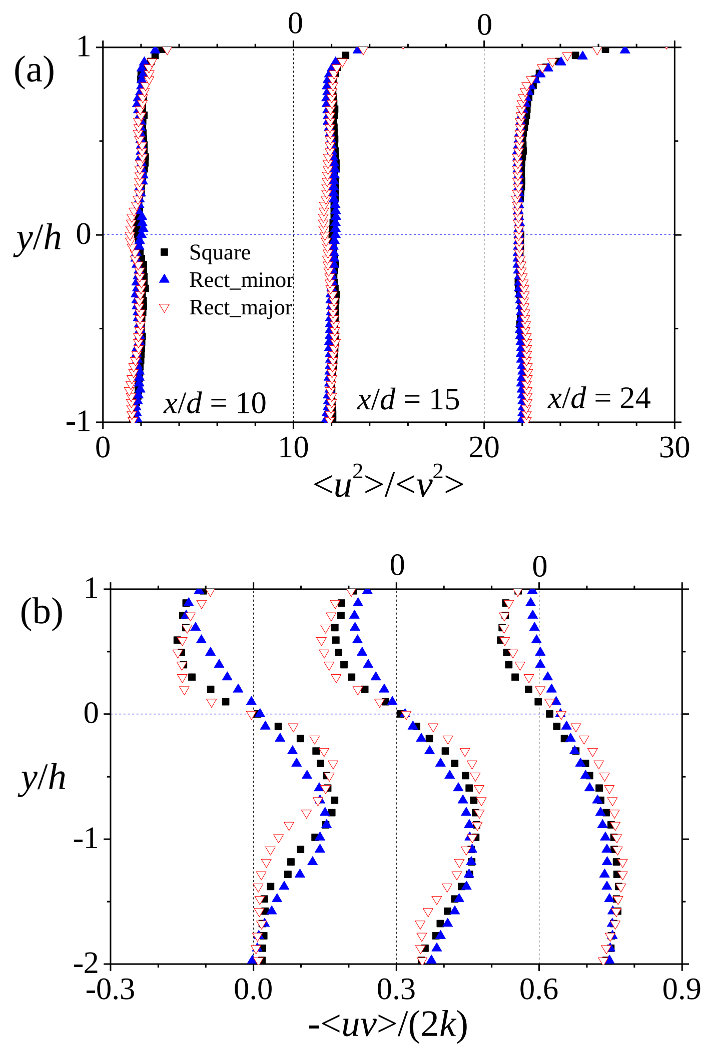

Figure 5.13. Surface-normal profiles of (a) stress ratio and (b) structure parameter for square, Rect_minor and Rect_major jet at the selected *x/d* locations.

streamwise locations which is comparable to a self-similar free jet (Hussein et al., 1994) that supports negligible effect of a free surface. In the upper shear layer, the attenuation of the peak with the increase of streamwise distance, which is consistent with the result of Reynolds shear stress in Fig. 5.12c for various nozzle geometries, implies a faster damping of Reynolds shear stress relative to turbulent kinetic energy at the presence of a free surface. As mentioned in Chapter 4, the reduced value of the structure parameter from

0.15, which is equivalent to the modeling coefficient of $(-\langle uv\rangle/k)^2 \approx 0.09$, indicates a limitation of the standard eddy viscosity models in the upper shear layer. Similar damping of the structure parameter in the shear layer close to a boundary was reported in previous surface and wall attaching jets (Agelin-Chaab and Tachie, 2011c; Essel and Tachie, 2018).

5.4.1.4 Production of turbulence

The Reynolds stresses are further investigated using the production terms in their transport equations. The production of streamwise Reynolds normal stress (P_{u^2}), surface-normal Reynolds normal stress (P_{v^2}) and Reynolds shear stress (P_{-uv}) are estimated using Equation 4.6 to 4.8 as follows:

$$P_{u^2} = -2\,(\langle u^2\rangle\, \partial U/\partial x + \langle uv\rangle\, \partial U/\partial y)$$

$$P_{v^2} = -2\,(\langle v^2\rangle\, \partial V/\partial y + \langle uv\rangle\, \partial V/\partial x)$$

$$P_{-uv} = \langle u^2\rangle\, \partial V/\partial x + \langle v^2\rangle\, \partial U/\partial y$$

The profiles of normalized production terms are shown in Fig. 5.14. The production of streamwise Reynolds normal stress is shown in Fig. 5.14a. The distribution of P_{u^2} is positive in both the upper and lower shear layers, indicating P_{u^2} as a source of energy. In all three jets, the peak values of the production term occur within the shear layers away from the centerline. As noted in previous investigations of the round free jet (e.g., Panchapakesan and Lumley 1993; Bogey and Bailly, 2009), this can be attributed to the steep gradients in the mean velocity profile in the shear layers. In the upper shear layer, P_{u^2} is attenuated with increasing streamwise distance. Between the square and

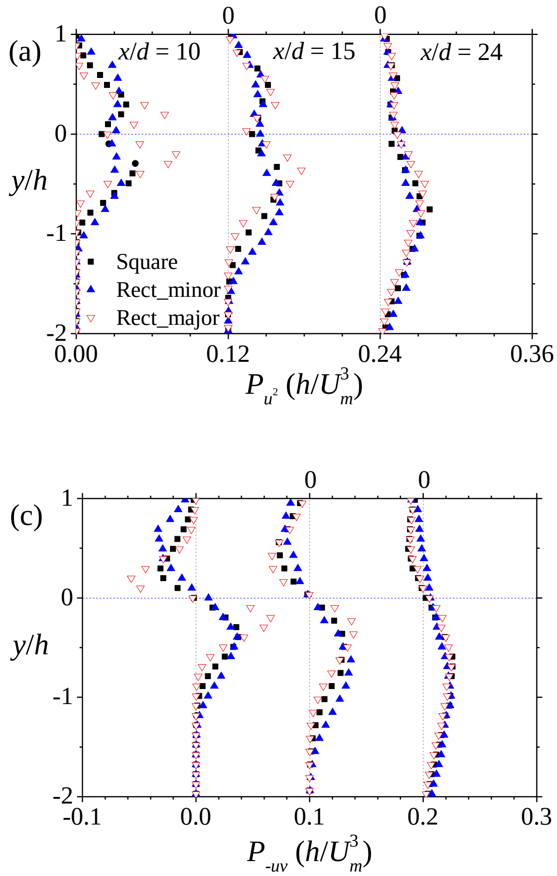

Figure 5.14. Surface-normal profiles of production of Reynolds stresses and turbulent kinetic energy for square, Rect_minor and Rect_major jet at the selected *x/d* locations: (a) Production of streamwise Reynolds normal stress, (b) production of surface-normal Reynolds normal stress, (c) production of Reynolds shear stress and (d) production of turbulent kinetic energy.

Rect_minor nozzle, no distinct features are revealed by using either nozzle. Re-orientation of the rectangular nozzle caused an approximately 40% increase in the peak value of P_{u^2} at x/d = 10 when compared to the square and Rect_minor jets. The effect diminishes, though, as the Rect_major jet evolves in the interaction region. In the lower shear layer, the profiles evolve in a similar manner between x/d = 10 and 15. The relative large peak values in the major plane of the rectangular jet can be partly attributed to the larger values of the corresponding Reynolds shear stress and mean strain rate $\partial U/\partial y$. In the far field of the interaction region, P_{u^2} is unaffected by nozzle geometry.

The production of surface-normal Reynolds normal stress (P_{v^2}) is shown in Fig. 5.14b. The profiles indicate that P_{v^2} is affected by nozzle geometry and orientation in the near and intermediate zones of the interaction region. For the square and Rect_minor jets, P_{v^2} is predominantly negative in the core jet and positive away from the axis. The negative values, representing energy loss in the core jet, can be attributed to the behaviour of the terms in P_{v^2} equation. In the core jet, $-\langle uv \rangle \approx 0$ so that $P_{v^2} \approx -2\langle v^2 \rangle \partial V/\partial y$. Profiles of the mean surface-normal velocity reported at a similar streamwise location (Tay et al., 2017) show that $\partial V/\partial y$ is positive within the core of the square and Rect_minor jets. For these cases, this would cause a negative production of $\langle v^2 \rangle$ as indicated in the figure. These results are also in agreement with those reported in the literature (e.g., Panchapakesan and Lumley, 1993; Bogey and Bailly 2009). The positive peak observed in the Rect_major jet can be explained by negative values of $\partial V/\partial y$ in the core jet (Tay et al. 2017, for example). For the Rect_minor jet, the large magnitude of the peak value at x/d = 10 is attributable to relatively large values of $\langle v^2 \rangle$ and $\partial V/\partial y$ compared to the square jet. As the jets evolve downstream, the peak values are attenuated both in the core jet and away from the axis. The attenuation of P_{v^2} with increasing distance is more dramatic in comparison to that observed for P_{u^2}, and is indicative of the damping effect of the free surface on the surface-normal velocity fluctuations. In the far field of the lower shear layer, the areas of the zones of significant P_{v^2} are very small in comparison to P_{u^2}.

This indicates that the production of $<v^2>$ is associated with the turbulence generated by the small-scale vortices at the edge of the shear layer, while P_{u^2} is due to the large-eddy structure that is still growing with the jet.

Figure 5.14c shows the profiles of the production term in the transport equation for the Reynolds shear stress, P_{-uv}. The profiles of P_{-uv} bear a close resemblance to those of the Reynolds shear stress and the mean strain rate, $\partial U/\partial y$ (not shown herein) in the shear layers. At the near and intermediate locations, the Rect_minor nozzle has no effect on the peak values of P_{-uv}, except for extending the region of significant production in the upper and lower shear layers. Re-orientation of the rectangular nozzle enhances the peak values of P_{-uv} and moves their locations closer to the jet axis. The enhancements by Rect_major diminish with increasing streamwise distance in the interaction region. As noticed in the production profiles for the normal stress components, interaction of the upper shear layer with the free surface suppresses the levels of P_{-uv} relative to the lower shear layer. The most dramatic reduction in P_{-uv} occurs in the Rect_minor jet due to the severe attenuation of Reynolds shear stress in the upper shear layer. In the lower shear layer, P_{-uv} is independent of nozzle geometry and orientation.

The production of turbulent kinetic energy (P_k) is estimated using Equation 4.9 and 4.10 as

$$P_k = - (<u^2> \partial U/\partial x + <v^2> \partial V/\partial y) - (<uv> \partial U/\partial y + <uv> \partial V/\partial x).$$

The profiles of normalized P_k are shown in Fig. 5.14d. The distributions of P_k mirror those of the streamwise Reynolds normal stress, P_{u^2}, including the outward broadening of the region of significant turbulent kinetic energy production by the Rect_minor configuration in comparison to the square nozzle, which is offset as the P_k is attenuated by the free surface, and the more substantially enhanced peak values of P_k in Rect_major compared to Rect_minor at $x/d \approx 10$ and 15. At the most downstream location, the influence of nozzle geometry and orientation vanishes. It is noted that the dominance of the normal component, $P_n = -(\langle u^2\rangle\, \partial U/\partial x + \langle v^2\rangle\, \partial V/\partial y)$ and shear component, $P_s = -(\langle uv\rangle\, \partial U/\partial y + \langle uv\rangle\, \partial V/\partial x)$ to P_k at the jet center and within the shear layers, respectively (not shown herein) is consistent with the result as mentioned in Chapter 4.

The profiles of the production terms, with the exception of P_{v^2}, indicate substantial levels of turbulence production in the lower shear layer over an increasingly larger surface-normal range of the shear layer. This should be expected since the increasing influence of the free surface may cause the Reynolds stresses and turbulent kinetic energy to be transported by diffusion from the upper shear layer across the centerline to feed the production of these stresses in the lower shear layer. The ever-widening regions of significant turbulence production are consistent with the streamwise growth of the larger-scale structures in the interaction region.

5.4.1.5 Triple velocity products

In order to investigate the transport of Reynolds stresses and turbulent kinetic energy in the surface-normal direction along which the growth of the jets is confined, profiles of the following triple velocity products are shown in Fig. 5.15: $\langle u^2v\rangle$, $\langle v^3\rangle$, $\langle uv^2\rangle$ and $(\langle u^2v\rangle + \langle v^3\rangle)$. The profiles of the surface-normal transport of $\langle u^2\rangle$ (Fig. 5.15a) indicate turbulent diffusion of the Reynolds normal stress towards the free surface

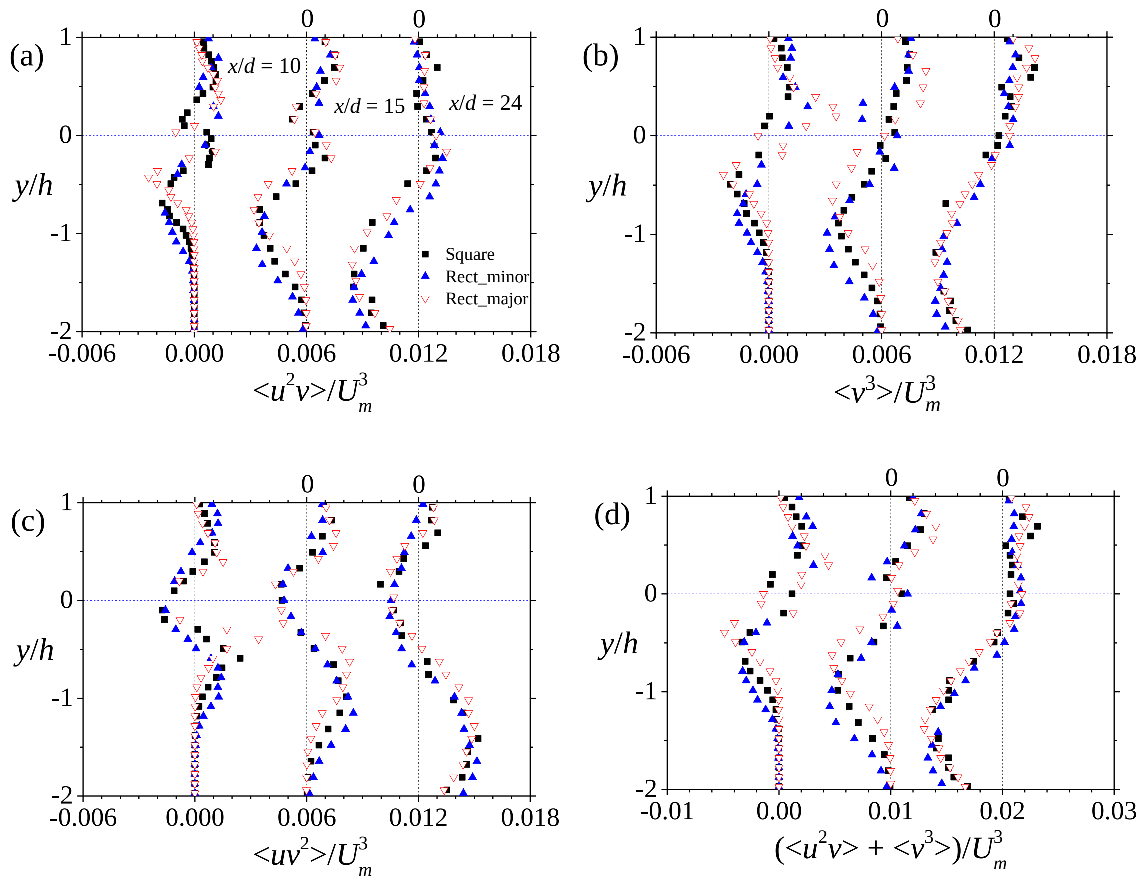

Figure 5.15. Surface-normal profiles of triple velocity products for square, Rect_minor and Rect_major jet at the selected *x/d* locations: (a) $<u^2v>/U_m^3$, (b) $<v^3>/U_m^3$, (c) $<uv^2>/U_m^3$ and (d) $(<u^2v> + <v^3>)/U_m^3$.

from the location of maximum Reynolds stress production in the upper shear layer. There is no significant difference among the profiles in the upper shear layer, except for a broader peak in the Rect_major jet at $x/d \approx 10$. The broader peak would suggest a slower turbulent diffusion towards the free surface in comparison to the square and Rect_minor jets. As the level of interaction increases the diffusion is considerably damped by the free surface and is of little consequence. In the lower shear layer, the profiles suggest significant turbulent transport of streamwise Reynolds normal stress by diffusion towards the ambient fluid from the location of maximum production of $<u^2>$. This represents an energy gain by the ambience by turbulent diffusion of $<u^2>$ fed by the energy loss by diffusion from the core jet. The gentler slope of the Rect_minor profiles on the leeward side of the peaks from the free surface suggest a reduction in energy lost by the jet to the ambience. The results are qualitatively similar for the surface-normal turbulent transport of $<v^2>$ (Fig. 5.15b). However, the parts of the profiles close to the free surface are almost parallel to the *y*-axis, suggesting negligible diffusion of $<v^2>$ towards the surface. This is consistent with the surface-normal damping of the *v*-fluctuations. The surface-normal turbulent transport of the Reynolds shear stress (Fig. 5.15c) reaches two positive peaks, one in either shear layer and a negative peak in the core jet. In the upper shear layer, there is a diffusion of Reynolds shear stress towards the free surface with the energy gain associated with the process being supplied by the energy loss by diffusion on the leeward side of the peak. The diffusion of Reynolds shear stress towards the free surface is progressively damped with increasing x/d as the mixing zone rapidly shrinks in the interaction region. The effect is more dramatic for Rect_minor than the other configurations. On the centerline, the production of Reynolds shear stress is zero. The profiles have a negative peak on the axis to ensure that the loss in energy by diffusion above the centerline is balanced by the gain in energy by diffusion below the axis. A similar negative peak in the core jet was reported in round free jets (Hussein et al., 1994; Panchapakesan and Lumley, 1993) and surface attaching jets (Sankar et al., 2008). In the lower shear layer, the gain in energy by diffusion towards the centerline is supplied by the loss in energy by diffusion on the leeward side of the peak. This suggests a turbulent transport of Reynolds shear stress from the lower shear layer to the upper shear layer through a series of alternating energy losses and gains by diffusion across the centerline to compensate for the shrinkage of the mixing zone in the upper shear layer. As shown subsequently, this phenomenon is supported by large spatial coherence of the two-point cross-correlation function, extending from the upper to lower shear layer. Figure 5.15d shows that the surface-normal transport of the turbulent kinetic energy follows the same trend as $<u^2v>$ and $<v^3>$. The peak values of the correlation ($<u^2v>+<v^3>$) are diminishing with increasing *x/d* in the upper shear layer as the turbulent kinetic energy is redistributed from the surface-normal fluctuations to the parallel fluctuations. The profiles do not exhibit any systematic dependency on nozzle geometry, except for a characteristic growth in peak value in the major plane of the rectangular nozzle at *x/d* = 10, for instance. In the lower shear layer, the Rect_major configuration produces up to about 75% and 50% in the correlation on the windward side of the peak value from the free surface at *x/d* ≈ 10 and 15, respectively, in comparison to the square and Rect_minor jets. On the leeward side of the peak values, there is an outward growth of ($<u^2v>+<v^3>$) in the Rect_minor jet of approximately 40% - 70% and 33% - 75% at *x/d* ≈ 10 and 15, respectively, when compared to square and Rect_major jets. At the far downstream location, the profiles do not converge especially close to the edges of the shear layers.

The triple correlation results show that there are slight differences among the data in the far field of the interaction region. This suggests that the triple correlations are more sensitive to differences in nozzle geometry than the mean velocity and second order moments. The present distributions in the lower shear layer are in qualitative agreement with those reported in previous round jets (Hussein et al., 1994; Panchapakesan and

Lumley, 1993). The damping of the triple correlations in the upper shear layer is consistent with the measurements reported by Sankar et al. (2008) for surface attaching jets. The diffusion of the Reynolds stresses towards the free surface is consistent with the mechanisms for generating the surface current that consists of ejection of vortical structures from the main jet.

5.4.1.6 Skewness and flatness factors

In order to provide a deeper insight of the effect of nozzle geometry on the velocity fluctuations, skewness and flatness factors are examined. In turbulent flows, the skewness factor is used to measure the temporal asymmetry in the probability density function of the velocity fluctuations, while the flatness factor is used to investigate the presence of spikes (or intermittency) in the fluctuating signal. Profiles of the skewness factor of the fluctuating streamwise velocity are shown in Fig. 5.16a. For all geometries, S_u is zero on the jet centerline and mostly positive in the upper shear layer within the early to intermediate parts of the interaction region. The positive values of S_u would imply that the instantaneous streamwise velocity is more frequently higher than its mean value in these regions. S_u makes positive excursions from vertical axis with the largest amplitude in the major plane of the rectangular jet compared to the square and Rect_minor jets. The amplitude of the positive excursion rapidly decays with increasing streamwise distance in the interaction region. The decay is even more dramatic for the Rect_minor jet in comparison to the other jets. At $x/d \approx 24$, the S_u distribution is nearly Gaussian ($S_u \approx 0$) regardless of nozzle geometry or orientation. In the lower shear layer, S_u is predominantly positive in all geometries and makes larger excursions from the vertical axis than

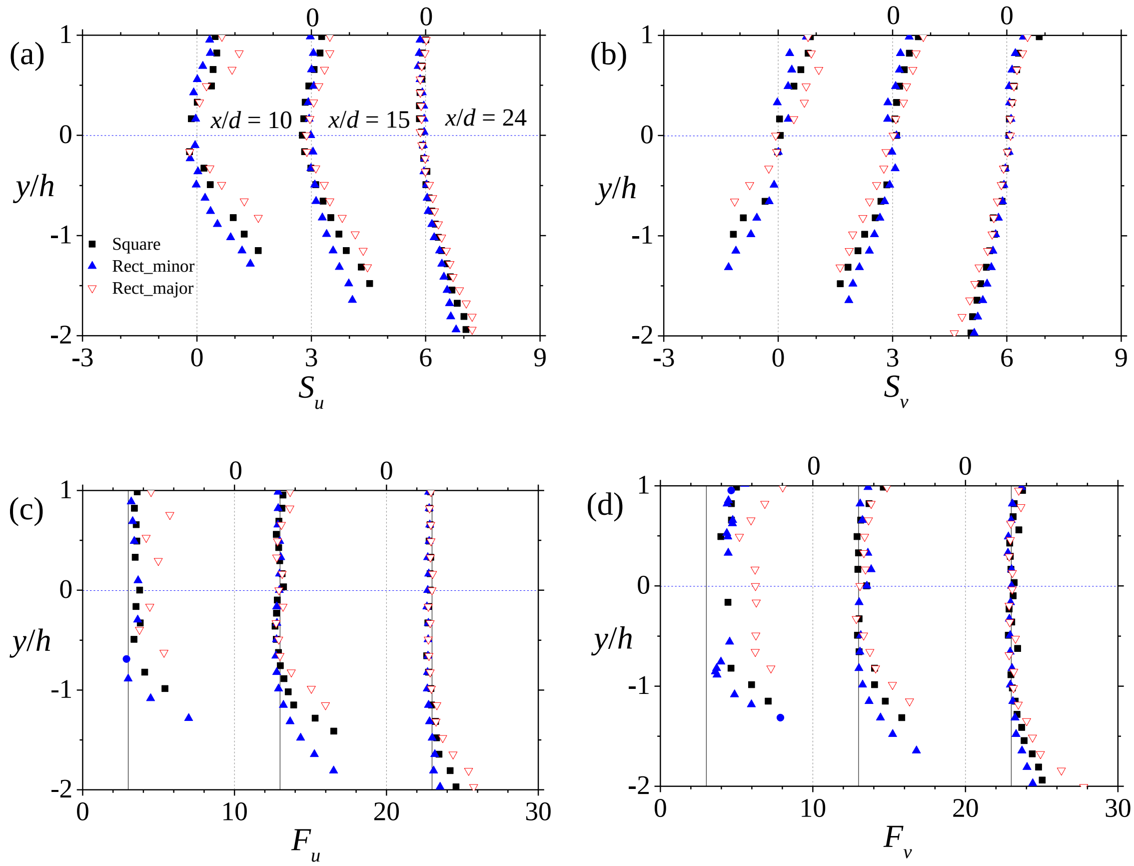

Figure 5.16. Surface-normal profiles of skewness and flatness factors for square, Rect_minor and Rect_major jet at the selected *x/d* locations: (a) skewness for streamwise velocity fluctuation, (b) skewness for surface-normal velocity fluctuation, (c) flatness for streamwise velocity fluctuation and (d) flatness for surface-normal velocity fluctuation. Solid vertical lines in (c) and (d) indicate the Gaussian value of the flatness.

corresponding profiles in the upper shear layer. The amplitudes in Rect_major are the largest as well, rising to about 38% and 70%, respectively, when compared to the square and Rect_minor jets at $x/d \approx 10$; 25% and 64%, respectively, at $x/d \approx 15$, and diminishing to lower margins of approximately 8% and 25%, respectively, at $x/d \approx 24$. The profiles of the skewness factor of fluctuating surface-normal velocity, S_v, are shown in Fig. 5.16b. S_v is predominantly positive near the free surface, Gaussian on the axis and predominantly negative in the lower shear layer. Negative values of S_v in the lower shear layer would imply that the extreme negative v more frequently occurs in this region expanding in downward direction. With increasing streamwise distance in the upper shear layer, the values of S_v near the free surface are decreasing but $S_v \neq 0$ at the most downstream location. This behaviour is due to the strong anisotropy of the velocity fluctuations near the free surface. The positive values of S_v when paired with the positive values of S_u in the upper shear layer are consistent with the turbulent transport of high-speed fluid towards the free surface. At the most downstream location, the profiles collapse within the uncertainty limits. In the lower shear layer, Rect_major shows a tendency to increase the skewness of the v-fluctuations relative to the square jet, while Rect_minor displays a tendency to reduce S_v relative to the square jet. At $x/d \approx 24$, the profiles of the square and Rect_minor jets are in good agreement, but both are approximately 33% lower than that of the Rect_major jet at $y/h = -2$. The negative values of S_v paired with the positive values of S_u in the lower shear layer are consistent with the turbulent transport of high-speed fluid away from the centerline into the ambient fluid.

Figures 5.16c and 5.16d show the flatness factors, F_u and F_v, respectively. The values of F_u and F_v are approximately equal to the Gaussian value of 3 over a significant surface-normal extent of the shear layers at $x/d \approx 15$ and 24. At $x/d \approx 10$, F_u values from the square and Rect_minor jets are comparable and approximately Gaussian across nearly the entire width of the jets. The corresponding values of F_v are also comparable but not Gaussian. At both locations, the u- and v-fluctuations have more frequent spikes in the major plane of the rectangular nozzle. In the lower shear layer, F_u and F_v attain relatively high values near the jet boundaries. These high values are due to the intermittency of the fluctuations near the turbulent/non-turbulent interface (T/NTI) of the lower shear layer. It can also be noticed that for the flatness factors as well, the effect of the Rect_minor configuration is the tendency to return the profiles to a Gaussian distribution. Altogether, the F_u and F_v profiles suggest that the intermittent region of the jet (T/NTI) in the lower shear layer is strongly dependent on nozzle geometry and orientation. It should be pointed out that the profiles of the skewness and flatness factors in the lower shear layer are in good agreement with similar measurements reported by Wygnanski and Fiedler (1969) in the self-similar region.

5.4.2 Surface-normal profiles with similarity scaling

In order to examine the self-similarity for various nozzle geometries, the distributions of streamwise mean velocity and Reynolds stresses with the conventional similarity variables, $y_{0.5}$ and U_m are presented in this section. Results from the square, Rect_minor and Rect_major jets at the streamwise locations, x/d = 10, 15 and 20 in the surface jet region are presented. Results from a self-similar free jet reported by Hussein et al. (1994) is included for comparison.

5.4.2.1 Streamwise mean velocity

Figure 5.17 shows the profiles of the streamwise mean velocity at the selected streamwise locations. The profiles from the three jets are staggered relative to one another in order to facilitate side-by-side comparison of the data. The dashed horizontal line in the figure denotes the jet centerline. The profiles are benchmarked against data from both

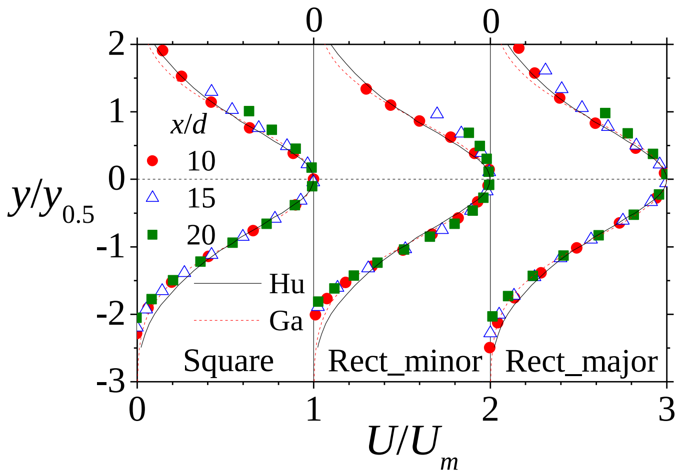

Figure 5.17. Surface-normal profiles of streamwise mean velocity using similarity variables for square, Rect_minor and Rect_major jet at the selected *x/d* locations. Hu: Self-similar profiles from Hussein et al. (1994), Ga: Gaussian distribution.

Hussein et al. (1994) and that calculated using the Gaussian mean streamwise velocity distribution (Rajaratnam and Humphries, 1984) as in Equation 4.13:

$U/U_m = \exp(-\ln 2\,(y/y_{0.5})^2)$

In the lower shear layer, the present mean streamwise velocity profiles exhibit self-similarity. They are also in reasonable agreement with the Gaussian profile and that of Hussein et al. (1994), except near the jet boundary where the present values are about 5% – 10% lower in comparison. These differences can be attributed to the presence of recirculation near the lower wall of the test section. In the lower shear layer of all three jets, only the near profile ($x/d \approx 10$) closely matches the benchmark profiles. Farther downstream, the mean velocity is becoming increasingly large as the location of the maximum mean streamwise velocity moves towards the surface. Also, the surface-normal extent of the profiles diminishes because the upper shear layer ceases to grow in the interaction region while the normalizing scale, $y_{0.5}$, is still growing.

5.4.2.2 Reynolds stresses

The similarity profiles of the streamwise Reynolds normal stress, $<u^2>/U_m^2$, are shown in Fig. 5.18a. At the near location ($x/d \approx 10$) of the square jet, the profile maintains some semblance of the saddle shape of the streamwise Reynolds stress with two off-axis peak values. The saddle shape broadens at the more distant locations as the profiles attain self-similarity in the upper and lower shear layers. The profiles are asymmetric about the jet axis in the interaction region. This is because, the free surface suppressed the peak values of the Reynolds stress in the upper shear layer relative to the peaks in the lower shear layer. The Rect_minor profiles show self-preservation neither in the lower shear layer nor the upper shear layer. In the lower shear layer, $<u^2>/U_m^2$ is still evolving with the peak value at $x/d \approx 20$ exceeding that of free jet by approximately 10%. For the Rect_major jet, the present data collapse relatively well in the upper and lower shear layers, and there is good agreement with that of the free jet in the lower shear layer. In the upper shear layer, the asymmetry caused by the confinement reduced the peak value by approximately 18% relative to the free jet. The streamwise evolutions of the surface-normal Reynolds normal stress, $<v^2>/U_m^2$, profiles presented in Fig. 5.18b are qualitatively similar to the streamwise Reynolds stress. However, in the upper shear layer, there is a characteristic dip of the tail of the curves toward the centerline of the jet. This is consistent with the damping of the surface-normal velocity fluctuations near the free surface. Also, for a given nozzle geometry, the peak values of the surface-normal Reynolds stress are

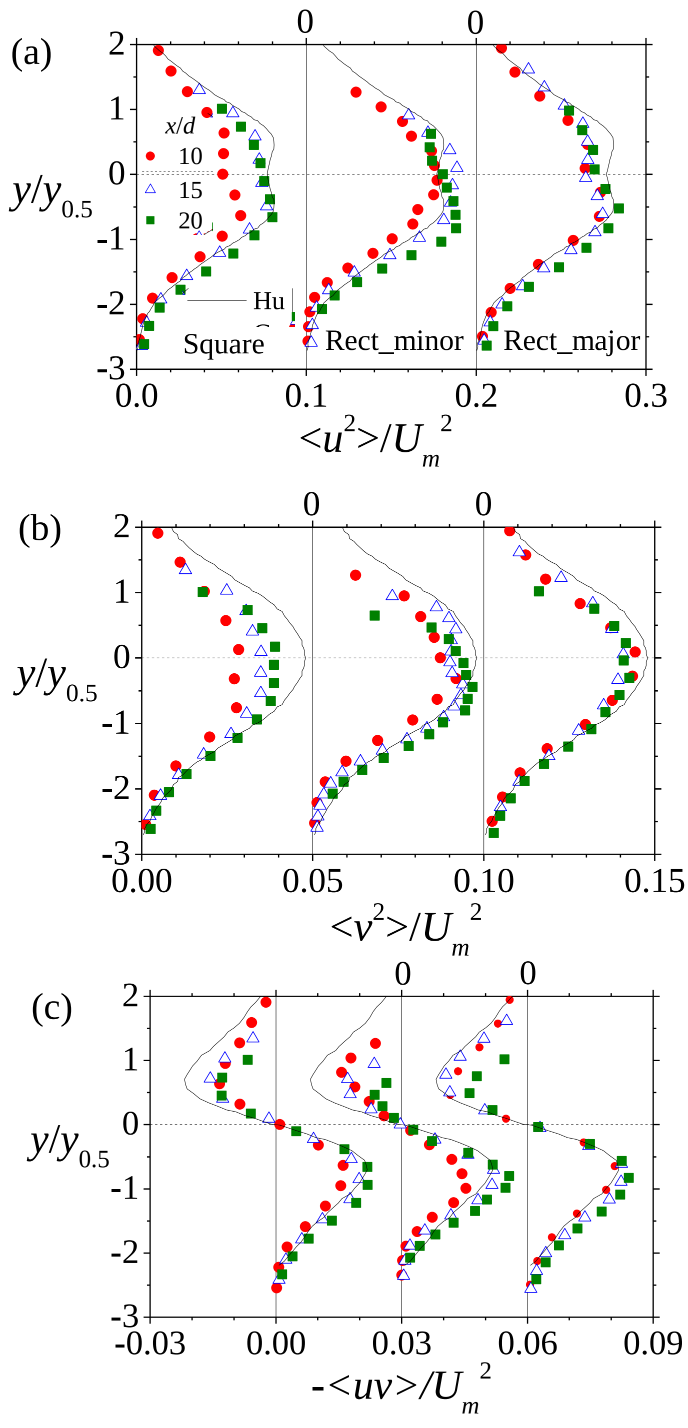

Figure 5.18. Surface-normal profiles of Reynolds stresses using similarity variables for square, Rect_minor and Rect_major jet at the selected *x/d* locations: (a) streamwise Reynolds normal stress, (b) surface-normal Reynolds normal stress and (c) Reynolds shear stress. Hu: Self-similar profiles from Hussein et al. (1994).

considerably lower than those of the streamwise Reynolds stress. This indicates the existence of strong anisotropy in the Reynolds stresses within the jets.

Figure 5.18c shows the similarity profiles of the Reynolds shear stress, -$<uv>/U_m^2$. The data in the upper and lower shear layers of the square jet attain near-similarity. Also, there is reasonable agreement with the benchmark profile of Hussein et al. (1994) in the lower shear layer. No such agreement is observed in the upper shear layer because the free surface reduces the area of significant Reynolds shear stress (mixing zone) relative to the free jet. In the minor plane of the rectangular jet, the Reynolds shear stress measured in the lower shear layer is still evolving; and has the largest peak at $x/d \approx 20$. This peak is approximately 12% higher than that of the benchmark profile. In the upper shear layer, the peak Reynolds shear stress is decaying as the mixing region shrinks rapidly with streamwise distance. At $x/d \approx 10$, the reduction in peak value of the Reynolds shear stress relative to the free jet is approximately 36%. By $x/d \approx 20$, this difference has widened to approximately 72%. For the Rect_minor jet, this provides a rough indication of the damping of the Reynolds shear stress producing motions in the upper shear layer relative to the lower shear layer. In the major plane of the rectangular jet, the Reynolds shear stress profiles collapse fairly well onto the benchmark profile within the lower shear layer. In the upper shear layer, no significant differences were observed between the free jet and the profiles at the near and intermediate locations. At $x/d \approx 20$, the reduction in peak value due to shrinkage of the mixing region is approximately 36% compared to the free jet. The Reynolds shear stress results in the rectangular nozzle suggest that the Rect_major orientation is more important for providing better mixing of the jet in the far field region. This should be contrasted with the Rect_minor orientation that provides better mixing in the near field region.

The similarity results presented herein suggest that the mean streamwise velocity profile measured in the interaction region is streamwise-invariant only in the lower shear layer; and resembles the self-preserving profile of a free jet. These results are independent of nozzle geometry. For the Reynolds stresses, on the contrary, even in the lower shear layer, self-similarity is confined to a limited region of the shear layer. The extent of this region does not show any systematic dependency on nozzle geometry. Similar discrepancies in the far field evolution of the Reynolds stresses have been reported for turbulent free jets (e.g., Wygnanski and Fiedler, 1969). Wygnanski and Fiedler (1969), for instance, suggested that the second-order moments require longer development distances, typically, some 50 – 70 diameters downstream of the nozzle to become self-preserving. Similarity of present Reynolds stress profiles improves in the major plane of the rectangular nozzle and the results compare more favourably with the free jet. This is not surprising considering the delayed onset of interaction of the Rect_major shear layer with the free surface.

5.5 Two-Point Correlation

To study the effect of a free surface on large-scale structure and integral length scales of surface attaching jets for various nozzle geometries, two-point correlations of the velocity fluctuations and the swirling strength are obtained. As mentioned in Chapter

2, The correlation functions, R_{AB} between two arbitrary quantities: A and B at a reference location, (x_{ref}, y_{ref}) are calculated using equation 2.14 as follows:

$$R_{AB}\left(x_{ref}+\Delta x, y_{ref}+\Delta y\right)=\frac{\langle A\left(x_{ref}, y_{ref}\right) B\left(x_{ref}+\Delta x, y_{ref}+\Delta y\right)\rangle}{\sigma_A\left(x_{ref}, y_{ref}\right) \sigma_B\left(x_{ref}+\Delta x, y_{ref}+\Delta y\right)}$$

where, Δx and Δy are the spatial separations between A and B in the streamwise and transverse directions, respectively; and σ_A and σ_B are the root-mean-square of A and B at (x_{ref}, y_{ref}) and ($x_{ref} + \Delta x$, $y_{ref} + \Delta y$), respectively. In the present study, two-point correlations are performed at various surface-normal locations of y_s/d = 0.5 and 1 in the upper shear layer and y_s/d = 3 in the lower shear layer all at a streamwise distance of x/d = 20 in the jet-surface interaction region. Iso-contours of the correlation functions obtained from square, Rect_minor and Rect_major jets are presented herein.

5.5.1 Two-point correlation between the velocity fluctuations

Iso-contours of the two-point auto-correlation function of the streamwise velocity fluctuation, R_{uu} are shown in Fig. 5.19. The most defining characteristic of R_{uu} is that the contours of the correlation are profoundly elongated in the streamwise direction. At $y_s/d \approx 0.5$, the contours of the correlation function are still attached to the free surface. This provides evidence of large-scale vortical structures near the free surface that have been ejected from the jet (e.g., Madnia and Bernal, 1994; Walker et al., 1995). The attached contours have relatively shallow streamwise inclination angles of approximately 12º ± 1.5º. These values are consistent with the value of approximately 11º reported for wall jets (Agelinchaab and Tachie, 2011b) and zero pressure gradient turbulent boundary

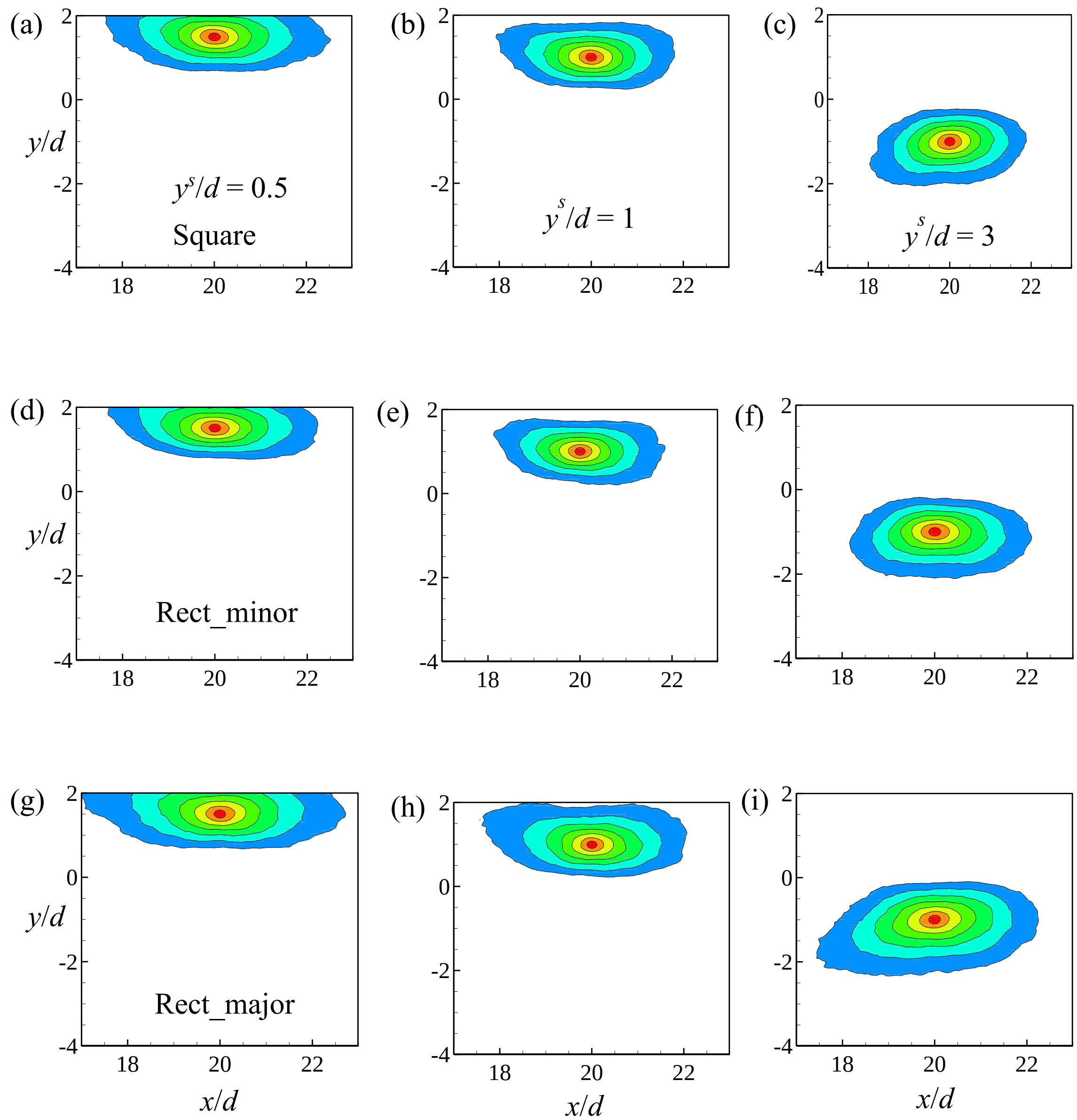

Figure 5.19. Iso-contours of R_{uu} for square, Rect_minor and Rect_major jet at various surface-normal locations at x/d = 20: (a) Square jet at y_s/d = 0.5, (b) square jet at y_s/d = 1, (c) square jet at y_s/d = 3, (d) Rect_minor jet at y_s/d = 0.5, (e) Rect_minor jet at y_s/d = 1, (f) Rect_minor jet at y_s/d = 3, (g) Rect_ major jet at y_s/d = 0.5, (h) Rect_ major jet at y_s/d = 1 and (i) Rect_ major jet at y_s/d = 3. Contour levels vary from 0.3 to 0.9 at intervals of 0.1.

layers (Volino et al., 2009). At larger distances from the free surface, the extent of significant R_{uu} correlation, as well as the streamwise inclination angle of the contours is decreasing. In the upper shear layer, the Rect_minor configuration decreases the spatial dimensions of the contours relative to the square jet. The Rect_major jet enhances the correlation in relation to the Rect_minor jet. At $y_s/d \approx 3.0$, the contours are almost parallel to the free surface because of the reduced influence of the free surface in the lower shear layer. Also, Rect_minor has no singnificant influence on the correlation here in comparison to the square jet. However, re-orientation of the nozzle caused enhancements in the correlation with respect to the Rect_minor orientation.

Figure 5.20 shows the contours of the spatial auto-correlation function of the surface-normal velocity, R_{vv}. The contours are elongated in the surface-normal direction and attached to the free surface for reference locations close to the free surface. At larger distances from the surface, the R_{vv} contours show the opposite trend to that of R_{uu}, which consists of enhanced growth with distance away from the free surface. This growth persists into the lower shear layer and is indicative of the reduced damping of the surface-normal velocity fluctuations. The most dramatic enhancements occur in the Rect_major jet, both in the upper and lower shear layer.

Figure 5.21 shows the contours of the spatial two-point cross-correlation, R_{uv}. The two-point cross-correlation can be used to provide a rough indication of average size and shape of the structures responsible for mixing in the shear layers. Specifically, it is caused by the turbulent motions that transport low-momentum ambient fluid into the faster moving jet and fast ejections from the jet into the surrounding fluid. For a free jet,

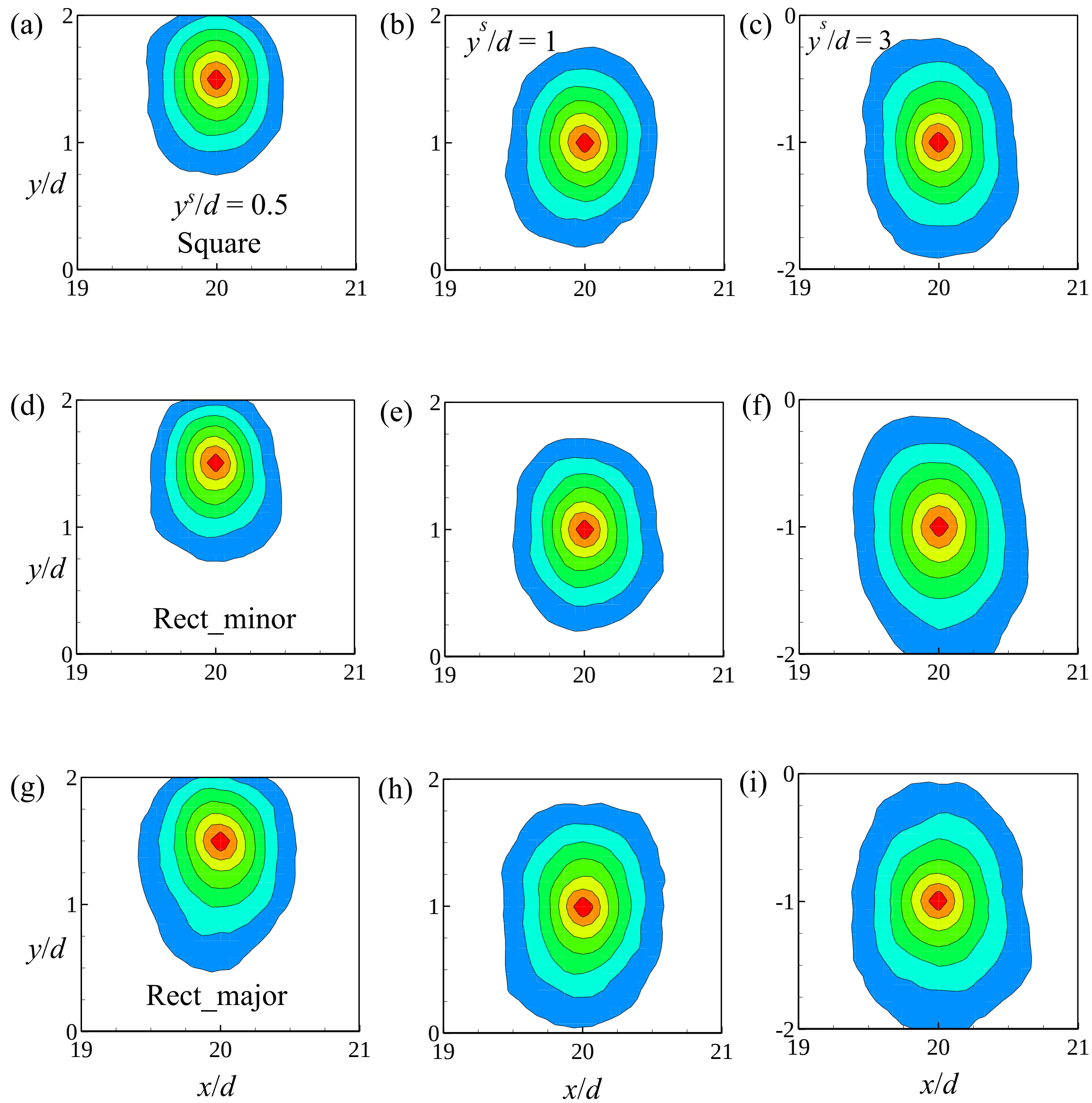

Figure 5.20. Iso-contours of R_{vv} for square, Rect_minor and Rect_major jet at various surface-normal locations at x/d = 20: (a) Square jet at y_s/d = 0.5, (b) square jet at y_s/d = 1, (c) square jet at y_s/d = 3, (d) Rect_minor jet at y_s/d = 0.5, (e) Rect_minor jet at y_s/d = 1, (f) Rect_minor jet at y_s/d = 3, (g) Rect_ major jet at y_s/d = 0.5, (h) Rect_ major jet at y_s/d = 1 and (i) Rect_ major jet at y_s/d = 3. Contour levels vary from 0.3 to 0.9 at intervals of 0.1.

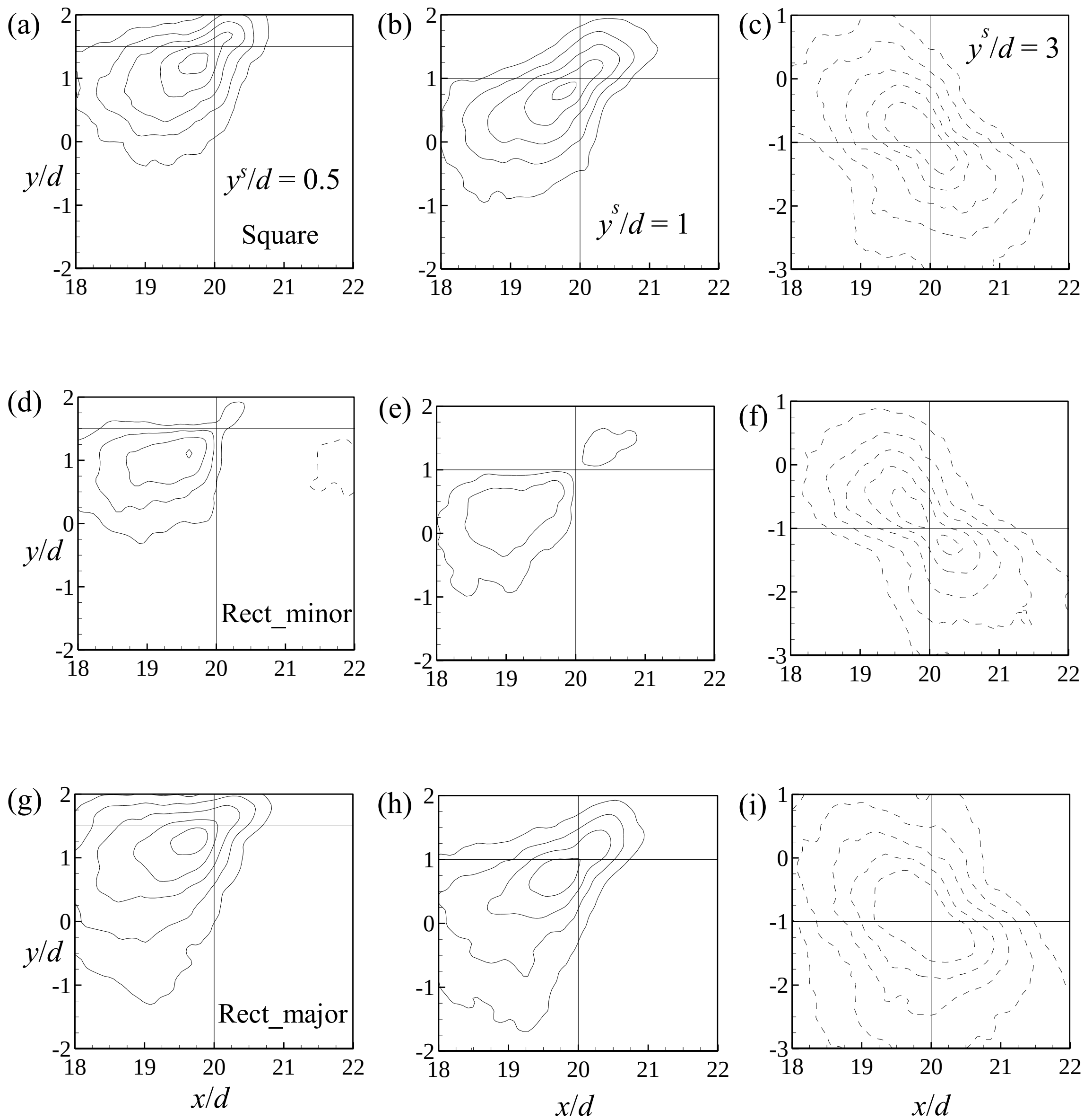

Figure 5.21. Iso-contours of R_{uv} for square, Rect_minor and Rect_major jet at various surface-normal locations at x/d = 20: (a) Square jet at y_s/d = 0.5, (b) square jet at y_s/d = 1, (c) square jet at y_s/d = 3, (d) Rect_minor jet at y_s/d = 0.5, (e) Rect_minor jet at y_s/d = 1, (f) Rect_minor jet at y_s/d = 3, (g) Rect_ major jet at y_s/d = 0.5, (h) Rect_ major jet at y_s/d = 1 and (i) Rect_ major jet at y_s/d = 3. Contour levels vary from -0.3 to 0.1 and 0.1 to 0.3 at intervals of 0.05. Dashed contours indicate the negative correlation.

R_{uv} at reference locations on the centerline has positive and negative contours on either side of the jet centerline (as mentioned in Chapter 4) due to the anti-symmetry of the Reynolds shear stress about the jet axis. At $x/d \approx 20$, the cross-correlation function is predominantly positive in the upper shear layer, with reduced spatial coherence in the Rect_minor jet but enhancement in the Rect_major jet. It is remarkable that even at reference locations close to the free surface, parts of the R_{uv} correlation extend into the lower shear layer. It does not only show that the velocity fluctuations captured by the correlation are due to the same large-scale structure but also supports the idea of the turbulent diffusion of Reynolds shear stress from the lower shear layer to feed the deficit created in the upper shear layer by the free surface (see Fig. 5.15c). In the lower shear layer (y_s/d = 3), the negative correlation that corresponds to contribution of opposite-signed u and v, spreads over the flow region more than the corresponding upper shear layer (y_s/d = 1) which is more intense for Rect_major jet, supporting increased spatial size of the coherent structures. The dramatic enhancements of the R_{uv}, R_{vv} and R_{uu} correlations in the far field of the Rect_major jet compared to the other configurations point to the Rect_major orientation as a more plausible choice for mixing enhancement in the far field region over the square and Rect_minor jets.

The effect of the nozzle geometry on the average size of turbulent scales is examined using the streamwise and surface-normal extents of the auto-correlation functions along the jet centerline. Following the approach mentioned in Chapter 4, the streamwise and surface-normal extents are estimated as the distance from the self-correlation peak to the minimum correlation level of 0.3 in the streamwise and surface-normal direction, respectively. The streamwise evolution of the streamwise extents of R_{uu} and R_{vv} (Lx_{uu} and Lx_{vv}, respectively); and the surface-normal extents of R_{uu} and R_{vv} (Ly_{uu} and Ly_{vv}, respectively) for the four nozzle geometries are shown in Fig. 5.22. The streamwise spatial scale Lx_{uu}/d (Fig. 5.22a) varies almost linearly with x/d within $5 \leq x/d \leq 15$ and mimics the streamwise growth of the jet half-width. Within $5 \leq x/d \leq 15$ the profiles from the circular, square and Rect_minor jets collapse fairly well onto a line of approximate slope 0.057. For the Rect_major jet, however, the structures grow more gradually first due to the axis-switching, following a line of approximate slope 0.051. Beyond $x/d \approx 15$, the structures vary rapidly in the major plane of the rectangular nozzle, causing an increase in slope of the profile to approximately 0.114. This is consistent with the structures growing rapidly in the far field of the Rect_major configuration, promoting mixing in the far field region. The profiles Lx_{vv}/d (Fig. 5.22b) are independent of nozzle geometry over the entire range of measurement. After the initial region, the profiles collapse reasonably well to a least-squares straight line of approximate slope 0.017. This is about one-third the growth rate of the streamwise spatial scale. Figure 5.22c shows profiles of the surface-normal extent of R_{uu} for the upper shear layer. The spatial scale is independent of nozzle geometry. In the initial region, the Ly_{uu}/d declines by about 30% to a minimum at $x/d \approx 5$. Downstream of this location, it increases monotonically following a least-squares line of approximate slope 0.025. The corresponding profiles for R_{vv} (Ly_{vv}/d) are shown in Fig. 5.22d. For this case, no near field decline is observed. Instead, all the measurements collapsed onto a single least-squares line of approximate slope 0.025. The similarity in growth rates with the streamwise counterpart is a manifestation of the almost linear growth of the jets. Figure 5.22e shows the streamwise evolution of the surface-

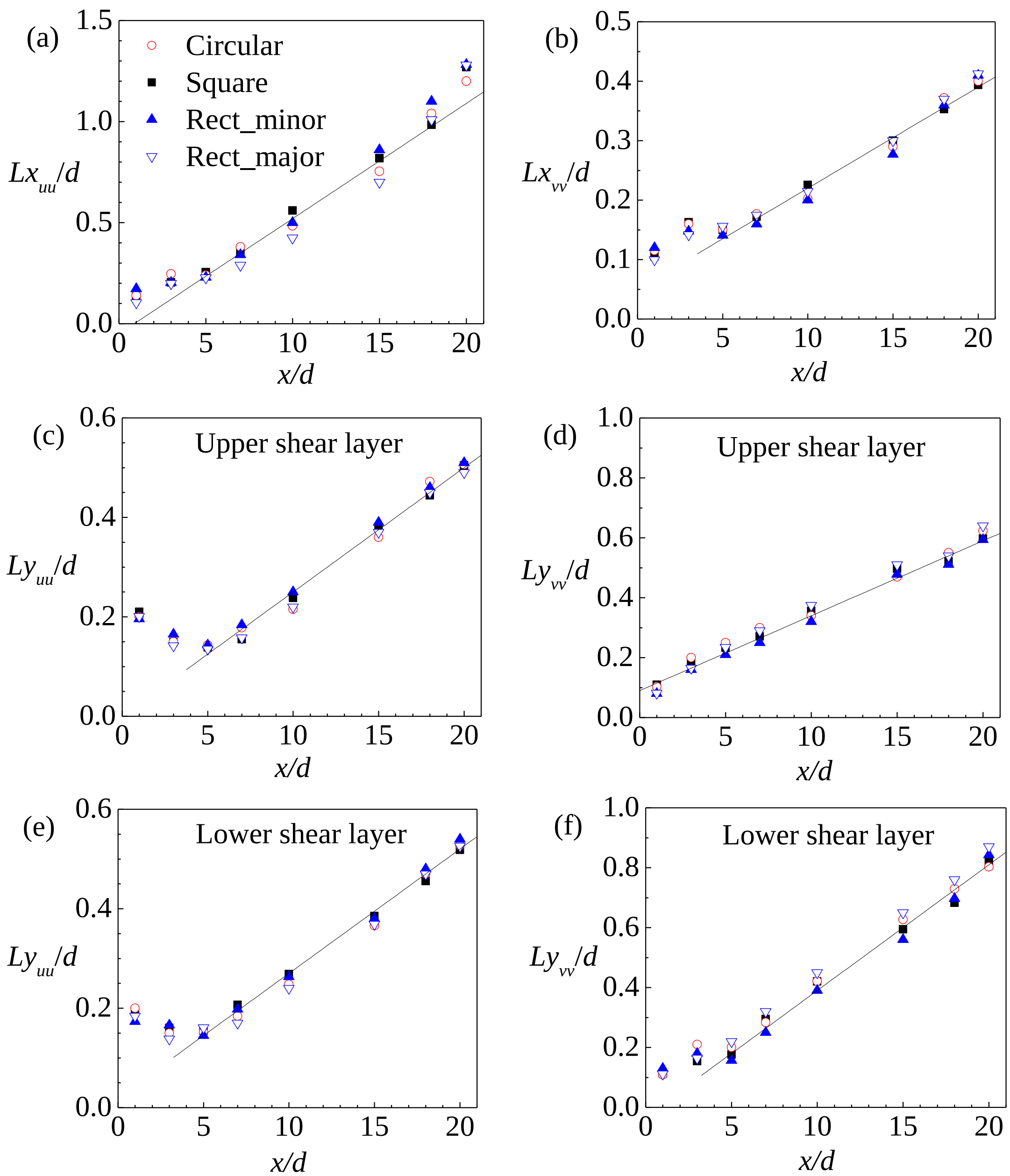

Figure 5.22. Variation of the integral scales of the auto-correlation functions with streamwise distance for various nozzle geometries along the jet centerline: (a) Streamwise integral scale of R_{uu}, (b) streamwise integral scale of R_{vv}, (c) surface-normal integral scale of R_{uu} in the upper shear layer, (d) surface-normal integral scale of R_{vv} in the upper shear layer, (e) surface-normal integral scale of R_{uu} in the lower shear layer and (f) surface-normal integral scale of R_{vv} in the lower shear layer.

normal extent of R_{uu} in the lower shear layer. These profiles are almost similar to those measured in the upper shear layer, indicating a nearly uniform surface-normal growth of large-scale structures. The profiles of the surface-normal extent of R_{vv} in the lower shear layer are presented in Fig. 5.22f. The values of Ly_{vv}/d are nearly independent of nozzle geometry and approximately follow a straight line of slope 0.042. This is about 40% larger than slope of the Ly_{vv}/d profiles in the upper shear layer. The disparity can be attributed to damping of the surface-normal velocity fluctuations by the free surface in the upper shear layer. It is noted that the present growth rate of Lx_{uu} and Ly_{uu} are approximately 26% higher and lower, respectively compared to a free jet by Aleyasin et al. (2018), where contoured nozzle was used. The discrepancy can be attributed to different initial and boundary conditions, such as: the enhanced mixing by an orifice nozzle used in the present study than contoured nozzle (Mi et al., 2001) leads to higher expansion of the shear layer, while the surface confinement limits the shear layer growth.

5.5.2 Two-point correlation between the swirling strength and velocity fluctuations

The spatial extent and strength of the velocity fields associated with the vortices within the shear layers for various nozzle geometries are examined using two-point correlations of the swirling strength and velocity fluctuations. Iso-contours of the auto-correlation function, $R_{\lambda\lambda}$ are shown in Fig. 5.23. The contours are compact and more rounded than those for the longitudinal and surface-normal correlations. Neither are they attached to the free surface for reference locations centered at $y^s/d = 0.5$. The reason for these characteristics is that the $R_{\lambda\lambda}$ correlations are produced by the smaller-scale vortices along the edge of the shear layer. These vortices were revealed to be the spanwise vortex

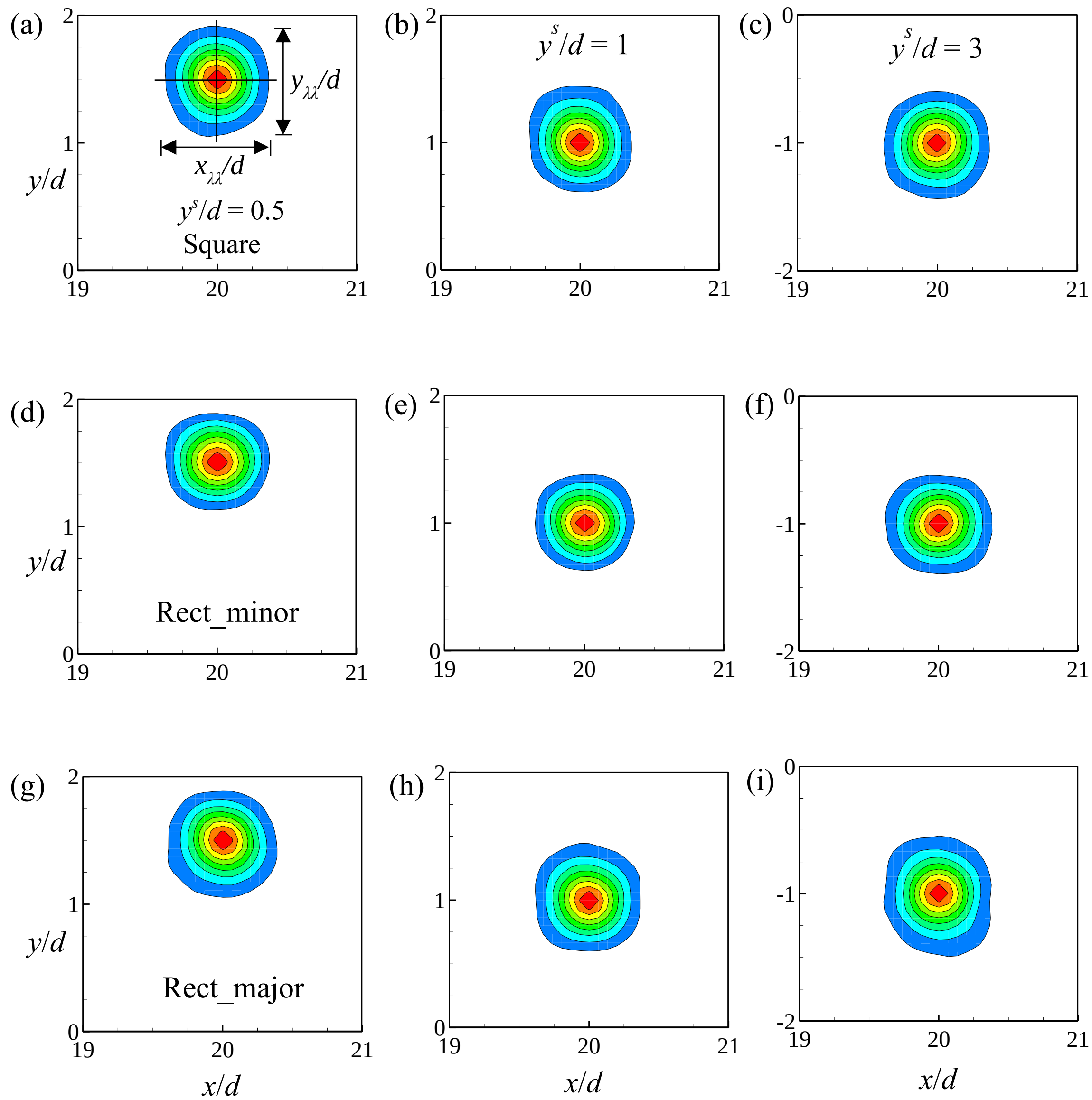

Figure 5.23. Iso-contours of $R_{\lambda\lambda}$ for square, Rect_minor and Rect_major jet at various surface-normal locations at x/d = 20: (a) Square jet at y_s/d = 0.5, (b) square jet at y_s/d = 1, (c) square jet at y_s/d = 3, (d) Rect_minor jet at y_s/d = 0.5, (e) Rect_minor jet at y_s/d = 1, (f) Rect_minor jet at y_s/d = 3, (g) Rect_ major jet at y_s/d = 0.5, (h) Rect_ major jet at y_s/d = 1 and (i) Rect_ major jet at y_s/d = 3. Contour levels vary from 0.2 to 0.9 at intervals of 0.1.

cores produced by the Kelvin-Helmholtz roll-up of the edge of the shear layer. Following the approach in Chapter 4, the total streamwise and surface-normal extents of $R_{\lambda\lambda}$ ($x_{\lambda\lambda}$ and $y_{\lambda\lambda}$, respectively) are estimated as the distance between the intersection points of the minimum correlation contour ($R_{\lambda\lambda}$ = 0.2) and the horizontal and vertical straight lines passing through the reference location, respectively as shown in Fig. 5.23a. Results depict a modest decrease of $x_{\lambda\lambda}/d$ (up to 15%) than $y_{\lambda\lambda}/d$ at the reference locations irrespective of nozzle geometry, indicating lesser pronounced growth of the vortices in the streamwise direction. This is further reflected by negligible effect of the free surface and nozzle geometry on $x_{\lambda\lambda}/d$. For the surface-normal extent; Rect_minor jet shows reduced extent (up to 12% at y_s/d = 0.5, for instance) compared to square and Rect_major jet due to reduced strain rate at downstream.

Figure 5.24 presents the iso-contours of two-point cross-correlation between the swirling strength and streamwise velocity fluctuation, $R_{\lambda u}$. Zero contour is shown in the figure which demarcates the positive and negative correlations. The retrograde (anti-clockwise) and prograde (clockwise) vortex core at the reference locations in the upper (y_s/d = 0.5 and 1) and lower shear layer (y_s/d = 3), respectively are reflected by the orientation of the positive and negative correlation around the reference location. With increasing distance from the surface, the negative correlations are strengthened because there is less damping of the spanwise vortex cores. This holds true for the square and Rect_major jets. For the Rect_minor jet, however, the spatial coherence of the velocity field around the reference location is lost. This is consistent with the damping of the R_{uu} and R_{uv} correlations from the surface in the minor plane of the rectangular jet. Moving

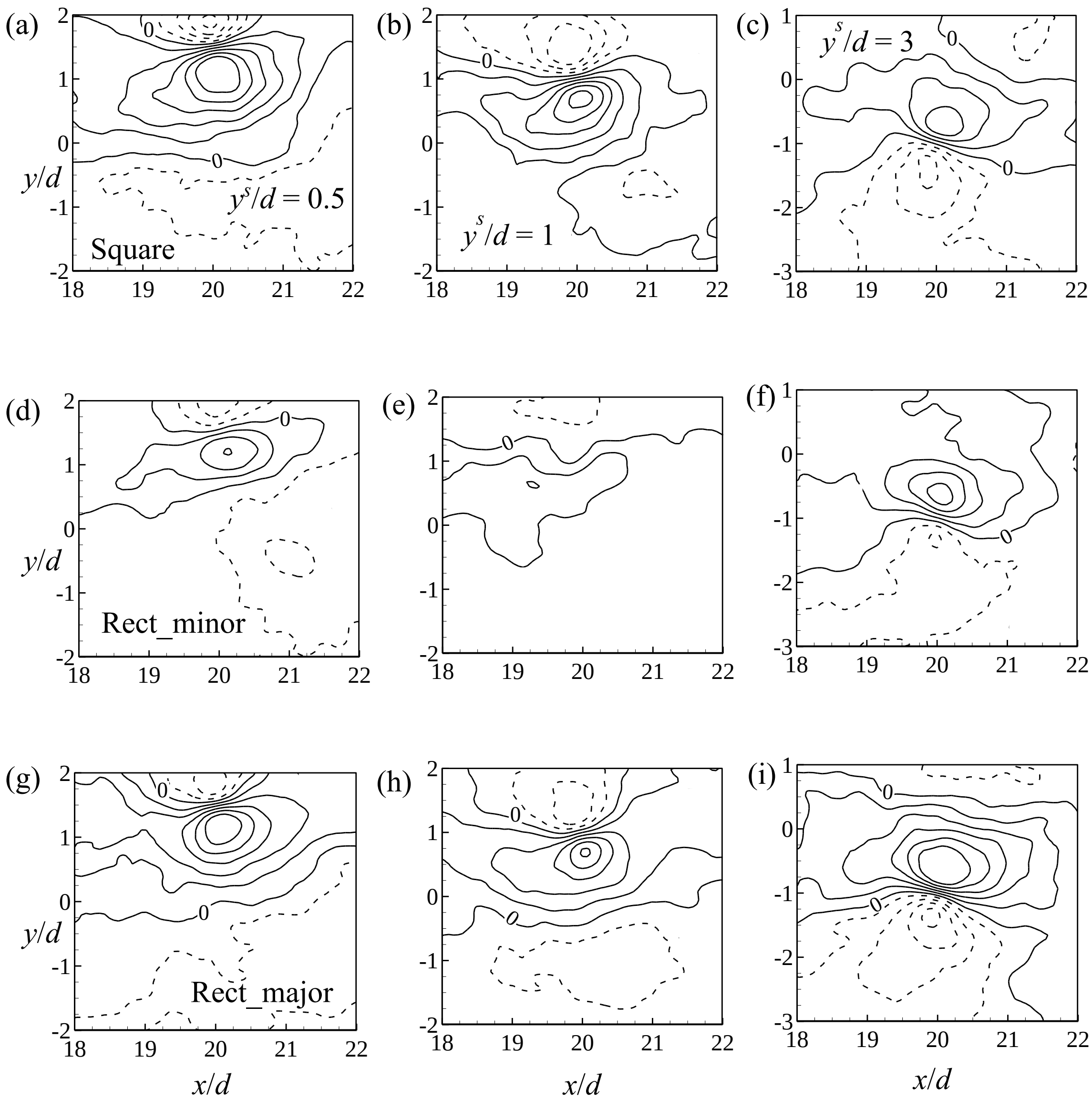

Figure 5.24. Iso-contours of $R_{\lambda u}$ for square, Rect_minor and Rect_major jet at various surface-normal locations at x/d = 20: (a) Square jet at y_s/d = 0.5, (b) square jet at y_s/d = 1, (c) square jet at y_s/d = 3, (d) Rect_minor jet at y_s/d = 0.5, (e) Rect_minor jet at y_s/d = 1, (f) Rect_minor jet at y_s/d = 3, (g) Rect_ major jet at y_s/d = 0.5, (h) Rect_ major jet at y_s/d = 1 and (i) Rect_ major jet at y_s/d = 3. Contour levels vary from - 0.1 to 0.1 at intervals of 0.02. Dashed contours indicate the negative correlation.

outwards the upstream inclination angle of the contours increases from 80º to 84º for square; 63º to 78º for Rect_minor and 75º to 77º for Rect_major. For the square and Rect_major jets, a small negative $R_{\lambda u}$ correlation is captured in the upper shear layer, which corresponds to the retrograde vortex in the on the same helix as the prograde vortex. In the lower shear layer ($y_s/d \approx 3$), the correlation contours are inclined at approximately 71º, 84º and 77º, square, Rect_minor and Rect_major jets, respectively.

Figure 5.25 shows the iso-contours of the two-point cross-correlation between the swirling strength and surface-normal velocity fluctuation, $R_{\lambda v}$. The orientation of the positive and negative $R_{\lambda v}$ supports the presence of the retrograde and prograde vortex cores within the shear layers. The contours show enhancement with distance away from the free surface for the square and Rect_major jets but rapid decorrelation in the case of the Rect_minor jet. In the upper shear layer, the contours of the square and Rect_major jets exhibit slight inclinations of approximately 7º to the upstream direction. This inclination angle is reduced to approximately zero in the Rect_minor jet. In the lower shear layer, the contours reversed and show the velocity field pattern around a prograde vortex. The contours are inclined at angles of approximately 7º, 5º and 12º for square, Rect_minor and Rect_major jet, respectively. It is noted that the inclination angles for $R_{\lambda u}$ and $R_{\lambda v}$ of the square jet in the lower shear layer are comparable to the result in Chapter 4.

The turbulent scales are further investigated in terms of the streamwise and surface-normal extents of $R_{\lambda\lambda}$ along the jet centerline. The variation of the total streamwise ($x_{\lambda\lambda}/d$) and surface-normal ($y_{\lambda\lambda}/d$) extents with respect to x/d for the four nozzle geometries

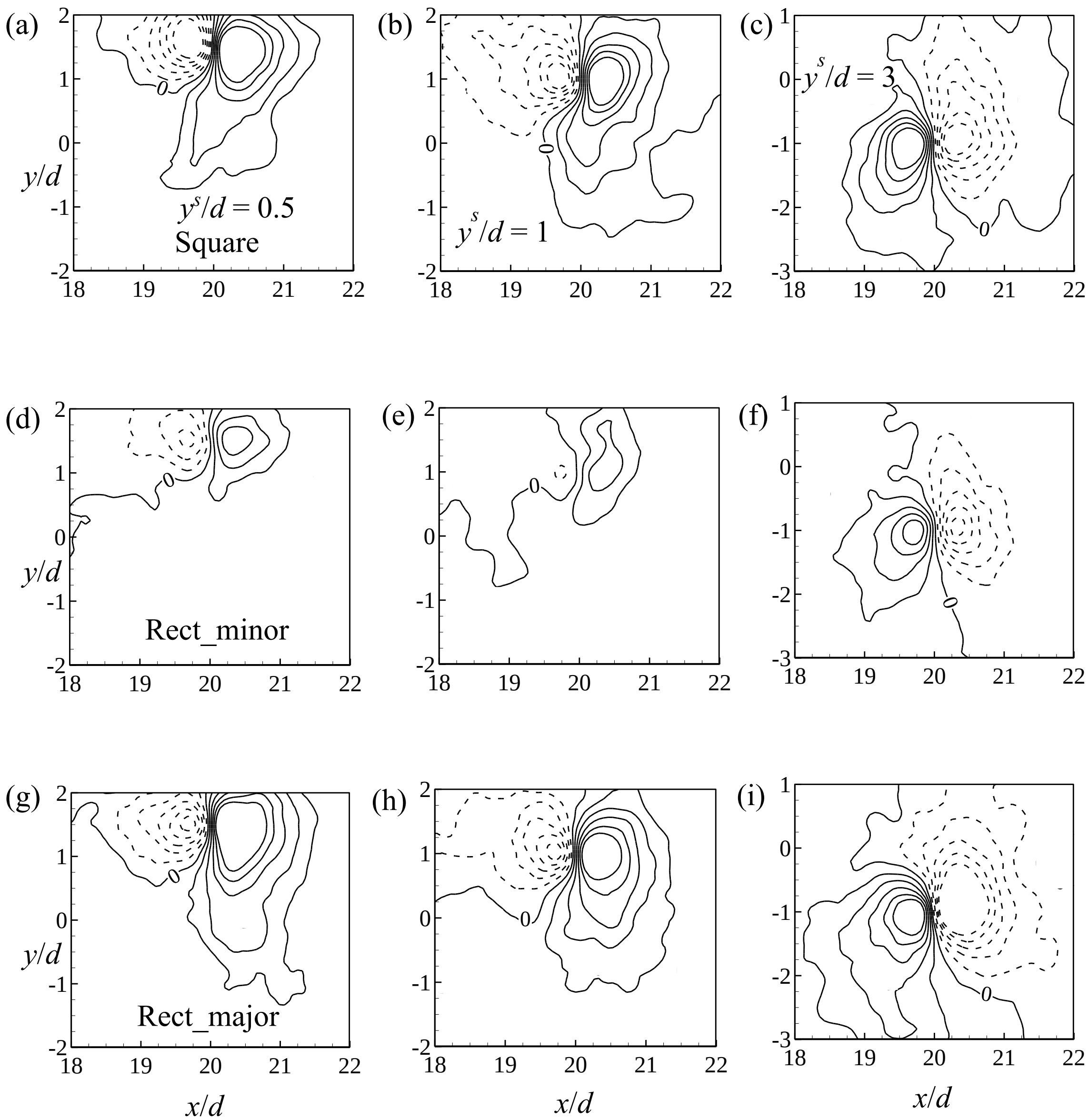

Figure 5.25. Iso-contours of $R_{\lambda v}$ for square, Rect_minor and Rect_major jet at various surface-normal locations at x/d = 20: (a) Square jet at y_s/d = 0.5, (b) square jet at y_s/d = 1, (c) square jet at y_s/d = 3, (d) Rect_minor jet at y_s/d = 0.5, (e) Rect_minor jet at y_s/d = 1, (f) Rect_minor jet at y_s/d = 3, (g) Rect_ major jet at y_s/d = 0.5, (h) Rect_ major jet at y_s/d = 1 and (i) Rect_ major jet at y_s/d = 3. Contour levels vary from - 0.1 to 0.1 at intervals of 0.02. Dashed contours indicate the negative correlation.

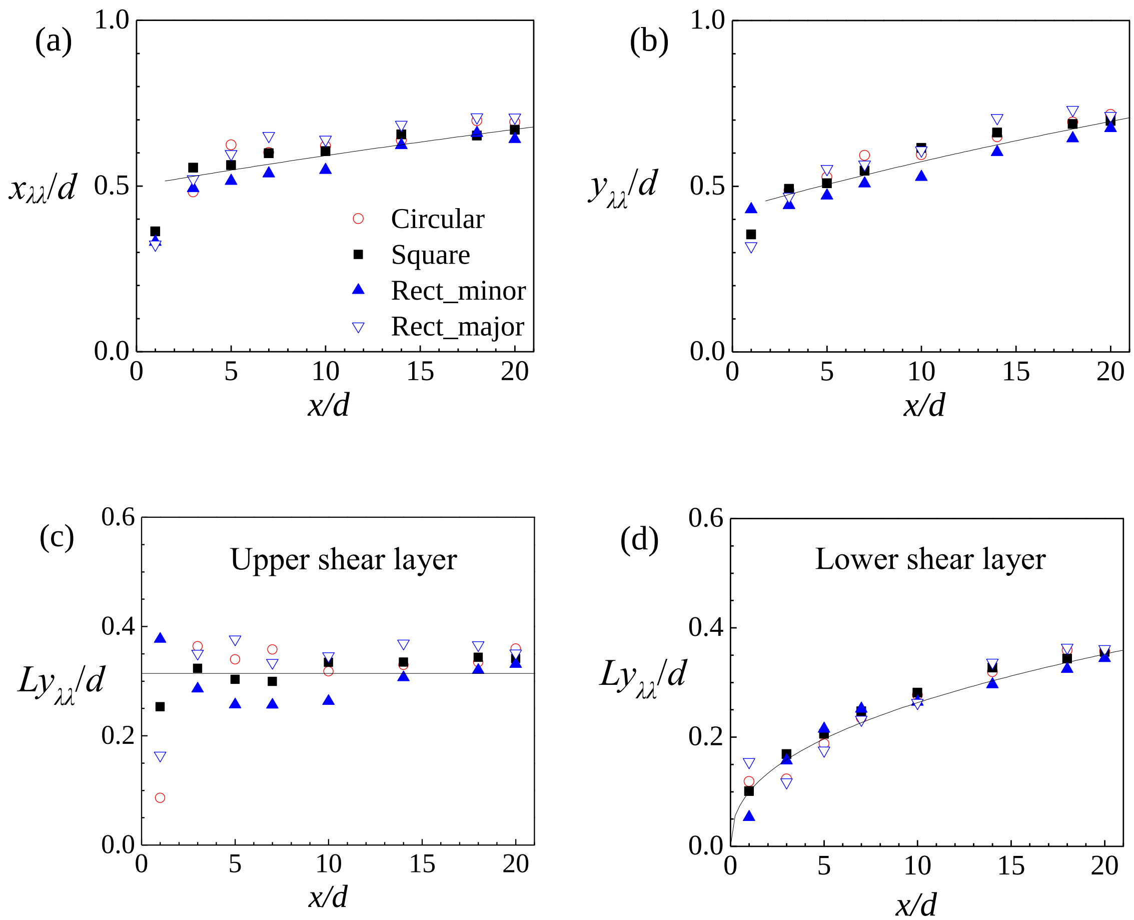

Figure 5.26. Variation of the integral scales of $R_{\lambda\lambda}$ with streamwise distance for various nozzle geometries along the jet centerline: (a) Total streamwise integral scale, (b) total surface-normal integral scale, (c) surface-normal integral scale in the upper shear layer and (d) surface-normal integral scale in the lower shear layer. Solid lines in (a), (b) and (d) are least squares curve fit.

are shown in Figs. 5.26a and 5.26b, respectively. The profiles of $x_{\lambda\lambda}/d$ rise rapidly in the near field region, not unlike the centerline turbulence intensity distributions. $x_{\lambda\lambda}/d$ increases more gradually within $3 \leq x/d \leq 15$ and levels off within the far downstream region. The Rect_minor jet reduced $x_{\lambda\lambda}/d$ within $3 \leq x/d \leq 10$ relative to the square jet with the differences reaching about 12%. Within the same region, the Rect_major jet increased the spatial scale relative to the Rect_minor jet by up to approximately 18%. These differences become smaller in the far field of the interaction region. The profiles for the surface-normal spatial scale, $y_{\lambda\lambda}/d$ (Fig. 5.26b) follow the same trend as the streamwise spatial scale, except for a more rapid rise in the near-exit region. Farther downstream, the profiles from the square and circular jets compare fairly well. However, there are similar reductions of up to approximately 6% in the minor plane of the rectangular jet and enhancements of 14% in the Rect_major jet. These differences diminish as the influence of nozzle geometry weakens farther out. In order to investigate the surface confinement effect on the turbulent scale, the data in Fig. 5.26b is splitted into two parts of the surface-normal extent for the upper and lower shear layer relative to the self-correlation peak ($Ly_{\lambda\lambda}$). Figure 5.26c shows profiles of surface-normal extent of $R_{\lambda\lambda}$ measured in the upper shear layer. Large discrepancies occur in data near the jet exit and may reflect differences in the initial vortices shed from the jet exits. The behaviour of the profiles mirrors that of the vorticity thickness, where in the Rect_minor jet, for instance, there is a region of relatively constant values of $Ly_{\lambda\lambda}$. Profiles of surface-normal extent of $R_{\lambda\lambda}$ measured in the lower shear layer are shown in Fig. 5.26d. $Ly_{\lambda\lambda}/d$ is a monotonically increasing function of streamwise distance and is nearly independent of nozzle geometry in the far field region. It was observed that the square and circular jet profiles reported in Figs. 5.26a, 5.26b and 5.26d can be approximated by the following curve:

$$y^{**} = 0.1\,(x/d - x_4)^b \qquad (5.5)$$

where, y^{**} is the normalized extent; b and x_4 are the increasing rate and a fitting parameter, respectively. The value of b and x_4 are summarized in Table 5.5.

Table 5.5. Summary of the fitting parameters for y^{**} profiles irrespective of nozzle geometry.

y^{**}	b	x_4	**Range**
$x_{\lambda\lambda}/d$	0.50	-25	$3 \leq x/d \leq 20$
$y_{\lambda\lambda}/d$	0.55	-14	
$Ly_{\lambda\lambda}/d$	0.42	0	

5.6 Joint Probability Density Functions

The effect of the nozzle geometry on velocity fluctuation correlation within the shear layers is further examined using joint probability density function (JPDF), $P(u, v)$. It also provides information about different turbulent events in Reynolds shear stress production. Results obtained at the same reference locations to the two-point correlation analysis are presented in Fig. 5.27. The abscissa and ordinate divide the plot into the following four quadrants: Q1, Q2, Q3 and Q4 representing fast entrainment of ambient fluid, slow entrainment of ambient fluid, slow ejection and fast ejection, respectively based on the orientation of the upper and lower shear layers as shown in Figs. 5.27a and 5.27c, respectively. The contours are elliptical for non-isotropic turbulence, where the innermost contours correspond to high-probability, but low-amplitude velocity fluctuations and outermost contours correspond to rare but large-amplitude velocity fluctuations. This implies that the total Reynolds shear stress calculated at this location will be determined both by the amplitude and frequency of the (u, v) pairs. The inclination of the iso-contours towards Q2 and Q4 irrespective of nozzle geometry, indicates slow

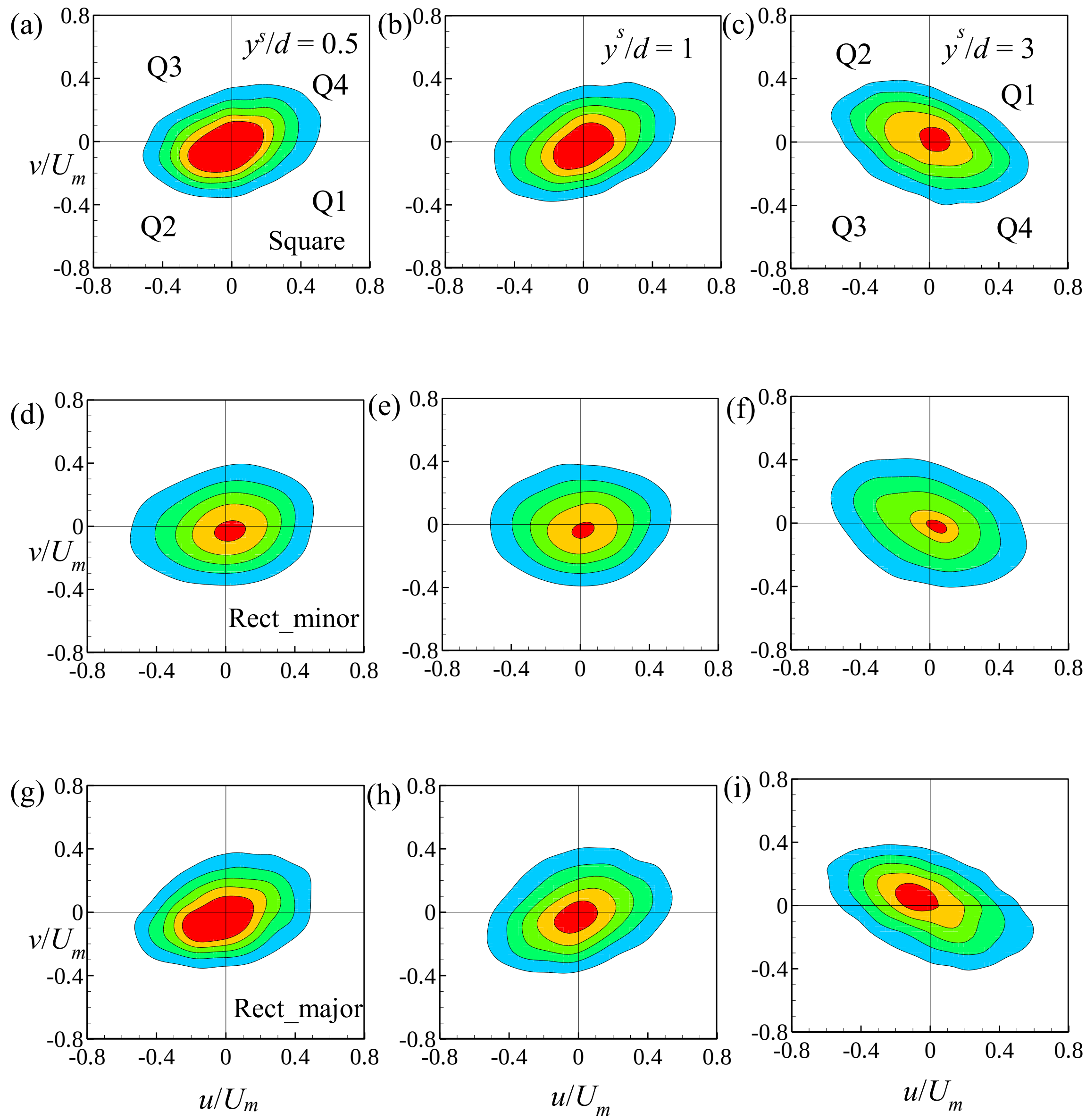

Figure 5.27. Iso-contours of JPDF for square, Rect_minor and Rect_major jet at various surface-normal locations at x/d = 20: (a) Square jet at y_s/d = 0.5, (b) square jet at y_s/d = 1, (c) square jet at y_s/d = 3, (d) Rect_minor jet at y_s/d = 0.5, (e) Rect_minor jet at y_s/d = 1, (f) Rect_minor jet at y_s/d = 3, (g) Rect_ major jet at y_s/d = 0.5, (h) Rect_ major jet at y_s/d = 1 and (i) Rect_ major jet at y_s/d = 3. Contour levels vary from 0.5 to 2.5 at intervals of 0.5.

entrainment and fast ejection to be the major contributor to Reynolds shear stress, -<*uv*>. In the upper shear layer of the Rect_minor jet, the contours are more inclined in favour of the fluctuating streamwise velocity axis. This is consistent with the more rapid decay of the Reynolds shear stress in this jet compared to the other configurations. Values of the inclination angle of the contours are estimated based on the slope of the least-squares linear fit through the maximum probability point and the extreme points on the outermost contour level. The values are estimated to be approximately 23.5º ± 0.3º and 24.5º ± 1.5º for the square and Rect_major jets. This is reduced to approximately 17.6º and 11.4º at $y_s/d \approx 0.5$ and 1.0 by the Rect_minor configuration. At $y_s/d \approx 3.0$, the angle of inclination is unaffected by nozzle geometry. From the free surface towards the lower shear layer, the amplitude of the high frequency events decreases for all cases; and is accompanied by more elongation of the outermost contours in favour of Q2-Q4. This is an indication of the decrease in size and peak values of the Reynolds shear stress in the upper shear layer relative to the lower shear layer. Furthermore, it is noticed that in the upper shear layer the Rect_minor configuration reduces the area of the maximum JPDF contour relative to those of the square and Rect_major jets. This decline was also seen in the skewness factors of *u* and *v*; and indicates a decline in high frequency instantaneous positive *u* and *v*-fluctuations in the Rect_minor jet. The results presented here indicate that for the rectangular nozzle, the effect of nozzle re-orientation is to restore the inclination of the contours in the upper shear layer and increase the intermittency of the fluctuations in the lower shear layer.

Figure 5.28 shows the iso-contours of the weighted JPDF (WJPDF), $uvP(u, v)$ to supplement the JPDF results, which also provides insight into the strength of the correlation. The WJPDF exhibits plots with two pairs of positive and negative lobes. In the upper shear layer, the positive lobes are considerably larger than the negative lobes, supporting the dominance of the Q2 and Q4 events in producing the mean Reynolds shear stress. As the Reynolds shear stress rapidly declines in the interaction region of the Rect_minor jet, the positive contours shrink in size when compared to the square and Rect_major nozzles. In the minor plane of the rectangular jet, all the contours are approximately parallel to the u-axis, implying that there is very little correlation between the instantaneous velocity fluctuation pairs, (u, v). This will have a diminishing effect on the total Reynolds shear stress. In the lower shear layer, the first and third quadrants contributed to the positive contours, and therefore have no significant effect on the Reynolds shear stress. The large negative contours confirm the dominant influence of the Q2 and Q4 fluctuations in determining the relatively high positive values of Reynolds shear stress in the lower shear layer.

5.7 Proper Orthogonal Decomposition

In order to investigate the effect of nozzle geometry on the dynamic role of the energetic structures, the proper orthogonal decomposition (POD) is performed. The snapshot approach of the POD analysis (Sirovich, 1987), described briefly in Appendix A, is applied in the present study. Results obtained from the first (Plane1) and the last (Plane 3) measurement plane are discussed in this section. It should be noted that the vertical and horizontal edges of the two planes are trimmed in order to exclude spurious

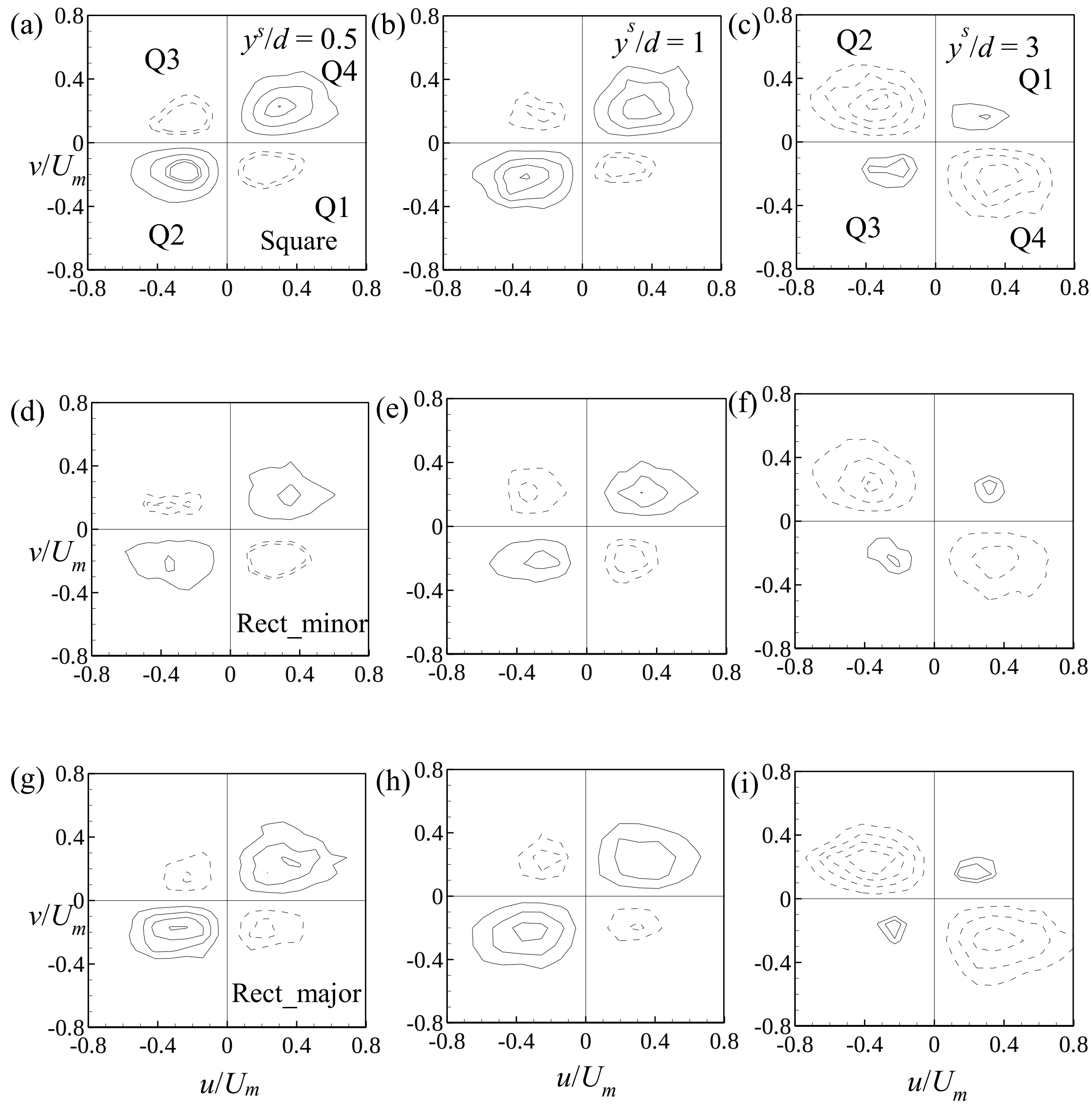

Figure 5.28. Iso-contours of WJPDF for square, Rect_minor and Rect_major jet at various surface-normal locations at x/d = 20: (a) Square jet at y_s/d = 0.5, (b) square jet at y_s/d = 1, (c) square jet at y_s/d = 3, (d) Rect_minor jet at y_s/d = 0.5, (e) Rect_minor jet at y_s/d = 1, (f) Rect_minor jet at y_s/d = 3, (g) Rect_ major jet at y_s/d = 0.5, (h) Rect_ major jet at y_s/d = 1 and (i) Rect_ major jet at y_s/d = 3. Contour levels vary from -0.0016 to -0.0004 and 0.0004 to 0.0016 at intervals of 0.0004. Dashed contours indicate the negative correlation.

data at the extremities of the planes from the analysis. This reduces the streamwise extents of Plane 1 and Plane 3 to $0.5 \leq x/d \leq 7$ and $17 \leq x/d \leq 23.5$, respectively, and the surface normal extent of each plane is $6.45d$ starting from the surface-normal location $0.05d$ below the free surface.

5.7.1 Convergence of turbulent kinetic energy

A convergence test is performed to determine if the present sample size of N_s = 5000 snapshots is sufficient for the POD analysis. In the convergence test, the turbulent kinetic energy content in the individual POD mode (fractional energy) and the cumulative energy for the mode numbers, m are obtained using varying number of snapshots from N_s = 300 to 5000. Since the results for the four nozzle configurations are the same, profiles for the square jet in Plane 1 and Plane 3 are presented in Fig. 5.29. Results show collapsed profiles of the fractional and cumulative energy for $N_s \geq 4000$. Thus, the 5000 snapshots used in the present study are sufficient to converge the POD results.

5.7.2 Fractional and cumulative energy distribution

The energy spectra for different nozzle geometries are examined using the fractional and cumulative energy distribution in POD modes in Fig. 5.30. Results obtained from Plane 1 and Plane 3 for the first 50 modes are presented to investigate the energy content in the near field and interaction region, respectively. The variation of fractional energy with mode number follows an exponential distribution (Nyantekyi-Kwakye et al., 2015b; Aleyasin et al., 2018). In Plane 1 (Fig. 5.30a), the fractional energy of the first POD mode is nearly independent of nozzle geometry (about 2.7% for circular and

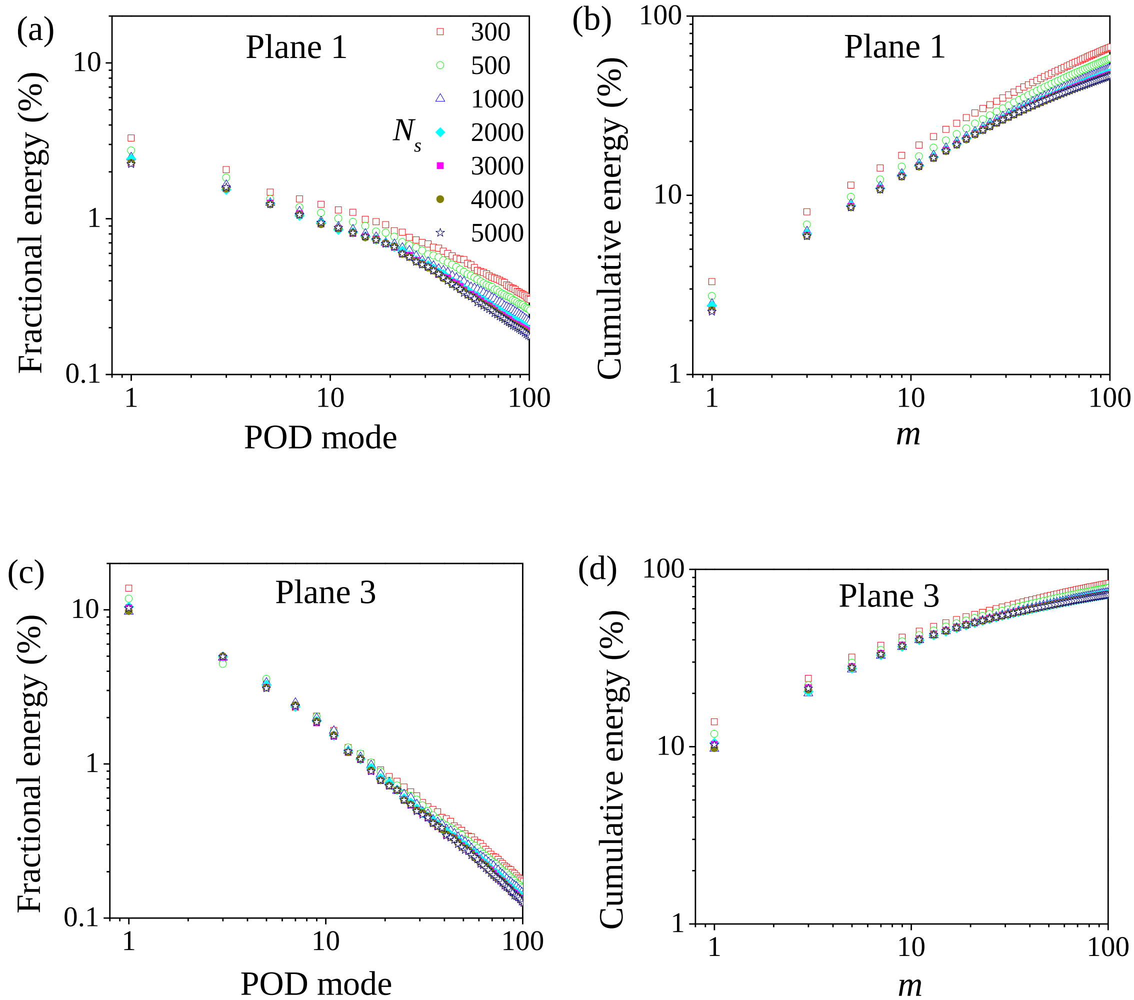

Figure 5.29. Fractional and cumulative energy distribution obtained using various number of snapshots in (a - b) Plane 1 and (c - d) Plane 3 for the square jet.

Rect_major jet; and 2.3% for square and Rect_minor jet), which is consistent with the self-similarity of the streamwise spatial scale in the near field region. In the succession up to mode number 10, there is approximately up to 27% reduction in modal energy for the non-circular jets in comparison to the circular jet. This can be partly attributed to the break-down of the large-scale structures in the non-circular jets, introduced by the non-uniform curvature of the exit perimeter. With increasing mode order, the fractional

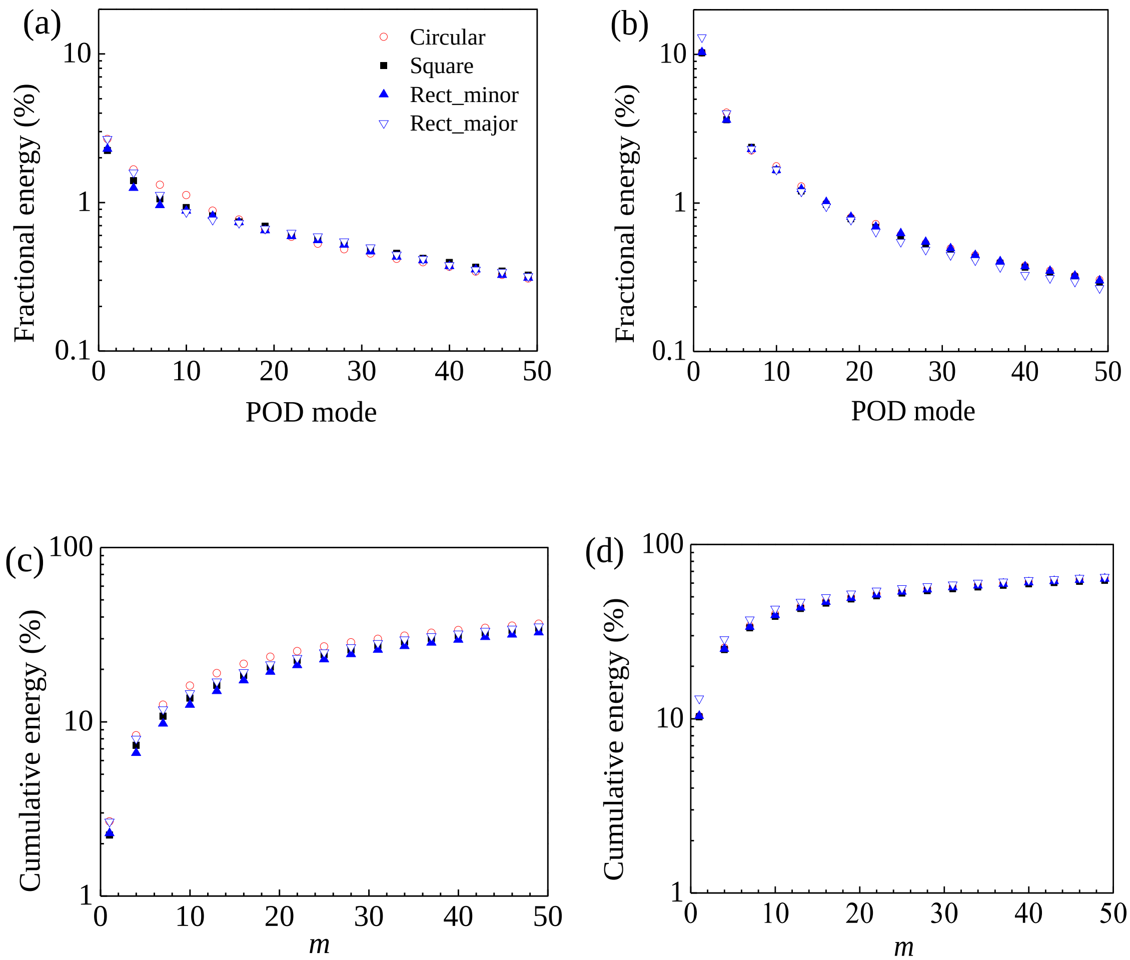

Figure 5.30. Variation of fractional and cumulative energy with the mode numbers for various nozzle geometries: (a) Fractional energy in Plane 1, (b) fractional energy in Plane 3, (c) cumulative energy in Plane 1 and (d) cumulative energy in Plane 3.

energies collapse and decay rapidly, reaching less than approximately 4% by the 50th mode. It is noted that the result of Rect_minor jet in the 1st mode is about 70% lower than wall attaching Rect_minor jet by Nyantekyi-Kwakye et al. (2015b) at a similar offset height ratio (H/d = 2.5), which is consistent with the flow filed occupied by less energetic eddies at the presence of a free surface as discussed in Chapter 4. The profiles of the fractional energy measured in Plane 3 are shown in Fig. 5.30b. In Plane 3, the fractional energy contributions of the first POD mode are about 4 to 5 times larger than those in Plane 1, suggesting the presence of more energetic eddies in the interaction region than in the near field region. In Plane 3, the major-axis orientation of the rectangular nozzle caused an approximately 21% increase in mode1 in comparison to the Rect_minor jet. These results are consistent with the increasing size of the length scales in the interaction region, as well as the more rapid growth of the two-point correlation in the major plane of the rectangular nozzle. With increasing mode order, the profiles collapse onto a single exponential curve. Compared to Plane 1, the results indicate a more rapid modal energy decay in Plane 3, which would imply a faster convergence of the POD basis set in this case than in Plane 1. Similar observations were reported in previous free and wall attaching jet studies (Nyantekyi-Kwakye et al., 2015b; Aleyasin et al., 2018).

The variation of the cumulative energy with mode order in Plane 1 and Plane 3 are shown in Figs. 5.30c and 5.30d, respectively. In Plane 1, the results indicate that in order to capture the same amount of total turbulent kinetic energy, a smaller number of lower-order POD modes will be required in the circular jet than in the square, Rect_minor and Rect_major jets. For instance, to capture approximately 30% of the total energy in Plane 1, this will require the first m = 32 low-order modes as compared to m = 36 for the square and Rect_major jets; and m = 42 for the Rect_minor jet. These values are indicative of the energy convergence speeds of each POD. A comparitibly faster convergence for circular jet can be attributed to higher energy content in the lower order modes as mentioned earlier. In the interaction region, even fewer modes are required to capture the same 30% of the total energy: roughly 6 low-order modes for the various test cases. The reduced number of low-order modes in the interaction region is indicative of faster energy convergence, and by inference, larger-scale eddies in this region compared to the near field region. This is consistent with similar rapid energy convergence in the far field region of offset wall jets (Nyantekyi-Kwakye et al., 2015b) and free jets (Aleyasin et al., 2018). It is noted that to capture a specific cumulative energy of 30% for instance, higher number of m (m = 42) is required for the present Rect_minor jet in Plane 1 than those (m = 7) for wall attaching jet by Nyantekyi-Kwakye et al. (2015b), indicating slower energy convergence due to lower energy content for the surface attaching jet.

5.7.3 Reconstructed velocity vectors

To provide insight into the spatial structure of the individual POD modes for the different exit geometries, vector plots of the eigenfunctions were generated. For free shear flows, the spatial distributions of the eigenfunctions have a striking similarity to both the small- and large-scale structure of the shear layer. Figure 5.31 shows the vector plots of 1st, 3rd, 5th and 10th POD modes for the square jet in Plane 1. These modes contain approximately 2.2%, 1.6%, 1.2% and 0.9% of the total turbulent kinetic energy, respectively. The most energetic mode, which is considered to represent the flapping motion of the shear layer is shown in Fig. 5.31a. The plot shows a large-scale region of high-momentum fluid ($u > 0$, $v < 0$) between $x/d \approx 2$ and $x/d \approx 7$ below the jet centerline, whose size is increasing in the streamwise direction. There are two counter-clockwise (positive) vortices centered on the jet axis: a small vortex located at $x/d \approx 3.8$ and a much larger vortex located at $x/d \approx 7$, which has a surface-normal scale of approximately $2d$. The large vortical structure near the edge of the measurement plane is consistent with the

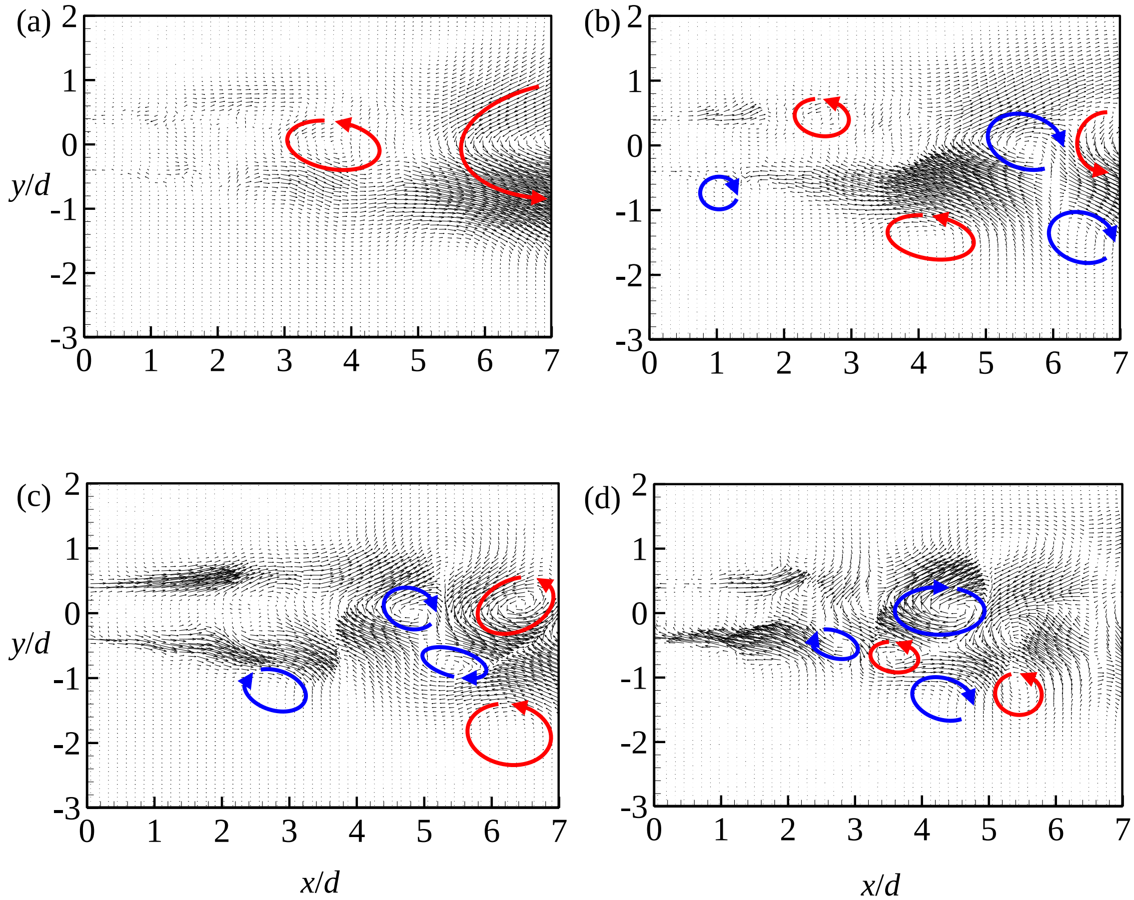

Figure 5.31. Vector plots of the POD modes for square jet in Plane 1: (a) mode 1, (b) mode 3, (c) mode 5 and (d) mode 10.

idea of smaller-scale vortices merging to form larger-scale structures as described by Winant and Browand (1974). For the higher order modes (Figs. 5.31b – 5.31d), the vector plots reveal structures having almost the same shape as the shear layers, but with a noticeable downward bent relative to the free surface. This characteristic bent away from the free surface can be attributed to the confinement imposed on the jet. The plots also show spanwise vortices with alternating directions of rotation at the edge of the shear layers. This suggests that the higher order modes are responsible for the flow dynamics of the smaller-scale counter-rotating spanwise vortex cores at the edge of the shear layers.

Qualitatively similar results were reported in POD of wall attaching jets (Nyantekyi-Kwakye et al., 2015b) and surface attaching jets (Shinneeb et al., 2011; Wen et al., 2014a, 2014b) that showed that the spatial POD modes govern the development of the shear layer vortices. Figure 5.32 shows the vector plots of the 1st, 3rd, 5th and 10th POD modes for the Rect_minor and Rect_major jets in Plane 1. These modes contain approximately 2.3%, 1.4%, 1.1% and 0.9% of the total energy, respectively for Rect_minor jet; and 2.7%, 1.7%, 1.3% and 0.9% of the total energy, respectively for Rect_major jet. The results indicate a similarly elongated zone of high-momentum fluid ($u > 0$, $v < 0$) below the jet axis for the first mode of each jet. However, compared to the square, only the Rect_major jet still has the relatively large positive spanwise vortex at the edge of the field of view. The absence of the merged vortex at $x/d \approx 7$ for the Rect_minor jet can be explained by the larger inclination angle of the high-momentum structure in the Rect_minor jet compared to the square and Rect_major jets. This is consistent with the more rapid expansion of the Rect_minor jet compared to the other jets. Thus, the Rect_minor jet expanded so rapidly that it affected the vortex pairing and merging process by bringing the individual vortices farther apart. Re-orientation of the rectangular jet caused the high-momentum structure to almost parallel to the jet axis, which is consistent with the delayed expansion of the Rect_major jet caused by the axis-switching effect. For the higher-order modes (3, 5 and 10), the amount of inclination of the shear layer leaves an imprint in the spatial distributions of the modes. Also, the smaller-scale spanwise vortices of alternating sense of rotation are still dominant features of the vector fields of the higher-order modes, but those in the Rect_minor jet appear to be less organised than in the square and Rect_major jets.

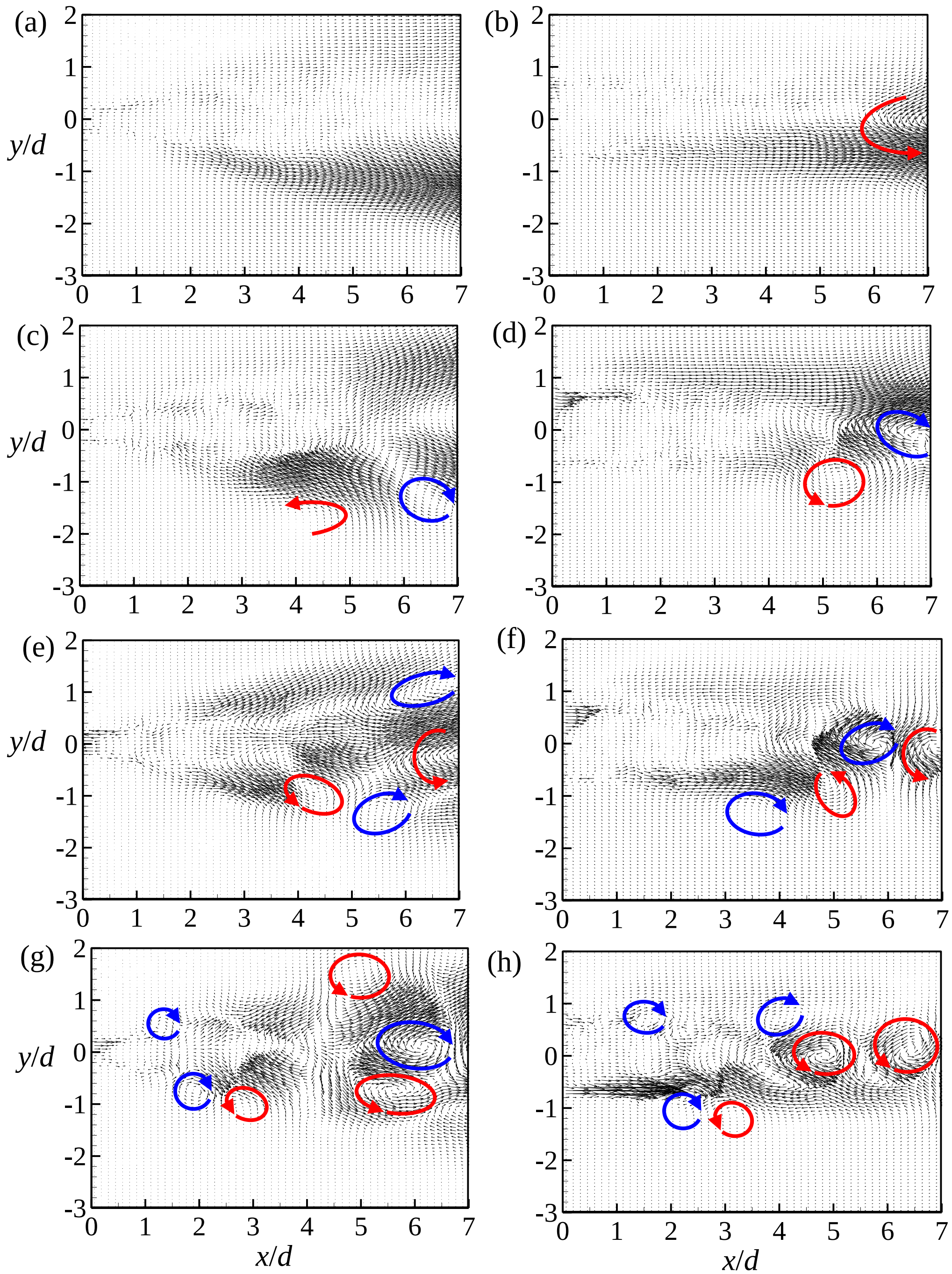

Figure 5.32. Vector plots of the POD modes for rectangular jets in Plane 1: (a) mode 1 for Rect_minor, (b) mode 1 for Rect_major, (c) mode 3 for Rect_minor, (d) mode 3 for Rect_major, (e) mode 5 for Rect_minor, (f) mode 5 for Rect_major, (g) mode 10 for Rect_minor and (h) mode 10 for Rect_major jet.

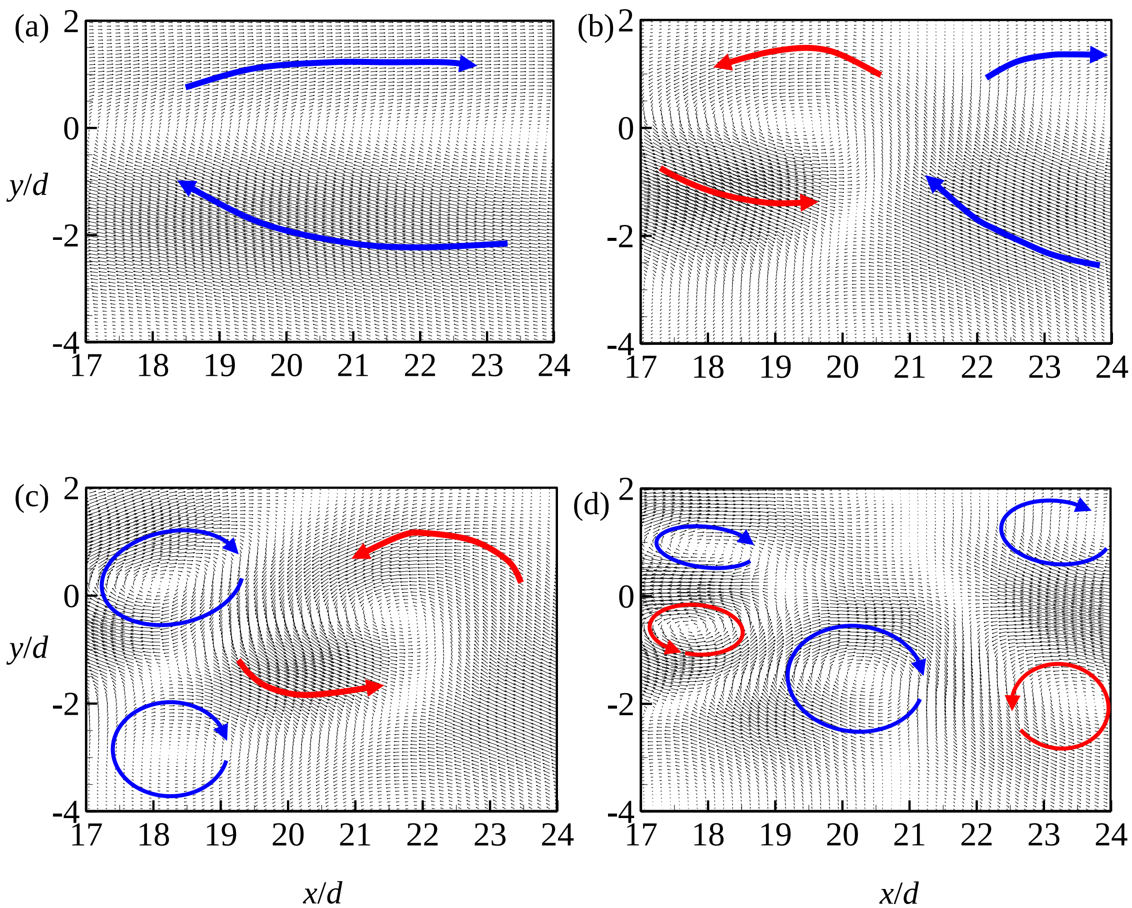

Figure 5.33. Vector plots of the POD modes for square jet in Plane 3: (a) mode 1, (b) mode 3, (c) mode 5 and (d) mode 10.

Figure 5.33 shows the spatial distributions of the 1st, 3rd, 5th and 10th POD modes in Plane 3 of the square jet. These modes contain approximately 10%, 5.0%, 3.1% and 1.7% of the total energy, respectively. The first POD mode presents the appearance of a massive negative (clockwise rotating) vortex with the jet centerline as its axis. The large size of the vortex is in agreement with the rapid growth of the large-scale structures in the interaction region to produce more energetic turbulent structures with faster energy convergence than in the near field region. For the higher-order modes, the spatial fields

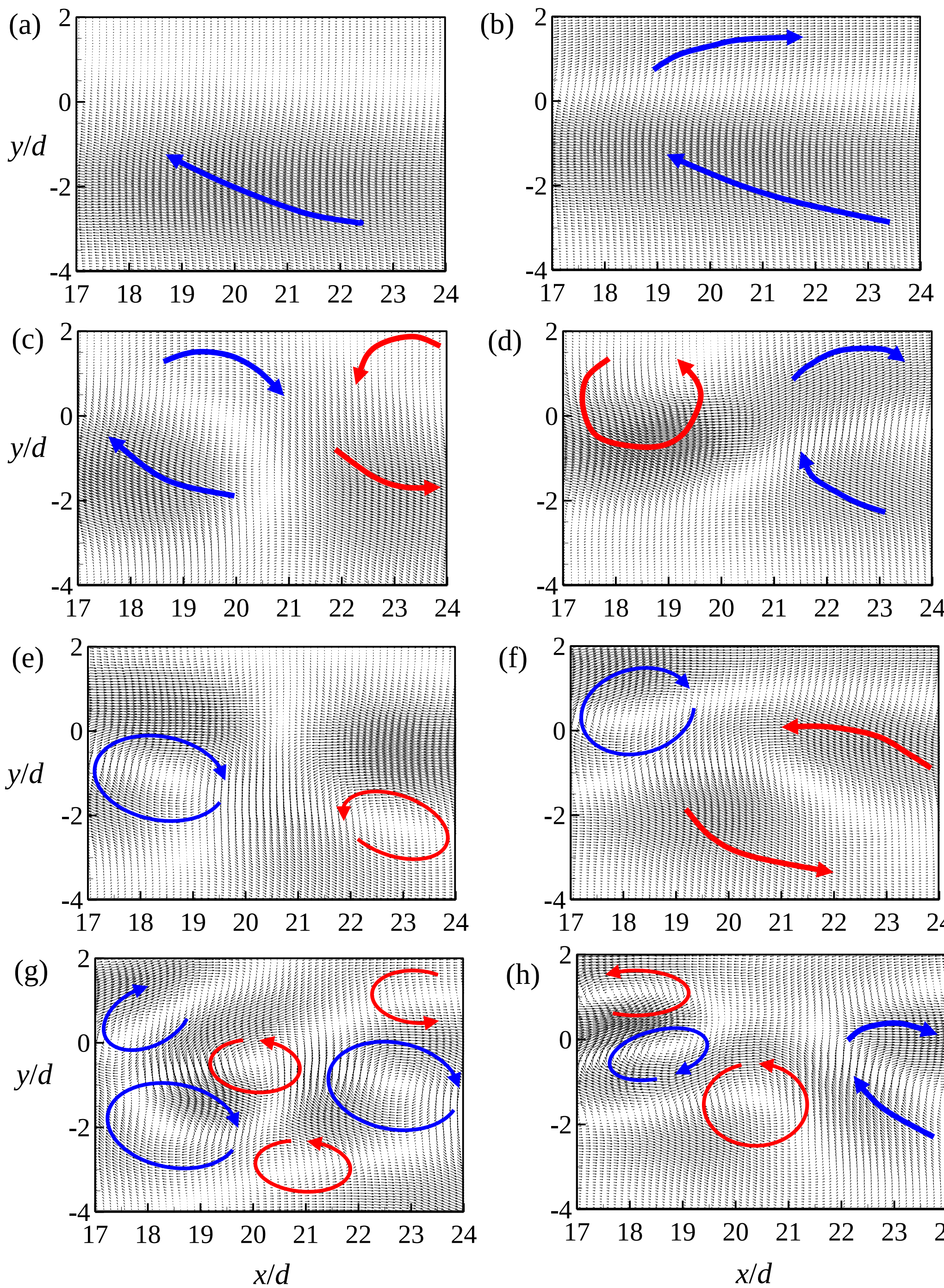

Figure 5.34. Vector plots of the POD modes for rectangular jets in Plane 3: (a) mode 1 for Rect_minor, (b) mode 1 for Rect_major, (c) mode 3 for Rect_minor, (d) mode 3 for Rect_major, (e) mode 5 for Rect_minor, (f) mode 5 for Rect_major, (g) mode 10 for Rect_minor and (h) mode 10 for Rect_major jet.

are characterized by two or more randomly arranged spanwise vortex cores, whose spatial dimensions are considerably larger than corresponding distributions in Plane 1. Fig. 5.34 shows the spatial distributions of the 1st, 3rd, 5th and 10th POD modes in Plane 3 of the rectangular jets. These modes contain approximately 10%, 4.8%, 3.2% and 1.7% of the total energy, respectively for Rect_minor jet; and 13%, 5.3%, 3.6% and 1.7% of the total energy, respectively for Rect_major jet. Qualitatively similar results are obtained in Plane 3 of the rectangular jets. There is however, a marked difference between the mode 1 spatial distributions for the Rect_minor and Rect_major jets; the upper shear layer of the Rect_minor jet does not any circulation, while that of the Rect_major jet shows flow circulation corresponding to that of a negative (clockwise) vortex. There is no large-scale flow circulation in the upper shear layer of Rect_minor because most of the energy in the shear layer is used to drive the surface current. For the higher-order modes, the alternating positive and negative vortices occur but they show no systematic dependency on nozzle geometry or orientation of the rectangular nozzle.

CHAPTER 6

CONCLUSIONS AND RECOMMENDATIONS

In this chapter, a summary and the major conclusions of the present work are reported. This is followed by providing recommendations for future work on this research area.

6.1 Summary

The main goal of this study was to investigate experimentally the effects of offset height and nozzle exit geometry on the turbulent characteristics and structures of submerged jets interacting with a free surface at low Reynolds number (Re = 5500). Orifice-type nozzles were used to produce the jet flow. In order to investigate the effects of offset height, four offset height ratios, h/d = 1, 2, 3 and 4 were tested using a square nozzle. For the nozzle geometry effect, the jets were discharged from the following four nozzles: a circular nozzle, a square nozzle, a rectangular nozzle with minor axis oriented parallel to the surface-normal direction, and the rectangular nozzle with major axis oriented parallel to the surface-normal direction all at a fixed offset height ratio of h/d = 2. A particle image velocimetry system was used to perform the velocity measurements in the vertical symmetry plane of the jets.

The mixing and entrainment characteristics of the jets are investigated using the potential core length, attachment length, local maximum streamwise mean velocity decay and half-velocity width. The jet-surface interaction is examined using streamwise mean surface velocity, velocity defect, vorticity thickness and surface turbulence intensities. Turbulent statistics up to the fourth order moment including the Reynolds stresses and their production terms, triple velocity products, skewness and flatness of the velocity fluctuations are also reported. Finally, the effects of the offset height and the nozzle geometry on the coherent structures are investigated using Galilean decomposition, linear stochastic estimation, two-point correlations of the velocity fluctuations and swirling strength, joint probability density function and proper orthogonal decomposition (POD).

6.2 Major Conclusions

The major conclusions of the offset height and nozzle geometry effects on the surface attaching jet characteristics are as follows:

6.2.1 Offset height effect

- The maximum velocity decay rate increases from 0.149 to 0.217 with offset height ratio from $h/d = 1$ to 4 due to faster entrainment and mixing, and reaches to a comparable value to a free jet for $h/d \geq 3$. The mean attachment length increases linearly with increasing offset height ratio at a rate of about 3.0 for $h/d \geq 2$.
- The linear growth rate of the vorticity thickness reduces from 0.180 at an offset height ratio of $h/d = 4$ to a negligible value for $h/d = 1$ indicating a reduced growth of the vortices generated from the near-field instability.

- The surface turbulence intensities indicate a dramatic reduction in surface-normal turbulence intensity levels than the streamwise turbulence intensity, and this reduction is more severe for a shorter offset height.
- The surface-normal profiles of the mean and turbulent statistics show that the diminishing of the mean shear near the free surface causes a reduction of spanwise mean vorticity and Reynolds shear stress in the upper shear layer. A reduction in offset height also leads to attenuation of the production terms, triple velocity correlations and the fourth order moments especially in the upper shear layer.
- In the interaction region, the spatial coherence of the velocity fluctuations reduces more in the upper shear layer than in the lower shear layer. The POD results indicate a slower fractional energy convergence for a shallower jet because of the reduction in the size of the structures under confinement.

6.2.2 Nozzle geometry effect

- The rectangular nozzle in minor-axis orientation (Rect_minor) exhibits a shorter potential core length (up to 33%) and a faster maximum velocity decay rate (up to 28%) compared to the other nozzle configurations due to its enhanced near-field mixing and entrainment characteristics; this leads to a wider shear layer expansion and shorter attachment length (up to 38%).
- Rect_minor jet enhances the linear growth rate of the vorticity thickness (up to 70%) in the near-field region than the other configurations, which is consistent with its wider shear layer expansion.

- In the interaction region, the damping of the surface-normal velocity fluctuations at the free surface is more severe in Rect_minor jet due to a stronger interaction of that jet with the free surface.
- Surface-normal profiles of the turbulent statistics show that the attenuation of Reynolds shear stress, the production terms, triple correlations and the fourth order moments in the upper shear layer due to confinement is more dramatic in the Rect_minor jet compared to the other configurations. Major-axis orientation of the rectangular nozzle (Rect_major), on the other hand, has the effect of enhancing these turbulent quantities over most of the interaction region, suggesting a better mixing performance of this configuration in the intermediate-flow region before reaching to self-similarity.
- In the interaction region, the re-orientation of the rectangular nozzle to major axis increases the spatial coherence of the velocity fluctuations compared to the other configurations. The POD results show that the fractional energy contribution of the most dominant mode is about 21% higher for the Rect_major jet, which is consistent with the two-point correlation measurements.

6.3 Recommendations for Future Work

A complete measurement of Reynolds stresses of surface attaching jets could not be made in this research due to the obvious limitation of the current planar PIV system. It is recommended that volumetric flow field measurement techniques such as a tomographic PIV system, which provides measurements of all the three velocity components (3C) and a finite volume (3D), should be used in future studies to provide the complete measurement of the velocity gradient and Reynolds stress tensors. This would reveal more information about three-dimensional structures and the complete vorticity field under surface confinement.

Another shortcoming of the current PIV system is its inability to provide temporal evolution of the flow. A time-resolved PIV technique would allow measurements of temporally-resolved velocity fields which will facilitate an in-depth investigation of the temporal evolution of the velocity field by examining time scales, time-space correlations, energy spectra and other temporal characteristics of the flow structures.

Furthermore, the present and previous surface attaching jets were studied mostly using circular, square and rectangular nozzles. Free jet studies have clearly demonstrated significant dependency of the turbulent and mixing characteristics on nozzle geometries. Therefore, a thorough investigation of the interaction between the free surface and jet flows produced from other nozzles such as elliptic and triangular geometries is necessary, and would be useful for optimal design of hydraulic structures, and many other engineering and environmental applications involving a free surface interaction.

APPENDIX A

METHOD OF PROPER ORTHOGONAL DECOMPOSITION

In this section, the method of the proper orthogonal decomposition (POD) technique is described. As mentioned earlier, the snapshot method of POD analysis proposed by Sirovich (1987) is adopted in the present study. The procedure of the method following the approach by Meyer et al. (2007) is as follows:

Assume, the total number of snapshot capturing the instantaneous flow field by PIV is denoted by N_s, and the number of the velocity vectors in each snapshot is M_v. The current velocity measurement is performed in a two-dimensional plane. The fluctuating velocities in the streamwise and surface-normal direction are denoted by u_p^q and v_p^q, respectively. Here, p and q indexes correspond to M_v and N_s, respectively (i.e., p = 1, 2, 3, …, M_v; and q = 1, 2, 3, …, N_s).

The ensemble-average velocity ($\overline{u}$) for a set of snapshots, i.e., instantaneous velocities ($\hat{u}$) is calculated by

$$\overline{u} = \frac{1}{N_s} \sum_{q=1}^{N_s} \hat{u}^q \tag{A.1}$$

Then, the fluctuating velocity is obtained by subtracting the mean velocity from the instantaneous velocity field as follows:

$$u = \hat{u} - \bar{u} \tag{A.2}$$

For the fluctuating velocity components, the following matrix (X) is arranged:

$$X = u^1 \;\; u^2 \; \dots \; u^{N_s} = \begin{bmatrix} u_1^1 & u_1^2 & \dots & u_1^{N_s} \\ \vdots & \vdots & \vdots & \vdots \\ u_{M_v}^1 & u_{M_v}^2 & \dots & u_{M_v}^{N_s} \\ v_1^1 & v_1^2 & \dots & v_1^{N_s} \\ \vdots & \vdots & \vdots & \vdots \\ v_{M_v}^1 & v_{M_v}^2 & \dots & v_{M_v}^{N_s} \end{bmatrix} \tag{A.3}$$

and the $N_s \times N_s$ auto-covariance matrix is obtained as

$$C = X^T X \tag{A.4}$$

From the auto-covariance matrix, a set of N_s eigenvalues, λ^i and corresponding orthonormal eigenvectors, $\boldsymbol{A}^i$ are obtained which satisfy the following relation:

$$CA^i = \lambda^i A^i \tag{A.5}$$

where, $i = 1, \ldots, N_s$. Noted that the Eigenvalues are arranged in a decreasing order,

$$\lambda^1 > \lambda^2 > \ldots > \lambda^{N_s} > 0 \tag{A.6}$$

The eigenvectors in Equation A.5 are projected on the original velocity field and the normalized POD modes (ϕ^i) of the eigenfunctions are constructed as follows:

$$\phi^i = \frac{\sum_{q\text{-}1}^{N_s} A_q^i \, u^q}{\left\| \sum_{q\text{-}1}^{N_s} A_q^i \, u^q \right\|} \tag{A.7}$$

where, A_q^i is the qth component of the eigenvector corresponding to λ^i from Equation A.5 and $\|.\|$ is the L_2-norm which is defined as

$$\|y\| = \sqrt{y_1^2 + y_2^2 + \ldots + y_{M_v}^2} \tag{A.8}$$

It is noted that the turbulent kinetic energy content in each POD mode is represented by the eigenvalues, λ^i. The total energy (E_T) is obtained by the summation of the eigenvalues in all N_s modes as

$$E_T = \sum_{i=1}^{N_s} \lambda^i \tag{A.9}$$

and the fractional energy in each mode is calculated as

$$E_\lambda = \frac{\lambda^i}{E} \tag{A.10}$$

The data set corresponding to the fluctuating velocity components obtained by doing experiment are projected onto the calculated eigenfunctions and the expansion or POD coefficients (a_i) of each mode is calculated as follows:

$$a^q = \Psi^T u^q \tag{A.11}$$

Where, $\Psi = \left[\phi^1 \; \phi^2 \ldots \; \phi^{N_s}\right]$.

Then, the reconstructed fluctuating velocity is obtained by

$$u^q = \sum_{i=1}^{q} a_i^q \phi^i = \Psi a^q \tag{A.12}$$

The average least-squares truncation error is estimated following the approach by Cizmas et al. (2003) as follows:

$$\varepsilon_m = \overline{\left\| u^q - \sum_{i=1}^{m} a_i^q \phi^i \right\|^2} \tag{A.13}$$

where, m denotes the number of modes used to reconstruct the flow field data.

APPENDIX B

REYNOLDS NUMBER EFFECT ON THE CHARACTERISTICS OF SURFACE JET

As mentioned earlier that the effects of Reynolds number on the turbulent characteristics of surface attaching jets are investigated by conducting experiments at various Reynolds numbers ranging from Re = 2300 to 11900 for a fixed offset height ratio of h/d = 2. In this section, results obtained from various Reynolds numbers are presented. The local Froude numbers are estimated and the variation of the local Froude number for different exit Froude numbers is discussed. Subsequently, the effects of Reynolds number on the instantaneous velocity field; the exit profiles of streamwise mean velocity and streamwise turbulence intensity; potential core length; attachment length; maximum velocity decay rate; spread rate; entrainment coefficient; profiles of streamwise mean velocity and turbulence intensities along the free surface; and the surface-normal profiles of streamwise mean velocity and Reynolds stresses are discussed.

B.1 Effect of Froude Number

Froude number is significant to characterize the surface waves generated by the flow. In the present study, the exit Froude number (Fr) varies from 0.5 to 2.7. Since this is a spatially evolving flow, a local Froude number (Fr_{local}) based on the local maximum

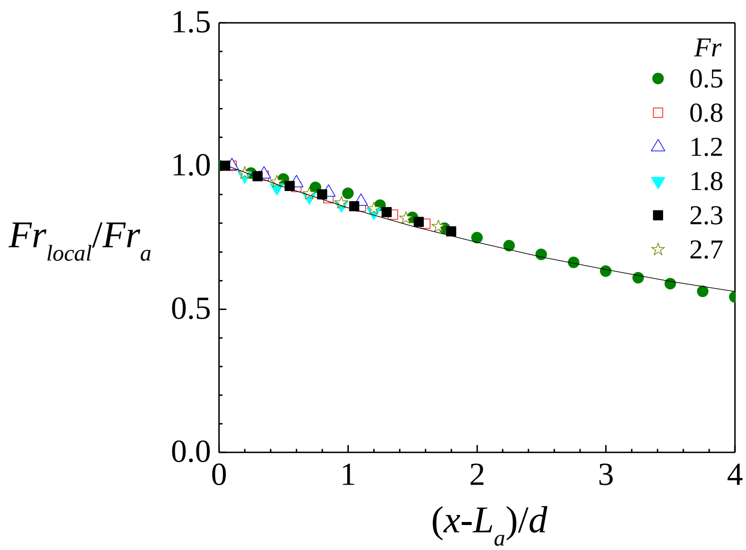

Figure B.1. Streamwise evolution of local Froude number for various exit Froude numbers.

velocity (U_m) and the local jet half-width ($y_{0.5}$), is estimated following the approach by Walker et al. (1995) as

$$Fr_{local} = U_m/(2gy_{0.5})^{0.5} \tag{B.1}$$

Since no surface waves are formed before the attachment point (AP), Fr_{local} is irrelevant in the pre-attachment region (Walker et al., 1995). Thus, this analysis focuses only on the surface jet region so that the streamwise distance is measured relative to AP. Figure B.1 shows the variation of Fr_{local}/Fr_a with streamwise distance for all the test conditions, where Fr_a is the local Froude number at AP, and $(x\text{-}L_a)/d = 0$ corresponds to AP. It should be noted that the range of Fr_a for the present test conditions ($0.69 \le Fr_a \le 2.70$) is within the range of $0.36 < Fr_a < 8.01$ reported by Walker et al. (1995). The profiles are identical and independent of Reynolds number. They exhibit the classical decreasing trend of Fr_{local}

with streamwise distance, which is well described by the following least-squares curve fit shown in the figure by the solid line:

$$Fr_{local}/Fr_a = 34\,(x' + 9)^{-b} \tag{B.2}$$

where, $x' = (x\text{-}L_a)/d$, and b is the decreasing rate. The value of b is estimated as 1.6 irrespective of the exit Froude number (Fr) indicating negligible effect of Fr on the spatial evolving of the jets in the absence of the surface waves in the interaction region.

B.2 Instantaneous Flow Field

The instantaneous velocity fields of the jets at Re = 2300 (the lowest Reynolds number) and Re = 7900 (a representative of high Reynolds number) are presented in Fig. B.2. The free surface is located at the top of each plot, that is, at y/d = 2. Galilean decomposition is applied by subtracting a convective velocity of $0.15U_j$ from the velocity field following the approach by Agrawal and Prasad (2002) which allows to expose the vortices propagating at that velocity roughly at the turbulent-nonturbulent interface (edges of the shear layers in the instantaneous velocity field). The turbulent-nonturbulent interface is significant as the entrainment mechanism takes place mostly at the edge of the jet (Westerweel et. al., 2005). The interface is marked by the zero velocity contour lines in the figure. The decomposition reveals anti-clockwise (retrograde) and clockwise (prograde) rotating vortices at the edge of the upper and lower shear layer, respectively. Contours of signed swirling strength are superimposed on the plots to highlight the counter rotating spanwise vortices at the interface. Opposite signed swirling strength contour pairs close to the upper and lower edges, at $x/d \approx 0.5$ and 1.5 as observed for both

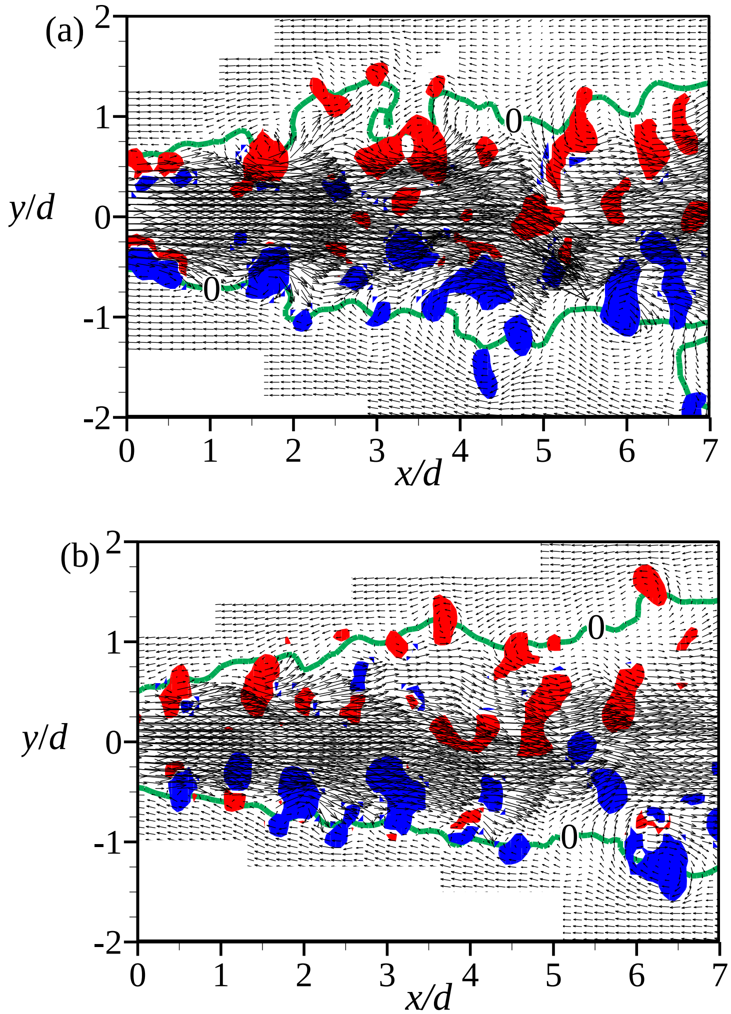

Figure B.2. Instantaneous velocity field for (a) *Re* = 2300 and (b) *Re* = 7900.

Reynolds numbers, could be considered as a result of typical generation of ring shaped structures in near field region of the jet (Tandalam et al., 2010). The rotating motion of the large-scale structures at the turbulent-nonturbulent interface are mainly responsible for the engulfing of ambient fluid in the entrainment process. The effect of Reynolds number on the jet-surface interaction is evident in the figure: for instance, the vortical structures along with the swirling strength contours close to the free surface ($y/d \geq 1$) are less pronounced for lower Reynolds number (*Re* = 2300) at $x/d > 3$, indicating weaker vorticity field that could be attributed to the kinematic condition of the free surface which reduces the strain rate close to it after early attachment.

B.3 Jet Exit Profiles of Mean Velocity and Turbulence Intensity

The streamwise mean velocity and streamwsie turbulence intensity profiles at a near exit location, x/d = 0.25 are shown in Fig. B.3 for different Reynolds numbers examined. The velocity profiles show typical top-hat shape near the exit (Ghasemi et al., 2015) and there is no dependency of these profiles on Reynolds number. As expected, double-peak profiles of streamwise turbulence intensity, $<u^2>^{0.5}$ are observed near the jet exit. The peak value of $<u^2>^{0.5}$ is approximately 31% of U_j irrespective of Reynolds number. The minimum $<u^2>^{0.5}$ at the nozzle center is approximately 2.2% of U_j which is also nearly independent of Reynolds number. Similar observation regarding the Reynolds number dependency on the exit mean velocity and turbulent intensity was reported by Ghasemi et al. (2015) while the Reynolds numbers were varied from Re = 10000 to 41400.

B.4 Contours of Streamwise Mean Velocity

Iso-contours of normalized streamwise mean velocity, U/U_j for Re = 2300 and 7900 are shown in Fig. B.4 to examine the effect of Reynolds number in the near field region ($0 \leq x/d \leq 7$) qualitatively. The contour plots show the surface-normal expansion of the jet with streamwise distance. The jet at lower Reynolds number (Re = 2300, Fig. B.4a) exhibits a faster expansion in the near exit region ($0 < x/d < 2$) compared to downstream region, $x/d > 2$; while the results for the jet at the higher Reynolds number (Re = 7900, Fig. B.4b) show a nearly linear expansion of the shear layers from the jet exit.

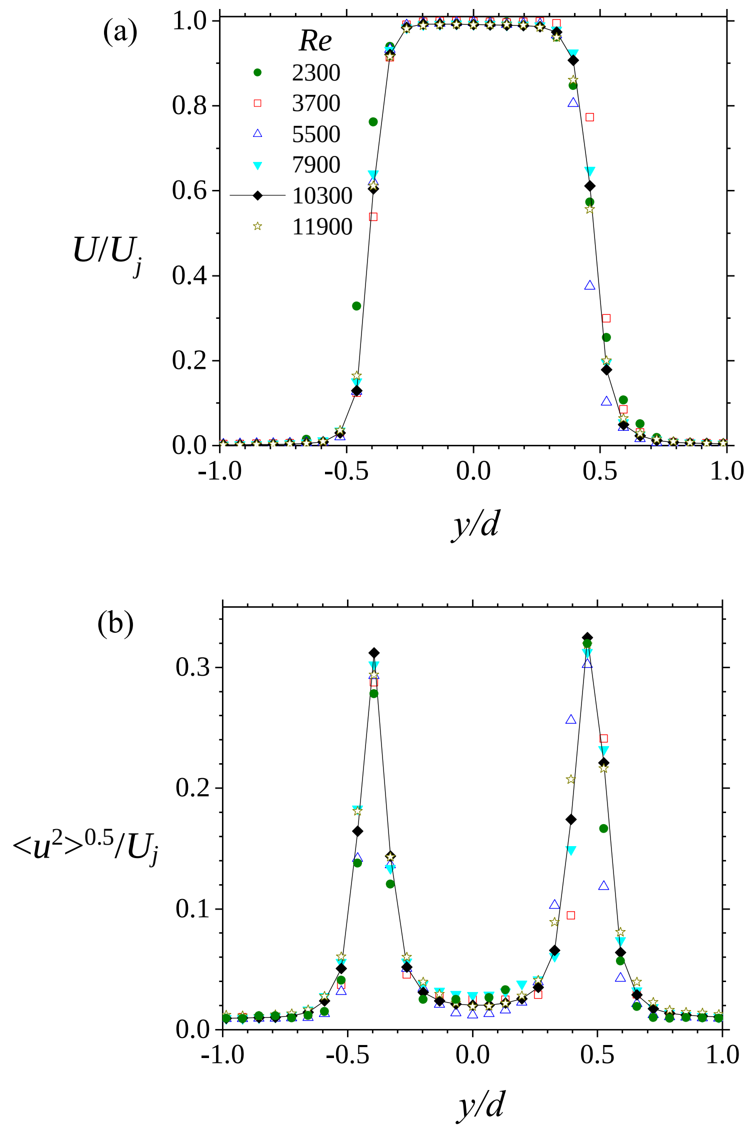

Figure B.3. Profiles of mean velocity and turbulence intensity close to the nozzle exit at x/d = 0.25 for various Reynolds numbers: (a) streamwise mean velocity and (b) streamwise turbulence intensity.

This could be partially a sign of relatively enhanced mixing in the near exit region at lower Reynolds number which reflects the finding regarding the Reynolds number effect on free jet mixing (Kwon and Seo, 2005; Mi et al., 2013). Furthermore, the linear expansion from the jet exit for the higher Reynolds number jet could be attributed to its higher momentum

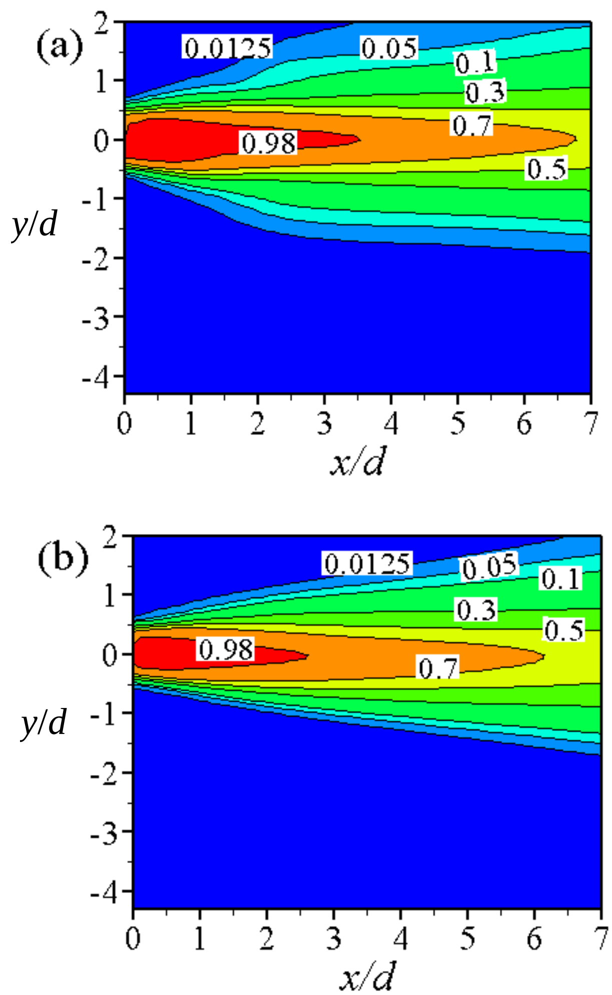

Figure B.4. Iso-contours of streamwise mean velocity for (a) *Re* = 2300 and (b) *Re* = 7900.

flux. Also, the interaction between the upper shear layer and the free surface (the top of each plot) is evident in the figure.

B.5 Potential Core Length and Attachment Length

The mixing characteristics of turbulent jets in near field region are often reflected by the length of the potential core region within which local maximum streamwise mean velocity is reduced up to about 98% of U_j (Aleyasin et al., 2017a). The potential core

Table B.1. Summary of potential core length and attachment length for various Reynolds numbers.

Re	***L_p/d***	***L_a/d***
2300	3.5	3.5
3700	3.0	5.9
5500	2.1	6.4
7900	2.6	6.3
10300	2.6	5.7
11900	2.1	5.8

lengths (L_p) at various Reynolds numbers are summarized in Table B.1. Potential core length is estimated as $L_p/d = 3.5$ at $Re = 2300$ and reduces to $L_p/d = 2.6 \pm 0.5$ at $Re \geq 3700$. A reduction of the potential core length at higher Reynolds number could be partly attributed to a stronger interaction between the shear layers due to higher momentum flux. The present value of potential core length at $Re \geq 3700$ is lower than the value of L_p/d = 3.3 reported previously for free square jet produced from a sharp contraction nozzle at Re = 10000 (Aleyasin et al., 2017a). The lower potential core length observed in the present study is consistent with better near field mixing for the jet using orifice nozzle compared to contraction nozzle (Quinn, 2006).

The attachment length (L_a) is an important characteristic of boundary attaching flows. As mentioned earlier, for surface attaching jets, entrainment and mixing of ambient fluid cause the expansion of the shear layers and finally, the upper shear layer attaches to the free surface (see Fig. B.4), where AP indicates the onset of the interaction between the jet and the free surface. The attachment lengths, determined as the streamwise distance from the nozzle exit to the location where the minimum streamwise mean velocity contour ($U/U_j \approx 0.0125$ obtained from the dynamic range of the PIV system) attaches to the free surface as shown in Fig. B.4 for example, at various Reynolds numbers are summarized in Table B.1. The attachment length increases from $L_a/d = 3.5$ to 5.9 with the increase of Reynolds number from $Re = 2300$ to 3700. Shorter attachment length at lower Reynolds number could be considered as an artifact of larger expansion of shear layer in the near exit region as discussed earlier. With the increase of Reynolds number at $Re \geq 3700$, the attachment lengths show comparable values of $L_a/d = 6.0 \pm 0.4$. For a similar offset height ($h/d = 2$) but at a much higher Reynolds number ($Re = 40000$), Sankar et al., (2008) reported $L_a/d = 5$, which is comparable to $L_a/d = 5.8$ reported in the present study at $Re =$ 11900 indicating Reynolds number independency of the attachment length at higher Reynolds number. It is noted that similar result regarding the independency of Reynolds number on the attachment length at higher Reynolds number was reported in previous studies where the jet attaches to the bottom solid wall (e.g., Agelin-Chaab and Tachie, 2011c).

B.6 Streamwise Evolution of Local Maximum Mean Velocity, Half-Velocity Width and Entrainment Coefficient

The mixing and entrainment characteristics of the jets are further investigated using local maximum streamwise mean velocity decay, jet half-velocity width and entrainment coefficient. Discussion on the effect of Reynolds number on these quantities is provided below. It is noted that in order to reduce data abundance, four Reynolds number cases (Re = 2300, 3700, 7900 and 11900) are shown in the respective figures which does not change the discussions of the Reynolds number effects on the profiles.

B.6.1 Local maximum mean velocity decay

The variation of local maximum streamwise mean velocity (U_j/U_m) as a function of streamwise distance at various Reynolds numbers is shown in Fig. B.5a. The profiles are nearly independent of x/d starting from the nozzle exit (x/d = 0) to a streamwise distance which corresponds to the potential core length. Beyond the potential core, U_m decays with streamwise distance mainly as a result of entrainment and mixing with the ambient fluid. The decay rate is quantified by a least-squares fit of the following straight line to the linear portion of the U_j/U_m profile as shown in the figure by a solid line (Equation 1.1):

$$U_j/U_m = K_d\ (x/d - x_o/d)$$

where, K_d and x_o are the decay rate and kinematic virtual origin, respectively. The decay rate is estimated as 0.150 within $3 < x/d < 8$ irrespective of Reynolds number at $Re \geq 3700$. With the decrease of Reynolds number to Re = 2300, the decay rate slightly increases (approximately 3%) which is an indication of better mixing at low Reynolds number jets as previously reported (Kwon and Seo, 2005; Mi et al., 2013). Comparing with free jet using similar square orifice nozzle at Re = 17000 within $6 \leq x/d \leq 14.5$ (Aleyasin et al., 2017b), the present results show approximately 12% lower decay rate. The slower decay rate of surface attaching jet could be partially attributed to reduced entrainment in the

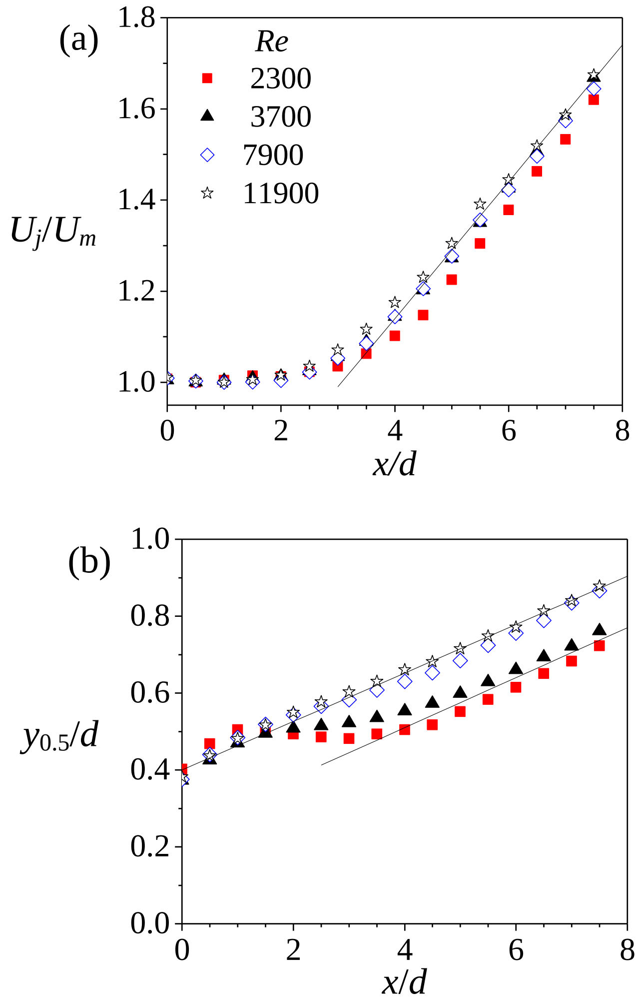

Figure B.5. Streamwise evolution of local maximum streamwise mean velocity decay and half-velocity width for various Reynolds numbers: (a) Maximum velocity decay, (b) half-velocity width.

upper shear layer of the jet due to surface confinement as observed in previous surface attaching jets (Madnia and Bernal, 1994).

B.6.2 Half-velocity width

The jet spread is typically characterized by the half-velocity width ($y_{0.5}$). The variation of the half-velocity width with streamwise distance is shown in Fig. B.5b. The spread rate is estimated by a least-squares fit of the following straight line (Equation 1.3) to the linear portion of the profile as shown in the figure:

$$y_{0.5}/d = K_s\ (x/d - x_g/d)$$

where, K_s and x_g denote the spread rate and geometric virtual origin, respectively. The spread rate is estimated as 0.063 within $0 < x/d < 8$ irrespective of Reynolds number at $Re \geq 3700$. A modest increase (approximately 3%) of the spread rate at $Re \leq 3700$ within $0 < x/d < 8$ is consistent with earlier observation that superior mixing occurs at lower Reynolds numbers. Since the jet spread is estimated from the lower shear layer of the jet (see Fig. 1.1), it was expected that it would show similar spread rate to a free jet as per previous surface attaching jet study (Tay et al., 2017). However, the present results are 22% lower than the spread rate of free jet (0.081) reported by Aleyasin et al. (2017b) within $6 \leq x/d \leq 14.5$. This disparity could be attributed to the streamwise range within which the spread rate is estimated which indicates the sensitivity of the shear layer development in near field region.

B.6.3 Mass flux and entrainment coefficient

Mass flux (ϕ_m) is estimated in x-y plane and the streamwise distributions of normalized ϕ_m is shown in Fig. B.6a. As expected, the normalized mass flux increases with streamwise distance. The increasing rate is estimated by a least-squares fit of the following curve as shown in the figures by the solid and dashed lines:

$$y^* = (x/d - x_1)^{m'} \tag{B.3}$$

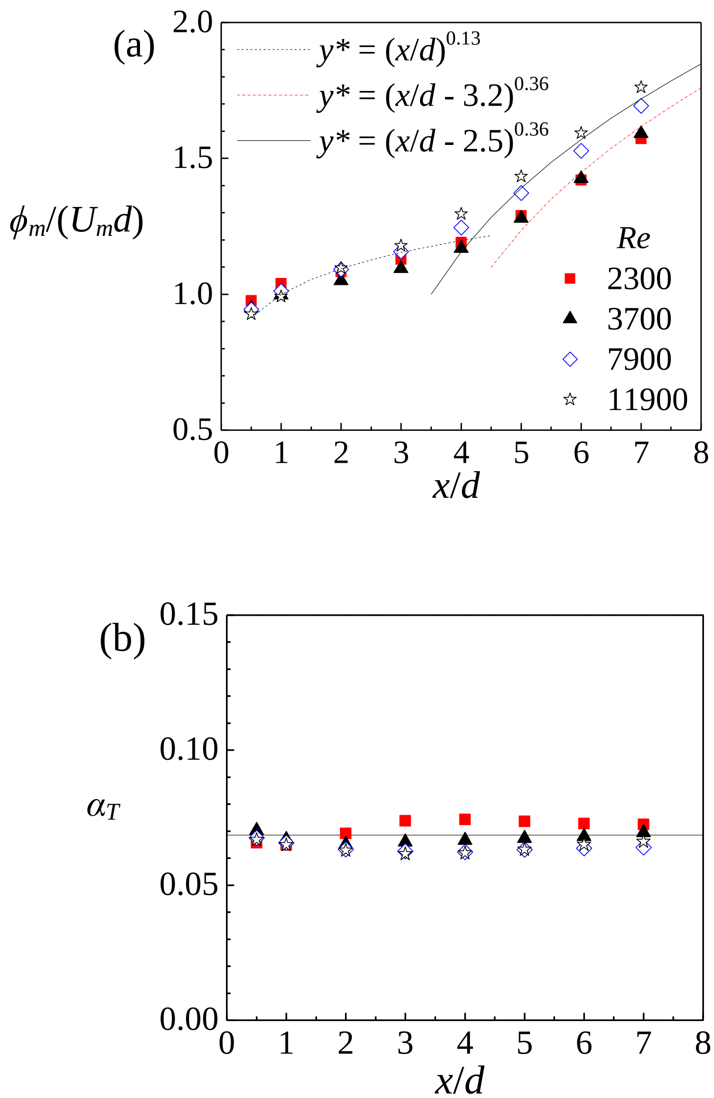

Figure B.6. Streamwise evolution of mass flux and entrainment coefficient for various Reynolds numbers: (a) mass flux and (b) entrainment coefficient.

where, $y^* = \phi/(U_m d)$; m' and x_1 are the increasing rate and a fitting parameter, respectively. The results show that within the potential core ($0 < x/d < 4$), the mass flux develops at a rate of $m' = 0.13$ and beyond the potential core, this rate increases approximately 64%

irrespective of Reynolds number. The implication is that changing the Reynolds number does not significantly influence the distribution of the mass flux.

Entrainment coefficient (α_T) is estimated following the approach proposed by Baddour et al. (2006). This could provide an insight into surface-normal entrainment and be useful to estimate the total entrainment velocity when using entrainment models to predict entrainment characteristics of surface attaching jets. The entrainment coefficient is calculated as

$$\alpha_T = 0.5\, K_s\, \phi_m/(U_m\, y_{0.5}) \tag{B.4}$$

The distribution of entrainment coefficient is shown in Fig. B.6b. The entrainment coefficient is independent of Reynolds number showing a constant value of α_T = 0.068 (indicated by a horizontal straight line in the figure) in near field region. It should be noted that α_T typically reduces with the jet development further downstream due to reduction of entrainment with the increase of streamwise distance as per previous jet study (Baddour et al., 2006).

B.7 Streamwise Evolution of Surface Velocity and Turbulence Intensities

The interaction of the jet with the free surface in the near field region at various Reynolds numbers is investigated using profiles on the streamwise mean velocity, mean velocity defect and turbulence intensities along the free surface. As mentioned in Chapter

4, the mean and turbulent quantities obtained at about two interrogation area sizes (≈ 2 mm) below the air-water interface of the PIV images are reported as the surface data.

B.7.1 Streamwise mean surface velocity and velocity defect

The profiles of the streamwise mean velocity along the free surface are shown in Fig. B.7a. The dashed horizontal line in the figure indicates the minimum streamwise mean velocity level, $U/U_j = 0.0125$ at the free surface. As expected from previous studies (e.g., Madnia & Bernal, 1994; Tay et al., 2017), the streamwise mean surface velocity, U_s starts increasing after the attachment point. U_s starts increasing earlier at $Re = 2300$ compared to the higher Reynolds number cases due to its earlier attachment to the free surface at $x/d \approx 3.5$. After that the surface velocity increases at a comparably lower rate (approximately 55%) that could be partially attributed to lower momentum of the jet causing weaker jet-surface interaction. The profiles are nearly independent of Reynolds number at $Re \geq 3700$ in the interaction region, $x/d > 6$.

In order to explore the velocity scale for the surface profiles, mean velocity defect, ΔU is calculated using Equation 4.1 as

$$\Delta U = U_m - U_s$$

and the profiles of ΔU at various Reynolds numbers are presented in Fig. B.7b. U_m is used for the normalization to obtain collapsed profiles as shown in Chapter 4. Negligible surface velocity before the attachment point ($x/d < 6$) is reflected in the $\Delta U/U_m$ profile showing almost constant value ($\Delta U/U_m \approx 1$). After that $\Delta U/U_m$ decreases almost linearly in the near field region. The decreasing trend of the profile indicates that the free surface

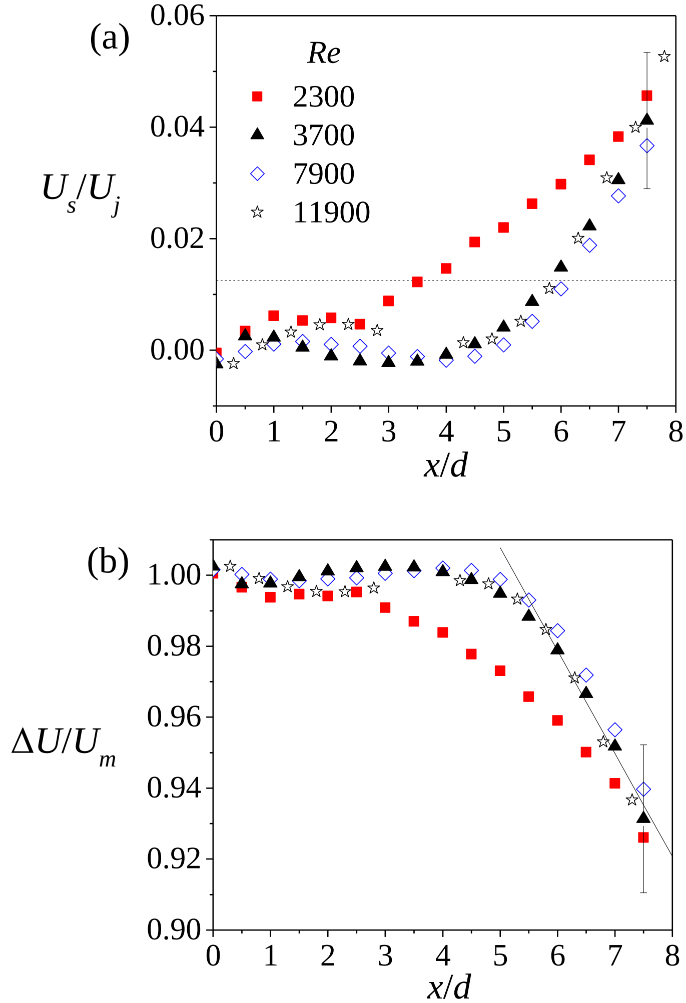

Figure B.7. Streamwise evolution of streamwise mean surface velocity and velocity defect for various Reynolds numbers: (a) streamwise mean surface velocity and (b) mean velocity defect.

tends to achieve the local maximum streamwise mean velocity as mentioned in Chapter 4. The decay rate of $\Delta U/U_m$ is estimated by least-squares straight line fitting on the profile as shown in the figure by a solid line, where the slope of the straight line indicates the decay rate. The decay rate is estimated as 0.029 at $Re \geq 3700$ within $5 < x/d < 8$. With the decrease of Reynolds number to Re = 2300, ΔU profile shows consistent result with the surface velocity profile resulting earlier onset of the decay due to early attachment with a rate of approximately 48% lower and tends to collapse with higher Reynolds number profiles at the very end of the current flow field examined. This supports the weaker interaction of lower Reynolds number jet with the free surface.

B.7.2 Turbulence intensities along the free surface

Figure B.8 shows the profiles of streamwise and surface-normal turbulence intensities ($<u^2>^{0.5}$ and $<v^2>^{0.5}$, respectively) along the free surface. Based on the discussion in Chapter 4, the velocity scale ΔU is used for normalization to collapse the profiles onto a universal curve. It is noted that the magnitude of surface turbulence intensities before the attachment point are negligible and after that the turbulence intensities start increasing with streamwise distance as reported in Chapter 4. The growth rates of $<u^2>^{0.5}/\Delta U$ and $<v^2>^{0.5}/\Delta U$ are estimated by least-squares straight line fitting on the profiles as shown in the figure by a solid line, where the slope of the straight line indicates the growth rate. The growth rates of $<u^2>^{0.5}/\Delta U$ and $<v^2>^{0.5}/\Delta U$ profiles are 0.020 and 0.012, respectively at $Re \geq 3700$. This Reynolds number dependency of the surface turbulence intensities is consistent with the $\Delta U/U_m$ profile discussed earlier. Lower growth rate of $<v^2>^{0.5}/\Delta U$ compared to $<u^2>^{0.5}/\Delta U$ is an indication of damping of $<v^2>^{0.5}$ by the free surface where, transfer of turbulent kinetic energy from its surface-normal component to the streamwise and spanwise components occurs as previously reported by Anthony and Willmarth (1992). This also causes large scale anisotropy at the free surface as mentioned in Chapter 4.

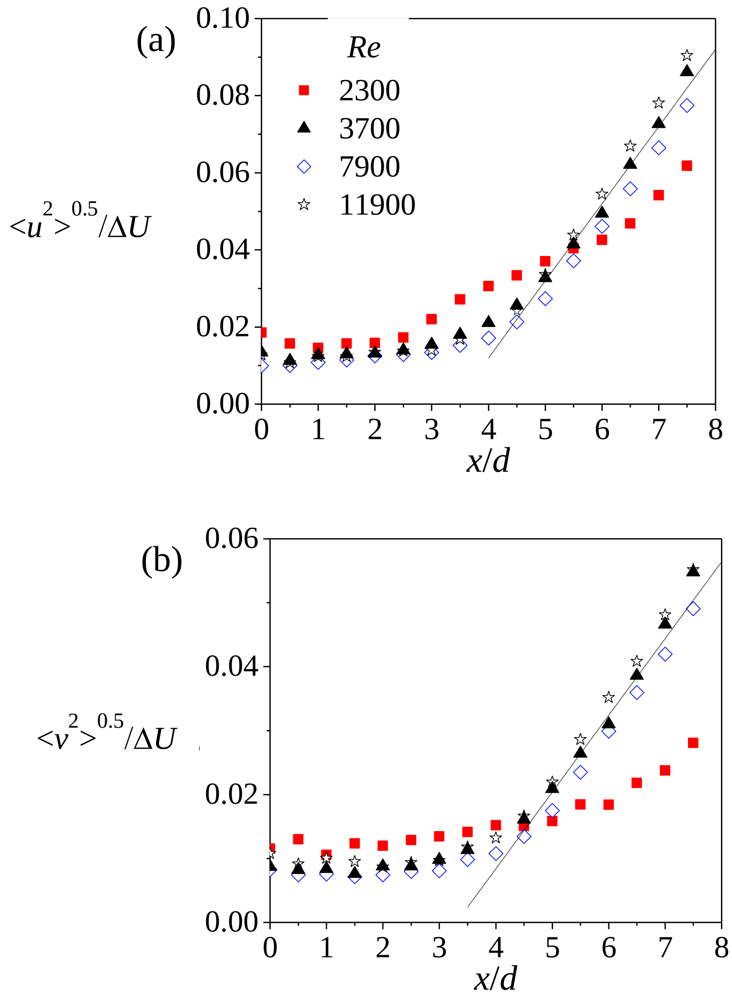

Figure B.8. Streamwise evolution of turbulence intensities along the free surface for various Reynolds numbers: (a) Streamwise turbulence intensity and (b) surface-normal turbulence intensity.

B.8 Surface-Normal Distribution of Mean Velocity and Reynolds Stresses

Effects of Reynolds number on the surface-normal distribution of mean velocity and turbulent quantities are discussed in this section. One-dimensional profiles of

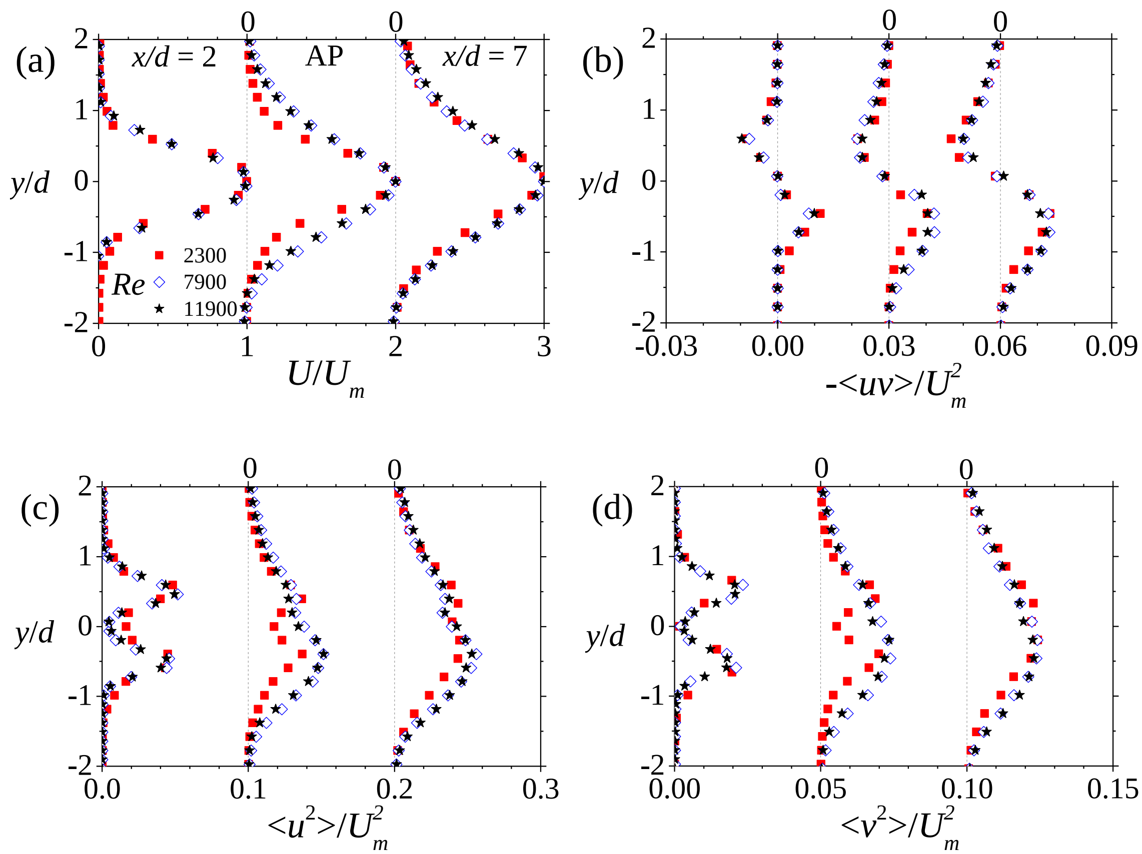

Figure B.9. Surface-normal profiles of mean velocity and Reynolds stresses at selected streamwise locations for various Reynolds numbers: (a) streamwise mean velocity, (b) Reynolds shear stress, (c) streamwise Reynolds normal stress and (d) surface-normal Reynolds normal stress.

streamwise mean velocity and Reynolds stresses at selected streamwise locations are presented in Fig. B.9. The selected streamwise locations are: x/d = 2, a location in the pre-attachment region; AP, at the attachment point; and x/d = 7, a location in the surface jet region. Profiles at the minimum (Re = 2300), maximum (Re = 11900) and an intermediate Reynolds number (Re = 7900) are shown for comparison. The length and the velocity scales used for normalization are d and U_m, respectively. It is noted that the free surface is located at the top of each plot, that is, at y/d = 2.

B.8.1 Streamwise mean velocity

The profiles of streamwise mean velocity (*U*) are shown in Fig. B.9a. As expected, *U* profiles follow Gaussian-like distribution up to AP; after that, positive streamwise mean velocity starts appearing at the free surface. Furthermore, results show that *U* profiles are nearly independent of Reynolds numbers except for the location at AP. At that location, the deviation of the profile at *Re* = 2300 relative to higher Reynolds number cases could be attributed to the early attachment at that lower Reynolds number.

B.8.2 Reynolds stresses

Figure B.9b shows the profiles of Reynolds shear stress, -<*uv*>. The profiles are also independent of Reynolds number. The almost anti-symmetric profiles of -<*uv*> up to AP as per previous surface attaching jet study (Sankar et al., 2008) is also evident in the present study at different Reynolds numbers. After AP, the free surface causes a damping of -<*uv*> close to the free surface as reported in previous surface attaching jet study (e.g., Sankar et al., 2008) and in Chapter 4; which is observed in the present study at *x/d* = 7, for instance, where the peak value of normalized -<*uv*> in the upper shear layer is approximately 22% lower than that in the lower shear layer. Lower peak of -<*uv*> in the upper shear layer could be partly attributed to the suppression of the large scale vortical structures in that shear layer due to surface confinement as discussed in Chapter 4.

Regarding the Reynolds number dependency of the profiles of Reynolds normal stresses ($\langle u^2 \rangle$ and $\langle v^2 \rangle$ in Fig. B.9c and B.9d, respectively), the results are consistent with the results for the mean velocity and Reynolds shear stress. For instance, the profiles of $<u^2>$ and $<v^2>$ at Re = 2300 deviate from the profiles for higher Reynolds number at AP showing typical double-peak profiles due to shorter attachment length. This double peak of Reynolds normal stresses in the near field region is common in turbulent jets (Aleyasin, et. al., 2017a; Sankar et al., 2008) which gradually vanishes with streamwise distance due to increase of centerline turbulence intensity because of the interaction of the shear layers. Large scale anisotropy as reported in chapter 4 is evident in $<u^2>$ and $<v^2>$ profiles, where $<v^2>$ shows lower value compared to $<u^2>$.

B.9 Summary of the Results

Experiments are conducted to investigate the characteristics of the jets interacting with a free surface at low and moderate Reynolds numbers. The Reynolds numbers investigated are varied from 2300 to 11900, while the offset height ratio is maintained at 2. Since the free surface remains almost undisturbed as mentioned in Chapter 3, effect of Froude number is negligible on the spatial evolving of the jet.

Galilean decomposition of instantaneous velocity field reveals that the effect of free surface is to weaken the vorticity field in the upper shear layer for lower Reynolds number jet. There is no significant influence of Reynolds number on the potential core length $Re \geq 3700$. The enhanced mixing in near field at lower Reynolds number is reflected on the attachment length of the jet showing early attachment to the free surface. However, the attachment length is nearly independent of Reynolds number at $Re \geq 3700$. Also, there is no significant influence of Reynolds number on the estimated maximum velocity decay and spread rates of the jets at $Re \geq 3700$.

The surface velocity measurements depict the increase of streamwise mean surface velocity after the attachment point and the profiles are nearly independent of Reynolds number at $Re \geq 3700$ in the interaction region, $x/d > 6$. The surface turbulence intensities exhibit similar Reynolds number dependency.

The one-dimensional profiles of mean velocity and Reynolds stresses are nearly independent of Reynolds number investigated except in the location of the attachment point which is sensitive at lower Reynolds number. The free surface dampens Reynolds shear stress close to the free surface which could be partly attributed to the suppression of the large-scale vortical structures due to surface confinement.

APPENDIX C

STATISTICAL CONVERGENCE RESULT

The accuracy of the PIV result largely depends on the number of snap shots (N_s) taken to measure the velocity field. Therefore, an initial convergence test was carried out to determine the sufficient number of snap shots for converged statistics. The convergence test was performed by varying the sample size from N_s = 2000 to 5000 for a square jet with an offset height ratio of h/d = 2 at a Reynolds number, Re = 5500.

Figures C.1 and C.2 show the profiles of the mean and turbulent statistics up to the third order moment at x/d = 5, a location before the attachment point; and at x/d = 20, a location in the jet-surface interaction region, respectively for the sample sizes, N_s = 2000, 4000 and 5000. Results depict no significant variation of the profiles for $N_s \geq 4000$. Thus, the sample size of N_s = 5000 used in the present study is sufficient to obtain converged statistics.

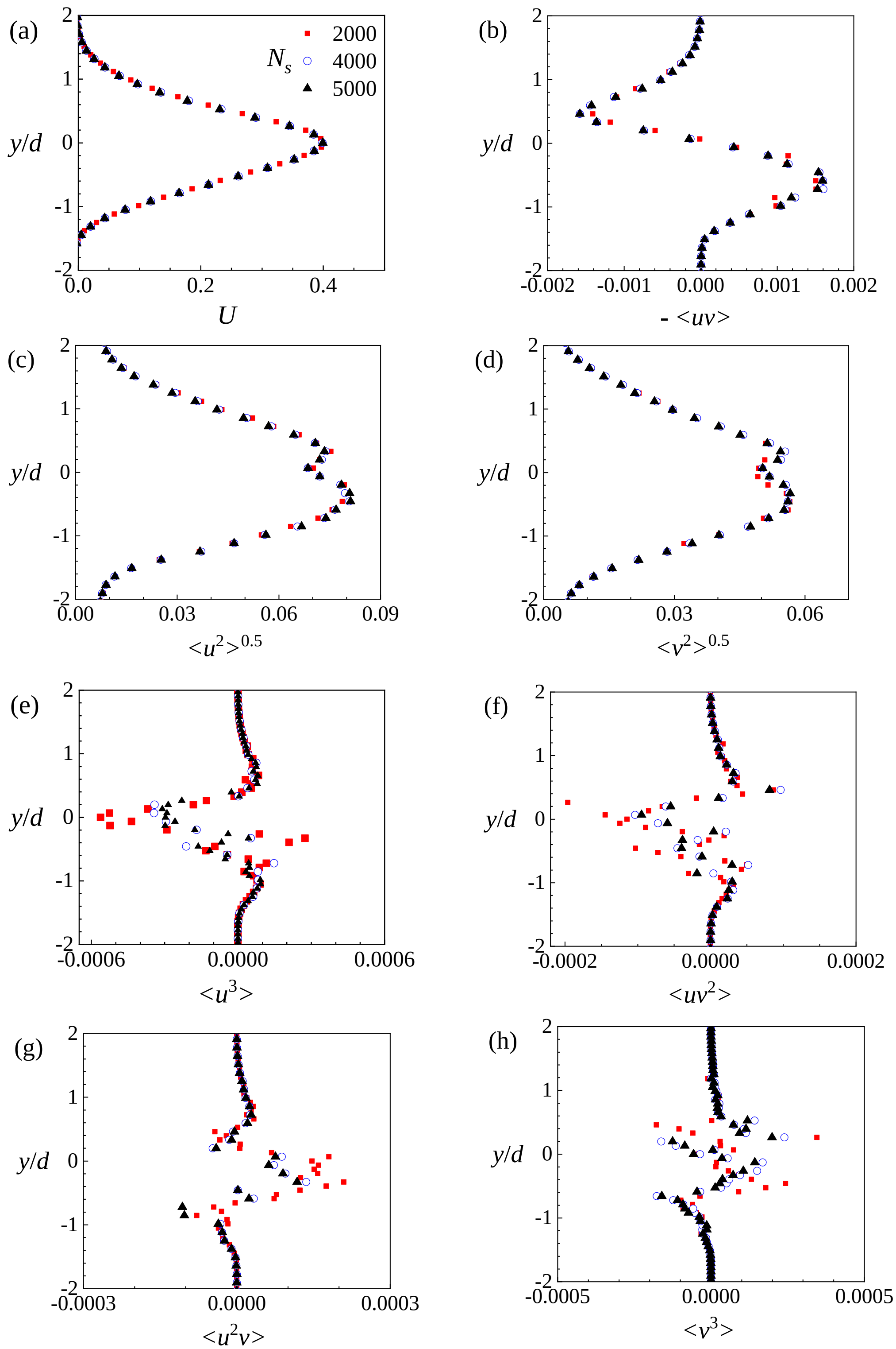

Figure C.1. Turbulence statistics with different sample sizes for square jet with *h/d* = 2 at *x/d* = 5. The *x*-axis is in SI unit.

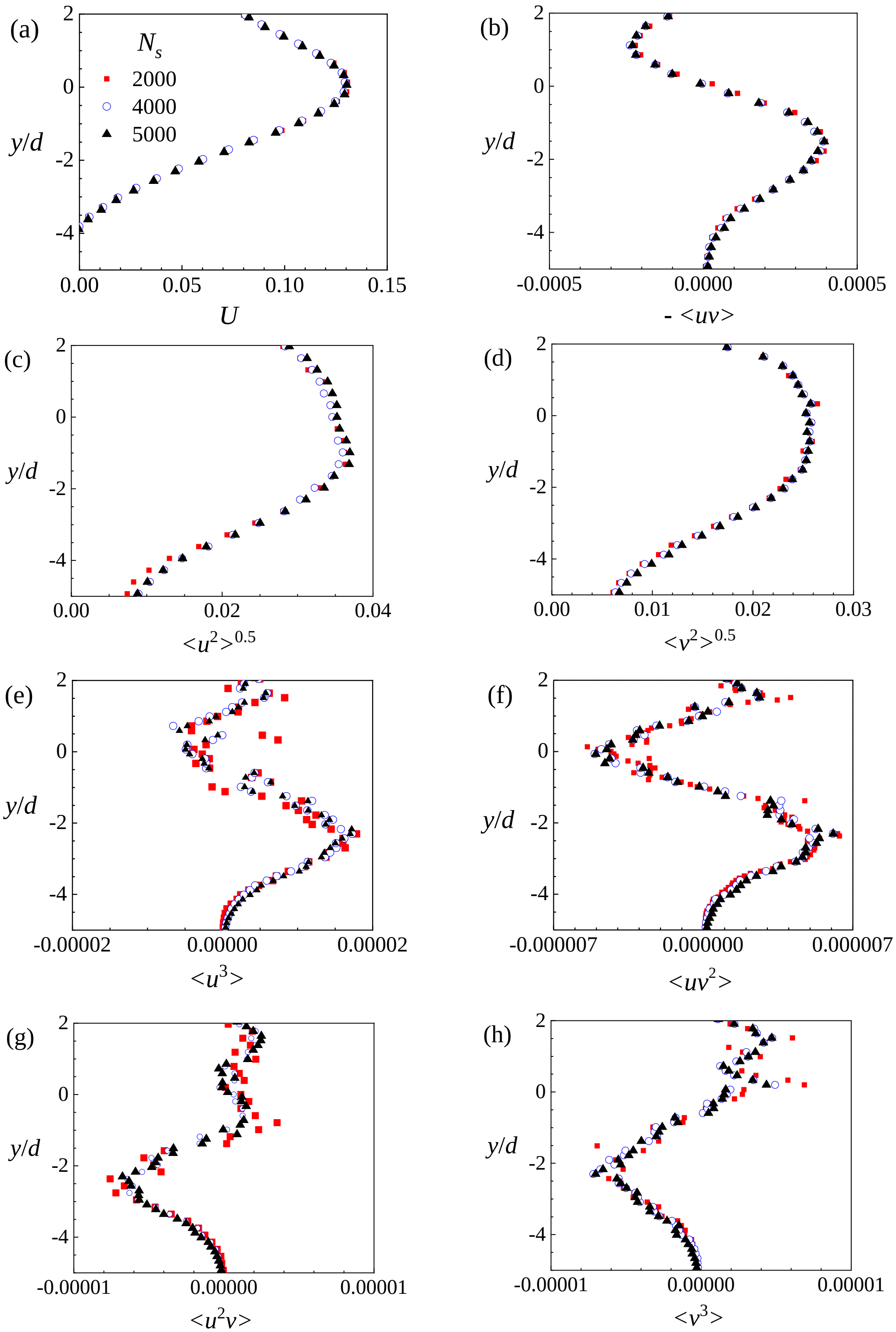

Figure C.2. Turbulence statistics with different sample sizes for square jet with *h/d* = 2 at *x/d* = 20. The *x*-axis is in SI unit.

APPENDIX D

EFFECT OF SPATIAL RESOLUTION ON TURBULENCE STATISTICS

This appendix provides results obtained from an initial data processing by varying particle image velocimetry interrogation area (IA) sizes. This initial data processing allows assessment of the effects of spatial resolution on the mean velocity and higher order turbulence statistics. The resolution test was performed using the following three IA sizes: 32 pixels × 32 pixels with 50% overlap, 32 pixels × 16 pixels with 50% overlap, and 16 pixels × 32 pixels with 50% overlap.

The results of the resolution test for the two extreme conditions of the experiments related to offset height effect, $h/d = 1$ and 4 are shown in Fig. D.1 and D.2, respectively. Profiles up to the third order moment are shown in the figures at $x/d = 10$, a location in the surface jet region for $h/d = 1$ and close to the surface jet region for $h/d = 4$. The results showed that the mean and turbulent quantities were almost independent of the spatial resolutions tested except for some scattered data in case of 16 pixels × 32 pixels for higher order moments. The scattered data could be attributed to the small number of particles within the IA when the streamwise spatial extent of the IA is reduced from 32 pixels to 16 pixels. Based on these observations, 32 pixels × 32 pixels was selected as the IA size for the data processing in the present study.

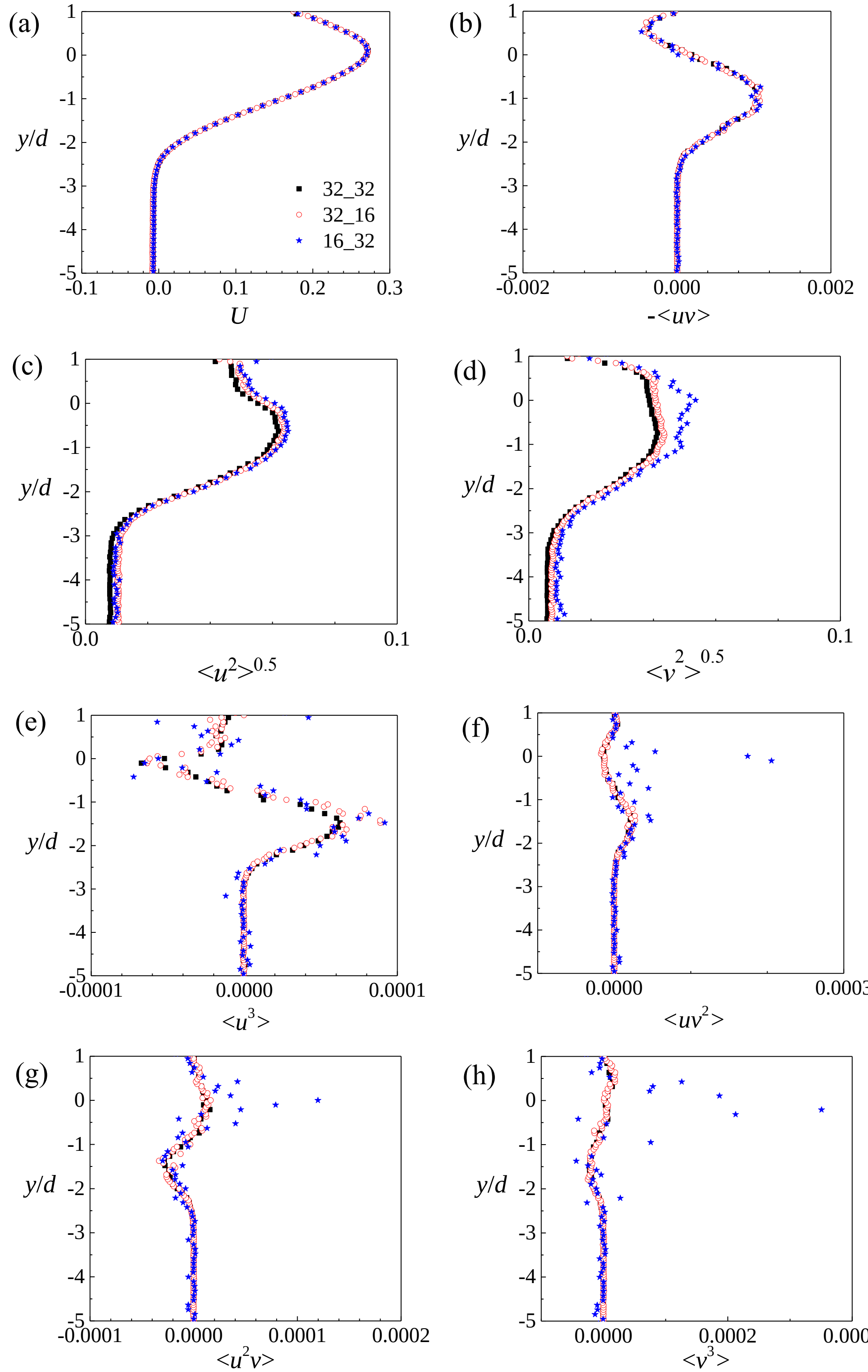

Figure D.1. Turbulence statistics with different IA sizes for *h/d* = 1 at *x/d* = 10. The *x*-axis is in SI unit.

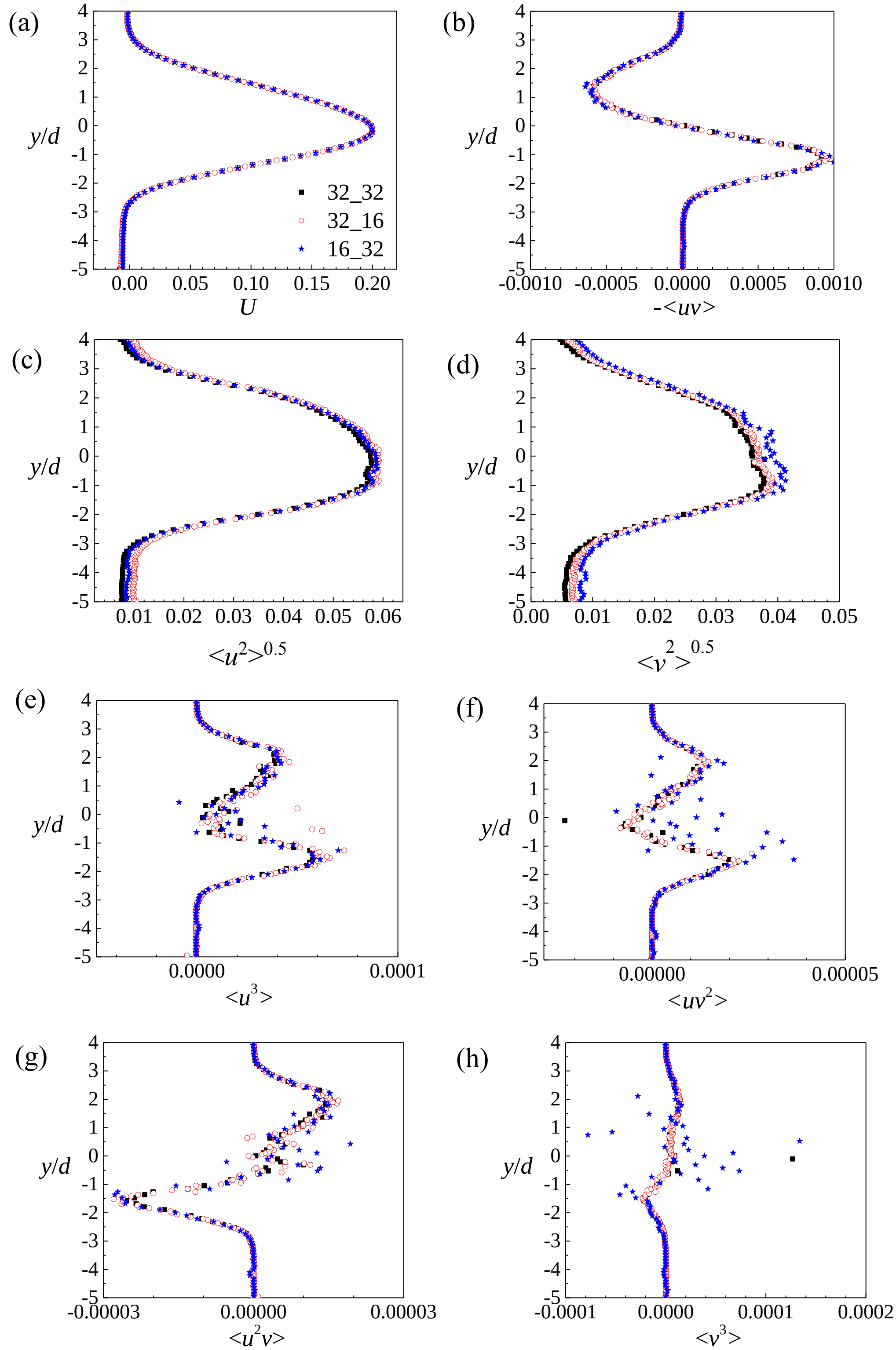

Figure D.2. Turbulent statistics with different IA sizes for *h/d* = 4 at *x/d* = 10. The *x*-axis is in SI unit.

APPENDIX E

EXPERIMENTAL UNCERTAINTY ANALYSIS

This appendix provides details of the procedure followed in estimating the uncertainties in the experimental variables. Estimating the uncertainty of the mean velocity is presented as a sample calculation.

E.1 Methodology of Estimating Uncertainty

The AIAA methodology derived by Coleman and Steele (1995) was used to estimate the uncertainties. The procedure is outlined as follows. For a given measurement system, if a measured variable, R, can be expressed as a function of independent variables, X_1, X_2, X_3, ..., X_n, the total uncertainty E_R in R can be quantified as

$$E_R^2 = B_R^2 + P_R^2 \tag{E.1}$$

where B_R and P_R are the total systematic and random errors in R caused by uncertainties in the determination of the X_i's. The combined systematic and random errors in the independent variables are found by expanding B_R and P_R in a Taylor series. Dropping higher order terms in the expansion would result in expressions of the form

$$B_R{}^2 = \sum_{i=1}^{n} \theta_i{}^2 B_i{}^2 + 2\sum_{i=1}^{n-1} \sum_{k=i+1}^{n} \theta_i \theta_k B_{ik}{}^2 \tag{E.2}$$

and

$$P_R{}^2 = \sum_{i=1}^{n} \theta_i{}^2 P_i{}^2 + 2\sum_{i=1}^{n-1}\sum_{k=i+1}^{n} \theta_i \theta_k P_{ik}{}^2 \tag{E.3}$$

where $\theta_i = \partial R/\partial X_i$ are called sensitivity coefficients, B_i and P_i are the systematic and random uncertainty limits in X_i, and B_{ik} and P_{ik} are the correlated systematic and random uncertainty limits in X_i and X_k. Combining Equations E.2 and E.3 yields the equation

$$E_R{}^2 = \sum_{i=1}^{n} \theta_i{}^2 B_i{}^2 + 2\sum_{i=1}^{n-1}\sum_{k=i+1}^{n} \theta_i \theta_k B_{ik}{}^2 + \sum_{i=1}^{n} \theta_i{}^2 P_i{}^2 + 2\sum_{i=1}^{n-1}\sum_{k=i+1}^{n} \theta_i \theta_k P_{ik}{}^2 \tag{E.4}$$

which is called the error propagation equation for variable R. Expressions for B_i, B_{ik}, P_i, and P_{ik} are of the form $B_i = Kb_i$, $B_{ik} = K^2 b_{ik}$, $P_i = KS_i$, $P_{ik} = KS_{ik}$, where b_i, b_{ik}, S_i, and S_{ik} are estimates of the systematic and random uncertainty limits. The confidence coefficient factor, K is derived from a Student K distribution. For a large number of observations ($N_s \geq 10$), $K = 2$ at the 95% confidence level.

In the present analysis, the systematic uncertainty limits were obtained from the manufacturer's specifications supplied with the PIV system. The random uncertainty limits of the measured variables were calculated using the alternate approach suggested by Stern et al. (1999). In the alternate approach, assuming correlated random uncertainties are negligible, rather than compounding the elemental random uncertainty limits as in Equation E.3, P_R can be obtained from repeatability tests on R. If S_R is the standard deviation of N_s samples of R, then P_R is given by

$$P_R = \frac{KS_R}{\sqrt{N_s}} \tag{E.5}$$

where, K = 2 for a sample size $N_s \geq 10$ at the 95% confidence level. The standard deviation is calculated from

$$S_R = \left[\sum_{k=1}^{N_s} \frac{\left(R_k - \langle R \rangle\right)^2}{N_s - 1} \right]^{1/2} \tag{E.6}$$

where $\langle R \rangle$ is the mean value of the N_s samples of R given by

$$\langle R \rangle = \frac{1}{N_s} \sum_{k=1}^{N_s} R_k \tag{E.7}$$

E.2 Sample Calculation of Uncertainty

In the present measurements, the systematic error in the mean velocity is considered to be of the same order as the error in the instantaneous velocities. In PIV, the instantaneous velocity at a point is the average fluid velocity over an interrogation area and is given by

$$U_i = \frac{\Delta s}{M_f \Delta t} \tag{E.8}$$

where i = 1 and 2, Δt is the time between laser pulses, Δs is the particle displacement from the correlation algorithm, and M_f is the camera magnification. Using Equation E.2 and assuming no correlated systematic uncertainty limits in the independent variables, the systematic uncertainty limit in U_i is given by

$$B_{U_i}{}^2 = \theta_{\Delta s}{}^2 B_{\Delta s}{}^2 + \theta_{\Delta t}{}^2 B_{\Delta t}{}^2 + \theta_{M_f}{}^2 B_{M_f}{}^2 \quad \text{(E.9)}$$

The sensitivity coefficients are given by

$$\theta_{\Delta s} = \frac{\partial U_i}{\partial \Delta s} = \frac{1}{M_f \Delta t}, \ \theta_M = \frac{-\Delta s}{M_f{}^2 \Delta t} \ \text{ and } \ \theta_{\Delta t} = \frac{-\Delta s}{M_f \Delta t^2} \quad \text{(E.10)}$$

The uncertainty estimation in the mean velocity, U is illustrated for the square jet as a representative case. The procedure is summarized in Table E.1 along with the manufacturer's specifications for the systematic uncertainty limits in Δs, Δt and M_f. Also shown is the mean value of the streamwise velocity at the centerline of the jet at the exit. The calculations were based on a magnification of M_f = 24.4 pixels/mm (based on FOV of 84 × 84 mm^2), where the camera pixel pitch is d_{pitch} = 7.4µm.

Table E.1. Systematic uncertainty limits of the mean streamwise velocity near the exit.

Variable	**Magnitude**	$\boldsymbol{B_X}$	$\boldsymbol{\theta_X}$	$\boldsymbol{B_X\theta_X}$	$\boldsymbol{(B_X\theta_X)^2}$
Δs (pix)	11.60E+00	1.27E-02	1.56E+01	1.98E-01	3.92E-02
M_f	24.40E+01	2.00E-01	-7.41E+00	-1.48E+00	2.20E+004
Δt (s)	2.63E-03	1.00E-07	-6.87E+04	-6.87E-03	4.72E-05
U (m/s)	5.54E-01	-	-	-	-

$$B_{U_i}{}^2 = \sum (B_{X_i} \theta_{X_i})^2 = 2.23$$

$$B_{U_i} = 1.5$$

Total systematic uncertainty limit, B_R = 1.5/5.54E-01 = 2.7 %.

To compute the random uncertainty limit, a total of 5000 instantaneous images were captured, and divided into 10 sets of 500 images per set. The mean velocity, $U(x, y)$ was calculated for each set to yield 10 different values of U for each grid location. The values of U at $y/d = 0$ at the exit were extracted, and averaged to give a mean value of 0.554 m/s with a standard deviation of 2.24 % in accordance with Equations E.6 and E.7. From Equation E.5, this yields a random uncertainty limit approximately of $P_R = 1.4\%$.

Using Equation E.1 the total experimental uncertainty in the streamwise mean velocity is

$$E_R = \sqrt{2.7^2 + 1.4^2} \approx 3.0\%.$$

BIBLIOGRAPHY

Adrian, R.J., Chung, M.K., Hassan, Y., Nithianandan, C.K., and Tung, A.T.-C, 1989. Approximation of turbulent conditional averages by stochastic estimation. Physics of Fluids A, 1(6), 992 – 998.

Adrian, R.J., 1991. Particle imaging techniques for experimental fluid mechanics. Ann. Rev. Fluid Mech., 23, 261-304.

Adrian, R.J., Christensen, K.T., and Liu, Z.-C., 2000a. Analysis and interpretation of instantaneous turbulent velocity fields. Experiments in Fluids, 29, 275 – 290.

Adrian, R.J., Meinhart, C.D., and Tomkins, C.D., 2000b. Vortex organization in the outer region of the turbulent boundary layer. Journal of Fluid Mechanics, 422,1–54.

Agelin-Chaab, M. and Tachie, M.F., 2011a. Characteristics of turbulent three-dimensional wall jets. Journal of Fluids Engineering, 133, 1-12. DOI: 10.1115/1.4003277.

Agelin-Chaab, M. and Tachie, M.F., 2011b. Characteristics and structure of turbulent 3D offset jets. International Journal of Heat and Fluid Flow, 32, 608–620.

Agelin-Chaab, M. and Tachie, M.F., 2011c. Characteristics of turbulent three-dimensional offset jets. Journal of Fluids Engineering, 133, 1–9.

Agrawal, A. and Prasad, A.K., 2002. Properties of vortices in the self-similar turbulent jet. Experiments in Fluids, 33, 565-577.

Aleyasin, S.S., Tachie, M.F., and Koupriyanov, M., 2017a. PIV Measurements in the near and intermediate field regions of jets issuing from eight different nozzle geometries. Flow Turbul. Combust. 99, 329-351. DOI: https://doi.org/10.1007/s10494-017-9820-3.

Aleyasin, S.S., Tachie, M.F., and Koupriyanov, M., 2017b. Statistical properties of round, square, and elliptic jets at low and moderate Reynolds numbers. J. Fluids Eng. 139(10), 101206. DOI: 10.1115/1.4036824.

Aleyasin, S.S., Fathi, N., Tachie, M.F., Vorobieff, P., and Koupriyanov, M., 2018. On the development of incompressible round and equilateral triangular jets due to Reynolds number variation. Journal of Fluids Engineering, 140(11), 111202. DOI: 10.1115/1.4040031.

Anthony, D.G. and Willmarth, W.W., 1992. Turbulence measurement in a round jet beneath a free surface. J. Fluid Mech., 243, 699-720.

Antonia, R.A, Chambers, A.J, Britz, D., and Browne, L.W.B., 1986. Organized structures in a turbulent jet: topology and contribution to momentum and heat transport. J. Fluid Mech., 172, 211-229. DOI: https://doi.org/10.1017/S0022112086001714.

Ashcroft, G. and Zhang, X., 2005. Vortical structures over rectangular cavities at low speed. Physics of Fluids, 17(1), id. 015104, DOI: https://doi.org/10.1063/1.1833412.

Baddour, R.E., Zaghloul, A., and Martinuzzi, R., 2006. Entrainment properties of plane surface-jets in shallow current. Journal of Hydraulic Engineering, 132(4), 363-370.

Ball, C.G., Fellouah, H., and Pollard, A., 2012. The flow field in turbulent round free jets. Progress in Aerospace Sciences, 50, 1–26.

Bi, W., Sugii, Y., Okamoto, K., and Madarame, H., 2003. Time-resolved proper orthogonal decomposition of the near-field flow of a round jet measured by dynamic particle image velocimetry. Measurement Science and Technology, 14, L1–L5.

Bian, S., Driscoll, J.F., Elbing, B.R., and Ceccio, S.L., 2011. Time resolved flow-field measurements of a turbulent mixing layer over a rectangular cavity. Exp. Fluids. 51, 51-63.

Bogey, C. and Bailly, C., 2006. Large eddy simulations of transitional round jets: Influence of the Reynolds number on flow development and energy dissipation. Phys. Fluids, 18, id. 065101. DOI: https://doi.org/10.1063/1.2204060.

Bogey, C. and Bailly, C., 2009. Turbulence and energy budget in a self-preserving round jet: direct evaluation using large eddy simulation. J. Fluid Mech. 627, 129-160.

Bourque, C. and Newman, B.G., 1960. Reattachment of a two-dimensional incompressible jet to an adjacent flat plate. Aero. Quart., 11, 201–232.

Breuer, K.S. and Sirovich, L., 1991. The use of Karhunen-Loève procedure for the calculation of linear eigenfunctions. J. Comp. Phys., 96, 277-296.

Bridges, J.E. and Hussain, A.K.M.F., 1987. Roles of initial condition and vortex pairing in jet noise. Journal of Sound and Vibration, 117 (2), 289-311. DOI: https://doi.org/10.1016/0022-460X(87)90540-2.

Brown, G.L. and Roshko, A., 1974. On density effects and large structure in turbulent mixing layers. Journal of Fluid Mechanics, 64(4), 775-816. DOI: https://doi.org/10.1017/S002211207400190X.

Capone, A., Soldati, A., and Romano, G.P., 2013. Mixing and entrainment in the near field of turbulent round jets. Exp Fluids, 54 (1), 1434. DOI: 10.1007/s00348-012-1434-x.

Chen, N. and Yu, H., 2014. Mechanism of axis switching in low aspect-ratio rectangular jets. Computers and Mathematics with Applications, 67, 437–444.

Christensen, K.T. and Adrian, R.J., 2001. Statistical evidence of hairpin vortex packets in wall turbulence. J. Fluid Mech., 431, 433 – 443.

Cizmas, P.G., Palacious, A., Brien, T.O., and Syamlal, M., 2003. Proper orthogonal decomposition of spatio-temporal patterns in fluidized beds. Chem. Eng. Sci., 58, 4417–4427.

Coleman, H.W. and Steele, W.G., 1995. Engineering applications of experimental uncertainty analysis. AIAA Journal, 33(10), 1888-1896.

Craft, T.J., Kidger, J.W., and Launder, B.E., 2000. Second-moment modelling of developing and self-similar 3D turbulent free-surface jets. International Journal of Heat and Fluid Flow, 21, 338-344.

Crow, S.C. and Champagne, F.H., 1971. Orderly structure in jet turbulence. Journal of Fluid Mechanics, 48(3), 547-591. DOI: https://doi.org/10.1017/S0022112071001745.

Davis, M.R. and Winarto, H., 1980. Jet diffusion from a circular nozzle above a solid plane. J. Fluid Mech., 101(1), 201-221.

Deo, R.C., Mi, J., and Nathan, G.J., 2007. The influence of nozzle aspect ratio on plane jets. Experimental Thermal and Fluid Science, 31(8), 825-838. DOI: 10.1016/j.expthermflusci.2006.08.009.

Dimotakis, P.E., Miake-Lye, R.C., and Papantoniou, D.A., 1983. Structure and dynamics of round turbulent jets. Physics of Fluids, 26, 3185. DOI: https://doi.org/10.1063/1.864090.

Ead, S.A. and Rajaratnam, N., 2001. Plane turbulent surface jets in shallow tailwater, J. Fluid Eng., 123, 121-127.

Essel E.E. and Tachie M.F., 2015. Roughness effects on turbulent flow downstream of a backward facing step. Flow Turbul. Combust. 94, 125–153.

Essel, E.E, Nematollahi, A., Thacher, E.W., and Tachie, M.F., 2015. Effects of upstream roughness and Reynolds number on separated and reattached turbulent flow. J. Turbul. 16(9), 872–899.

Essel, E.E. and Tachie, M.F., 2018. Submerged turbulent twin jets interacting with a free surface and a solid wall. International Journal of Heat and Fluid Flow, 71, 27–38. DOI: https://doi.org/10.1016/j.ijheatfluidflow.2018.03.004.

Evans, J.T., 1955. Pneumatic and similar breakwaters. Proceedings of the Royal Society A, 231(1187), 457-466.

Fellouah, H., Ball, C.G., and Pollard, A., 2009. Reynolds number effects within the development region of a turbulent round free jet. International Journal of Heat and Mass Transfer, 52, 3943–3954.

Fiedler, H.E., 1988. Coherent structures in turbulent flows. Prog. Aerosp. Sci., 25(3), 231–269.

Forliti, D.J., Strykowski, P.J., and Debatin, K., 2000. Bias and precision errors of digital particle image velocimetry. Experiments in Fluids, 28(5), 436–447.

Gamard, S., Jung, D., and George, W.K., 2004. Downstream evolution of the most energetic modes in a turbulent axisymmetric jet at high Reynolds number. Part 2. The farfield region. J. Fluid Mech., 514, 205–230.

Gao, N. and Ewing, D., 2007. Experimental investigation of planar offset attaching jets with small offset distances. Exp. Fluids, 42, 941–954.

Gentile, V., Schrijer, F.F.J., Oudheusden, B.W.van, and Scarano, F., 2016. Afterbody effects on axisymmetric base flows. AIAA Journal, 54(8), 2285-2294.

Ghasemi, A., Roussinova, V., Balachandar, R., and Barron, R.M., 2015. Reynolds number effects in the near-field of a turbulent square jet. Experimental Thermal and Fluid Science, 61, 249–258.

Gordeyev, S.V. and Thomas, F.O., 2000. Coherent structure in the turbulent planar jet. Part1. Extraction of proper orthogonal decomposition eigenmodes and their self-similarity. J. Fluid Mech., 414, 145 - 195.

Gordeyev, S.V. and Thomas, F.O., 2002. Coherent structure in the turbulent planar jet. Part 2. Structural topology via POD eigenmode projection. J. Fluid Mech., 460, 349-380.

Grinstein, F.F., Gutmark, E., and Parr, T., 1995. Near field dynamics of subsonic free square jets. A computational and experimental study. Phys. Fluids. 7(6), 1483-1497. DOI: https://doi.org/10.1063/1.868534.

Grinstein, F.F., 2001. Vortex dynamics and entrainment in rectangular free jets. J. Fluid Mech., 437, 69 - 101.

Gutmark, E. and Wygnanski, I., 1976. The planar turbulent jet. J. Fluid Mech., 73(3), 465-495.

Gutmark, E.J., Schadow, K.C., Parr, T.P., Hanson-Parr, D.M., and Wilson, K.J., 1989. Noncircular jets in combustion systems. Exps. Fluids, 7, 248.

Gutmark, E. and Grinstein, F.F., 1999. Flow control with noncircular jets. Annu. Rev. Fluid Mech. 31, 239–272.

Hanjalić, K. and Launder, B.E., 1980. Sensitizing the dissipation equation to irrotational strains. J. Fluids Eng., 102(1), 34-40. DOI: doi:10.1115/1.3240621.

Hashiehbaf, A. and Romano, G.P., 2013. Particle image velocimetry investigation on mixing enhancement of non-circular sharp edge nozzles. Int. J. Heat Fluid Flow, 44, 208–221.

Hassan, M.El and Meslem, A., 2010. Time-resolved stereoscopic particle image velocimetry investigation of the entrainment in the near field of circular and daisy-shaped orifice jets. Physics of Fluids, 22, id. 035107. DOI: https://doi.org/10.1063/1.3358465.

Ho, C.M. and Gutmark, E., 1987. Vortex induction and mass entrainment in a small-aspect-ratio elliptic jet. J. Fluid Mech., 179, 383 - 405.

Holmes, P., Lumley, J.L., and Berkooz, G., 1996. Turbulence, coherent structures, dynamical systems and symmetry. Cambridge University Press, New York.

Hussain, A.K.M.F. and Clark, A.R., 1981. On the coherent structure of the axisymmetric mixing layer - A flow-visualization study. Journal of Fluid Mechanics, 104, 263-294. DOI: 10.1017/S0022112081002917.

Hussain, A.K.M.F. and Zaman, K.B.M.Q., 1981. The ‘preferred mode’ of the axisymmetric jet. Journal of Fluid Mechanics, 110, 39-71. DOI: https://doi.org/10.1017/S0022112081000608.

Hussain, A.K.M.F., 1983. Coherent structures - reality and myth. Physics of Fluids, 26(10), 2816 – 2850.

Hussain, A.K.M.F., 1986. Coherent structures and turbulence. Journal of Fluid Mechanics, 173, 303–356.

Hussain, F. and Husain, H.S., 1989. Elliptic jets. Part 1. Characteristics of unexcited and excited jets. Journal of Fluid Mechanics, 208, 257-320,

Hussein, H.J., Capp, S.P., and George, W.K., 1994. Velocity measurements in a high-Reynolds-number, momentum-conserving, axisymmetric, turbulent jet. Journal of Fluid Mechanics, 258, 31–75.

Hutchins, N., Hambleton, W.T., and Marusic, I., 2005. Inclined cross-stream stereo particle image velocimetry measurements in turbulent boundary layers. J. Fluid Mech. 541, 21-54.

Iqbal, M.O. and Thomas, F.O., 2007. Coherent structure in a turbulent jet via a vector implementation of the proper orthogonal decomposition. J. Fluid Mech., 571, 281–326.

Krothapalli, A., Baganoff, D., and Karamcheti, K., 1981. On the mixing of rectangular jets. J. Fluid Mech., 107, 201 - 220.

Koshigoe, S., Gutmark, E., and Schadow, K., 1989. Initial development of non-circular jets leading to axis switching. AIAA J., 27, 411.

Kwon, S.J. and Seo, I.W., 2005. Reynolds number effects on the behaviour of a nonbuoyant round jet. Exp. Fluids, 38, 801–812.

Lai, M.K.Y., Vijay, M.M., and Zou, C., 1991. Computational fluid dynamics analysis of submerged cavitating water jets. Proc. 6th American Water Jet Conference (August, Houston, USA), Labus, T.J. (Ed.), Water Jet Technology Association, St. Louis, USA, paper 31, 411-426.

Lan, K. and Jorgenson, J.W., 2001. A hybrid of exponential and Gaussian functions as a simple model of asymmetric chromatographic peaks. Journal of Chromatography A, 915, 1–13. DOI: https://doi.org/10.1016/S0021-9673(01)00594-5.

Liepmann, D. and Gharib, M., 1992. The role of streamwise vorticity in the near-field entrainment of round jets. Journal of Fluid Mechanics, 245, 643-668.

Lozanova, M. and Stankov, P., 1998. Experimental investigation on the similarity of a 3D rectangular turbulent jet. Experiments in Fluids, 24(5–6), 470–478.

Lu, S.S. and Willmarth, W.W., 1973. Measurement of the structure of the Reynolds stress in a turbulent boundary layer. Journal of Fluid Mechanics, 60, 481 – 511.

Lumley, J.L., 1967. The structure of inhomogeneous turbulent flow. In Atmospheric Turbulence and Radio Wave Propagation (ed. Yaglon, A.M., and Tatarski, V.I.), 167-178, Nauka, Moscow.

Lund, T.S., 1986. Augmented thrust and mass flow associated with two-dimensional jet reattachment. AIAA J., 24, 1964–1970.

Madnia, C.K. and Bernal, L.P., 1994. Interaction of a turbulent round jet with the free surface. J. Fluid Mech., 261, 305-332.

Manivannan, P. and Sridhar, B.T.N., 2013. Characteristic study of non-circular incompressible free jet. Thermal Science, 17(3), 787-800.

McMullan, W.A., Gao, S., and Coats, C.M., 2007. A comparative study of inflow conditions for two-and three-dimensional spatially developing mixing layers using large eddy simulation. International Journal of Numerical Methods in Fluids, 55, 589–610.

Meyer, E.K., Pedersen, J.M., and Özcan, O., 2007. A turbulent jet in crossflow analysed with proper orthogonal decomposition. J. Fluid Mech., 583, 199-227.

Mi, J., Nathan, G.J., and Nobes, D.S., 2001. Mixing characteristics of axisymmetric free jets from a contoured nozzle, an orifice plate and a pipe. Journal of Fluids Engineering, 123(4), 878-883.

Mi, J., Kalt, P., Nathan, G.J., and Wong, C.Y., 2007. PIV measurements of a turbulent jet issuing from round sharp-edged plate. Experiments in Fluids, 42(4), 625–637.

Mi, J. and Nathan, G.J., 2010. Statistical properties of turbulent free jets issuing from nine differently-shaped nozzles. Flow Turbulence Combust. 84, 583–606.

Mi, J., Kalt, P., and Nathan, G.J., 2010. On turbulent jets issuing from notched-rectangular and circular orifice plates. Flow Turbulence Combust, 84, 565–582. DOI: 10.1007/s10494-009-9239-6.

Mi, J., Xu, M., and Zhou, T., 2013. Reynolds number influence on statistical behaviors of turbulence in a circular free jet. Physics of Fluids, 25, 075101. DOI: https://doi.org/10.1063/1.4811403.

Namer, I. and Ötügen, M.V., 1988. Velocity measurements in a plane turbulent air jet at moderate Reynolds numbers. Experiments in Fluids, 6, 387-399.

Nasr, A. and Lai, J.C.S., 1998. A turbulent plane offset jet with small offset ratio. Experiments in Fluids, 24, 47-57.

Nematollahi, A. and Tachie, M.F., 2018. Time-resolved PIV measurement of influence of upstream roughness on separated and reattached turbulent flows over a forward-facing step. AIP Advances, 8(10), id. 105110. DOI: https://doi.org/10.1063/1.5063455.

Nozaki, T., Hatta, K., Nakashima, M., and Matsumura, H., 1981. Reattachment flow issuing from a finite width nozzle (Report 2. Effects of initial turbulence intensity). Bull JSME, 24(188), 363–369.

Nyantekyi-Kwakye, B., Clark, S., Tachie, M.F., Malenchak, J., and Muluye, G., 2015a. Flow characteristics within the recirculation region of 3D turbulent offset jet. J. Hydraul. Res., 53(2), 230-242.

Nyantekyi-Kwakye, B., Tachie, M.F., Clark, S., Malenchak, J., and Muluye, G., 2015b. Experimental study of the flow structures of 3D turbulent offset jets. J. Hydraul. Res., 53(6), 773–786.

Obot, N.T., Graska, M.L., and Trabold, T.A., 1984. The near field behaviour of round jets at moderate Reynolds numbers. Canadian Journal Chemical Engineering, 62(5), 587-593. DOI: 10.1002/cjce.5450620503.

Ong, L. and Wallace, J.M., 1998. Joint probability density analysis of the structure and dynamics of the vorticity field of a turbulent boundary layer. J. Fluid Mech., 367, 291–328.

Paillat, S. and Kaminski, E., 2014. Second-order model of entrainment in planar turbulent jets at low Reynolds number. Physics of Fluids, 26, 045110. DOI: https://doi.org/10.1063/1.4871521.

Panchapakesan, N.R., and Lumley, J.L., 1993. Turbulence measurements in axisymmetric jets of air and helium. Part 1. Air jet. J. Fluid Mech. 246, 197-223.

Pelfrey, J.R.R. and Liburdy, J.A., 1986. Mean flow characteristics of a turbulent offset jet. J. Fluids Eng., 108(1), 82-88. DOI: doi:10.1115/1.3242548.

Petersen, R.A. and Samet, M.M., 1988. On the preferred mode of jet instability. Journal of Fluid Mechanics, 194, 153-173. DOI: https://doi.org/10.1017/S0022112088002939.

Pope, S.B., 2000. Turbulent Flows. Cambridge University Press.

Prasad, A.K., Adrian, R.J., Landreth, C.C., and Offutt, P.W., 1992. Effect of resolution on the speed and accuracy of particle image velocimetry interrogation. Experiments in Fluids, 13(2–3), 105–116.

Quinn, W.R. and Militzer, J., 1988. Experimental and numerical study of a turbulent free square jet. Phys. Fluids 31(5), 1017-1025.

Quinn, W.R. and Militzer, J., 1989. Effects of nonparallel exit flow on round turbulent free jets. International Journal of Heat and Fluid Flow, 10(2), 139-145.

Quinn, W.R., 1992. Turbulent free jet flows issuing from sharp-edged rectangular slots: The influence of slot aspect ratio. Experimental Thermal and Fluid Science, 5(2), 203 – 215. DOI: https://doi.org/10.1016/0894-1777(92)90007-R.

Quinn, W.R., 2005. Measurements in the near flow field of an isosceles triangular turbulent free jet. Exp. Fluids, 39(1), 111–126.

Quinn, W.R., 2006. Upstream nozzle shaping effects on near field flow in round turbulent free jets. European Journal of Mechanics - B/Fluids, 25(3), 279-301.

Quinn, W.R., 2007. Experimental study of the near field and transition region of a free jet issuing from a sharp-edged elliptic orifice plate. European Journal of Mechanics B/Fluids, 26, 583–614.

Quinn, W.R. and Azad, M., 2013. Mean flow and turbulence measurements in a turbulent free cruciform jet. Flow, Turbulence and Combustion, 91(4), 773–804.

Raffel, M., Willert, C.E., and Kompenhans, J., 1998. Particle image velocimetry: A practical guide Springer, New York.

Rainford, J.P. and Khan, A.A., 2009. Investigation of circular jets in shallow water. Journal of Hydraulic Research, 47(5), 611–618.

Rajaratnam, N. and Humphries, J.A., 1984. Turbulent non-buoyant surface jets. Journal of Hydraulic Research, 22(2), 103-115.

Ricou, F.P. and Spalding, D.B., 1961. Measurements of entrainment by axisymmetrical turbulent jets. Journal of Fluid Mechanics, 11(1), 21-32. DOI: https://doi.org/10.1017/S0022112061000834.

Robinson, S.K., 1991. Coherent motion in the turbulent boundary layer. Annual Review of Fluid Mechanics, 23, 601 – 639.

Sakai, Y., Tanaka, N., and Kushida, T., 2006a. On the development of coherent structure in a plane jet (Part 1, Characteristics of two-point velocity correlation and analysis of eigenmodes by the KL expansion). JSME Int. J., Series B, 49(1), 115-124.

Sakai, Y., Tanaka, N., Yamamoto, M., and Kushida, T., 2006b. On the development of coherent structure in a plane jet (Part 3, Multi-point simultaneous measurement of main streamwise velocity and the reconstruction of velocity field by the KL expansion). JSME Int. J., Series B, 49(3), 722-730.

Sankar, G., Balachandar, R., and Carriveau, R., 2008. Tailwater effects on the characteristics of a square jet near a free-surface. Journal of Hydraulic Research, 46(4), 504–515.

Sankar, G., Balachandar, R., and Carriveau, R., 2009. Characteristics of a three-dimensional square jet in the vicinity of a free surface. Journal of Hydraulic Engineering, 135(11), 989-994.

Sawyer, R.A., 1960. The flow due to a two dimensional jet issuing parallel to a flat plate. J. Fluid Mech., 9, 543–561.

Sfeir, A.A., 1979. Investigation of three-dimensional turbulent rectangular jets. AIAA J., 17, 1055 - 1060.

Shinneeb, A.-M., 2006. Confinement effects in shallow water jets. University of Sasketchewan, Saskatoon, Ph.D. Thesis.

Shinneeb, A.-M., Bugg, J.D., and Balachandar, R., 2008a. Quantitative investigation of vortical structures in the near-exit region of an axisymmetric turbulent jet. Journal of Turbulence, 9 (19), 1–20.

Shinneeb, A.-M., Balachandar, R., and Bugg, J.D., 2008b. Analysis of coherent structures in the far-field region of an axisymmetric free jet identified using particle image velocimetry and proper orthogonal decomposition. Journal of Fluids Engineering, 130, 1-9. DOI: 10.1115/1.2813137.

Shinneeb, A.-M., Bugg, J.D., and Balachandar, R., 2011. Coherent structures in shallow water jets. Journal of Fluids Engineering. 133, 1-14. DOI: 10.1115/1.4003194.

Sirovich, L., 1987. Turbulence and the dynamics of coherent structures, Part 1: Coherent structures. Quart. J. Appl. Math., 45(3), 561 – 571.

Stern, F., Muste, M., Beninati, M.-L., and Eichinger, W.E., 1999. Summary of experimental uncertainty assessment methodology with example. IIHR

Technical Report No. 406, Iowa Institute of Hydraulic Research, College of Engineering, The University of Iowa.

Swean, Jr., T.F., Ramberg, S.E., Plesniak, M.W., and Stewart, M.B., 1989. Turbulent surface jet in channel of limited depth. Journal of Hydraulic Engineering, 115(12), 1587-1606.

Tandalam, A., Balachandar, R., and Barron, R., 2010. Reynolds number effects on the near-exit region of turbulent jets. Journal of Hydraulic Engineering, 136(9), 633-641. DOI: 10.1061/(ASCE)HY.1943-7900.0000232.

Tay, G.F.K., Mishra, A., Kuhn, D.C.S, and Tachie, M.F., 2017. Free surface effects on the statistical properties of a submerged rectangular jet. Physics of Fluids, 29, 025101. DOI: 10.1063/1.4975155.

Terashima, O., Onishi, K., Sakai, Y., Nagata, K., and Ito, Y., 2014. Simultaneous measurement of all three velocity components and pressure in a plane jet. Measurement Science and Technology, 25. DOI: 10.1088/0957-0233/25/5/055301.

Tian, J., Roussinova, V., and Balachandar, R., 2012. Characteristics of a jet in the vicinity of a free surface. Journal of Fluids Engineering, 134, 1-12.

Tsuchiya, Y., Horikoshi, C., and Sato, T., 1986. On the spread of rectangular jets. Exps. Fluids, 4, 197 - 204.

Tsunoda, H., Shimizu, Y., and Kashiwagi, T., 2006. Plane offset jet discharged into water of finite depth. JSME Int. Journal, 49, 1111-1117.

Ukeiley, L. and Murray, N., 2005. Velocity and surface pressure measurements in an open cavity. Exp. Fluids. 38, 656-671.

Volino, R.J., Schultz, M.P., and Flack, K.A., 2007. Turbulence structure in rough- and smooth-wall boundary layers. J. Fluid Mech., 592, 263-293.

Volino, R.J., Schultz, M.P., and Flack, K.A., 2009. Turbulence structure in a boundary layer with two-dimensional roughness. J. Fluid Mech., 635, 75-101.

Wallace, J.M. and Brodkey, R.S., 1977. Reynolds stress and joint probability density distributions in the *u*-*v* plane of a turbulent channel flow. The Physics of Fluids, 20(3), 351. DOI: https://doi.org/10.1063/1.861897.

Wallker, D.T., Chen, C.-Y., and Willmarth, W.W., 1995. Turbulent structure in free-surface jet flows. J. Fluid Mech., 291, 223-261.

Wen, Q., Kim, H.D., Liu, Y.Z., and Kim, K.C., 2014a. Dynamic structures of a submerged jet interacting with a free surface. Experimental Thermal and Fluid Science, 57, 396–406.

Wen, Q., Kim, H.D., Liu, Y.Z., and Kim, K.C., 2014b. Structure analysis of a low Reynolds number turbulent submerged jet interacting with a free surface. Journal of Fluids Engineering. 136, 1-16. DOI: 10.1115/1.4027620.

Westerweel, J., 1997. Fundamentals of digital particle image velocimetry. Measurement Science and Technology, 8, 1379 – 1392.

Westerweel, J., Fukushima, C., Pedersen, J.M., and Hunt, J.C.R., 2005. Mechanics of turbulent-non-turbulent interface of a jet. Physical Review Letters, 95, id. 174501. DOI: https://doi.org/10.1103/PhysRevLett.95.174501.

Winant, C.D. and Browand, F.K., 1974. Vortex pairing: the mechanism of turbulent mixing-layer growth at moderate Reynolds number. Journal of Fluid Mechanics, 63(2), 237-255. DOI: https://doi.org/10.1017/S0022112074001121.

Wygnanski, I. and Fiedler, H., 1969. Some measurements in the self-preserving jet. J. Fluid Mech., 38, 577-612.

Xu, G. and Antonia, R.A., 2002. Effect of different initial conditions on a turbulent round free jet. Exp. Fluids, 33, 677 – 683.

Xu, M., Zhang, J., Mi, J., Nathan, G.J., Kalt, P.A.M., 2013. PIV measurements of turbulent jets issuing from triangular and circular orifice plates. Science China Physics, Mechanics and Astronomy, 56(6), 1176–1186.

Yule, A.J., 1978. Large-scale structure in the mixing layer of a round jet. Journal of Fluid Mechanics, 89(3), 413-432. DOI: https://doi.org/10.1017/S0022112078002670.

Zhou, J., Adrian, R.J., Balachandar, S., and Kendall, T.M., 1999. Mechanisms for generating coherent packets of hairpin vortices in channel flow. Journal of Fluid Mechanics, 387, 353 – 396.

Zhou, X. and Hitt, D.L., 2004. Proper orthogonal decomposition analysis of coherent structures in a transient buoyant jet. Journal of Turbulence, 5(1), id 28. DOI: 10.1088/1468-5248/5/1/028.